Wave models for the flexural vibrations of thin plates

Model of the vibrations of polygonal plates by the image source method
Vibration damping using the acoustic black hole effect

Jacques Cuenca

Doctoral thesis in Acoustics
Université du Maine, Le Mans, France, 2009

Université du Maine, Académie de Nantes
Doctoral School of Science Engineering, Geoscience and Architecture

Doctoral Thesis in Acoustics

Wave models for the flexural vibrations of thin plates

Model of the vibrations of polygonal plates by the image source method

Vibration damping using the acoustic black hole effect

Jacques Cuenca

Defended on the 20th October in front of the examining committee:

W. Desmet	Professor, Dept. of Mechanical Engineering, K.U. (Leuven)	Reviewer
B.R. Mace	Professor, ISVR (Southampton)	Reviewer
J.R.F Arruda	Professor, Faculdade de Engenharia Mecânica, Unicamp (Campinas)	Examiner
E. Foltête	Professor, FEMTO-ST (Besançon)	Examiner
V.V. Krylov	Professor, Dept. of Aeronautical and Automotive Engg. (Loughborough)	Examiner
E. Labiole	Development Engineer, Thales Alenia Space (Toulouse)	Examiner
C. Pezerat	Professor, LAUM (Le Mans)	Examiner
V. Martin	CNRS Research Director, IJLRDA (Paris)	Chairman
F. Gautier	Professor, LAUM (Le Mans)	Supervisor
L. Simon	Professor, LAUM (Le Mans)	Co-supervisor

Université du Maine, Académie de Nantes
École Doctorale: Sciences Pour l'Ingénieur, Géosciences, Architecture

Thèse de doctorat
Spécialité: Acoustique

Vibrations de flexion de plaques minces: approches ondulatoires

Modèle des vibrations de plaques polygonales basé sur la méthode des sources image

Absorption passive de vibrations par l'effet de trou noir acoustique

Jacques Cuenca

Soutenue le 20 octobre devant le jury composé de :

W. Desmet	Professeur, Dept. of Mechanical Engineering, K.U. (Louvain)	Rapporteur
B.R. Mace	Professeur, ISVR (Southampton)	Rapporteur
J.R.F Arruda	Professeur, Faculdade de Engenharia Mecânica, Unicamp (Campinas)	Examinateur
E. Foltête	Professeur, FEMTO-ST (Besançon)	Examinateur
V.V. Krylov	Professeur, Dept. of Aeronautical and Automotive Engg. (Loughborough)	Examinateur
E. Labiole	Ingénieur de Développement, Thalès Alenia Space (Toulouse)	Examinateur
C. Pezerat	Professeur, LAUM (Le Mans)	Examinateur
V. Martin	Directeur de Recherche CNRS, IJLRDA (Paris)	Président de jury
F. Gautier	Professeur, LAUM (Le Mans)	Directeur de thèse
L. Simon	Professeur, LAUM (Le Mans)	Co-directeur de thèse

Abstract

Flexural vibrations of thin structures are strongly related to sound radiation and structural damage, for which they deserve careful attention in many domains of science and engineering. Two aspects that are of crucial importance are accurate tools for the prediction and analysis of vibrations, which require appropriate modelling methods and numerical tools, and efficient vibration damping. The first aim of this thesis is to develop a model for predicting the flexural vibrations of thin polygonal plates of arbitrary convex shape in the medium and high frequency ranges. The second aim is to contribute to the development and understanding of the acoustic black hole effect as an alternative technique for passive vibration damping. Those two topics are developed in two separate parts.

In the first part of the dissertation, a model of the flexural vibrations of thin convex polygonal plates based on the image source method is presented. Considering a polygonal plate excited by a harmonic point source, the image source method consists in describing the successive wave reflections on the boundaries of the plate as contributions from virtual sources, obtained by successive symmetries of the original source with respect to the boundaries. First, the approach is applied to simply supported polygonal plates, which present the particularity that the reflection coefficient of the boundaries does not depend on the angle of incidence of waves. Then, the approach is generalised to the case of arbitrary boundary conditions in the case of individual plates and plate assemblies. This is achieved by representing the contributions of the different image sources as continuous sums of elementary waves. The relative weights of such elementary waves are determined by the reflection and transmission matrices of the boundaries, obtained from a state vector approach. It is shown that the method is particularly suitable for mid- and high-frequency dynamics, in that its accuracy is improved with an increase in frequency or structural damping. A tool for estimating the Young's modulus and structural damping ratio of highly damped flat panels is also proposed, using the image source method as a means of separately identifying the influence of stiffness and damping in the response.

The second part of the dissertation is an investigation on vibration damping using the acoustic black hole effect. It is well known that a flexural wave travelling in a thin plate or beam slows down in a zone of decreasing thickness. Thus, if the thickness decreases sufficiently smoothly to zero, the wave velocity reaches zero and the wave stops travelling, without being reflected back. Such is the principle of the so-called acoustic

black hole effect. Because of technological difficulties in achieving such a thickness profile, a thin damping layer partially covering the structure allows to compensate for non-zero reflection, leading to efficient vibration damping with a low amount of additional mass. In the present study, a model of the flexural vibrations of such profile is proposed, allowing to determine optimal geometrical and material properties for the damping layer allowing to maximise vibration damping. Experimental studies are then carried on plates whose boundaries induce a focusing of waves towards a zone treated with the thickness profile. The measured responses show a reduction of vibration level up to 20 decibels. An alternative implementation of the acoustic black hole effect is investigated, consisting in decreasing wave velocity near the edge of a beam by decreasing its Young's modulus. This is achieved by using a temperature gradient in a shape-memory polymer, leading to similar results to those obtained by a geometrical control of thickness. Finally, combining the thermoelastic and geometrical approaches leads to significant vibration damping.

Acknowledgements

This thesis was done in the Laboratoire d'Acoustique de l'Université du Maine (LAUM) in Le Mans, France, and represents three years of work, from September 2006 to September 2009. I would like to thank the people who contributed to the work presented herein and also those who made the PhD adventure an enjoyable experience.

First of all, I would like to give special thanks to my supervisors, Professors François Gautier and Laurent Simon. I am extremely grateful to them for their confidence, enthusiasm and constant encouragements during these three years. I particularly appreciate their rigour and dynamism, which they shared with me with remarkable pedagogy. Thanks to them I was able to get involved in many research and teaching activities, on which working together was very formative. I am also grateful to them for their trust on me in responsibilities such as supervising student projects. Their constant good mood and positiveness on our activities motivated me to go further everyday. I consider myself very lucky to have had François and Laurent as supervisors.

I am very grateful to Professors Brian Mace and Wim Desmet for having reviewed this thesis and to Roberto Arruda, Emmanuel Foltête, Victor Krylov, Vincent Martin, Charles Pezerat, Eric Labiole for their participation in the examination. I greatly appreciate their interest in the ideas developed here, and in particular their pragmatism and rigour. Their comments and corrections helped me in having a more mature overview of my work.

The scientific and administrative contexts of this work played a very important role. I want to thank the director of LAUM, Yves Aurégan, and succeeding co-directors, Jean-Michel Génevaux and Rachid El Guerjouma, for their remarkable work on the administration of the laboratory and their contribution to the life of Université du Maine. Also, from them I learnt many aspects of how research really works, in terms of organisation and strategy. This work was done in the framework of the research activities of the vibrations, guided acoustics and flow acoustics group (équipe vibrations, acoustique guidée et écoulement) of LAUM. I thank all the participants of that group for their interest in each other's investigations, thus making it possible to improve the coherence between all research directions, including the work presented herein.

In the framework of the acoustic black hole project, I had the opportunity to work closely with Vasil Georgiev, post-doctoral fellow, Miguel Molerón, Master's student and Hervé Mézière, design engineer. The project would not have been possible without them and I am very grateful for that. Since the beginning of the project, we were in collaboration with Professor Victor Krylov from Loughborough University. Many thanks to him for sharing with us his knowledge and experience about the acoustic black hole effect. The experimental studies carried out on plates and beams of different shapes would not have been possible without the personnel of the mechanics workshop of the Institut Universitaire de Technologie (IUT) of Le Mans, Serge Collin, Yves Carbonnel and especially Stanislas Renard and Alain Aragot. Many thanks to them for their remarkable work and admirable precision in making the plates used for the experiments. Other people helped in the various experiments and they should be greatly acknowledged. Amongst them are Adil Ayouch and Professor Samuel Gougeon of École Nationale Supérieure d'Ingénieurs du Mans (ENSIM), who were particularly helpful in settling the infrared camera used for some experiments. Also, some students were involved in preliminary experimental studies on different aspects of this thesis, in the framework of projects that I supervised together with Professors François Gautier and Laurent Simon. Thanks to the students Samuel Pinson, Mathieu Buzaré, Bo Lu, Florent Le Courtois, Julie Aka and Jean-Philippe Binet for their enthusiasm and perseverance. I also thank other members of LAUM, Claude Depollier, Nicolas Joly, Guillaume Penelet, Nicolas Dauchez, and Michel Bruneau for the very fruitful discussions that we had, for their help with technical aspects and for their advise. Many thanks to Jean-Michel Génevaux for carefully reading this thesis and giving me very pertinent suggestions for improvement.

External collaborations played a very important role throughout this three years. I would like to thank Sylvain Germès, Christophe Chaut and Jean-Luc Vojtovicki from Henkel Adhesive Technologies for providing us with a car floor panel sample. Also, the study presented in the last chapter of this thesis would not have been possible without Emmanuel Foltête, Jan Klesa and their collaborators from FEMTO-ST, Besançon. They provided us with the material and the data needed as a start point for performing the numerical and experimental investigations. Many thanks to them. I am very grateful to Vincent Martin, who asked the most pertinent questions during my presentations at different international conferences. The discussions we had played a very important role in developing the image source approach presented herein and in clarifying several ideas. Thanks to Charles Pézerat and Laurent Maxit from INSA, Lyon, for their interest in the image source approach and its application to structural dynamics. I also want to thank Jean-Philippe Roux, Olivier Robin and Marie-Hélène Moulet from the Centre d'Études Vibro-Acoustiques pour l'Automobile (CEVAA), Rouen, for their interest in the acoustic black hole project.

My financial support was provided by the Ministère de l'Éducation Nationale et de la Recherche Scientifique. Also, the financial support of Vasil Georgiev was provided by the French region Pays de la Loire. Thanks to those organisations for supporting research. I hope his will continue to be the case for future generations.

Many thanks to the colleagues with whom I worked in the preparation of teaching material for the different degrees in Acoustics of Université du Maine I participated in: Bruno Brouard, Olivier Dazel, Catherine Potel, Laurent Simon, Christophe Ayrault, François Gautier, Nicolas Dauchez, Frédéric Ablitzer, Thierry Le Van Suu and Olivier Richoux. Also many thanks to all the students for their continuous (yet many times discontinuous) efforts.

I am deeply indebted to all the staff of LAUM and to the PhD students with whom I shared these three years, especially to Adrien Pelat, Anne Degroot, Stéphane Griffiths, Benoît Mérit, Tony Valier-Brasier and Frédéric Ablitzer for their help and support, for our many and very fruitful conversations on our everyday lives. Many thanks to Ygaäl Renou, Guillaume Nief, Jean-Loïc Le Carrou, Mathias Rémy, Marcos Pinho, Antonin Novák, Claude Inserra, Olivier Doutres, Sylvain Mézil, Mohamed Khelil, Mourad Bentahar, Yousra Baccouche, Simon Félix, Bertrand Lihoreau and Vincent Tournat. These three years would not have been the same without them and without their friendship.

During this last year, I had the opportunity (and the honour!) of being part of the amateur baroque music ensemble *Rondo Crannasiano*, with whom I enjoyed very much playing and discovering beautiful (and some times not so beautiful) pieces. I wish to express my gratitude to Jean-Pierre Dalmont, Véronique Dubois, Amandine Gatien, Olivier Dazel, Joël Gilbert and Frédéric Ablitzer for all the time spent together.

Finally, I want to thank my friends and my family, especially my parents and my brother, for their constant support and comprehension, for their encouragements and for their accompaniment throughout the ups and downs during all these years.

Contents

Abstract i

Acknowledgements iii

List of symbols xi

Introduction 1

I Model of the vibrations of polygonal plates by the image source method 7

1 Introduction to the image source method 9
- 1.1 General considerations on flexural wave motion in thin plates 9
- 1.2 Motivation for using an image source approach 12
  - 1.2.1 Statement of the problem 12
  - 1.2.2 Integral formulation of the flexural vibrations of a polygonal plate 12
  - 1.2.3 Discussion 15
- 1.3 The image source method and its applications 16
  - 1.3.1 General considerations 16
  - 1.3.2 Previous developments of the image source method 17
- 1.4 Overview of the proposed approach 17

2 The image source method for simply supported polygonal plates 19
- 2.1 Introduction 20
- 2.2 Green's functions of convex polygonal plates 21
  - 2.2.1 Statement of the problem 21
  - 2.2.2 Modal expansion of the Green's function 22
  - 2.2.3 Image source method (ISM) 23
  - 2.2.4 Obtaining a modal expansion of the Green's function from ISM . . 24
  - 2.2.5 Examples 26
- 2.3 Effect of truncation of the image source cloud 32
  - 2.3.1 Truncation of the image source cloud 32
  - 2.3.2 Influence of structural damping on the accuracy of AISM 34

2.3.3 Application of AISM to an arbitrary polygonal plate 36
2.3.4 Influence of the truncation radius on the accuracy of AISM 38
2.4 Conclusion 39
2.A Construction of the image source cloud 41
2.B Elementary cells of equilateral and half-equilateral triangular plates . . . 43
2.B.1 Half-equilateral triangular plate 43
2.B.2 Equilateral triangular plate 44
2.C Asymptotic modal overlap factor 45

3 Model of boundary conditions of plates by a state vector approach 47
3.1 Model of flexural wave motion by the state vector approach 47
3.1.1 Global and local coordinates 48
3.1.2 Matrix form of the equations of motion 49
3.1.3 Specifying the eigenvalue and eigenvector matrices 50
3.2 Model of the boundary conditions 53
3.2.1 Reflection matrix of a plate edge 53
3.2.2 Scattering matrix of a junction between two plates 54
3.3 Some examples 56
3.3.1 Edges 56
3.3.2 Junctions 61
3.4 Conclusion 62

4 Harmonic Green's functions of semi-infinite and polygonal plates 65
4.1 Introduction 66
4.2 Green's function of an infinite plate 67
4.3 Green's function of a semi-infinite plate 68
4.3.1 Formulation of the problem 68
4.3.2 Validation of the formulation for simply supported, roller supported, clamped and free boundary conditions 70
4.4 Green's function of a convex polygonal plate 71
4.4.1 Formulation of the problem 71
4.4.2 Geometrical construction of image sources 72
4.4.3 Image sources of first order 73
4.4.4 Image sources of second and higher orders 73
4.4.5 Domain of applicability of the solution 75
4.5 Numerical implementation 76
4.6 Results 76
4.6.1 Levy-type plate: comparison to the exact solution 77
4.6.2 Arbitrary polygonal plates: comparison to finite element method . 78
4.7 Conclusion 80
4.A Green's function of an infinite plate in rectangular coordinates 82
4.B Case of reflection without angular dependence 83
4.C Discrete Fourier transform 84
4.D Variable separation in different coordinate systems 85
4.E Arbitrary polygonal plate with free boundaries 86

5 On the extension of the image source method to plate assemblies 89
5.1 Statement of the problem . . . 89
5.2 Image source method for an assembly of two plates . . . 90
5.2.1 Geometrical construction of image sources . . . 90
5.2.2 Model of the junction . . . 91
5.2.3 Displacement field of the assembly . . . 93
5.3 Validation . . . 95
5.3.1 Virtual junction between two rectangular plates . . . 95
5.3.2 Virtual junction between two arbitrarily polygonal plates . . . 96
5.4 Conclusion . . . 97

6 Measurement of complex bending stiffness of a flat panel 101
6.1 Introduction . . . 102
6.2 Model . . . 103
6.2.1 Green's problem of the flexural motion of the plate . . . 103
6.2.2 Solution by the image source method . . . 104
6.3 Experimental setup . . . 107
6.3.1 Description of the experimental setup . . . 107
6.3.2 Calibration of the measurement system . . . 107
6.4 Estimation of the bending stiffness of the panel . . . 108
6.4.1 Modulus of the bending stiffness . . . 109
6.4.2 Young's modulus and structural damping ratio . . . 110
6.5 Conclusion . . . 111

II Vibration damping in beams and plates using the acoustic black hole effect 113

7 Acoustic black hole effect in thin plates 115
7.1 Introduction . . . 116
7.2 Existing models . . . 116
7.2.1 Model of Mironov . . . 116
7.2.2 Model of Krylov . . . 118
7.2.3 Discussion . . . 120
7.3 Model of the acoustic black hole effect by the state vector approach . . . 120
7.3.1 Flexural vibrations of a variable-thickness beam covered with a damping layer . . . 120
7.3.2 Numerical implementation . . . 123
7.3.3 Illustration of the black hole effect . . . 124
7.3.4 Effect of the different parameters of the damping layer . . . 126
7.3.5 Simulated driving-point mobilities . . . 131
7.4 Experimental results on elliptical plates . . . 131
7.5 Vibration damping in polygonal plates using the black hole effect . . . 134
7.5.1 Statement of the problem . . . 134
7.5.2 Manufacturing of the plates . . . 135
7.5.3 Experimental results . . . 136
7.5.4 Model by the image source method . . . 138

7.6 Conclusion 139

8 Acoustic black hole effect in shape-memory materials 143
8.1 Introduction 143
8.2 Model 144
8.2.1 Statement of the problem 144
8.2.2 Determination of the complex Young's modulus of the material . . 144
8.2.3 Numerical simulations 147
8.3 Experimental observations 149
8.3.1 Experimental setup 149
8.3.2 Experimental results 150
8.4 Conclusion 150

Conclusion 153

References 159

List of symbols

The following list summarises the main mathematical symbols used throughout this document, with their respective unit and a short description. Where no unit is given, the symbol is either unitless or corresponds to a matrix whose rows or columns have different units.

General symbols

$\mathbb{C}$	Set of complex numbers.
$\mathbb{R}$	Set of real numbers.
$\mathbb{I}$	Set of imaginary numbers.
Ω	Spatial domain occupied by a given plate; also refers to the plate itself.
$\partial\Omega$	Edges of plate Ω.
$\partial^2\Omega$	Vertices of plate Ω.

Time, frequency, space and wavenumber variables

t	s	Time.
f	s^{-1}	Frequency.
ω	$\mathrm{rad}\cdot\mathrm{s}^{-1}$	Circular frequency.
$\mathbf{r}$	m	Spatial coordinate vector.
x, y	m	Spatial coordinates in the global coordinate system.
ξ, μ	m	Spatial coordinates in the local coordinate system of a plate boundary.
α	rad	Angle between global and local coordinate systems.
n, l	m	Outgoing normal and tangential coordinates to a boundary.
z	m	Space variable normal to the plate surface.
$\mathbf{k}$	m^{-1}	Wavenumber vector of flexural waves.
k_x, k_y	m^{-1}	Components of the wavenumber vector in the global coordinate system.
k_ξ, k_μ	m^{-1}	Components of the wavenumber vector in the local coordinate system.

Physical parameters of plates

h	m	Plate thickness.
S	m^2	Plate surface area.
p	m	Plate perimeter.
ρ	$\mathrm{kg{\cdot}m^{-3}}$	Density.
η		Structural damping ratio.
E_0	Pa	Young's modulus.
E	Pa	Complex Young's modulus, $E = E_0(1-j\eta)$, according to time convention $e^{-j\omega t}$.
ν		Poisson's ratio.
D	$\mathrm{Pa{\cdot}m^3}$	Flexural rigidity or bending stiffness.
k_f	$\mathrm{m^{-1}}$	Flexural wavenumber.
c_ϕ	$\mathrm{m{\cdot}s^{-1}}$	Phase velocity of flexural waves.
c_γ	$\mathrm{m{\cdot}s^{-1}}$	Group velocity of flexural waves.

Vibrational field variables

w	m	Plate transverse displacement.
θ_ξ		Plate slope along ξ axis.
θ_μ		Plate slope along μ axis.
M_ξ	N	Bending moment acting on a cross-section of normal ξ.
M_μ	N	Bending moment acting on a cross-section of normal μ.
$M_{\xi\mu}$	N	Twisting moment, equal to $M_{\mu\xi}$.
Q_ξ	$\mathrm{N{\cdot}m^{-1}}$	Shear force on a cross-section of normal ξ.
Q_μ	$\mathrm{N{\cdot}m^{-1}}$	Shear force on a cross-section of normal μ.
V_ξ	$\mathrm{N{\cdot}m^{-1}}$	Total shear force on a cross-section of normal ξ.
V_μ	$\mathrm{N{\cdot}m^{-1}}$	Total shear force on a cross-section of normal μ.

Modal properties of flexural vibrations

n	s	Modal density.
$\Delta\omega_p$	$\mathrm{s^{-1}}$	-3 dB-bandwidth of resonance p.
$\delta\omega_p$	$\mathrm{s^{-1}}$	Circular frequency interval between resonances p and $p+1$.
Q		Quality factor of a resonance.
MOF		Modal overlap factor.

Green's functions

$H_0^{(1)}$		Hankel's function of order zero of the first kind.
G_∞	m	Green's function of an infinite plate.
G_Ω	m	Green's function of a semi-infinite or polygonal plate.
G_s	m	Contribution of image source s to G_Ω.
$G_s^{(\mathrm{I})}$	m	Contribution of first order image source s to G_Ω.
$G_s^{(\mathrm{II})}$	m	Contribution of second or higher order image source s to G_Ω.

Image source method

$\mathcal{D}_\Omega$		Image source cloud of plate Ω.
$\mathcal{E}$		Elementary pattern of a periodic image source cloud.
$\mathcal{P}_\Omega$		Periodisation function of a periodic image source cloud.
V		Zone of validity of an image source.
N_v		Number of vertices of a polygonal plate.
v_n		Vertices of a polygonal plate, with $n = 1, 2, \ldots, N_v$.
r_c	m	Characteristic length of a polygonal plate.
r_t	m	Truncation distance of the image source cloud.
γ		Truncation parameter $\gamma = r_t / r_c$.
$\mathbf{r}_0$	m	Position of the original source.
$\mathbf{r}_s$	m	Position of image source s.
$A_{pp}^{(s)}$		Amplitude weight of source s including only propagating-to-propagating wave reflection.

State vector representation

$\mathbf{W}$		State vector.
$\mathbf{H}$		Transition matrix.
$\mathbf{\Lambda}$	m^{-1}	Eigenvalue matrix.
$\mathbf{E}$		Eigenvector matrix.
$\mathbf{V}$		Wave vector.
$\mathbf{V}_+$		Forward-travelling wave vector.
$\mathbf{V}_-$		Backward-travelling wave vector.
$\mathbf{P}$		State propagator matrix.
$\mathbf{Q}$		Wave propagator matrix.
$\mathbf{B}$		Boundary matrix.
$\mathbf{J}$		Junction matrix.
$\mathbf{R}$		Reflection matrix.
$\mathbf{R}_{--}$		Reflection matrix of a boundary of plate Ω_-.
$\mathbf{R}_{++}$		Reflection matrix of a boundary of plate Ω_+.
$\mathbf{T}$		Transmission matrix.
$\mathbf{T}_{-+}$		Transmission matrix from plate Ω_- to plate Ω_+.
$\mathbf{T}_{+-}$		Transmission matrix from plate Ω_+ to plate Ω_-.
R_{ir}		Term of the reflection matrix of a boundary representing the coupling between incident (i) and reflected (r) propagating (p) and evanescent (e) waves, e.g. $R_{pp}, R_{ep}, R_{pe}, R_{ee}$.
T_{it}		Term of the transmission matrix of a boundary representing the coupling between incident (i) and transmitted (t) waves.

Acoustic black hole effect

T	s	Travel time of a wave in a plate or beam.
R		Reflection coefficient of a black hole edge for propagating waves.
$\mathbf{R}$		Reflection matrix of an edge.
$\mathbf{Z}$	$\mathrm{kg{\cdot}s^{-1}}$	Impedance matrix of a beam.
$h(x)$	m	Thickness of a black hole beam or plate, varying with coordinate x.
ε		Sharpness parameter of the black hole wedge.
b	m	Beam width.
ρ_l	$\mathrm{kg{\cdot}m^{-1}}$	Density of the damping layer.
E_l	Pa	Young's modulus of the damping layer.
η_l		Structural damping ratio of the damping layer.
h_l	m	Thickness of the damping layer.
l	m	Length of the damping layer.
x_i	m	Distance from the beginning of the black hole profile to its tip.
x_t	m	Truncation length of the black hole profile.
x_{obs}	m	Observation point.
τ	K	Temperature.

Operators and miscellaneous symbols

∇	$\mathrm{m^{-1}}$	Del vector differential operator.
Δ	$\mathrm{m^{-2}}$	Laplacian operator.
$\mathcal{F}_\xi$		Fourier transform from variable ξ to a dual variable k_ξ, also noted $\bar{w}(k_\xi) = \mathcal{F}\left[w(\xi)\right]_{(k_\xi)}$.
$\mathcal{F}_\xi^{-1}$		Inverse Fourier transform from variable k_ξ to variable ξ, also noted $w(\xi) = \mathcal{F}^{-1}\left[\bar{w}(k_\xi)\right]_{(\xi)}$.
$*$		Convolution operator.
ϕ^*		Complex conjugate of function ϕ.
$\mathrm{diag}(a_i)$		Diagonal matrix based on series a_i.
$\tilde{G}$		Approximation of function G.
ε		Error estimation.

Introduction

The seek for quality and reliability of structures in aerospace, aeronautic and automotive industries, civil engineering and many other domains of science and technology requires constant evolution and improvement of the existing models and theories for understanding structural vibrations. Amongst such wide range of applications, flexural vibrations of thin structures are strongly related to sound radiation and structural damage, for which they represent a major issue. In particular, mid- and high-frequency vibration problems require new analytical and numerical models for answering to the increasing requirements. Also, efficient methods of vibration damping are of critical need in research and industry. The aim of this thesis is to develop a model for predicting the flexural vibrations of thin polygonal plates of arbitrary convex shape in the medium and high frequency ranges by using the image source method and to contribute to the development and understanding of the acoustic black hole effect as an alternative technique for passive vibration damping.

Context of the study

The first objective of this thesis concerns the prediction of the flexural vibrations of plates of arbitrary polygonal shape and arbitrary boundary conditions. A considerable number of methods exist for obtaining the response of such structures. Analytical modal expansion is probably the most intuitive and widely known method for calculating the response of a finite domain to a given excitation. It has been extensively used to predict the vibrations of plates of various shapes and properties [60]. However, in spite of the simplicity of its basic concept, analytical modal expansion is limited to few geometries and sets of boundary conditions. The foremost criticism that can be made in this context is that a particular method is needed for obtaining the modal shapes and natural frequencies of almost every plate shape. Furthermore, at high frequencies and in the presence of damping, modal density is substantial, such that considering modes individually is not appropriate, which renders modal methods unpractical.

Such analytical methods are difficult to adapt to arbitrary geometries and numerical tools are therefore needed. Today, the most widely used methods for predicting and analysing the vibrations of structures of complex shapes are certainly finite element methods (FEM) [102], which are based on the spatial discretisation of the structure. The major advantage of these approaches is that they are well adapted to structures of almost any geometrical shape. However, the maximum frequency of validity of FEM

is imposed by the dimension of the discretisation elements, which must be significantly smaller than the wavelength. As a consequence, calculation times become prohibitive in high-frequency situations. As an example, solving a complete FEM model of a passenger vehicle up to frequencies of several hundreds of cycles per second can be a matter of one to three weeks of computation in today's standard high-performance computers. A similar concept, the boundary element method (BEM) [7], relies on the spatial discretisation of the structure boundary and has comparable limitations with frequency.

Another family of vibration prediction methods is statistical energy analysis (SEA). SEA is based on the description of coupled vibrating structures and/or acoustical cavities in terms of power flows [63], within the assumption of high modal density. In the original version of SEA [62], each sub-structure is characterised by its average vibration level in space and time. The major advantage of SEA is that it provides fast estimations of vibration levels and power flows for very complex structure assemblies. However, the main difficulties for the practical use of SEA are the determination of pertinent subsystems and the estimation of the coupling loss factors at junctions between substructures.

Because of the limitations of FEM and SEA, new methods constantly arise and are developed. Extensions and improvements of SEA have arisen, allowing to predict the spatial distribution of vibrations within sub-structures (see for example the work of Le Bot [9]). Several other methods are extensions of FEM or SEA or are based on hybrid FEM-SEA approaches (see for example Refs. [9, 13]), which are intended to take advantage of the complementary frequency ranges of applicability of FEM and SEA. Also, hybrid wave-FEM methods have been developed [25, 66, 97] for the analysis of structures that present symmetry properties in one direction of space, i.e. waveguides or periodic structures. In such methods, the cross-section of the waveguide is modelled by using a finite element approach, while the motion in the direction presenting symmetry is described as a superposition of travelling waves, thus leading to relatively small numerical models, capable of modelling waveguides with complex cross-sections. Rather different formalisms have also been developed. The wave-based method (WBM) [24, 83, 95] is one of them and consists of an expansion of the response of a finite domain in terms of wave functions, which are solutions of the governing equations. The individual contribution weights of such functions are determined by the boundary conditions. Such method is suitable for mid-frequency acoustic and structural acoustic applications of individual and coupled structures for geometries of moderate complexity [94]. Hybrid FEM-WBM computation tools also exist [41]. Another method that has gained recent attention is the variational theory of complex rays [58, 88], which consists in describing the dynamic field of a finite structure as a superposition of interior modes, edge modes and corner modes. Such method is applicable in a mid-frequency context. Specifically for plate vibration, other ray-based methods exist, for example for predicting time averaged vibration field spatial distributions for individual and coupled plates in high frequencies [12]. An extensive bibliographic review of mid- and high-frequency methods is also given in Ref. [12].

The approach that is proposed in the present document consists in the application of the image source method to flexural vibrations of plates. The image source method is widely used in room acoustics for predicting the sound field, the impulse response and reverberation time of enclosed acoustical cavities [2, 8, 16, 23, 53, 57, 59]. For an enclosed

domain originally excited by a point source, the image source method consists in representing successive wave reflections on the domain boundaries by virtual sources obtained from successive symmetries of the original source with respect to the boundaries. It has gained recent interest as an alternative method to modal approaches and boundary element formulations in acoustics [14, 36, 68–70, 72]. The starting point of the present study on the image source method is the work of Gunda et al. [38, 39], who showed its robustness in the case of flexural vibrations of semi-infinite and rectangular plates. In fact, the main particularity of the method is that its accuracy increases with frequency and structural damping. Therefore, it represents a potentially interesting method for mid- and high-frequency vibration modelling and analysis. On this basis, the aim of the first part of this dissertation is to evaluate the pertinence of an image source approach for describing flexural vibrations of plates in a high frequency and high structural damping context.

The second objective of this thesis concerns passive damping of flexural vibrations. For the construction of automotive, aeronautic and aerospace vehicles, light-weight materials are of crucial importance for the reduction of fuel consumption. However, vibration damping of such structures often requires significant amounts of added mass. One of the most common damping techniques for plates and shells consists in covering the structures with viscoelastic layers [15, 48], as done for the various panels present in aircraft and automotive vehicles. On the other hand, different solutions exist for achieving vibration damping with low amounts of added mass. For example, it is well-known that an adequate manner of damping plate vibrations without covering layers is by reducing wave reflections from edges. Furthermore, plates with reasonably absorbing boundaries can be of great use for conducting experiments requiring infinite plate conditions, as for example flexural wave localisation [101]. Moreover, semi-infinite plate or beam conditions are required for the experimental characterisation of boundary conditions [29, 77, 78, 86]. One example of realisation is the work of Vemula et al. [96], who proposed a configuration involving a gradual change in impedance at the edges of a bar, using a side-by-side juxtaposition of bars of different materials. In such arrangement, the stiffness of the compound bar gradually decreases towards the edge, where a viscoelastic strip is placed.

The approach that is of particular interest in the present document was proposed by Krylov et al. [51, 52, 54–56] based on the work of Mironov [73] and consists of a bar or plate whose thickness smoothly decreases to zero over a finite distance, which is followed by a decrease of wave velocity. In fact, for a sufficiently smooth thickness profile, an incident flexural wave is slowed down until it is completely stopped and the wave does not reflect back. In practice, technological difficulties arise since the decreasing thickness profile is always truncated due to the limited precision of cutting machines. In this framework, the main difficulty is the optimisation of the geometrical and mechanical parameters for reducing wave reflection as much as possible. Such considerations have been theoretically, numerically and experimentally studied in one-dimensional configurations. The aim of the second part of this dissertation is to study the acoustic black hole effect in two-dimensional configurations as a means of damping flexural vibrations in plates and to investigate an alternative technique for decreasing wave velocity in beams by taking advantage of their thermoelastic properties.

Structure of the document

Part I is the major contribution of this thesis and consists of a model of the flexural motion of polygonal plates and polygonal plate assemblies, based on the image source method. Chap. 1 gives an introduction to the image source method, its applications and limitations. Chap. 2 discusses the application of the image source method to simply supported convex polygonal plates. Exact Green's functions of four different plate geometries are obtained and the convergence of the method for plates of arbitrary convex polygonal shapes is examined. Simply supported edges present the particularity that the reflection coefficient does not depend on the angle of incidence of waves. Therefore, arbitrary boundary conditions are modelled by using a state vector approach, in chap. 3. Chap. 4 presents a generalisation of the image source method to semi-infinite and convex polygonal plates with arbitrary boundary conditions. Chap. 5 discusses the application of the image source method to an assembly of two plates. Chap. 6 presents a method for measuring the Young's modulus and structural damping ratio of highly damped panels. This is done by comparing simulated driving-point mobilities using the image source method to experimental data.

Part II discusses the application of the acoustic black hole effect to flexural vibrations of thin plates and beams as a passive vibration damping method. In chap. 7, the application of the acoustic black hole effect to vibration damping in plates is investigated. A one-dimensional model and numerical tool of a beam with variable thickness and mechanical properties is presented. A practical two-dimensional implementation is presented, consisting of plates whose thickness decreases towards an inner point, in the form of a circular pit. Also, simulated responses using the image source method are compared to experimental results in the case of polygonal plates having one parabolic edge with an acoustic black hole pit in its focal zone. Chap. 8 is an investigation of the acoustic black hole effect in beams made of a shape memory polymer. Temperature-dependent material properties are used as an alternative technique for controlling the velocity of waves with a temperature gradient and therefore to reduce wave reflection from an edge. Numerical and experimental results are presented.

Below is an organisation chart that summarises the different chapters of this document with their corresponding titles. The arrows illustrate the direct links between the chapters and thus possible guidelines for reading. Chaps. 2 to 5 consist in the model of the vibrations of polygonal plates and plate assemblies by the image source method and thus are grouped together. Chap. 1 is an introduction to that model and chap. 6 is an experimental application. Chaps. 7 and 8 discuss different configurations for achieving the acoustic black hole effect. The link between the two parts of the thesis is that the image source method is used for modelling polygonal plates with an acoustic black hole boundary.

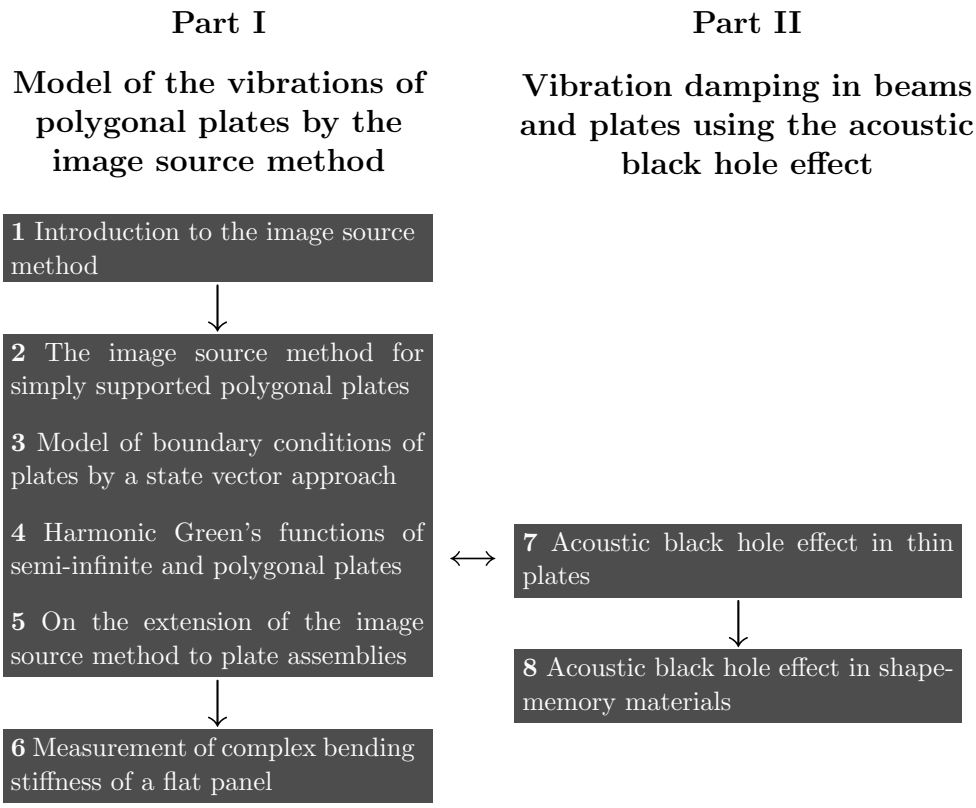
Part I
Model of the vibrations of polygonal plates by the image source method
Part II
Vibration damping in beams and plates using the acoustic black hole effect
1 Introduction to the image source method
2 The image source method for simply supported polygonal plates
3 Model of boundary conditions of plates by a state vector approach
4 Harmonic Green's functions of semi-infinite and polygonal plates
5 On the extension of the image source method to plate assemblies
6 Measurement of complex bending stiffness of a flat panel
7 Acoustic black hole effect in thin plates
8 Acoustic black hole effect in shape-memory materials

Part I

Model of the vibrations of polygonal plates by the image source method

Chapter 1

Introduction to the image source method

Abstract

The purpose of this chapter is to give a general insight into the image source method. First, the description of flexural motion of thin plates within the Kirchhoff assumptions is recalled in order to set the variables, coordinate systems and governing equations used throughout this document. Then, the integral representation of the Green's function of a polygonal plate is reviewed in order to justify the choice of the image source method for modelling high frequency vibrations. The applications and limitations of the method are then detailed. The two different approaches of the image source method that are developed in the following chapters are briefly presented here as an introduction.

1.1 General considerations on flexural wave motion in thin plates

The aim of this section is to introduce the different variables needed for describing flexural motion in a thin plate, and to derive the propagation equation for the transverse displacement. The motion of the plate is considered in the framework of Kirchhoff's theory of thin plates, which ignores shearing of cross sections and rotational inertia [81]. The plate is assumed to be isotropic, with thickness h, density ρ, Young's modulus E and Poisson's ratio ν. Fig. 1.1 shows the different forces and moments acting on a plate element of surface area $dxdy$ without any external force, centred at point (x, y) and at a given time t. The state of such surface element is described by the variables [34]

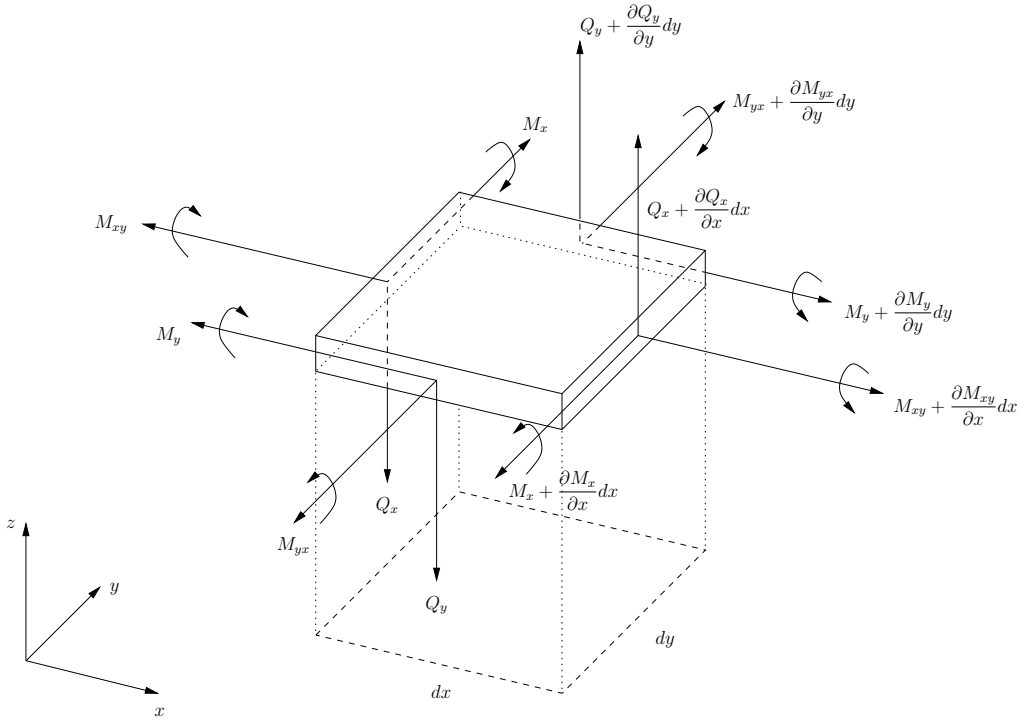

Figure 1.1: Surface element of a thin plate with applied forces and moments. After Graff [34].

$$w = w(x, y, t), \tag{1.1}$$

$$\theta_x = \frac{\partial w}{\partial x}, \tag{1.2}$$

$$\theta_y = \frac{\partial w}{\partial y}, \tag{1.3}$$

$$M_x = -D\left(\frac{\partial^2 w}{\partial x^2} + \nu \frac{\partial^2 w}{\partial y^2}\right), \tag{1.4}$$

$$M_y = -D\left(\frac{\partial^2 w}{\partial y^2} + \nu \frac{\partial^2 w}{\partial x^2}\right), \tag{1.5}$$

$$M_{xy} = M_{yx} = -(1-\nu)D\frac{\partial^2 w}{\partial x \partial y}, \tag{1.6}$$

$$Q_x = -D\left(\frac{\partial^3 w}{\partial x^3} + \frac{\partial^3 w}{\partial x \partial y^2}\right), \tag{1.7}$$

$$Q_y = -D\left(\frac{\partial^3 w}{\partial y^3} + \frac{\partial^3 w}{\partial x^2 \partial y}\right), \tag{1.8}$$

where w is the normal displacement, θ_x and θ_y are the slopes along x and y directions, M_x and M_y are the bending moments, M_{xy} and M_{yx} are the twisting moments, Q_x and

Q_y are the shear forces and

$$D = \frac{Eh^3}{12\,(1-\nu^2)} \tag{1.9}$$

is the flexural rigidity or bending stiffness of the plate. By using total shear forces, which include the effect of the twisting moments in the form

$$V_x = Q_x - \frac{\partial M_{xy}}{\partial y} = -D\left(\frac{\partial^3 w}{\partial x^3} + (2-\nu)\frac{\partial^3 w}{\partial x \partial y^2}\right), \tag{1.10}$$

$$V_y = Q_y - \frac{\partial M_{yx}}{\partial x} = -D\left(\frac{\partial^3 w}{\partial y^3} + (2-\nu)\frac{\partial^3 w}{\partial x^2 \partial y}\right), \tag{1.11}$$

the state of motion of the plate is described by variables w, θ_x, θ_y, M_x, M_y, V_x and V_y.

The governing equations for a portion of plate of infinitesimal surface area are [34]

$$\frac{\partial Q_x}{\partial x} + \frac{\partial Q_y}{\partial y} = \rho h \frac{\partial^2 w}{\partial t^2}, \tag{1.12}$$

$$\frac{\partial M_y}{\partial y} + \frac{\partial M_{xy}}{\partial x} - Q_y = 0, \tag{1.13}$$

$$\frac{\partial M_x}{\partial x} + \frac{\partial M_{xy}}{\partial y} - Q_x = 0. \tag{1.14}$$

Replacing Q_x and Q_y in Eq. (1.12) by their expressions as functions of the displacement w yields the propagation equation

$$\left(D\nabla^4 + \rho h \frac{\partial^2}{\partial t^2}\right) w(x,y,t) = f(x,y,t). \tag{1.15}$$

Considering harmonic excitation in the form $f \sim e^{-j\omega t}$, where ω is the circular frequency, gives the harmonic propagation equation

$$D\left(\nabla^4 - k_f^4\right) w(x,y;k_f) = f(x,y;k_f), \tag{1.16}$$

where k_f is the flexural wavenumber, given by

$$k_f = \left(\omega^2 \frac{\rho h}{D}\right)^{1/4}. \tag{1.17}$$

The phase and group velocities c_φ and c_γ of flexural waves assume the forms

$$c_\varphi = \frac{\omega}{k_f} = \left(\frac{Eh^2}{12\rho\,(1-\nu^2)}\right)^{1/4} \sqrt{\omega}, \tag{1.18}$$

$$c_\gamma = \frac{\partial \omega}{\partial k_f} = 2\left(\frac{Eh^2}{12\rho\,(1-\nu^2)}\right)^{1/4} \sqrt{\omega}. \tag{1.19}$$

Energy dissipation by dynamic deformation of structures is often referred to as structural damping. The main effect of the latter on periodic motion is a phase difference between

stress and strain [15], which can be taken into account by considering a complex Young's modulus according to the aforementioned time convention, in the form

$$E = E_0(1 - j\eta), \tag{1.20}$$

where η is the structural damping ratio [80].

1.2 Motivation for using an image source approach

1.2.1 Statement of the problem

The problem of interest is represented in Fig. 1.2 and consists of a harmonic source at point $\mathbf{r}_0$ creating a vibrational field in plate Ω, which is observed at point $\mathbf{r}$. The accurate description of the field in Ω, considering arbitrarily shaped polygonal boundaries $\partial\Omega$ and arbitrary boundary conditions, is the major difficulty and the main target of this thesis.

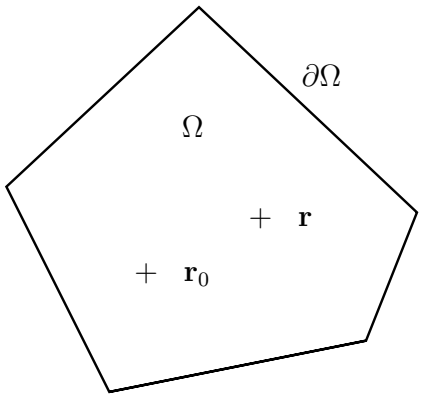

Figure 1.2: Polygonal plate Ω with boundaries $\partial\Omega$, harmonic source at $\mathbf{r}_0$ and observation point at $\mathbf{r}$.

Recalling Eq. (1.16), the Green's problem in the case of the flexural vibrations of a polygonal thin plate can be stated as

$$\begin{cases} D\left(\nabla^4 - k_f^4\right) G_\Omega(\mathbf{r}, \mathbf{r}_0; k_f) = \delta(\mathbf{r} - \mathbf{r}_0) & \mathbf{r} \in \Omega, \quad (1.21) \\ \text{Boundary conditions} & \mathbf{r} \in \partial\Omega, \quad (1.22) \end{cases}$$

where δ is the Dirac distribution and G_Ω is the Green's function of plate Ω.

1.2.2 Integral formulation of the flexural vibrations of a polygonal plate

A finite plate domain Ω whose boundary is denoted $\partial\Omega$ is considered. In order to derive the integral representation [61, 85] of the displacement field arising as the response to a

given excitation, Eq. (1.16) can be written for two states of vibration, as

$$\begin{cases} D\left(\nabla^4 - k_f^4\right) G_\infty(\mathbf{r}, \mathbf{r}_0; k_f) = \delta(\mathbf{r} - \mathbf{r}_0), & (1.23) \\ D\left(\nabla^4 - k_f^4\right) w(\mathbf{r}) = f(\mathbf{r}), & (1.24) \end{cases}$$

where $G_\infty(\mathbf{r}, \mathbf{r}_0; k_f)$ is the Green's function of the infinite plate for a harmonic point source at $\mathbf{r}_0$ and $w(\mathbf{r})$ is the displacement response to a given force per unit area $f(\mathbf{r})$, points $\mathbf{r}$ and $\mathbf{r}_0$ being strictly in domain Ω. The Green's function of the infinite plate is well known as the solution of Eq. (1.23) in polar coordinates [99]

$$G_\infty(\mathbf{r}, \mathbf{r}_0) = \frac{j}{8k_f^2 D}\left(H_0^{(1)}(k_f|\mathbf{r} - \mathbf{r}_0|) - H_0^{(1)}(jk_f|\mathbf{r} - \mathbf{r}_0|)\right), \tag{1.25}$$

where $H_0^{(1)}$ is the zeroth order Hankel's function of the first kind. An illustration of the real part of G_∞ is given in Fig. 1.3.

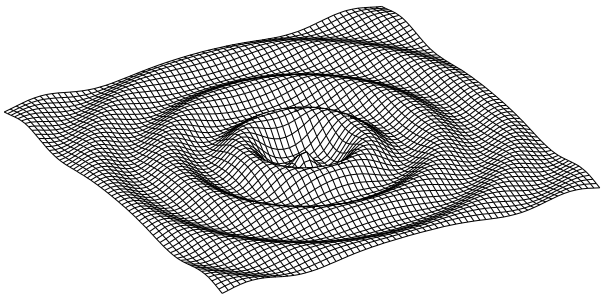

Figure 1.3: Real part of the Green's function of an infinite plate.

The product of each one of Eqs. (1.23) and (1.24) by the unknown function of the other yields

$$\begin{cases} w(\mathbf{r})D\nabla^4 G_\infty(\mathbf{r}, \mathbf{r}_0; k_f) - Dk_f^4 w(\mathbf{r})G_\infty(\mathbf{r}, \mathbf{r}_0; k_f) = \delta(\mathbf{r} - \mathbf{r}_0)w(\mathbf{r}), & (1.26) \\ G_\infty(\mathbf{r}, \mathbf{r}_0; k_f)D\nabla^4 w(\mathbf{r}) - Dk_f^4 G_\infty(\mathbf{r}, \mathbf{r}_0; k_f)w(\mathbf{r}) = f(\mathbf{r})G_\infty(\mathbf{r}, \mathbf{r}_0; k_f). & (1.27) \end{cases}$$

Equating these two expressions and integrating over domain Ω leads to the integral representation of the displacement field w in plate Ω in the form

$$w(\mathbf{r}_0) = \int_\Omega f(\mathbf{r})G_\infty(\mathbf{r}, \mathbf{r}_0; k_f)d\mathbf{r}^3 + D\int_\Omega \big(w(\mathbf{r})\nabla^4 G_\infty(\mathbf{r}, \mathbf{r}_0; k_f) - G_\infty(\mathbf{r}, \mathbf{r}_0; k_f)\nabla^4 w(\mathbf{r})\big)\, d\mathbf{r}^2, \tag{1.28}$$

which, by using the divergence theorem, can be written as

$$w(\mathbf{r}_0) = \int_\Omega f(\mathbf{r})G_\infty(\mathbf{r}, \mathbf{r}_0; k_f)d\mathbf{r}^3 + D\oint_{\partial\Omega} \nabla\left(w(\mathbf{r})\nabla^2 G_\infty(\mathbf{r}, \mathbf{r}_0; k_f) - G_\infty(\mathbf{r}, \mathbf{r}_0; k_f)\nabla^2 w(\mathbf{r})\right) d\mathbf{r}. \tag{1.29}$$

Writing the differential operator ∇ in local coordinates of the boundary, with n the outgoing normal coordinate and l the tangential coordinate, the derivative with respect to the latter vanishes because of the closed contour integral. The integral representation then assumes the form

$$w(\mathbf{r}_0) = \int_\Omega f(\mathbf{r}) G_\infty(\mathbf{r}, \mathbf{r}_0; k_f) d\mathbf{r}^3 + D \oint_{\partial\Omega} \left(\frac{\partial w}{\partial n}(\mathbf{r}) \Delta G_\infty(\mathbf{r}, \mathbf{r}_0; k_f) \right.$$
$$\left. + w(\mathbf{r}) \Delta \frac{\partial G_\infty}{\partial n}(\mathbf{r}, \mathbf{r}_0; k_f) - \frac{\partial G_\infty}{\partial n}(\mathbf{r}, \mathbf{r}_0; k_f) \Delta w(\mathbf{r}) - G_\infty(\mathbf{r}, \mathbf{r}_0; k_f) \Delta \frac{\partial w}{\partial n}(\mathbf{r}) \right) d\mathbf{r}. \quad (1.30)$$

Furthermore, denoting v_n $(n = 1, 2, \ldots, N_v)$ the vertices $\partial^2\Omega$ of the polygonal boundary $\partial\Omega$ and making use of Eqs. (1.3), (1.5), (1.6), (1.8) and (1.11) in the form

$$\theta_n = \frac{\partial w}{\partial n}, \quad (1.31)$$

$$M_n = -D \left(\frac{\partial^2 w}{\partial n^2} + \nu \frac{\partial^2 w}{\partial l^2} \right), \quad (1.32)$$

$$M_{ln} = M_{nl} = -(1-\nu) D \frac{\partial^2 w}{\partial l \partial n}, \quad (1.33)$$

$$Q_n = -D \Delta \frac{\partial w}{\partial n}, \quad (1.34)$$

$$V_n = Q_n - \frac{\partial M_{nl}}{\partial l}, \quad (1.35)$$

Eq. (1.30) can be written explicitly in function of the displacement, normal slope, bending moment, twisting moment and shear force for w and G_∞ as

$$w(\mathbf{r}_0) = \int_\Omega f(\mathbf{r}) G_\infty(\mathbf{r}, \mathbf{r}_0; k_f) d\mathbf{r}^3$$
$$+ \sum_{n=1}^{N_v} \int_{v_n}^{v_{n+1}} \left(G_\infty Q_n - w Q_n^{(\infty)} + \theta_n^{(\infty)} M_n - \theta_n M_n^{(\infty)} + \frac{\partial G_\infty}{\partial l} M_{ln} - \frac{\partial w}{\partial l} M_{ln}^{(\infty)} \right) d\mathbf{r}, \quad (1.36)$$

where superscript (∞) denotes quantities associated to G_∞. Integrating by parts the last two terms of the second integral yields

$$w(\mathbf{r}_0) = \int_\Omega f(\mathbf{r}) G_\infty(\mathbf{r}, \mathbf{r}_0; k_f) d\mathbf{r}^3$$
$$+ \sum_{n=1}^{N_v} \int_{v_n}^{v_{n+1}} \left(G_\infty V_n - w V_n^{(\infty)} + \theta_n^{(\infty)} M_n - \theta_n M_n^{(\infty)} \right) d\mathbf{r} + \sum_{n=1}^{N_v} \left[w M_{ln}^{(\infty)} \right]_{v_n}^{v_{n+1}}. \quad (1.37)$$

Here, the first integral is the direct contribution of the source to the total field of the plate, the second integral is a sum of individual contributions from the edges and the last term represents the individual contributions from the corners. The integral formulation can also be derived from the reciprocity principle, applied to two different states of deformation of the plate [5, 11].

Furthermore, the particular excitation

$$f(\mathbf{r}) = \delta(\mathbf{r} - \mathbf{r}_0) \tag{1.38}$$

yields the Green's function of the polygonal plate

$$w(\mathbf{r}) = G_\Omega(\mathbf{r}, \mathbf{r}_0). \tag{1.39}$$

Then, changing $\mathbf{r}$ into $\mathbf{r}'$ and $\mathbf{r}_0$ into $\mathbf{r}$ in Eq. (1.37) leads to the integral formulation of the Green's function of the polygonal plate

$$\begin{aligned} G_\Omega(\mathbf{r}, \mathbf{r}_0; k_f) =& G_\infty(\mathbf{r}, \mathbf{r}_0; k_f) \\ &+ \sum_{n=1}^{N_v} \int_{v_n}^{v_{n+1}} \Big(G_\infty(\mathbf{r}, \mathbf{r}_0; k_f) V_n^{(\Omega)}(\mathbf{r}, \mathbf{r}_0; k_f) - G_\Omega(\mathbf{r}, \mathbf{r}_0; k_f) V_n^{(\infty)}(\mathbf{r}, \mathbf{r}_0; k_f) \\ &\quad + \theta_n^{(\infty)}(\mathbf{r}, \mathbf{r}_0; k_f) M_n^{(\Omega)}(\mathbf{r}, \mathbf{r}_0; k_f) - \theta_n^{(\Omega)}(\mathbf{r}, \mathbf{r}_0; k_f) M_n^{(\infty)}(\mathbf{r}, \mathbf{r}_0; k_f) \Big) \, d\mathbf{r} \\ &+ \sum_{n=1}^{N_v} \left[G_\Omega(\mathbf{r}, \mathbf{r}_0; k_f) M_{ln}^{(\infty)}(\mathbf{r}, \mathbf{r}_0; k_f) \right]_{v_n}^{v_{n+1}}. \end{aligned} \tag{1.40}$$

1.2.3 Discussion

Eq. (1.40) shows that the Green's function of a polygonal plate can be expressed in the form of a superposition of a direct contribution from the source, a contribution from each edge and a contribution from each corner. Such description is pertinent for arbitrary geometries in that it reveals the different roles played by the internal domain and the boundaries, regardless of the specific shape of the latter. The numerical implementation of the integral representation is performed by using the boundary element method (BEM) (see e.g. [42, 92]), which relies on the discretisation of the boundary $\partial\Omega$ and is well-adapted to arbitrarily shaped enclosed domains. However, in such method, the maximum discretisation interval must be significantly smaller than the wavelength, which limits the maximum frequency of validity. In order to develop a method that is not limited by a maximum frequency, a different formalism allowing to take advantage of the separation of the Green's function in direct and boundary excitations must be employed. This is the purpose of using an image source approach, as described in the following.

The correspondence between the different terms of the integral formulation and a superposition of individual contributions of image sources representing successive wave reflections on the boundaries has been verified in the case of the Helmholtz equation by Martin et al. [14, 36, 68–70] (see also the doctoral thesis of Guignard [35]), showing that a representation in terms of image sources is not limited by a maximum frequency. This is a major motivation for developing a model based on the image source method.

1.3 The image source method and its applications

1.3.1 General considerations

Understanding reflected waves as if they were generated by virtual sources behind the obstacles is an intuitive yet robust description of reflection. A virtual source is the *image* of the original source by symmetry with respect to the boundary separating the real and virtual domains. Such virtual sources are henceforth referred to as *image sources*.

The image source method consists in describing the response of a bounded domain to a given source as the superposition of the direct field from the original source and the contributions of image sources, which represent successive reflections of waves on boundaries and are thus determined by successive symmetries of the original source with respect to the boundaries. Semi-infinite domains such as a reflecting plane or wedge allow a finite number of reflections, whereas finite domains such as vibrating beams or strings (one-dimensional), parallel mirrors (two-dimensional), polygonal vibrating plates (two-dimensional) or polyhedral rooms (three-dimensional) allow an infinite number of image sources. Fig. 1.4 shows some examples of two-dimensional semi-infinite and finite domains and their corresponding image source patterns.

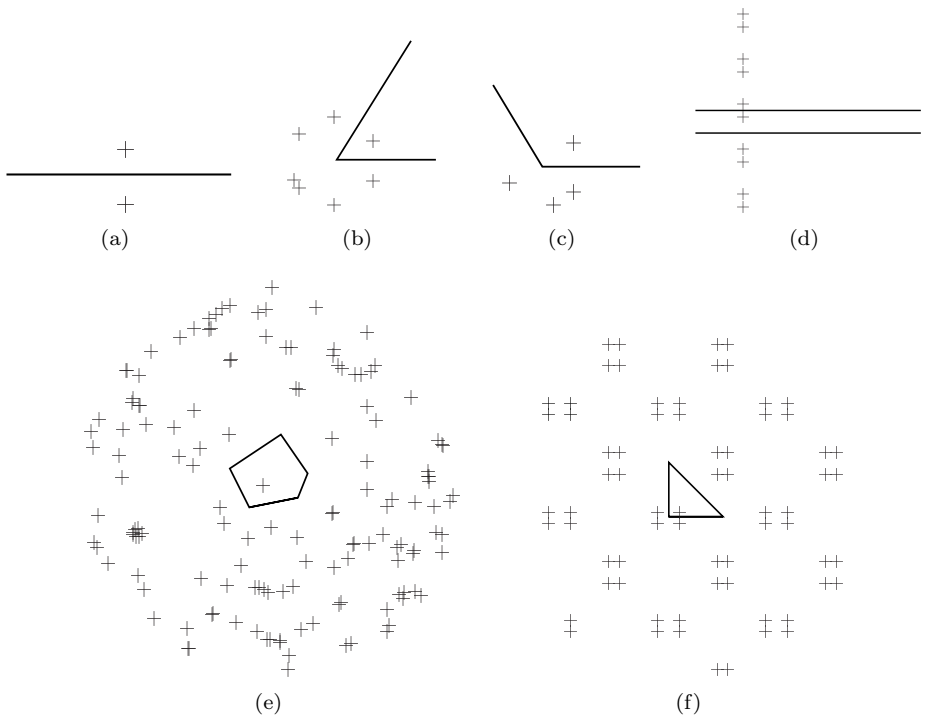

Figure 1.4: Examples of image source constructions for different two-dimensional geometries. (a) Semi-infinite domain, (b) sharp angle, (c) obtuse angle, (d) waveguide, (e) arbitrary polygon and (f) particular polygon.

1.3.2 Previous developments of the image source method

Room acoustics

Room acoustics is the discipline for which the image source method has been most extensively developed. A very large number of papers and monographs address the question of using image sources for predicting the sound field in enclosed spaces such as concert halls or small rooms. Amongst the most relevant for the present purposes is the work of Allen and Berkley [2], who used the image source method for the simulation of impulse responses of rectangular rooms and for synthesising reverberation, and the work of Borish [8], who extended the method to arbitrary polyhedra. General reviews of different techniques are given by Kuttruff [57] and by Cremer and Müller [16]. Those works give evidence of the development of sound synthesis for room acoustics with the advent of digital computers in the 1970's and 1980's. The image source method has been largely used for writing simulation software for room acoustics [23] and for predicting average parameters such as energy decay time or average sound distribution in enclosed spaces sound field, sound energy decay [53, 59]. Despite its extensive use, the method remains to some extent empirical, in that the existence of image sources is subjected to the satisfaction of a number of "rules", summarised by Mechel in a recent review [72]. However, as shown in chaps. 2 and 4, the conditions for the existence of image sources naturally follow from the fact that they must satisfy the boundary conditions.

Polygonal plate vibration

The application of the image source method to structural dynamics is more recent and has been less studied. In particular, Brunskog [10] derived harmonic Green's functions of clamped beams and Szilard [93] obtained static Green's functions of rectangular and isosceles right triangular plates, from which harmonic responses can be deduced. The most extensive work done on polygonal plate vibration has been achieved by Gunda et al. [37–39] and is one of the starting points of the present work. Those authors have shown that the image source method is an efficient description of the flexural vibrations of simply supported and roller supported thin rectangular plates, in that the obtained solutions converge towards exact solutions as frequency and/or damping increase.

1.4 Overview of the proposed approach

Image source method using a direct approach (chap. 2)

The reflection coefficient of a given boundary of a plate generally depends on the angle of incidence of waves. However, some special boundary conditions present a constant reflection coefficient. This is the case of simply supported edges, in which the reflection coefficient is -1 regardless of the angle of incidence of waves. For such boundaries, the amplitude weights of successive image sources are -1, +1, -1, etc., according to the number of reflections that they represent, i.e. the number of symmetries needed for their construction. The application of the image source method to such boundaries is then considered as direct, since the excitation of a given image source is determined by simply centring the Green's function of the associated infinite plate at the image source location

and applying the corresponding weight, i.e. -1 or +1 for a simply supported plate. The application of the image source method to simply supported plates is discussed in detail in chap. 2.

Model of boundary conditions by a matrix approach (chap. 3)

As mentioned above, simply supported edges are a very particular case in which reflection on the boundaries is irrespective of the angle of incidence of waves. Moreover, simply supported edges do not induce coupling between propagating and evanescent components of the incident and reflected fields. This is not the case for most types of boundary conditions. In fact, even commonly used boundary conditions such as clamped or free boundaries present a dependence on the angle of incidence of waves and induce propagating-to-evanescent reflection and vice-versa. For that reason, the model presented in chap. 2 must be generalised to arbitrary boundary conditions. The main idea for such generalisation is to represent the contribution of each image source to the total field of the plate as a continuous superposition of plane waves, which reflect on the edges according to the dependence imposed by the corresponding set of boundary conditions. The purpose of chap. 3 is then to provide a method for determining the reflection matrix of a plate edge or the scattering matrix of a junction between two plates that can be used in the image source method developed in the subsequent chapters. This is done by using a state vector approach, which is appropriate for separating the incident, reflected and transmitted waves at a discontinuity.

Image source method using a Fourier-based approach (chaps. 4, 5 and 6)

More general boundary conditions are characterised by reflection coefficients that present a dependence on the angle of incidence of waves. In this case, the original source is considered as the superposition of an infinite number of plane waves, which can be written as an inverse Fourier transform. In such description, each plane wave obeys a reflection law according to the value of the reflection coefficient for the corresponding angle of incidence. The modelling of individual plates with general edge boundary conditions by using the image source method is discussed in detail in chap. 4. The same formalism is then used in chap. 5 for investigating the possibility of extending the method to the case of an assembly of two plates. The model of chap. 4 is also applied to the measurement of the complex flexural rigidity of highly damped panels, in chap. 6.

Chapter 2

The image source method for calculating the vibrations of simply supported convex polygonal plates

This chapter is presented as an article published in the Journal of Sound and Vibration [20]. A preliminary study was also presented at a conference [18]. Also, appendix 2.C has been added at the end of this chapter as an alternative definition of the modal overlap factor used herein.

Abstract

The aim of this paper is to show that the image source method (ISM) can be used both for analytically calculating Green's functions of particular simply supported convex polygonal plates and for predicting medium and high frequency vibrations of arbitrarily shaped simply supported convex polygonal plates with controllable precision. In the first part of the paper, the method for obtaining the Green's function of a polygonal plate by ISM is developed. Examples for plates of different geometries (rectangle, isosceles right triangle, half-equilateral triangle and equilateral triangle) are given. In the second part of the paper, the pertinence of ISM for predicting medium and high frequency vibrations of arbitrarily shaped simply supported convex polygonal plates is investigated. An approximation based on the exclusion of image sources beyond a certain distance from the receiver is used in order to take advantage of the dissipation of vibrational energy through wave propagation. We investigate the influence of structural damping and truncation distance on the accuracy of such approximation. The computed responses are in good agreement with reference solutions, which are analytically known or obtained by the finite element method.

2.1 Introduction

An analysis of literature shows that there is a need of accurate prediction tools in the fields of acoustics and structural dynamics. In medium and high frequency ranges, Finite Element Methods (FEM) often require prohibitive calculation capabilities due to the need of a significant number of elements and to the high modal densities often encountered in structures. Although these methods are continuously extended to higher frequencies by computer hardware improvement, strong limitations still remain. Statistical Energy Analysis (SEA) [62] provides fast estimations of vibrational levels and power flows, for which it certainly remains the most popular method for such purposes. Determining pertinent subsystems, accurately estimating damping ratios and coupling loss factors are the main difficulties for the practical implementation of SEA.

As a consequence, several methods have been proposed, some as extensions of FEM and SEA, and some based on rather different formalisms. Among these, Mace et al. [66] developed an extension of FEM to high frequencies by post-processing finite element models using structure periodicity conditions. Le Bot [9] developed an extension of SEA in which the distribution of energy density inside each sub-system is predicted. Cotoni et al. [13] studied a hybrid FEM-SEA method for the prediction of medium frequency vibrations. Chae et al. [12] constructed a ray tube model with time averaged kinetic and potential energies for predicting vibrational field distributions for simple and coupled plates. They also gave a comprehensive bibliographic review of existent high frequency methods. Ladevèze [58] developed the Variational Theory of Complex Rays, which is based on the expansion of vibrations on a superposition of interior modes, edge modes and corner modes, applicable to medium frequency vibrations. Lastly, references to other improved finite element approaches can be found in [88]. The main inconvenient of methods based on a modal or a finite element description is that the number of modes or elements increases with frequency. On the other hand, formulations based on SEA provide quadratic results, so that no accurate prediction of phase phenomena such as interferences is possible.

Otherwise, formulations directly based on wave propagation are adequate for predicting the exact dynamic field in enclosed spaces without being disadvantaged by the large number of modes or elements at high frequencies. Among these, mainly two approaches are relevant: the ray-tracing technique and the image source method (ISM). These methods are widely used in room acoustics [2, 8, 16, 57, 72] and consist in predicting the dynamic field of an enclosed domain from the knowledge of the possible propagation paths between the source and an observation point. Such propagation paths can be described either as rays or as virtual sources. The ray-tracing model is often known as an approximation in which the directions of propagation are quantised and the receiver is a spherical volume. On the other hand, ISM consists in replacing the boundaries of the domain by mirror sources of the original source. The weights and locations of image sources are calculated in order to satisfy the boundary conditions of the domain. Moreover, ISM is analytical regardless of the specific shape of boundaries if these form a convex polygon, whereas other analytical methods such as modal analysis [34] or the superposition method [33] are only applicable to simple geometries. In spite of this, ISM has only been applied to academic polygonal geometries in structural dynamics [10, 39, 45] or used for predicting the vibrations of semi-infinite plates including

an heterogeneity [43, 44]. To the best of our knowledge, the most extensive work on ISM for polygonal plates has been done by Gunda et al. [39], who applied it to rectangular plates with simply supported and roller boundary conditions and observed a rapid convergence towards FEM and exact solutions in medium and high frequencies. However, ISM has not been applied or extended to polygonal plates of other shapes, which is a real need for modelling high frequency vibrations of plates.

The aim of this paper is to test the capability of ISM for predicting medium and high frequency vibrations of simply supported convex polygonal plates with controllable precision. The method allows as well to analytically calculate the Green's functions of plates of particular shape. We restrict our study to simply supported boundary conditions since the associated reflection coefficient is unitary and independent from the angle of incidence of waves. The paper is organised as follows. The general method for obtaining Green's functions from the ISM description is developed and illustrated by several examples in section 2.2. In section 2.3, the practical implementation of ISM is presented: The truncation of the image source generation process, which is the main difficulty known for this approach, is analysed and discussed.

2.2 Green's functions of convex polygonal plates using the image source method

The aim of this section is to develop a general method for obtaining Green's functions of polygonal plates from ISM. Statement of the problem and principles of the method are first described.

2.2.1 Statement of the problem

The studied system is a thin plate with an interior domain Ω and boundaries $\partial\Omega$ defining a convex polygon. The plate is assumed to be excited by an elementary point source at the location $\mathbf{r}_0$ (Fig. 2.1). In the following, harmonic motion is assumed and $e^{-j\omega t}$ time dependence is implicit. Flexural vibrations of the plate are considered in the

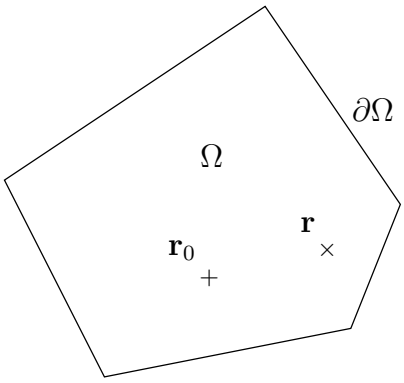

Figure 2.1: Polygonal plate with inside domain Ω and boundaries $\partial\Omega$. +, source; ×, receiver.

framework of Kirchhoff's theory. Simply supported edges are assumed, corresponding to zero displacement and zero bending moment boundary conditions on $\partial\Omega$. The Green's function G_Ω associated to the flexural vibrations of the plate is then a solution of the set of equations

$$\begin{cases} D\left(\nabla^4 - k_f^4\right) G_\Omega(\mathbf{r}, \mathbf{r}_0) = \delta(\mathbf{r} - \mathbf{r}_0) & \text{in } \Omega, \\ G_\Omega(\mathbf{r}, \mathbf{r}_0) = 0 & \text{on } \partial\Omega, \\ \dfrac{\partial^2 G_\Omega}{\partial n^2}(\mathbf{r}, \mathbf{r}_0) + \nu \dfrac{\partial^2 G_\Omega}{\partial l^2}(\mathbf{r}, \mathbf{r}_0) = 0 & \text{on } \partial\Omega, \end{cases} \tag{2.1}$$

where $D\left(\nabla^4 - k_f^4\right)$ is the differential operator governing flexural wave propagation, δ is the Dirac delta function, ν is the Poisson's ratio and n and l are respectively the normal and the tangent to the boundary [34]. The flexural wavenumber k_f can be written

$$k_f = \left(\omega^2 \frac{\rho h}{D}\right)^{1/4}, \tag{2.2}$$

where ρ and h are respectively the density and thickness of the plate and

$$D = \frac{E h^3}{12\left(1 - \nu^2\right)} \tag{2.3}$$

is the flexural rigidity of the plate, E being the Young's modulus. Structural losses are assumed to be spread in the medium without any damping mechanism at the boundaries. This can be taken into account by considering the damping ratio η as an imaginary part in the Young's modulus, which is written in the form

$$E = E_0(1 - j\eta). \tag{2.4}$$

Solving the set of equations (2.1) is the main target of the following.

2.2.2 Modal expansion of the Green's function

The solution of Eqs. (2.1) is classically expressed using a normal modal expansion [34], in the form

$$G_\Omega(x, y; x_0, y_0) = \sum_{\mu=1}^{+\infty} \frac{\phi_\mu(x_0, y_0)\phi_\mu(x, y)}{D\left(k_\mu^4 - k_f^4\right)}, \tag{2.5}$$

where ϕ_μ are real modal shapes, which are normalised to unity and obey the orthogonality relationship

$$\int_\Omega \phi_\mu \phi_{\mu'}^* d\Omega = \delta_{\mu\mu'}. \tag{2.6}$$

The modal shapes are determined as the solutions of the homogeneous set of equations

$$\begin{cases} D\left(\nabla^4 - k_\mu^4\right) \phi_\mu(\mathbf{r}) = 0 & \text{in } \Omega, \\ \phi_\mu(\mathbf{r}) = 0 & \text{on } \partial\Omega, \\ \dfrac{\partial^2 \phi_\mu}{\partial n^2}(\mathbf{r}) + \nu \dfrac{\partial^2 \phi_\mu}{\partial l^2}(\mathbf{r}) = 0 & \text{on } \partial\Omega. \end{cases} \tag{2.7}$$

Furthermore, the wavenumber k_μ is linked to the eigenvalue ω_μ associated to mode μ by the relationship

$$\omega_\mu = \sqrt{\frac{D_0}{\rho h}} k_\mu^2, \tag{2.8}$$

where D_0 is the real part of D.

2.2.3 Image source method (ISM)

ISM consists in replacing the finite plate Ω, excited by a point source at $\mathbf{r}_0$, by an infinite plate containing the original source plus image sources whose locations and amplitude weights are calculated in order to satisfy the boundary conditions [2, 8, 39, 72]. The locations of image sources are obtained by performing successive "mirror" reflections of the initial source on the edges $\partial\Omega$ of the plate. Simply supported boundary conditions are considered here, which are a very particular case since the associated reflection coefficient is $\mathcal{R} = -1$, i.e. unitary and independent from the angle of incidence of waves [34]. This implies that the function describing the locations of image sources is a sum of Dirac delta functions, with weights $+1$ or -1, according to the parity of reflections. As a convention, such function is here called the *image source cloud* of the studied system, noted $\mathcal{D}_\Omega(\mathbf{r}, \mathbf{r}_0)$ as it is a function of space $\mathbf{r}$ and initial source location $\mathbf{r}_0$ and is associated to the shape of the boundaries $\partial\Omega$. An example of the image source cloud of an arbitrarily convex polygonal plate is shown in Fig. 2.2. The step by step construction of the image sources cloud is given in more detail in Appendix 2.A.

Subsequently, the vibrational field at the receiver is obtained as the superposition of elementary contributions from all the sources. Eqs. (2.1) can then be written in the condensed form

$$D\left(\nabla^4 - k_f^4\right) G_\Omega(\mathbf{r}, \mathbf{r}_0) = \mathcal{D}_\Omega(\mathbf{r}, \mathbf{r}_0). \tag{2.9}$$

The boundary conditions are satisfied by the existence of an infinity of image sources, represented by the function $\mathcal{D}_\Omega(\mathbf{r}, \mathbf{r}_0)$. In order to infer an analytical expression of $G_\Omega(\mathbf{r}, \mathbf{r}_0)$, we use the Green's function G_∞ of the associated infinite plate [39]. For a point source located at $\mathbf{0}$, G_∞ is the solution of the equation

$$D\left(\nabla^4 - k_f^4\right) G_\infty(\mathbf{r}, \mathbf{0}) = \delta(\mathbf{r}) \tag{2.10}$$

and can be written as

$$G_\infty(\mathbf{r}, \mathbf{0}) = \frac{j}{8k_f^2 D}\left(H_0^{(1)}(k_f|\mathbf{r}|) - H_0^{(1)}(jk_f|\mathbf{r}|)\right), \tag{2.11}$$

where $H_0^{(1)}$ is the cylindrical Hankel's function of the first kind of order 0 and $|\mathbf{r}|$ is the source-to-receiver distance [75]. From Eqs. (2.9) and (2.10), the Green's function of the convex polygonal plate can be written as

$$G_\Omega(\mathbf{r}, \mathbf{r}_0) = \mathcal{D}_\Omega(\mathbf{r}, \mathbf{r}_0) * G_\infty(\mathbf{r}, \mathbf{0}). \tag{2.12}$$

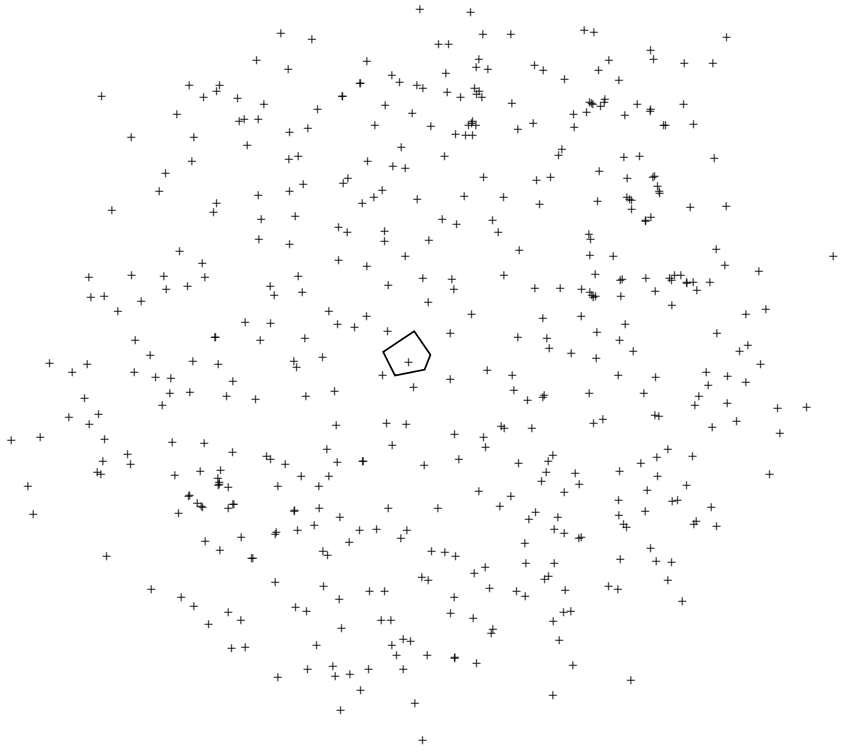

Figure 2.2: Image source cloud for an arbitrarily convex polygonal plate (first 12 reflections, giving rise to 483 image sources). ——, plate boundaries; +, sources.

In this convolution product, acting on variable $\mathbf{r}$, the infinite space Green's function is initially centered on $\mathbf{0}$, and $\mathcal{D}_\Omega$ acts as a translation, weighting and summation operator of the contributions of all sources.

Eq. (2.12) is the general ISM solution of Eqs. (2.1) for any simply supported convex polygonal plate. In the following, ISM is applied to plates of particular polygonal shapes that allow to express the Green's function analytically. The practical implementation of ISM and its application to convex polygonal plates of arbitrary shape are discussed in section 2.3.

2.2.4 Obtaining a modal expansion of the Green's function from ISM

Some special geometries of plates give rise to a spatially periodic image source cloud. The resulting Green's function G_Ω is then spatially periodic itself. Thus, by using Fourier series, G_Ω can be expressed as a function of discrete wavenumbers, which can be interpreted as a modal expansion of the Green's function. The identity between these two kinds of expressions of a function is usually known as the Poisson summation formula (see for example [75]).

The first step for obtaining such expression for the Green's function of the plate is to describe the spatially periodic image source cloud by using two functions, $\mathcal{P}_\Omega$ and $\mathcal{E}$, respectively a periodisation operator and an elementary cell. $\mathcal{P}_\Omega$ acts as a summation of $\mathcal{E}$ with translations. The image source cloud can then be written as the convolution product

$$\mathcal{D}_\Omega(\mathbf{r}, \mathbf{r}_0) = \mathcal{P}_\Omega(\mathbf{r}) * \mathcal{E}(\mathbf{r}, \mathbf{r}_0) \tag{2.13}$$

and the periodisation operator can be written in cartesian coordinates as

$$\mathcal{P}_\Omega(x, y) = \sum_{p=-\infty}^{+\infty} \sum_{q=-\infty}^{+\infty} \delta(x - p\lambda_x, y - q\lambda_y), \tag{2.14}$$

with λ_x and λ_y being the spatial periods of the image source cloud. Eq. (2.12) can then be written as

$$G_\Omega(x, y; x_0, y_0) = \sum_{p=-\infty}^{+\infty} \sum_{q=-\infty}^{+\infty} \delta(x - p\lambda_x, y - q\lambda_y) * \mathcal{E}(x, y; x_0, y_0) * G_\infty(x, y; 0, 0). \tag{2.15}$$

Since G_Ω is periodic, it can be expressed using a Fourier series, in the form

$$G_\Omega(x, y; x_0, y_0) = \sum_{m=-\infty}^{+\infty} \sum_{n=-\infty}^{+\infty} C_{mn} e^{-j(k_m x + k_n y)}, \tag{2.16}$$

where $k_m = m2\pi/\lambda_x$ and $k_n = n2\pi/\lambda_y$ describe the spatial periodicity of G_Ω and where

$$C_{mn} = \frac{1}{\lambda_x \lambda_y} \int_0^{\lambda_x} \int_0^{\lambda_y} G_\Omega(x, y; x_0, y_0) e^{j(k_m x + k_n y)} dx dy. \tag{2.17}$$

Eqs. (2.16) and (2.17) yield

$$G_\Omega(x, y; x_0, y_0) = \frac{1}{\lambda_x \lambda_y} \sum_{m=-\infty}^{+\infty} \sum_{n=-\infty}^{+\infty} \mathcal{F}\left[\mathcal{E}(x, y; x_0, y_0)\right]_{(k_m, k_n)} \mathcal{F}\left[G_\infty(x, y; 0, 0)\right]_{(k_m, k_n)} e^{-j(k_m x + k_n y)}, \tag{2.18}$$

where $\mathcal{F}$ denotes the Fourier transform, and is defined as

$$\mathcal{F}\left[f(\mathbf{r})\right]_{(\mathbf{k})} = \int_{\mathbb{R}^2} f(\mathbf{r}) e^{j\mathbf{k}\cdot\mathbf{r}} d\mathbf{r}, \tag{2.19}$$

Eq. (2.18) is consequently an expansion of the Green's function of the plate G_Ω on harmonic functions, i.e. a modal expansion. The equality between Eqs. (2.15) and (2.18) shows the equivalence between modal and image source expansions.

2.2.5 Examples

To the best of our knowledge, ISM has only been used for the analytical calculation of Green's functions in the case of beams [10] and one-dimensional acoustic cavities [75], where the image source cloud is a one-dimensional comb. The case of simply supported rectangular plates has been discussed by Gunda et al. [39], who compared ISM computations with a finite number of image sources to the exact solution. Furthermore, the image source cloud of isosceles right triangular, half-equilateral and equilateral triangles have already been qualitatively studied by Cremer and Müller [16]. They have pointed out that the well-organised source pattern results in a number of possible directions of ray propagation in the domain, but no derivation of the Green's functions of such plates has been developed.

One point in common between these plate geometries is that the image source cloud is spatially periodic. In the following examples, ISM is applied to simply supported polygonal plates of various shapes that lead to a periodic image source cloud. The geometries under consideration are: the rectangle, the isosceles right triangle, the half-equilateral triangle and the equilateral triangle. For each case, the elementary cell $\mathcal{E}$ and the periodisation operator $\mathcal{P}_\Omega$ are given, leading to analytical expression of the Green's function G_Ω, derived from Eq. (2.18).

2.2.5.1 Simply supported rectangular plate

Fig. 2.3 shows the image source cloud of a rectangular plate of dimensions L_x and L_y, simply supported at its four edges and excited by a point source at (x_0, y_0). The

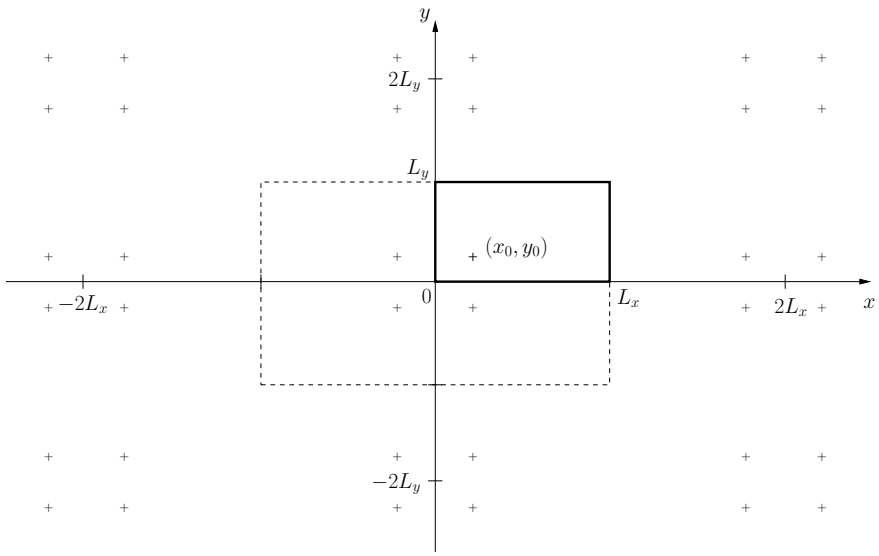

Figure 2.3: Image source cloud for a rectangular plate. ——, plate boundaries; +, sources; - - - -, elementary cell $\mathcal{E}$.

elementary cell can be taken as the subset of four sources located at $(\pm x_0, \pm y_0)$. Since

the reflexion coefficient is $\mathcal{R} = -1$, the latter is a quadrupole and can be written

$$\mathcal{E}(x,y;x_0,y_0) = \delta(x-x_0,y-y_0) - \delta(x-x_0,y+y_0) - \delta(x+x_0,y-y_0) + \delta(x+x_0,y+y_0). \tag{2.20}$$

The spatial periods of the cloud are $\lambda_x = 2L_x$ and $\lambda_y = 2L_y$, so that the periodisation operator, given by Eq. (2.14), can be written as

$$\mathcal{P}_\Omega(x,y) = \sum_{p=-\infty}^{+\infty} \sum_{q=-\infty}^{+\infty} \delta(x - p2L_x, y - q2L_y), \tag{2.21}$$

and the discrete wavenumbers are $k_m = m\pi/L_x$ and $k_n = n\pi/L_y$. The Green's function of the rectangular plate obtained by the image source method is then known from Eq. (2.13). The Fourier transform of $G_\infty(x,y;0,0)$ can be written as

$$\mathcal{F}\left[G_\infty(x,y;0,0)\right]_{(k_m,k_n)} = \frac{1}{D\left(\left(k_m^2+k_n^2\right)^2 - k_f^4\right)}. \tag{2.22}$$

Furthermore, it can be seen from Eq. (2.20) that

$$\mathcal{F}\left[\mathcal{E}(x,y;x_0,y_0)\right]_{(k_m,k_n)} = -4\sin(k_m x_0)\sin(k_n y_0). \tag{2.23}$$

Inserting (2.22) and (2.23) into (2.18) and rearranging sums on m and n leads to the modal expansion of the Green's function for the rectangular plate,

$$G_\Omega(x,y;x_0,y_0) = \frac{4}{L_x L_y} \sum_{m=1}^{\infty} \sum_{n=1}^{\infty} \frac{\sin(k_m x_0)\sin(k_n y_0)\sin(k_m x)\sin(k_n y)}{D\left(\left(k_m^2+k_n^2\right)^2 - k_f^4\right)}. \tag{2.24}$$

Furthermore, the eigenfrequencies of Eq. (2.8) are given by the zeros of the denominator in Eq. (2.24)

$$\omega_{mn} = \left(\frac{D}{\rho h}\right)^{1/2} \left(\left(\frac{m\pi}{L_x}\right)^2 + \left(\frac{n\pi}{L_y}\right)^2\right), \tag{2.25}$$

for $(m \geq 1, n \geq 1)$. Eq. (2.24) is the well-known solution for the rectangular plate [33, 34]. This simple example shows that ISM allows to obtain the Green's function for this academic geometry by using a rather different approach.

2.2.5.2 Simply supported isosceles right triangular plate

The image source cloud of the isosceles right triangular plate of side L with a point source at (x_0, y_0) is represented in Fig. 2.4.

The elementary cell can be separated into two quadrupoles of sources respectively located at $(\pm x_0, \pm y_0)$ and $(\pm(L-y_0), \pm(L-x_0))$. The response of this plate can thus be regarded as the superposition of responses of a square plate to opposite excitations at (x_0, y_0) and $(L-y_0, L-x_0)$, which was used by Szilard [93] for calculating the static deflection of this plate.

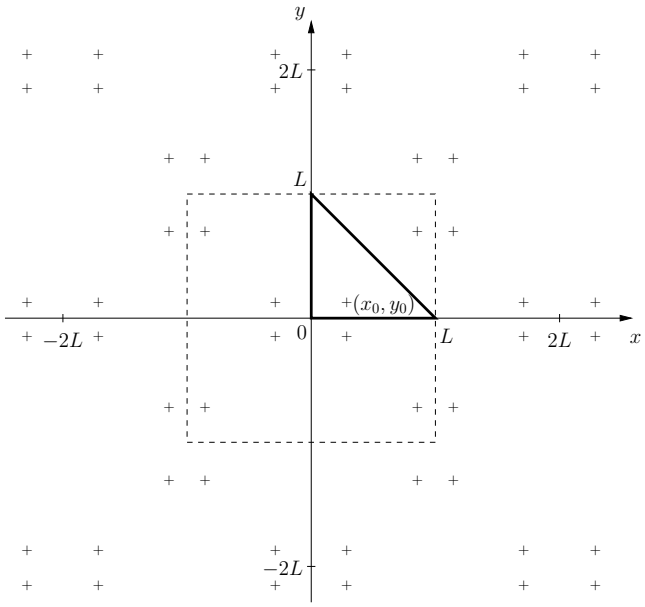

Figure 2.4: Image source cloud for the isosceles right triangular plate. ——, plate boundaries; +, sources; ----, elementary cell $\mathcal{E}$.

The elementary cell $\mathcal{E}$ and its Fourier transform can be respectively written as

$$\mathcal{E}(x,y,x_0,y_0) = \begin{cases} \delta(x-x_0, y-y_0) \\ -\delta(x-x_0, y+y_0) \\ -\delta(x+x_0, y-y_0) \\ +\delta(x+x_0, y+y_0) \end{cases} + \begin{cases} -\delta(x-(L-y_0), y-(L-x_0)) \\ +\delta(x-(L-y_0), y+(L-x_0)) \\ +\delta(x+(L-y_0), y-(L-x_0)) \\ -\delta(x+(L-y_0), y+(L-x_0)) \end{cases} \tag{2.26}$$

and

$$\mathcal{F}[\mathcal{E}(x,y,x_0,y_0)]_{(k_m,k_n)} = -4\sin(k_m x_0)\sin(k_n y_0) + 4\sin(k_m(L-y_0))\sin(k_n(L-x_0)). \tag{2.27}$$

The spatial periods of the cloud are $\lambda_x = 2L$ and $\lambda_y = 2L$, leading to the discrete wavenumbers $k_m = m\pi/L$ and $k_n = n\pi/L$ and to the periodisation operator

$$\mathcal{P}_\Omega(x,y) = \sum_{p=-\infty}^{+\infty} \sum_{q=-\infty}^{+\infty} \delta(x-p2L, y-q2L). \tag{2.28}$$

The Green's function G_∞ of the infinite plate is the same as the one used in section 2.2.5.1. By, inserting Eqs. (2.22) and (2.27) into Eq. (2.18), the Green's function for the

simply supported isosceles right triangular plate can be expressed as

$$G_\Omega(x,y,x_0,y_0) = \frac{4}{L^2}\sum_{m=1}^{+\infty}\sum_{n=1}^{+\infty}\frac{\sin(k_m x_0)\sin(k_n y_0)-\sin(k_m(L-y_0))\sin(k_n(L-x_0))}{D\left((k_m^2+k_n^2)^2-k_f^4\right)}\sin(k_m x)\sin(k_n y). \tag{2.29}$$

The zeros of the denominator in Eq. (2.29) are

$$\omega_{mn} = \left(\frac{D}{\rho h}\right)^{1/2}\left(\left(\frac{m\pi}{L}\right)^2+\left(\frac{n\pi}{L}\right)^2\right), \tag{2.30}$$

for $(m \geq 1, n \geq 1)$, which are the same as those in Eq. (2.25) for $L_x = L_y = L$. However, the numerator in Eq. (2.29) consists in a sum of two terms and therefore is cancelled for $m = n$, so that ω_{mm} are not singularities of G_Ω (i.e. eigenfrequencies).

2.2.5.3 Simply supported half-equilateral triangular plate

The image source cloud of the simply supported half-equilateral triangular plate of vertices $(0,0)$, $(L,0)$ and $(0,L/\sqrt{3})$ with a point source at (x_0,y_0) is represented in Fig. 2.5.

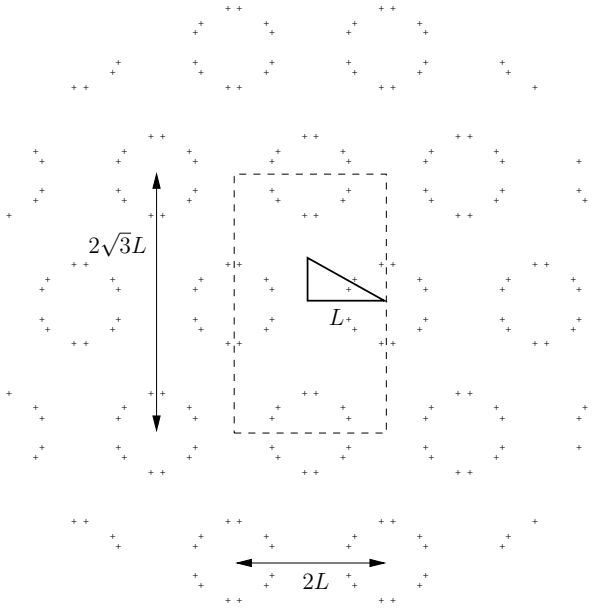

Figure 2.5: Image source cloud for the half-equilateral triangular plate. ——, plate boundaries; +, sources; ----, elementary cell $\mathcal{E}$.

The elementary cell $\mathcal{E}$ of the image source cloud can be written as the superposition of six quadrupoles of sources:

$$\mathcal{E}(x,y,x_0,y_0) = \sum_{i=1}^{6} \xi_i \begin{cases} \delta(x-x_i, y-y_i) \\ -\delta(x-x_i, y+y_i) \\ -\delta(x+x_i, y-y_i) \\ +\delta(x+x_i, y+y_i) \end{cases}, \tag{2.31}$$

where $\xi_i = \pm 1$ is a sequence giving the relative weight of these quadrupoles and $(\pm x_i, \pm y_i)$ $(i = 1, ..., 6)$ are the locations of the sources of each quadrupole (see Appendix 2.B.1 for the detailed expressions of (x_i, y_i) and ξ_i). Fourier Transform of $\mathcal{E}$ gives

$$\mathcal{F}[\mathcal{E}(x,y,x_0,y_0)]_{(k_m,k_n)} = -4 \sum_{i=1}^{6} \xi_i \sin(k_m x_i) \sin(k_n y_i). \tag{2.32}$$

Furthermore, the image source cloud is $2L$-periodic along x and $2\sqrt{3}L$-periodic along y, leading to $k_m = m\pi/L$ and $k_n = n\pi/\sqrt{3}L$ and

$$\mathcal{P}_\Omega(x,y) = \sum_{p=-\infty}^{+\infty} \sum_{q=-\infty}^{+\infty} \delta(x - p2L, y - q2\sqrt{3}L). \tag{2.33}$$

Application of Eq. (2.18) consequently leads to the Green's function for the simply supported half-equilateral plate

$$G_\Omega(x,y,x_0,y_0) = \frac{4}{\sqrt{3}L^2} \sum_{m=1}^{+\infty} \sum_{n=1}^{+\infty} \frac{\sum_{i=1}^{6} -\xi_i \sin(k_m x_i) \sin(k_n y_i)}{D\left((k_m^2 + k_n^2)^2 - k_f^4\right)} \sin(k_m x) \sin(k_n y). \tag{2.34}$$

The zeros of the denominator in Eq. (2.34) are

$$\omega_{mn} = \left(\frac{D}{\rho h}\right)^{1/2} \left(\left(\frac{m\pi}{L}\right)^2 + \left(\frac{n\pi}{\sqrt{3}L}\right)^2\right), \tag{2.35}$$

for $(m \geq 1, n \geq 1)$, and are the same as those in Eq. (2.25) for $L_x = L$ and $L_y = \sqrt{3}L$. As for the case of the isosceles right triangular plate, the circular frequencies ω_{mn} for which the numerator in Eq. (2.34) is cancelled are not eigenfrequencies.

2.2.5.4 Simply supported equilateral triangular plate

The image source cloud of the simply supported equilateral triangular plate of vertices $(0,0)$, $(L,0)$ and $(L/2, \sqrt{3}L/2)$ is represented in Fig. 2.6.

The elementary cell of the cloud can be written as

$$\mathcal{E}(x,y,x_0,y_0) = \sum_{i=1}^{12} \xi_i \delta(x - x_i, y - y_i), \tag{2.36}$$

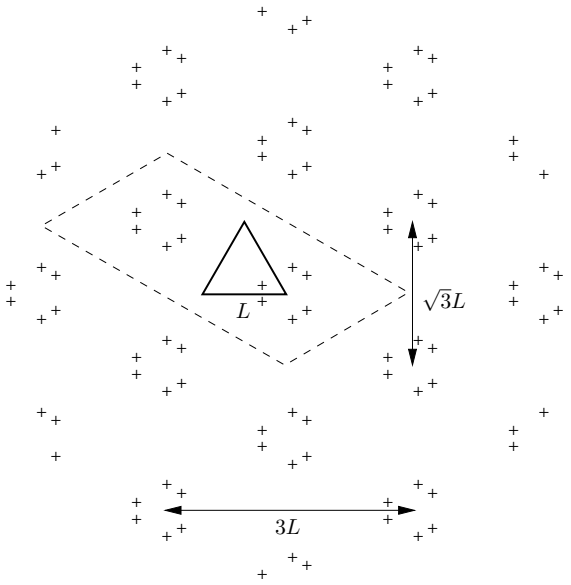

Figure 2.6: Image source cloud for the equilateral triangular plate. ——, plate boundaries; +, sources; ----, elementary cell $\mathcal{E}$.

where (x_i, y_i) $(i = 1, ..., 12)$ are the locations of the 12 sources that form the elementary cell and $\xi_i = \pm 1$ is a sequence giving the weight of each one of these sources (see Appendix 2.B.2 for the detailed expressions of (x_i, y_i) and ξ_i). The spatial periods of the cloud are $\lambda_x = 3L$ and $\lambda_y = \sqrt{3}L$, leading to $k_m = m2\pi/3L$ and $k_n = n2\pi/\sqrt{3}L$ and

$$\mathcal{P}_\Omega(x, y) = \sum_{p=-\infty}^{+\infty} \sum_{q=-\infty}^{+\infty} \delta(x - p3L, y - q\sqrt{3}L). \tag{2.37}$$

According to Eq. (2.18), the Green's function of the plate is then

$$G_\Omega(x, y, x_0, y_0) = \frac{1}{3L \cdot \sqrt{3}L} \sum_{m=-\infty}^{+\infty} \sum_{n=-\infty}^{+\infty} \frac{\sum_{i=1}^{12} \xi_i e^{jk_m x_i} e^{jk_n y_i}}{D\left((k_m^2 + k_n^2)^2 - k_f^4\right)} e^{-jk_m x} e^{-jk_n y}, \tag{2.38}$$

which can be written in the form

$$\begin{aligned} G_\Omega(x, y, x_0, y_0) \quad = \quad & \frac{4}{3^{3/2}L^2} \sum_{m=1}^{+\infty} \sum_{n=1}^{+\infty} \frac{\sum_{i=1}^{12} \xi_i \cos\left(k_m(x_i - x)\right) \cos\left(k_n(y_i - y)\right)}{D\left((k_m^2 + k_n^2)^2 - k_f^4\right)} \\ & + \frac{2}{3^{3/2}L^2} \sum_{m=1}^{+\infty} \frac{\sum_{i=1}^{12} \xi_i \cos\left(k_m(x_i - x)\right)}{D\left(k_m^4 - k_f^4\right)} \\ & + \frac{2}{3^{3/2}L^2} \sum_{n=1}^{+\infty} \frac{\sum_{i=1}^{12} \xi_i \cos\left(k_n(y_i - y)\right)}{D\left(k_n^4 - k_f^4\right)}. \end{aligned} \tag{2.39}$$

The zeros of the denominator in Eq. (2.38) are given by

$$\omega_{mn} = \left(\frac{D}{\rho h}\right)^{1/2} \left(\left(\frac{m2\pi}{3L}\right)^2 + \left(\frac{n2\pi}{\sqrt{3}L}\right)^2 \right), \tag{2.40}$$

for $(m \geq 0, n \geq 0)$ except $(m = 0, n = 0)$. Here again, the circular frequencies for which the numerator in Eq. (2.38) is cancelled are not eigenfrequencies.

From this section, we can draw the following conclusions. The Green's function of a polygonal plate can be computed by ISM. In the case of a periodic image source cloud $\mathcal{D}_\Omega$, an analytical expansion of the Green's function of the plate G_Ω can be obtained by means of a Poisson summation formula. It should be noticed that this analytical expansion can be obtained for all polygonal shapes which lead to periodic image source cloud.

2.3 Effect of truncation of the image source cloud

The aim of this section is to quantify the accuracy of the plate response calculated from a truncated image source cloud. On one hand, the main drawback for practical implementation of ISM is the need of an infinite number of image sources. On the other hand, a wave propagating in a real-world medium is subjected to geometrical attenuation and structural damping. As a consequence, image sources located far from the receiver do not significantly contribute to the vibrational field. An approximated formulation may then be considered by eliminating all image sources located outside an arbitrary radius from the receiver, as usually defined in room acoustics as the speed of sound times the reverberation time [2]. The flexural vibrations of polygonal plates can then be accurately described with a finite number of image sources and the precision of the estimation can be controlled. We henceforth refer to this formulation as the approximate image source method (AISM).

2.3.1 Truncation of the image source cloud

In order to investigate the influence of frequency, damping and source-to-receiver distance on wave propagation, the Green's function of an infinite plate, given in Eq. (2.11), can be asymptotically approximated following [75]

$$G_\infty(\mathbf{r}, \mathbf{r}_s) \simeq \tilde{G}_\infty(\mathbf{r}, \mathbf{r}_s) = -\frac{1}{8jk_f^2 D} \left(\frac{2}{\pi k_f |\mathbf{r} - \mathbf{r}_s|}\right)^{1/2} e^{j(k_f|\mathbf{r}-\mathbf{r}_s| - \frac{\pi}{4})}, \tag{2.41}$$

for $\mathrm{Re}\{k_f\}|\mathbf{r} - \mathbf{r}_s| \gg 1$, where $\mathbf{r}_s$ and $\mathbf{r}$ are respectively the locations of a source and a receiver in an infinite plate. In this formulation, evanescent waves are ignored. The modulus of $\tilde{G}_\infty$ decreases with increasing circular frequency ω, source-to-receiver distance

$|\mathbf{r}-\mathbf{r}_s|$, and structural damping ratio η, according to[1]

$$|\tilde{G}_\infty(\mathbf{r},\mathbf{r}_s)| \sim \omega^{-5/4}|\mathbf{r}-\mathbf{r}_s|^{-1/2}\left(1+\eta^2\right)^{-3/16}. \tag{2.42}$$

The truncation radius is defined as the distance $r_t = |\mathbf{r}-\mathbf{r}_s|$ over which the amplitude of a flexural wave becomes P times lower than for a propagation distance of reference r_c (Fig. 2.7).

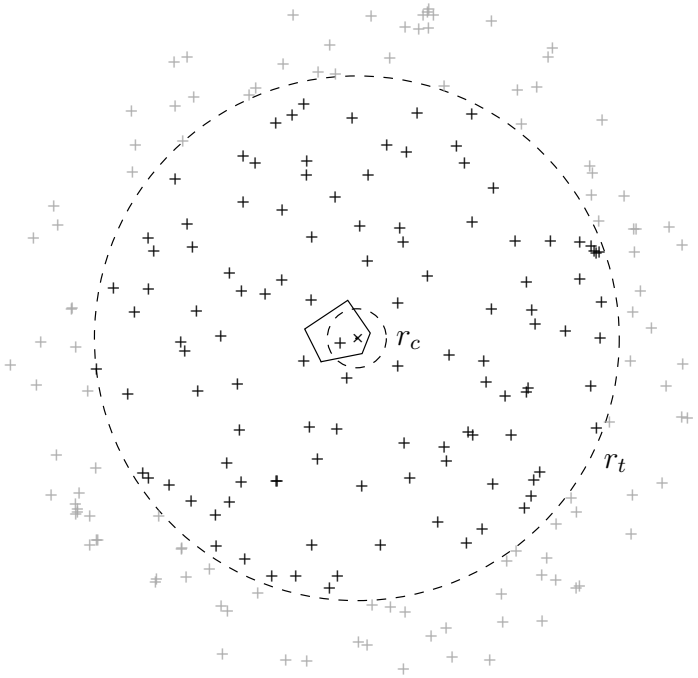

Figure 2.7: Example of image source cloud truncation for AISM. ——, plate boundaries; - - - -, characteristic and truncation circles of radii r_c and r_t centered on the receiver; +, sources taken into account for AISM; +, ignored image sources.

This criterion can be expressed as

$$|G_\infty(0,r_t)| = \frac{|G_\infty(0,r_c)|}{P}. \tag{2.43}$$

The choice of the distance r_c is arbitrary and may be taken as a characteristic length of the plate. We use the mean free path [62], which is the average distance between two

[1] *Corrigendum:* In the published article [20], Eq. (2.42) should read

$$|\tilde{G}_\infty(\mathbf{r},\mathbf{r}_s)| \sim \omega^{-5/4}|\mathbf{r}-\mathbf{r}_s|^{-1/2}\left(1+\eta^2\right)^{-3/16} e^{-\left(\omega^2\frac{\rho h}{D_0}\right)^{1/4}\frac{\eta}{4}|\mathbf{r}-\mathbf{r}_s|}.$$

Consequently, using the arbitrary truncation control parameter γ as defined in Eq. (2.45), Eq. (2.46) does not hold. However, the convergence of the AISM solution towards the ISM solution is still valid for $\gamma \to \infty$ or $P \to \infty$.

successive image sources, defined as

$$r_c = \frac{\pi S}{p}, \tag{2.44}$$

where S and p are respectively the total area and the perimeter of the plate. The distance r_t obtained from Eq. (2.43) is used for stopping the image source generation process. In order to control the truncation radius regardless of the geometry of the plate, we use the dimensionless parameter

$$\gamma = \frac{r_t}{r_c}. \tag{2.45}$$

Using the asymptotic expression (2.41) for $|G_\infty(0, r_t)|$ and for $|G_\infty(0, r_c)|$ in Eq. (2.43) allows to write

$$P \simeq \sqrt{\gamma}. \tag{2.46}$$

Thus, equations (2.43) and (2.45) are equivalent definitions of the truncation radius from arbitrary values of γ or P, such that $\gamma = +\infty$ and $P = +\infty$ correspond to the ISM solution.

2.3.2 Influence of structural damping on the accuracy of AISM

Since the vibrational energy of plates is dissipated during wave propagation, for a given truncation radius r_t, the accuracy of AISM increases with structural damping. We use the concept of Modal Overlap Factor (MOF) as an indicator of the effects of damping on the behaviour of the physical system. The MOF is commonly used in room acoustics and structural dynamics for determining the threshold between low and high frequency ranges [84]. It estimates the number of modes that overlap at a given frequency as the ratio between the $-3\,\mathrm{dB}$ bandwidth $\Delta\omega_\mu$ of a resonance and the frequency interval $\delta\omega_\mu$ between two successive resonances, as[2]

$$\mathrm{MOF} \;=\; \frac{\Delta\omega_\mu}{\delta\omega_\mu}. \tag{2.47}$$

For vibrating systems, the MOF generally increases with damping and frequency. The value for determining the threshold between low and high frequency ranges results from a semi-empirical observation of the behaviour of the system under consideration [84]. The value $\mathrm{MOF} = 1$ corresponds to a frequency for which the spacing between eigenfrequencies is equal to the $-3\,\mathrm{dB}$ bandwidth of resonances. This is consequently the frequency for which modes begin to overlap, here taken as the threshold between low and mid frequency ranges. Moreover, the value $\mathrm{MOF} = 3$ is chosen as the threshold between mid and high frequency ranges, such that an average of three successive resonances is in a resonance bandwidth. In room acoustics, the frequency for which $\mathrm{MOF} = 3$ is refered to as the Schroeder frequency [89].

In order to study the accuracy of AISM in low, mid and high frequency ranges, simulations are performed on a simply supported isosceles right triangular 2 mm-thick steel plate, with Young's modulus $E_0 = 210\,\mathrm{GPa}$, Poisson's ratio $\nu = 0.3$, density

[2] Please refer to appendix 2.C (not originally present in the paper [20]) for an asymptotic definition of the MOF.

$\rho = 7850\,\mathrm{kg.m}^{-3}$ and for two different structural damping ratios, $\eta = 0.03$ and $\eta = 0.05$. The vertices are located at $(0,0)$, $(L,0)$ and $(0,L)$, where $L = 1\,\mathrm{m}$. The source and the receiver are respectively located at $\mathbf{r}_0 = (0.2L, 0.1L)$ and $\mathbf{r} = (0.6L, 0.3L)$. Fig. 2.8 shows the corresponding image source cloud, truncated for $\gamma = 10.76$.

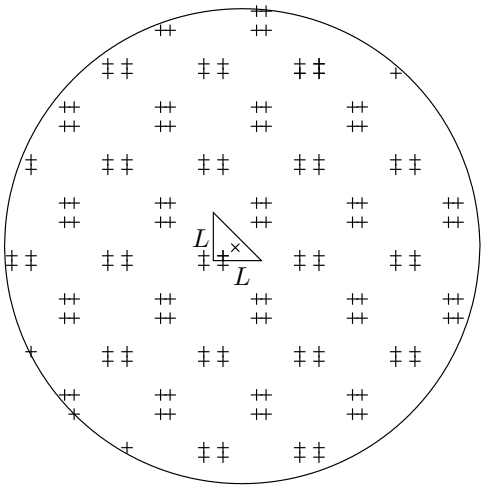

Figure 2.8: Image source cloud of the isosceles right triangular plate, for the truncation parameter $\gamma = 10.76$ ($r_t = 4.95\,\mathrm{m}$), containing 154 sources.

The MOF is usually calculated from the average spacing between resonances over the whole frequency range [62]. Nevertheless, for thin plates, eigenfrequencies are not equally spaced, and then the MOF does not follow a monotonic law of frequency. In particular, symmetries in the geometry induce multiple modes, also called degenerate modes, which lead to an infinite MOF at the corresponding eigenfrequency. Therefore, in order to estimate the low-mid and mid-high frequency thresholds, a smoothed curve is used by considering the local minimum of the MOF over a sliding window of 10 modes and then by fitting it to a first order polynomial in a least-squares sense. This underestimates the value of the modal overlap factor and consequently overestimates the values of the low-medium and medium-high frequency thresholds. Fig. 2.9 shows the MOF and its smoothed estimation as a function of frequency for $\eta = 0.03$ and $\eta = 0.05$, with the threshold frequencies corresponding to MOF = 1 and MOF = 3.

In order to evaluate the differences between AISM and the exact solution, the error at a particular frequency is estimated as

$$\text{error} = \left| \frac{G_\Omega^{(\text{AISM})} - G_\Omega^{(\text{ref})}}{G_\Omega^{(\text{ref})}} \right|, \tag{2.48}$$

where $G_\Omega^{(\text{ref})}$ is the exact solution of Eq. (2.29), calculated by modal expansion. Fig. 2.10 shows the modulus and the phase of AISM and exact solutions, and the associated error as a function of frequency. The estimated MOF thresholds delimit the three frequency ranges of the response, for which three different degrees of accuracy are obtained. The comparison between Figs. 2.10(a,c,e) and Figs. 2.10(b,d,f) shows that the accuracy of

AISM is improved for medium and high frequency ranges as structural damping is increased. In particular, good agreeement between AISM and the exact solution is reached in the modulus and in the phase where the response curve presents smooth variations. On the other hand, the accurate reconstruction of resonances and anti-resonances is especially difficult since it needs the interferences between a large number of image sources.

The accuracy of modal methods is known to behave oppositely with respect to damping. From a frequency point of view, damping widens resonances, which compels the consideration of a greater number of terms when implementing modal methods. From a spatial point of view, increasing damping reduces the contribution from sources located far from the receiver, and thus improves the accuracy of AISM. Furthermore, as the effect of damping is stronger at high frequencies than at low frequencies, the accuracy of AISM is improved with frequency.

2.3.3 Application of AISM to an arbitrary polygonal plate

In this section, a plate without any symmetry or particular geometrical property is studied. Simulations from AISM and Finite Element Method (FEM) are compared. The plate we use has the same material properties as those in 2.3.2, with a structural damping ratio $\eta = 0.07$. The vertices of the plate are located at $(0, 0)$, $(0.75, 0)$ and $(0.5625, 0.9)$ (in meters). FEM tests are performed using I-DEAS 12 NX ®, with linear interpolated quadrilateral elements. The average element length of the mesh is 3 mm, 18.6 times smaller than the wavelength of the highest eigenfrequency taken into account, i.e. 6332.9 Hz (mode number 320). The model has 40078 elements and 40534 nodes. For the AISM simulation, the characteristic length is $r_c = 0.39$ m. The truncation parameter is taken as $\gamma = 22.44$, which gives a truncation radius of $r_t = 8.71$ m, yielding 793 sources. Fig. 2.11 shows the plate with the locations of the sources and the receiver. For the damping ratio $\eta = 0.07$, the MOF = 1 and MOF = 3 frequency thresholds are respectively obtained at 248.2 Hz and 682.6 Hz.

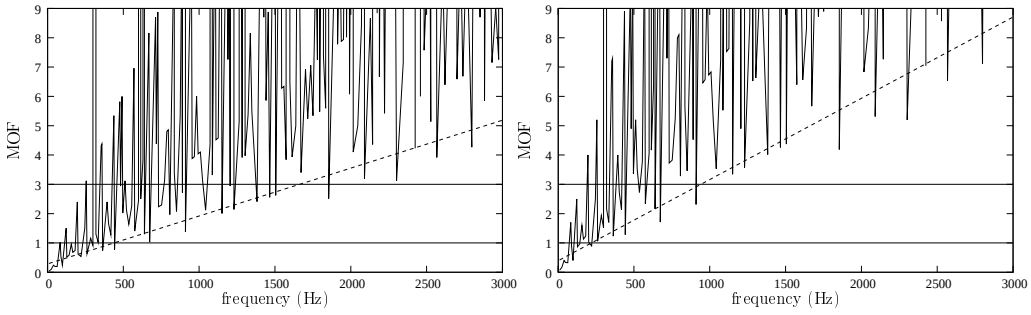

Figure 2.9: Modal Overlap Factor of the isosceles right triangular plate for two values of the structural damping ratio: (a) $\eta = 3 \cdot 10^{-2}$; (b) $\eta = 5 \cdot 10^{-2}$. ——, MOF; - - - -, least-squares fit of the local minimum.

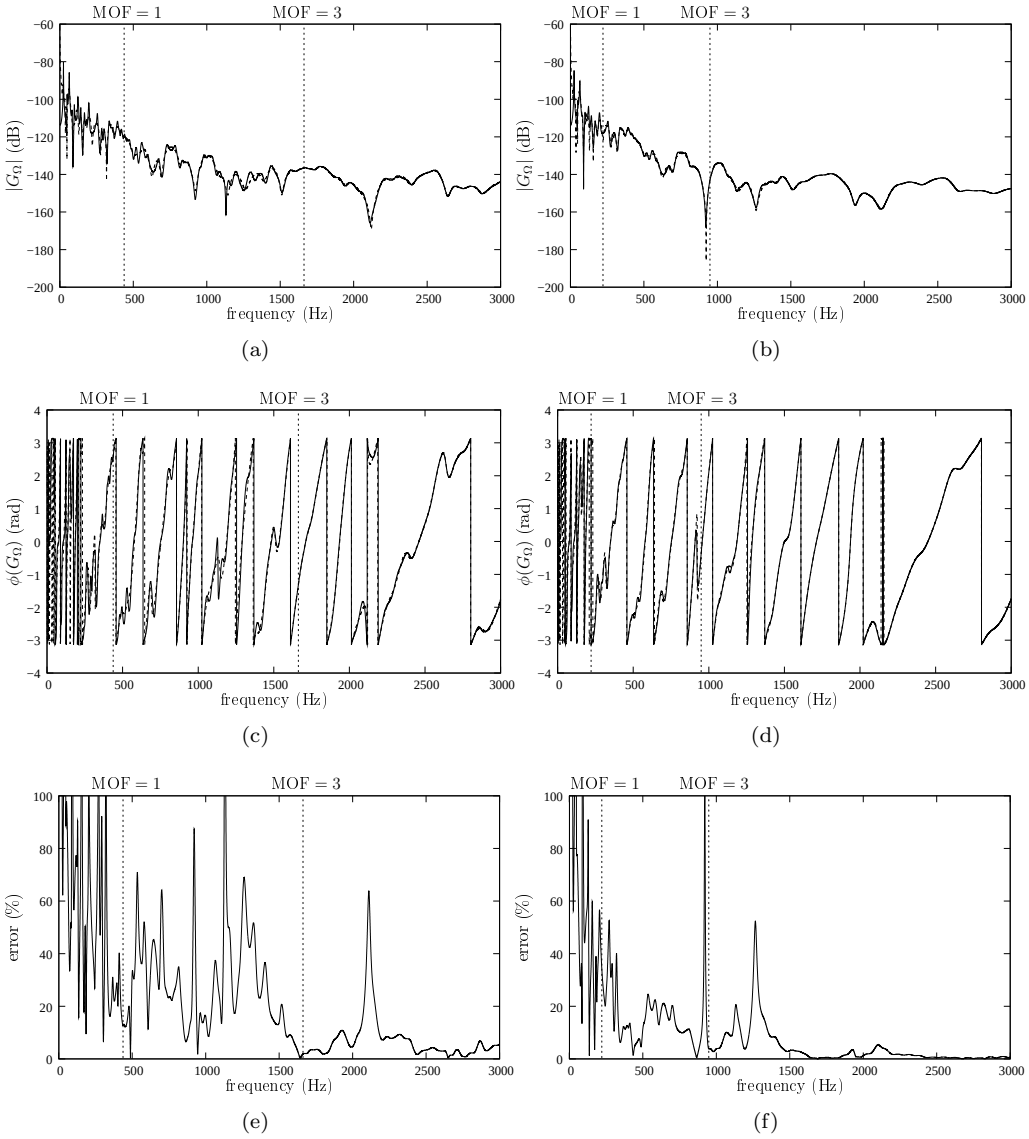

Figure 2.10: Frequency response function of the simply supported isosceles right triangular plate between source $\mathbf{r}_0$ and receiver $\mathbf{r}$, calculated by modal expansion and by AISM for the truncation parameter $\gamma = 10.76$, for two values of the structural damping ratio: (a) modulus, (c) phase and (e) error for $\eta = 3 \cdot 10^{-2}$; (b) modulus, (d) phase and (f) error for $\eta = 5 \cdot 10^{-2}$. ——, exact solution; - - - -, AISM.

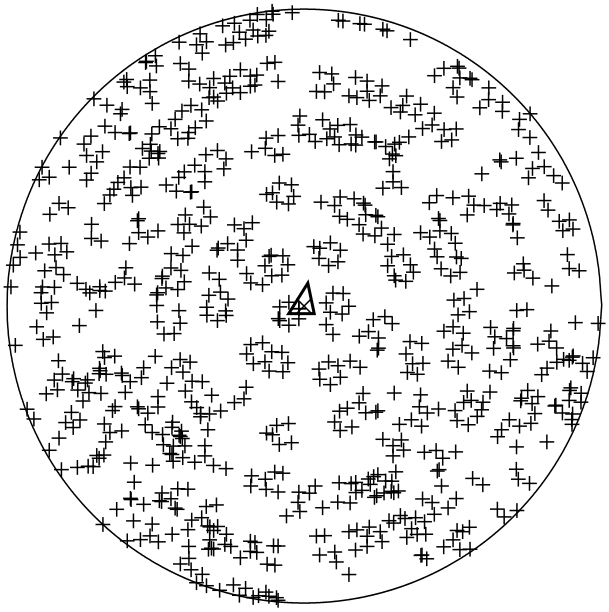

Figure 2.11: Triangular plate used for AISM and FEM simulations with the truncation parameter $\gamma = 22.44$. ——, plate boundaries; +, sources; ×, receiver; ——, truncature.

Fig. 2.12 shows the modulus and the phase of G_Ω estimated from AISM and FEM, and the associated error (Eq. (2.48), where $G_\Omega^{(\mathrm{ref})}$ is taken as the FEM estimation). The results exhibit a similar behaviour to those presented in Fig. 2.10. Large fluctuations in the modulus and on the phase lead to a considerable increase in the error, which is mainly due to the inability of the method to predict a strong resonant behaviour with a finite number of image sources. However, the accuracy of AISM is improved with frequency as the effects of structural damping are dominant over resonances of the system.

Furthermore, for estimating the vibrational behaviour of a plate, FEM needs the computation of the field on all the nodes of the model, while in AISM it is exclusively obtained at the observation point, allowing faster computations. As an example, for obtaining the responses shown in Fig. 2.12, AISM was approximately 40 times faster than FEM. The difference in terms of computation time is also linked to the simplicity of the AISM calculations, which consist in geometrical transformations for generating the image source cloud and then on a sum of the contributions of the sources for constructing the vibrational field at the receiver.

2.3.4 Influence of the truncation radius on the accuracy of AISM

The aim of this subsection is to study the convergence of AISM when increasing the truncation radius. For the purpose of predicting the mean value of the response of complex vibrating systems, Skudrzyk [90] pointed out that, for a plate with a driver or a receiver near an edge, the contribution of the nearest image source is usually strong enough to mask the reverberant field, and that including the effect of more image sources only sharpens the minima of the response curve. Fig. 2.13 shows the comparison between

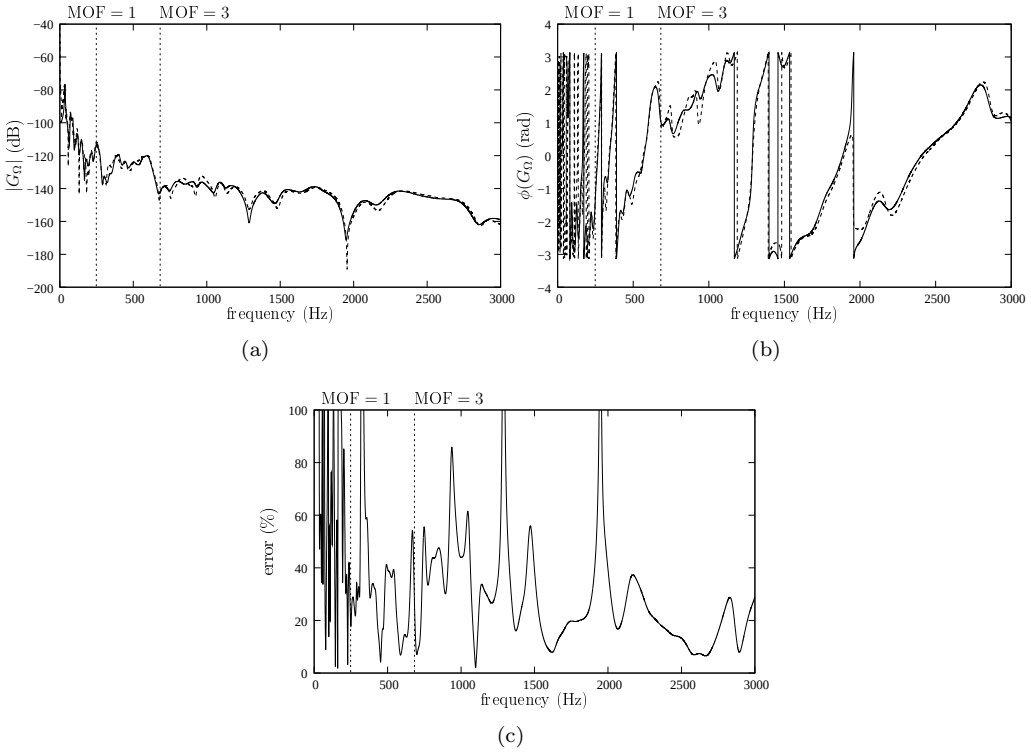

Figure 2.12: ISM and FEM simulations for the arbitrary polygonal plate of Fig. 2.11 for the damping ratio $\eta = 0.07$. (a) modulus, (c) phase and (e) error. ——, FEM solution; ----, AISM.

AISM estimation and exact Green's function G_Ω for the isosceles right triangular plate (Fig. 2.8) with $\eta = 0.03$, for two truncation radii, given by $\gamma = 6.15$ (52 sources) and $\gamma = 30.74$ (1255 sources).

The value $\gamma = 6.15$ leads to an estimation of a mean line of the response and, $\gamma = 30.74$ leads to a low error in medium and high frequency ranges. Thus, the accuracy can be controlled by broadening the cloud of image sources. Fig. 2.14 shows the error on the estimation of $|G_\Omega|$ averaged over the high frequency band (ending at 3 kHz) as a function of γ, from which the limit $\gamma \to \infty$ leading to the exact solution is confirmed.

2.4 Conclusion

The image source method (ISM) is a deterministic method that allows to calculate Green's functions for the flexural vibrations of simply supported convex polygonal plates. Based on this, we have exposed the general method for obtaining such Green's functions. Particular plate geometries leading to a spatially periodic image source cloud yield a spatially periodic Green's function, which can be expressed as a modal expansion by means of a Poisson summation formula. In this way, we have obtained new Green's functions for plates of particular geometries, i.e. rectangle, isosceles right triangle, half-

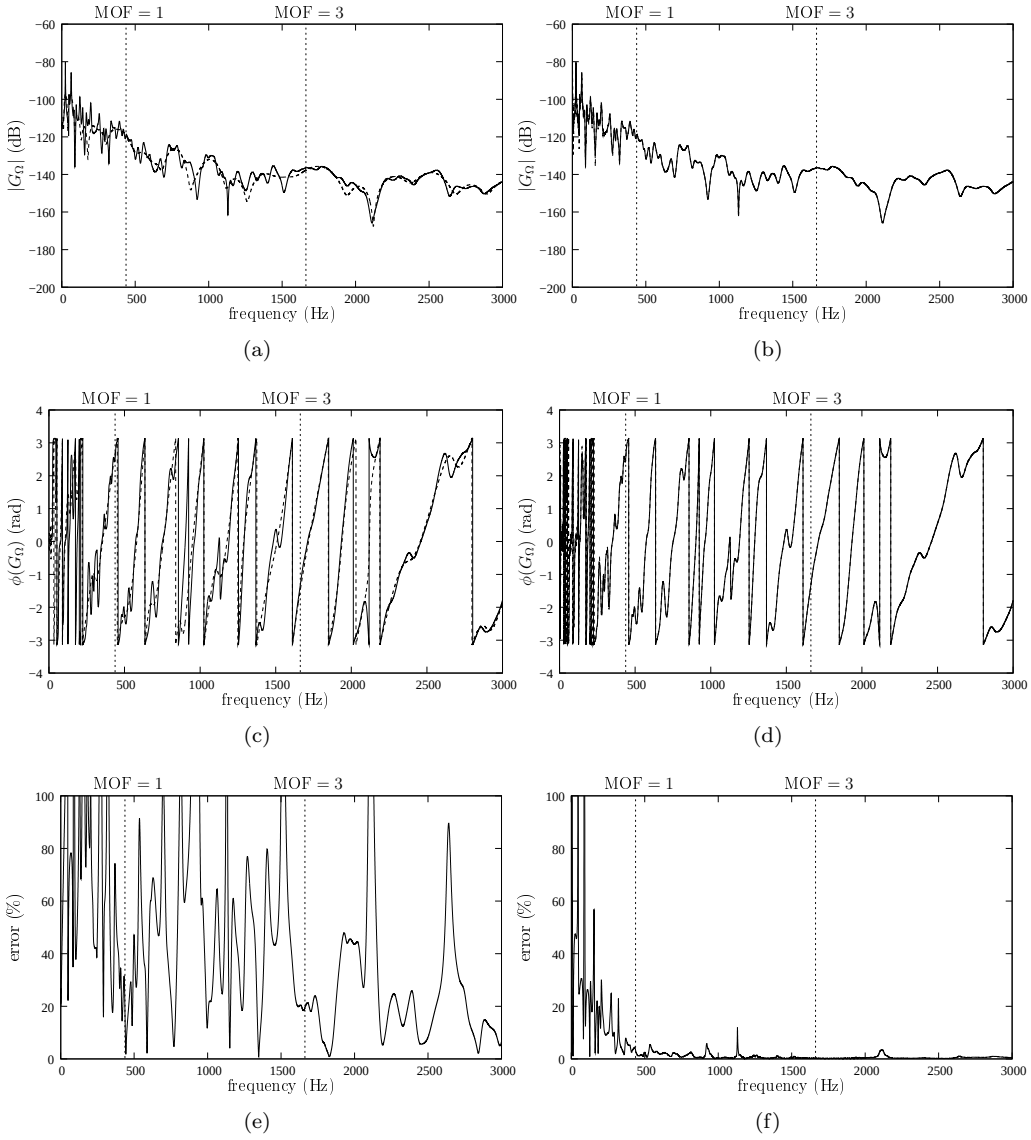

Figure 2.13: Frequency response of the isosceles triangular plate for two values of the truncation parameter: (a) modulus, (c) phase and (e) error for $\gamma = 6.15$; (b) modulus, (d) phase and (f) error for $\gamma = 30.74$. ——, exact solution; - - - -, AISM.

equilateral triangle and equilateral triangle. Subsequently, we have developed a tool for predicting the flexural vibrations of arbitrarily shaped convex polygonal plates, called the approximate image source method (AISM), which consists in truncating the image source cloud. The results show a convergence towards the exact or the FEM solutions as the truncation radius is increased, since more image sources are taken into account. In classical modal methods, the number of modes to take into account needs to be

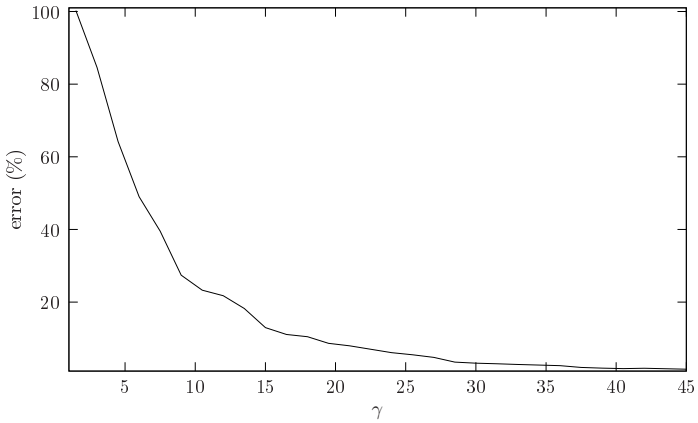

Figure 2.14: Error on the estimation of $|G_\Omega|$ as a function of γ for the isosceles right triangular plate, averaged over the high-frequency band.

increased for high frequencies and for a high damping ratio. On the contrary, since AISM is based on wave propagation, its accuracy is improved in high frequencies, where structural damping is predominant. In counterpart, AISM needs a large number of image sources for the analysis of highly reverberant fields since rapid amplitude and phase variations over frequency are present. However, with few sources in the truncation radius, AISM proves to be able to predict the mean line of the response. Finally, only simply supported boundaries have been considered, for which the reflection coefficient is unitary and omnidirectional. ISM can then be applied to plates with roller boundary conditions, but other kinds of boundaries need further investigation. Coupled structures, such as plate assemblies or stiffened plates [4] can also be investigated by adapting principles of ISM presented in this paper.

2.A Construction of the image source cloud

For a given edge E_p delimited by vertices V_p and V_{p+1}, the location of the image source $S_{m,p}$ relatively to the location of its so-called mother source S_m is determined by vector $\mathbf{S}_m\mathbf{S}_{m,p}$, which can be written as

$$\mathbf{S}_m\mathbf{S}_{m,p} = 2\left(\mathbf{S}_m\mathbf{V}_p + \mathbf{V}_p\mathbf{H}_p\right), \tag{2.49}$$

where H_p is the intersection point of vectors $\mathbf{S}_m\mathbf{S}_{m,p}$ and $\mathbf{V}_p\mathbf{V}_{p+1}$, as shown in Fig. 2.15 for the construction of source S_1 from source S_0 and edge E_1. Using absolute coordinates, the location of image source $S_{m,p}$ is described by vector $\mathbf{r}_{m,p}$, yielding

$$\mathbf{r}_{m,p} = -\mathbf{r}_m + 2\mathbf{v}_p + 2\frac{(\mathbf{r}_m - \mathbf{v}_p)\cdot(\mathbf{v}_{p+1} - \mathbf{v}_p)}{|\mathbf{v}_{p+1} - \mathbf{v}_p|^2}\left(\mathbf{v}_{p+1} - \mathbf{v}_p\right), \tag{2.50}$$

where $\mathbf{r}_m$ is the location of the mother source and $\mathbf{v}_p$ and $\mathbf{v}_{p+1}$ are the locations of the vertices defining E_p.

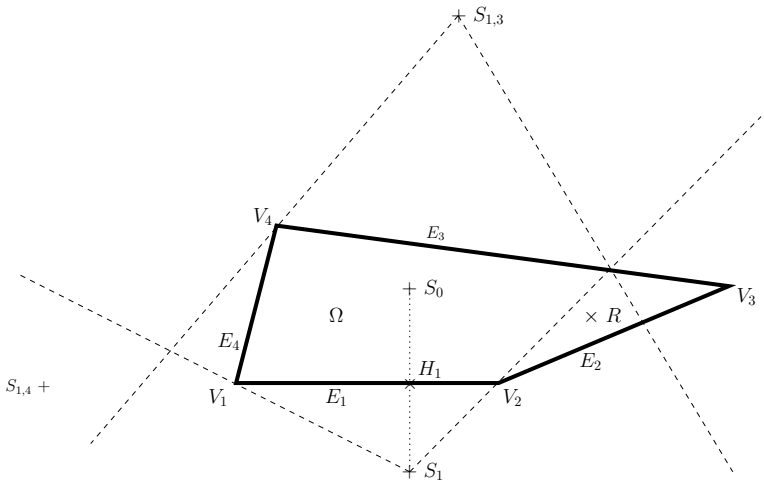

Figure 2.15: Example of image source geometrical construction. ——, plate boundaries; +, sources; ×, receiver; - - -, light zones limits.

The amplitude weights of the sources depend on the reflection coefficient of the boundaries and on the number n of reflections that lead to the source. Thus, for a plate with reflection coefficient $\mathcal{R}$, its amplitude weight is

$$A = (\mathcal{R})^n. \tag{2.51}$$

The reflection coefficient of simply supported edges is $\mathcal{R} = -1$, yielding

$$A = (-1)^n. \tag{2.52}$$

For example, in Fig. 2.15, the amplitude weigths of sources S_0, S_1 and $S_{1,3}$ are respectively $A_0 = 1$, $A_1 = -1$ and $A_{1,3} = 1$.

Furthermore, a given source contributes to the field at the receiver if it is visible from the receiver, i.e. if the receiver is in the "light" zone of the source. Additionally, a given source creates a new image source if the inside (i.e. the reflecting side) of the corresponding edge is in its light zone [67]. The same can be interpreted in terms of rays. Each image source contribution describes a vibrational ray in the plate. Thus, the existence of an image source relies on whether the corresponding ray path between the source and the receiver is possible or not. However, some precautions are to be taken into account since an image source that is invisible from the receiver can give rise to a visible image source. Fig. 2.15 shows an example of construction of the first image sources of a plate, in which some image sources do not contribute to the vibrational field at the receiver. $S_{1,2}$ does not exist because edge E_2 is out of the light zone of S_1. Moreover, S_1 does not contribute to the vibrational field at R, but its image source at E_3, $S_{1,3}$, does.

2.B Elementary cells of equilateral and half-equilateral triangular plates

2.B.1 Half-equilateral triangular plate

Fig. 2.16 shows the elementary cell of the half equilateral triangular plate.

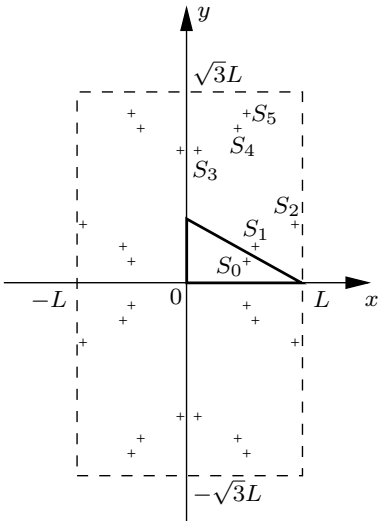

Figure 2.16: Elementary cell of the half-equilateral triangular plate. Six sources, denoted S_i $(i = 0, ..., 5)$ and located at (x_i, y_i), are necessary to describe this cell.

The coordinates of the principal source of each of the six quadrupoles that form this elementary cell (presented in section 2.2.5.3) are

$$\begin{aligned}
\begin{pmatrix} x_0 \\ y_0 \end{pmatrix} &\quad \textit{original source} \\
\begin{pmatrix} x_1 \\ y_1 \end{pmatrix} &= \frac{1}{2}\begin{pmatrix} L + x_0 - \sqrt{3}y_0 \\ -y_0 + \sqrt{3}(L - x_0) \end{pmatrix} \\
\begin{pmatrix} x_2 \\ y_2 \end{pmatrix} &= \frac{1}{2}\begin{pmatrix} L + x_0 + \sqrt{3}y_0 \\ y_0 + \sqrt{3}(L - x_0) \end{pmatrix} \\
\begin{pmatrix} x_3 \\ y_3 \end{pmatrix} &= \frac{1}{2}\begin{pmatrix} L - x_0 - \sqrt{3}y_0 \\ -y_0 + \sqrt{3}(L + x_0) \end{pmatrix} \\
\begin{pmatrix} x_4 \\ y_4 \end{pmatrix} &= \frac{1}{2}\begin{pmatrix} L - x_0 + \sqrt{3}y_0 \\ y_0 + \sqrt{3}(L + x_0) \end{pmatrix} \\
\begin{pmatrix} x_5 \\ y_5 \end{pmatrix} &= \begin{pmatrix} L - x_0 \\ \sqrt{3}L - y_0 \end{pmatrix},
\end{aligned} \tag{2.53}$$

where L is the length of the triangle base. The sequence giving the relative weights of the quadrupoles that form the elementary cell is, in the same order,

$$\xi_i = \{1, -1, 1, 1, -1, 1\}\,. \tag{2.54}$$

2.B.2 Equilateral triangular plate

Fig. 2.17 shows the elementary cell of the equilateral triangular plate.

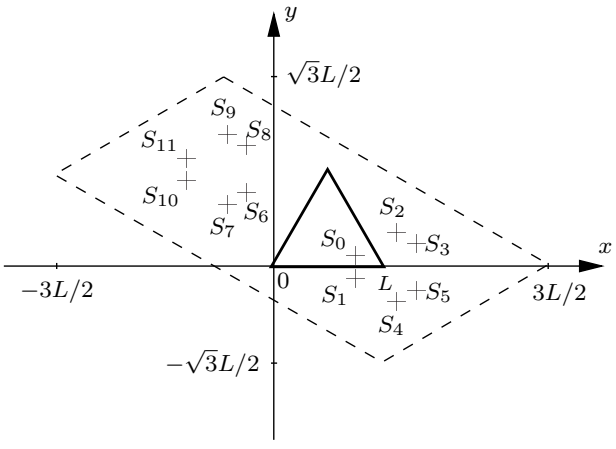

Figure 2.17: Elementary cell of the equilateral triangular plate. Twelve sources, denoted S_i $(i = 0, ..., 11)$ and located at (x_i, y_i), are necessary to describe this cell.

The coordinates of the sources of the the elementary cell (section 2.2.5.4) of this plate are

$$
\begin{aligned}
\begin{pmatrix} x_0 \\ y_0 \end{pmatrix} & \quad \textit{original source} \\
\begin{pmatrix} x_1 \\ y_1 \end{pmatrix} &= \begin{pmatrix} x_0 \\ -y_0 \end{pmatrix} \\
\begin{pmatrix} x_2 \\ y_2 \end{pmatrix} &= \frac{1}{2}\begin{pmatrix} 3L - \sqrt{3}y_0 - x_0 \\ \sqrt{3}L + y_0 - \sqrt{3}x_0 \end{pmatrix} \\
\begin{pmatrix} x_3 \\ y_3 \end{pmatrix} &= \frac{1}{2}\begin{pmatrix} 3L + \sqrt{3}y_0 - x_0 \\ \sqrt{3}L - y_0 - \sqrt{3}x_0 \end{pmatrix} \\
\begin{pmatrix} x_4 \\ y_4 \end{pmatrix} &= \frac{1}{2}\begin{pmatrix} 3L - \sqrt{3}y_0 - x_0 \\ -\sqrt{3}L - y_0 + \sqrt{3}x_0 \end{pmatrix} \\
\begin{pmatrix} x_5 \\ y_5 \end{pmatrix} &= \frac{1}{2}\begin{pmatrix} 3L + \sqrt{3}y_0 - x_0 \\ -\sqrt{3}L + y_0 + \sqrt{3}x_0 \end{pmatrix} \\
\begin{pmatrix} x_6 \\ y_6 \end{pmatrix} &= \frac{1}{2}\begin{pmatrix} \sqrt{3}y_0 - x_0 \\ y_0 + \sqrt{3}x_0 \end{pmatrix} \\
\begin{pmatrix} x_7 \\ y_7 \end{pmatrix} &= \frac{1}{2}\begin{pmatrix} -\sqrt{3}y_0 - x_0 \\ -y_0 + \sqrt{3}x_0 \end{pmatrix} \\
\begin{pmatrix} x_8 \\ y_8 \end{pmatrix} &= \frac{1}{2}\begin{pmatrix} \sqrt{3}y_0 - x_0 \\ 2\sqrt{3}L - y_0 - \sqrt{3}x_0 \end{pmatrix} \\
\begin{pmatrix} x_9 \\ y_9 \end{pmatrix} &= \frac{1}{2}\begin{pmatrix} -\sqrt{3}y_0 - x_0 \\ 2\sqrt{3}L + y_0 - \sqrt{3}x_0 \end{pmatrix} \\
\begin{pmatrix} x_{10} \\ y_{10} \end{pmatrix} &= \frac{1}{2}\begin{pmatrix} -3L + 2x_0 \\ \sqrt{3}L - 2y_0 \end{pmatrix} \\
\begin{pmatrix} x_{11} \\ y_{11} \end{pmatrix} &= \frac{1}{2}\begin{pmatrix} -3L + 2x_0 \\ \sqrt{3}L + 2y_0 \end{pmatrix},
\end{aligned}
\tag{2.55}
$$

where L is the length of the triangle side. The sequence giving the relative weights of the sources in the elementary cell is, in the same order,

$$\xi_i = \{1, -1, -1, 1, 1, -1, -1, 1, 1, -1, -1, 1\}. \tag{2.56}$$

2.C Asymptotic modal overlap factor

As pointed out in sec. 2.3.2, the modal overlap factor (MOF) is defined as the ratio of the -3dB bandwidth $\Delta\omega_p$ of a given resonance of circular frequency ω_p to the frequency interval $\delta\omega_p$ between two successive resonances, as

$$\mathrm{MOF}_p = \frac{\Delta\omega_p}{\delta\omega_p}, \tag{2.57}$$

which is a discrete function of frequency. An asymptotic MOF can be calculated from the average modal density. The average frequency interval $\delta\omega_p$ between two

successive resonances is directly related to the modal density n, defined as the number of eigenfrequencies per unit frequency, which can be written as

$$n(\omega_p) = \frac{1}{\delta\omega_p}. \tag{2.58}$$

For the flexural vibrations of a thin plate, the modal density assumes the high-frequency asymptotic form [62]

$$n(\omega) = \frac{S}{4\pi}\sqrt{\frac{\rho h}{D}}, \tag{2.59}$$

where S is the total surface area of the plate. The quality factor Q of a given resonance is defined as

$$Q = \frac{\omega_p}{\Delta\omega_p}. \tag{2.60}$$

The function describing each resonance of the plate is proportional to a filter function of the form

$$H(\omega) = \frac{1}{\omega_p^2 - \omega^2 - j\eta\omega_p^2}. \tag{2.61}$$

Thus, the circular frequencies $\omega_\pm$ which delimit the -3dB frequency bandwidth $\Delta\omega_p$ satisfy the equation

$$|H(\omega_\pm)| = \frac{1}{\sqrt{2}}|H(\omega_p)|, \tag{2.62}$$

which yields

$$\Delta\omega_p = \omega_+ - \omega_- = \omega_p\left(\sqrt{1+\eta} - \sqrt{1-\eta}\right). \tag{2.63}$$

For metallic plates in general, the structural damping ratio η is less than 0.1, which allows to write an approximated expresssion for Q in the form[3]

$$Q \simeq \frac{1}{1+\eta/2-(1-\eta/2)} = \frac{1}{\eta}. \tag{2.64}$$

Inserting Eqs. (2.58), (2.59), (2.60) and (2.64) in Eq. (2.57) yields

$$\mathrm{MOF}_p = \frac{\omega_p \eta S}{4\pi}\sqrt{\frac{\rho h}{D}}. \tag{2.65}$$

Thus, the average modal overlap factor at any circular frequency is

$$\mathrm{MOF} = \frac{\omega \eta S}{4\pi}\sqrt{\frac{\rho h}{D}}. \tag{2.66}$$

[3] In literature and in simulation software, it is usual to find and expression of the quality factor in the form $Q = 1/2\eta'$, which arises from the one-degree-of-freedom oscillator equation in the form

$$\ddot{u}(t) + 2\eta'\dot{u}(t) + \omega_0 u(t) = f(t).$$

The correspondence between the two definitions of the damping ratio is then $\eta = 2\eta'$. The definition used herein is compatible with Ref. [80].

Chapter 3

Model of the boundary conditions of thin plates using a state vector approach

Abstract

The purpose of this chapter is to establish a tool for describing wave reflection and transmission at plate edges and junctions, as a basis for the application of the image source method to plates with arbitrary boundary conditions. The formalism is based on a state vector approach, which consists in representing the field of a vibrating structure by a vector containing the displacement, the slope, the moment and the shear force at a given point. Such representation is adequate for describing boundary conditions as matrix equations. A wave vector containing the weights of propagating and evanescent waves travelling in the plate can be linked to the state vector by a variable change. Thus, appropriate use of the state and wave vectors allows to obtain the relative weights of elementary waves travelling in the plate from the boundary conditions, in the form of a reflection matrix in the case of plate edges and in the form of a scattering matrix in the case of junctions between two semi-infinite plates. First, the formalism is presented, including the link between the state and wave vectors. Then, the model of boundary conditions for edges and junctions is developed. Examples of application are given for different edges and junctions.

3.1 Model of flexural wave motion in thin plates by the state vector approach

As detailed in chap. 1, the flexural motion of a thin plate can be described by means of the displacement, slopes, moments and shear forces, which are mechanical variables describing the state of motion. Naturally, boundary conditions are expressed using the same variables. On the other hand, the understanding of wave scattering or reflection due to a particular edge or junction requires the use of a different type of variables,

which are the relative weights of propagating and evanescent waves that are incident, transmitted or reflected at a given boundary.

In this section, the state vector approach [26, 29, 65, 76, 77, 98] is applied to the flexural motion of thin plates in order to obtain the relation between the state variables and the components of the different waves that travel perpendicularly to a discontinuity in the plate. Such information is later used in sec. 3.2 for obtaining the scattering matrix of a junction between two plates and the reflection matrix of a plate edge. Examples of validation and application of the method are given in sec. 3.3.

3.1.1 Global and local coordinates

The pair of coordinates (x, y) is henceforth referred to as the global coordinate system of a given plate Ω. A local coordinate system (ξ, μ) is used for describing the variation of the state vector along particular directions of space such as for describing wave reflection and/or transmission at a given boundary $\partial\Omega$, as shown in Fig. 3.1.

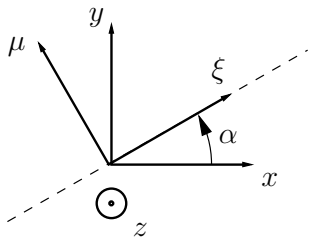

Figure 3.1: Global coordinates (x, y) and local coordinates (ξ, μ). The dashed line represents a given boundary of a plate.

The change of coordinates is defined as

$$\begin{cases} \xi = x\cos(\alpha) + y\sin(\alpha), & (3.1) \\ \mu = -x\sin(\alpha) + y\cos(\alpha), & (3.2) \end{cases}$$

where α is the angle between the two coordinate systems. Also, wavenumber coordinates are needed in the rest of this chapter. Thus, local coordinates (ξ, μ) are associated to wavenumber coordinates (k_ξ, k_μ). For a plate boundary located along axis ξ, k_ξ can be referred to as the 'axial' wavenumber coordinate, k_μ being the 'transverse' wavenumber coordinate. In the model of plate boundaries, presented in sec. 3.2, the different propagating and evanescent waves needed for describing wave reflection and transmission are related to different values of the transverse wavenumber coordinate.

For the sake of generality, local coordinates (ξ, μ) are used in what follows.

3.1.2 Matrix form of the equations of motion

The state of the cross-section of normal μ of a thin plate Ω is described by the state vector

$$\mathbf{W}(\xi,\mu) = \begin{bmatrix} w(\xi,\mu) \\ \theta_\mu(\xi,\mu) \\ M_\mu(\xi,\mu) \\ V_\mu(\xi,\mu) \end{bmatrix}, \tag{3.3}$$

where w, θ_μ, M_μ and V_μ are respectively the transverse displacement, the slope along the μ direction, the bending moment along μ and the shear force along μ. Torsional motion is henceforth ignored.

Without loss of generality, the ξ component of the state vector is assumed to describe a propagating wave towards the direction of the ξ axis given by the sign of k_ξ, such that

$$\mathbf{W}(\xi,\mu) = \mathbf{W}(k_\xi,\mu)e^{jk_\xi\xi}, \tag{3.4}$$

which is in accordance with the time convention $e^{-j\omega t}$ defined in chap. 1. As defined above, k_ξ is here the wavenumber coordinate associated to spatial coordinate ξ, referred to as the axial wavenumber coordinate, k_μ being the transverse wavenumber coordinate. Thus, the problem becomes one-dimensional, since the dependence on one of the two directions of space is known. Considering Eqs. (1.1), (1.3), (1.5) and (1.11) in the (ξ,μ) coordinate system, their derivatives with respect to μ, along with Eq. (1.16), yield the matrix form of the equations of motion [98],

$$\frac{\partial \mathbf{W}}{\partial \mu} = \mathbf{H}\mathbf{W}, \tag{3.5}$$

where

$$\mathbf{H}(k_\xi) = \begin{bmatrix} 0 & 1 & 0 & 0 \\ \nu k_\xi^2 & 0 & -1/D & 0 \\ 0 & 2(\nu-1)Dk_\xi^2 & 0 & 1 \\ -\rho h\omega^2 + (1-\nu^2)Dk_\xi^4 & 0 & \nu k_\xi^2 & 0 \end{bmatrix} \tag{3.6}$$

is a matrix relating the state vector to its derivative with respect to μ, referred to as a transition matrix [76]. Eq. (3.5) can be solved in the eigenspace of matrix $\mathbf{H}$, which is described by four eigenvalues and their corresponding eigenvectors. Each eigenvector E_i and its corresponding eigenvalue λ_i satisfy the equation

$$\mathbf{H}E_i = \lambda_i E_i, \tag{3.7}$$

where $i = 1,2,3,4$. Those eigenvalues and eigenvectors can be respectively gathered in eigenvalue and eigenvector matrices, as

$$\mathbf{\Lambda} = \mathrm{diag}\,(\lambda_1,\lambda_2,\lambda_3,\lambda_4) \tag{3.8}$$

and

$$\mathbf{E} = [E_1 \;\; E_2 \;\; E_3 \;\; E_4]\,. \tag{3.9}$$

Thus, a general relation for the whole set of eigenvalues and eigenvectors is established, as

$$\mathbf{HE} = \mathbf{\Lambda E}. \tag{3.10}$$

Here, $\mathbf{E}$ appears as the transition matrix from the eigenspace to the state vector space. Thus, applying the change of basis

$$\mathbf{W}(k_\xi, \mu) = \mathbf{EV}(k_\xi, \mu) \tag{3.11}$$

to Eq. (3.5) and noting that $\mathbf{E}$ is constant with respect to μ, leads to the equation

$$\frac{\partial \mathbf{V}}{\partial \mu} = \mathbf{\Lambda V}, \tag{3.12}$$

consisting of four independent equations, since $\mathbf{\Lambda}$ is diagonal. The solution of Eq. (3.12) can be written as

$$\mathbf{V}(k_\xi, \mu) = \mathbf{Q}(\mu, \mu_0)\mathbf{V}(k_\xi, \mu_0), \tag{3.13}$$

where

$$\mathbf{Q}(\mu, \mu_0) = e^{\mathbf{\Lambda}(\mu-\mu_0)} = \operatorname{diag}\left(e^{\lambda_i(\mu-\mu_0)}\right) \tag{3.14}$$

is the wave propagator matrix, also referred to as a transfer matrix [98], relating the wave vector at two different locations of the μ axis. The value μ_0 denotes an arbitrary reference location on the μ axis, appearing as an integration constant when solving Eq. (3.12). Applying the basis change, Eq. (3.11), from the eigenspace to the state vector space, to Eq. (3.13) yields the solution of the matrix equation of motion in the form

$$\mathbf{W}(k_\xi, \mu) = \mathbf{P}(\mu, \mu_0)\mathbf{W}(k_\xi, \mu_0), \tag{3.15}$$

where

$$\mathbf{P} = \mathbf{EQE}^{-1} \tag{3.16}$$

is the state propagator matrix, which links the state vector at two different locations on the μ axis of the plate. Eq. (3.13) represents the flexural motion of the plate as propagating or evanescent plane waves travelling in the positive or negative directions of the μ axis, according to eigenvalues λ_i.

3.1.3 Specifying the eigenvalue and eigenvector matrices

In this paragraph, the expressions of the eigenvalue and eigenvector matrices are derived. The eigenvalues can be classified according to the type of wave and travelling direction that each one of them is associated to, such that the eigenvalue matrix can be written as

$$\mathbf{\Lambda} = \operatorname{diag}\left(\lambda_{p-}, \lambda_{e-}, \lambda_{p+}, \lambda_{e+}\right), \tag{3.17}$$

where p and e denote propagating and evanescent waves, and $+$ and $-$ denote positive and negative travelling directions along the μ axis. For example, λ_{e-} corresponds to an evanescent wave decaying in the negative direction of μ axis. The eigenvector matrix is

ordered in the same manner, as

$$\mathbf{E} = \begin{bmatrix} E_{p-} & E_{e-} & E_{p+} & E_{e+} \end{bmatrix}. \tag{3.18}$$

The wave vector follows in the form

$$\mathbf{V} = \begin{bmatrix} V_{p-} \\ V_{e-} \\ V_{p+} \\ V_{e+} \end{bmatrix}, \tag{3.19}$$

where each term represents a propagating or evanescent wave travelling towards the positive or negative direction of the μ axis.

In order to specify the values of the different terms of $\mathbf{\Lambda}$ and $\mathbf{E}$, the solution of Eq. (1.16) is considered in the separated-variable form [34]

$$w(\xi, \mu; k_f) = \left(A e^{-j\sqrt{k_f^2 - k_\xi^2}\mu} + B e^{\sqrt{k_f^2 - k_\xi^2}\mu} + C e^{j\sqrt{k_f^2 - k_\xi^2}\mu} + D e^{-\sqrt{k_f^2 + k_\xi^2}\mu} \right) e^{jk_\xi \xi}, \tag{3.20}$$

which arises as a sum of propagating and evanescent plane waves. According to the $e^{-j\omega t}$ time convention, the term $A e^{-j\sqrt{k_f^2 - k_\xi^2}\mu}$ represents a propagating wave travelling towards the negative μ direction, the term $B e^{\sqrt{k_f^2 - k_\xi^2}\mu}$ represents an evanescent wave decaying towards the negative μ direction, and inversely for the other two terms. The expressions of $\mathbf{E}$ and $\mathbf{\Lambda}$ can easily be obtained by applying Eqs. (1.1), (1.3), (1.5) and (1.11) to the displacement field in the form of Eq. (3.20), such that Eq. (3.11) can be written as

$$\begin{bmatrix} w(k_\xi, \mu) \\ \theta_\mu(k_\xi, \mu) \\ M_\mu(k_\xi, \mu) \\ V_\mu(k_\xi, \mu) \end{bmatrix} = \mathbf{E} \begin{bmatrix} A e^{-j\sqrt{k_f^2 - k_\xi^2}\mu} \\ B e^{\sqrt{k_f^2 - k_\xi^2}\mu} \\ C e^{j\sqrt{k_f^2 - k_\xi^2}\mu} \\ D e^{-\sqrt{k_f^2 + k_\xi^2}\mu} \end{bmatrix} e^{jk_\xi \xi}, \tag{3.21}$$

where

$$\mathbf{E} = \begin{bmatrix} 1 & 1 & \cdots \\ -j\sqrt{k_f^2 - k_\xi^2} & \sqrt{k_f^2 + k_\xi^2} & \\ D\left(k_f^2 - (1-\nu)k_\xi^2\right) & -D\left(k_f^2 + (1-\nu)k_\xi^2\right) & \\ -Dj\sqrt{k_f^2 - k_\xi^2}\left(k_f^2 + (1-\nu)k_\xi^2\right) & -D\sqrt{k_f^2 + k_\xi^2}\left(k_f^2 - (1-\nu)k_\xi^2\right) & \end{bmatrix}$$

$$\begin{bmatrix} \cdots & 1 & 1 \\ & j\sqrt{k_f^2 - k_\xi^2} & -\sqrt{k_f^2 + k_\xi^2} \\ & D\left(k_f^2 - (1-\nu)k_\xi^2\right) & -D\left(k_f^2 + (1-\nu)k_\xi^2\right) \\ & Dj\sqrt{k_f^2 - k_\xi^2}\left(k_f^2 + (1-\nu)k_\xi^2\right) & D\sqrt{k_f^2 + k_\xi^2}\left(k_f^2 - (1-\nu)k_\xi^2\right) \end{bmatrix}. \tag{3.22}$$

The associated eigenvalue matrix is then

$$\mathbf{\Lambda} = \begin{bmatrix} -j\sqrt{k_f^2 - k_\xi^2} & 0 & 0 & 0 \\ 0 & \sqrt{k_f^2 + k_\xi^2} & 0 & 0 \\ 0 & 0 & j\sqrt{k_f^2 - k_\xi^2} & 0 \\ 0 & 0 & 0 & -\sqrt{k_f^2 + k_\xi^2} \end{bmatrix}. \tag{3.23}$$

Fig. 3.2 shows the real and imaginary parts of the different terms of the eigenvalue matrix $\mathbf{\Lambda}$, as functions of the axial wavenumber k_ξ. The figure shows that the terms $e^{\pm j\sqrt{k_f^2 - k_\xi^2}\mu}$ represent propagating waves in the two directions of the μ axis for $|k_\xi| < |k_f|$ and evanescent waves decaying in the two directions of the μ axis for $|k_\xi| > |k_f|$. Furthermore, the terms $e^{\pm\sqrt{k_f^2 - k_\xi^2}\mu}$ represent evanescent waves for any value of k_ξ. If structural damping is considered, as defined in Eq. (1.20), k_f is complex, with a small imaginary part compared to its real part. Thus, in this case, spatial dependence $e^{\pm j\sqrt{k_f^2 - k_\xi^2}\mu}$ represents waves that propagate with a slight decrease in amplitude with distance and spatial dependence $e^{\pm\sqrt{k_f^2 + k_\xi^2}\mu}$ represent decaying waves with a slow oscillatory behaviour. This can be observed in the central part of Fig. 3.2, where the rounded corners indicate that the curves are outside the real and imaginary planes.

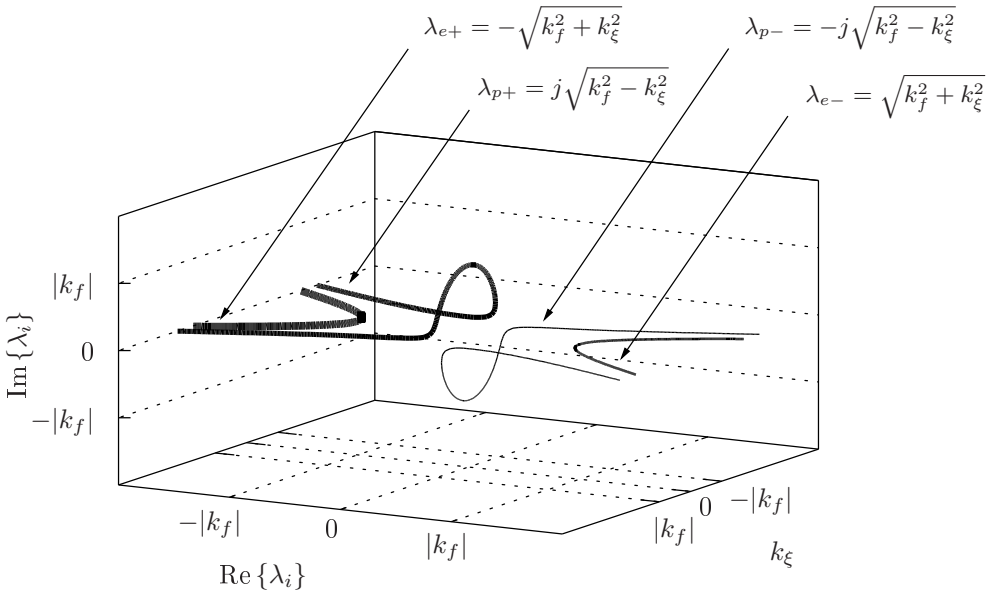

Figure 3.2: Different terms of the eigenvalue matrix $\mathbf{\Lambda}$. Thiner to thicker curves respectively represent eigenvalues λ_{p-}, λ_{e-}, λ_{p+} and λ_{e+}.

Gathering waves together according to their travelling direction allows to write condensed forms of the above expressions,

$$\mathbf{\Lambda} = \mathrm{diag}\,(\lambda_-, \lambda_+)\,, \tag{3.24}$$

$$\mathbf{E} = \begin{bmatrix}\mathbf{E}_- & \mathbf{E}_+\end{bmatrix}, \tag{3.25}$$

$$\mathbf{V}(k_\xi, \mu) = \begin{bmatrix}\mathbf{V}_- \\ \mathbf{V}_+\end{bmatrix}, \tag{3.26}$$

where subscripts $-$ and $+$ respectively represent waves travelling towards the negative and the positive directions of μ axis. Thus, further operations linking waves of types $\mathbf{V}_-$ and $\mathbf{V}_+$ allow to obtain the scattering matrix of a junction between two semi-infinite plates or the reflection matrix of a semi-infinite plate, as detailed hereafter.

3.2 Model of the boundary conditions

The purpose of this section is to present the determination of the reflection matrix of a plate edge and the scattering matrix of a junction between two semi-infinite plates by using the state vector formalism developed in the previous section. The reflection and scattering matrices that can be obtained using this approach are intended to be used in the image source method, detailed in chaps. 2, 4 and 5.

3.2.1 Reflection matrix of a plate edge

The aim of this paragraph is to determine the reflection matrix of the edge of a semi-infinite plate in a half-plane, e.g. $\mu > \mu_b$, as illustrated in Fig. 3.3.

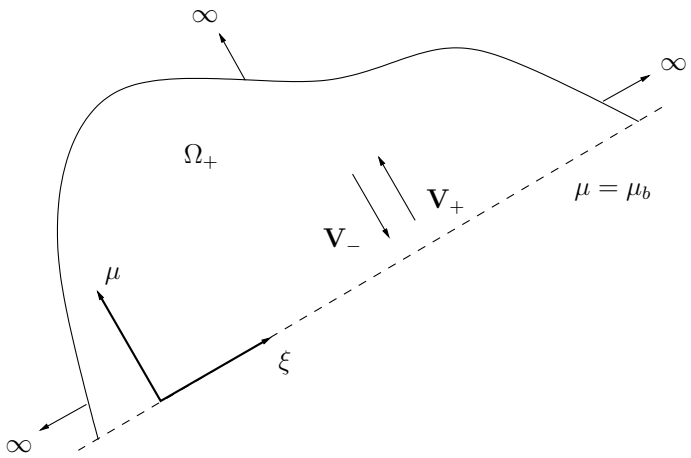

Figure 3.3: Edge of a semi-infinite plate Ω^+, located along line $\mu = \mu_b$. $\mathbf{V}_+$ and $\mathbf{V}_-$ respectively represent the wave vectors associated to incident and reflected fields.

The boundary conditions associated to the edge are given by a linear set of two equations involving the displacement, slope, moment and shear force, which can be

expressed using the boundary equation

$$\mathbf{B}(k_\xi)\mathbf{W}(k_\xi,\mu_b)=0, \tag{3.27}$$

where $\mathbf{B}$ is the boundary matrix, of dimension 2×4. The incident field on the boundary $\mathbf{V}_-$ and the reflected field $\mathbf{V}_+$, shown in Fig. 3.3, are linked together by a reflection matrix $\mathbf{R}$, following the relation

$$\mathbf{V}_+(k_\xi,\mu_b)=\mathbf{R}(k_\xi)\mathbf{V}_-(k_\xi,\mu_b). \tag{3.28}$$

In order to determine $\mathbf{R}$ from the knowledge of $\mathbf{B}$, Eq. (3.27) can be written using Eq. (3.11), as

$$\mathbf{B}(k_\xi)\mathbf{E}(k_\xi)\mathbf{V}(k_\xi,\mu_b)=0. \tag{3.29}$$

Using Eqs. (3.25) and (3.26) for separately writing incident and reflected waves yields

$$\begin{bmatrix}\mathbf{BE}_- & \mathbf{BE}_+\end{bmatrix}\begin{bmatrix}\mathbf{V}_-\\ \mathbf{V}_+\end{bmatrix}=0. \tag{3.30}$$

The reflection matrix is then

$$\mathbf{R}=-\left(\mathbf{BE}_+\right)^{-1}\left(\mathbf{BE}_-\right). \tag{3.31}$$

According to the order of the different terms in vectors $\mathbf{V}_-$ and $\mathbf{V}_+$, the reflection matrix can be written as

$$\mathbf{R}=\begin{bmatrix}R_{pp} & R_{ep}\\ R_{pe} & R_{ee}\end{bmatrix}, \tag{3.32}$$

where each term of the form R_{ir} represents reflection of incident wave i to reflected wave r, where i and r denote either propagating (p) or evanescent (e) waves.

3.2.2 Scattering matrix of a junction between two plates

The aim of this paragraph is to determine the scattering matrix of a junction between two semi-infinite plates Ω^- and Ω^+, located along $\mu=\mu_b$, as shown in Fig. 3.4. The abscissas of the boundary in Ω^- and Ω^+, infinitely near the junction, are respectively denoted μ_b^- and μ_b^+.

The scattering matrix of the junction between plates Ω^- and Ω^+ represents the coupling between waves travelling towards the junction, $\mathbf{V}^{\text{in}}$, and waves originating at the junction, $\mathbf{V}^{\text{out}}$. Such relation can be written as

$$\mathbf{V}^{\text{out}}=\mathbf{S}\mathbf{V}^{\text{in}}, \tag{3.33}$$

where vectors

$$\mathbf{V}^{\text{in}}(\mu_b)=\begin{bmatrix}V_+(\mu_b^-)\\ V_-(\mu_b^+)\end{bmatrix} \tag{3.34}$$

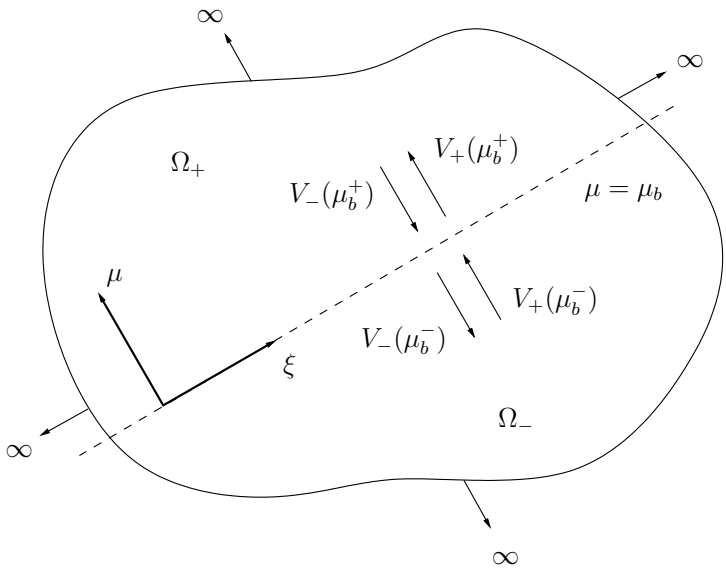

Figure 3.4: Junction between two semi-infinite plates Ω^- and Ω^+, located along line $\mu = \mu_b$. The different arrows represent the ingoing and outgoing waves at the junction.

and

$$\mathbf{V}^{\text{out}}(\mu_b) = \begin{bmatrix} V_+(\mu_b^+) \\ V_-(\mu_b^-) \end{bmatrix} \tag{3.35}$$

represent respectively the ingoing and outgoing waves at the junction, as shown in Fig. 3.4. The convention used for vectors $\mathbf{V}^{\text{in}}$ and $\mathbf{V}^{\text{out}}$ is chosen such that the scattering matrix assumes the form

$$\mathbf{S} = \begin{bmatrix} \mathbf{T}_{-+} & \mathbf{R}_{++} \\ \mathbf{R}_{--} & \mathbf{T}_{+-} \end{bmatrix}. \tag{3.36}$$

Matrices $\mathbf{R}_{--}$ and $\mathbf{R}_{++}$ are the reflection matrices of the junction in the semi-infinite domains Ω^- and Ω^+, respectively. Similarly, $\mathbf{T}_{-+}$ and $\mathbf{T}_{+-}$ are the transmission matrices from Ω^- to Ω^+ and from Ω^+ to Ω^-, respectively. Matrices $\mathbf{R}$ and $\mathbf{T}$ are of dimension 2×2 and can be respectively written as

$$\mathbf{R} = \begin{bmatrix} R_{pp} & R_{ep} \\ R_{pe} & R_{ee} \end{bmatrix} \tag{3.37}$$

and

$$\mathbf{T} = \begin{bmatrix} T_{pp} & T_{ep} \\ T_{pe} & T_{ee} \end{bmatrix}, \tag{3.38}$$

in which p and e respectively denote waves of propagating and evanescent kinds, such that each term in the form R_{ir} (resp. T_{it}) represents the coupling between an incident (i) propagating or evanescent wave and a reflected (r) (resp. transmitted (t)) propagating or evanescent wave.

In order to determine a general form of the scattering matrix, the boundary conditions can be written in the form of the joint coupling relation [64]

$$\mathbf{J}\begin{bmatrix}\mathbf{W}(\mu_b^-)\\ \mathbf{W}(\mu_b^+)\end{bmatrix} = \mathbf{0}, \tag{3.39}$$

where $\mathbf{J}$ is the junction matrix, of dimension 4×8. Respectively denoting $\mathbf{J}_-$ and $\mathbf{J}_+$ the left and right sub-matrices of $\mathbf{J}$, such that

$$\mathbf{J} = \begin{bmatrix}\mathbf{J}_- & \mathbf{J}_+\end{bmatrix}, \tag{3.40}$$

Eqs. (3.11), (3.39) and (3.40) yield the scattering matrix in the form

$$\mathbf{S} = \begin{bmatrix}-\mathbf{J}_+\mathbf{E}_+ & \mathbf{J}_-\mathbf{E}_-\end{bmatrix}^{-1}\begin{bmatrix}\mathbf{J}_-\mathbf{E}_+ & -\mathbf{J}_+\mathbf{E}_-\end{bmatrix}. \tag{3.41}$$

3.3 Some examples

The purpose of this section is to briefly illustrate the method for obtaining the reflection matrix of an edge and the method for obtaining the scattering matrix of a junction by giving selected examples of implementation. Given that the main part of the work on the image source method is carried out on individual polygonal plates, priority is here given to the determination of the reflection matrices of edges. Thus, the boundary conditions used in chaps. 2 and 4 for validating the method (simply supported, roller-supported, clamped and free edges) are here studied. A generic model of an edge parameterised by a translational stiffness and a rotational stiffness is also presented in order to explore the generality of the model as a means of including a wide variety of boundary conditions into the image source method. Two examples of junctions are presented. The first one is needed for validating the model of assemblies of polygonal plates presented in chap. 5 and consists of a 'virtual' junction representing continuity. The second one treats the often-encountered case of an internal support in a plate, here revisited as a junction between two semi-infinite plates.

3.3.1 Edges

3.3.1.1 Simply supported, roller supported, clamped and free edges

Tab. 3.1 summarises the boundary matrices of simply supported, roller supported, clamped and free edges and the corresponding reflection matrices that are obtained from Eq. (3.31). As a verification, it can be observed that the reflection matrices in Tab. 3.1 are in accordance with those of Tab. 4.1 (chap. 4), obtained by directly solving the boundary condition equations. As a complement to the table, Figs. 3.5 and 3.6 represent the real and imaginary parts of the different terms of the reflection matrices associated to clamped and free edges.

Simply supported, roller supported, clamped and free edges are the most commonly encountered boundary conditions in textbooks and also in research papers. As a matter of fact, apart from the roller support, which is difficult to realise in practice, a vast majority of the boundary conditions encountered in real planar structures can be accurately

Boundary matrix $\mathbf{B}$		Reflection matrix $\mathbf{R}(k_\xi, k_f)$
Simply supported	$\begin{bmatrix} 1 & 0 & 0 & 0 \\ 0 & 0 & 1 & 0 \end{bmatrix}$	$\begin{bmatrix} -1 & 0 \\ 0 & -1 \end{bmatrix}$
Roller supported	$\begin{bmatrix} 0 & 1 & 0 & 0 \\ 0 & 0 & 0 & 1 \end{bmatrix}$	$\begin{bmatrix} 1 & 0 \\ 0 & 1 \end{bmatrix}$
Clamped	$\begin{bmatrix} 1 & 0 & 0 & 0 \\ 0 & 1 & 0 & 0 \end{bmatrix}$	$\begin{bmatrix} -\dfrac{\sqrt{k_f^2+k_\xi^2}-j\sqrt{k_f^2-k_\xi^2}}{\sqrt{k_f^2+k_\xi^2}+j\sqrt{k_f^2-k_\xi^2}} & \dfrac{-2\sqrt{k_f^2+k_\xi^2}}{\sqrt{k_f^2+k_\xi^2}+j\sqrt{k_f^2-k_\xi^2}} \\ \dfrac{-2j\sqrt{k_f^2-k_\xi^2}}{\sqrt{k_f^2+k_\xi^2}+j\sqrt{k_f^2-k_\xi^2}} & \dfrac{\sqrt{k_f^2+k_\xi^2}-j\sqrt{k_f^2-k_\xi^2}}{\sqrt{k_f^2+k_\xi^2}+j\sqrt{k_f^2-k_\xi^2}} \end{bmatrix}$
Free	$\begin{bmatrix} 0 & 0 & 1 & 0 \\ 0 & 0 & 0 & 1 \end{bmatrix}$	$\begin{bmatrix} \dfrac{ad-bc}{ad+bc} & \dfrac{-2ac}{ad+bc} \\ \dfrac{-2bd}{ad+bc} & -\dfrac{ad-bc}{ad+bc} \end{bmatrix}$ $a = \left(k_f^2 + (1-\nu)k_\xi^2\right),$ $b = \left(-k_f^2 + (1-\nu)k_\xi^2\right),$ $c = -\sqrt{k_f^2+k_\xi^2}\left(k_f^2 - (1-\nu)k_\xi^2\right),$ $d = j\sqrt{k_f^2-k_\xi^2}\left(k_f^2 + (1-\nu)k_\xi^2\right).$

Table 3.1: Boundary matrices for simply supported, roller supported, clamped and free edges and corresponding reflection matrices obtained from Eq. (3.31).

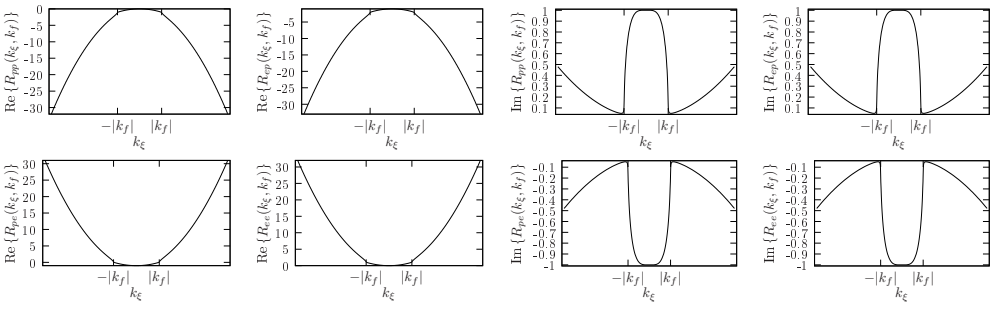

Figure 3.5: Reflection matrix of a clamped edge. (a) Real part; (b) Imaginary part.

represented by such boundary conditions. However, there is a significant difference between the reflection matrices associated to those four boundary conditions. In fact, as shown in Tab. 3.1, the reflection matrices related to simply supported and roller supported edges are constant with respect to the axial wavenumber coordinate k_ξ, which is not the case for clamped or free edges. The dependence on the axial wavenumber k_ξ can be related to a dependence on the angle of incidence of waves on the considered edge. In particular, in the interval $|k_\xi| < |k_f|$, the first term of the reflection matrix, R_{pp}, represents the direct coupling between incident and reflected propagating waves. In

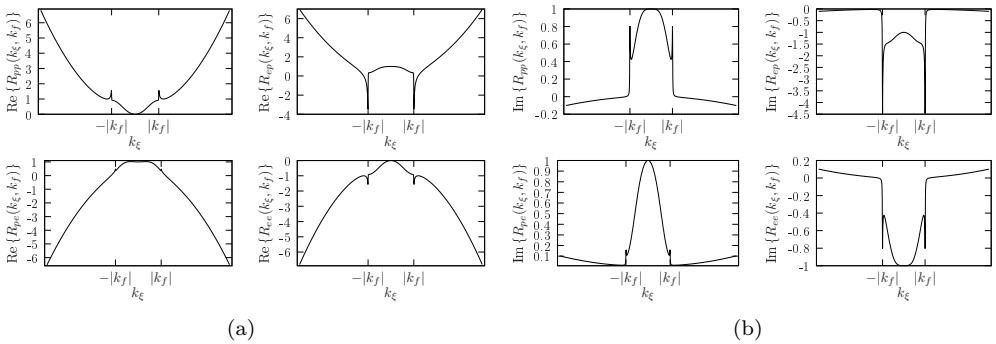

Figure 3.6: Reflection matrix of a free edge, with $\nu = 0.3$. (a) Real part; (b) Imaginary part.

such case, the angle of incidence θ of a propagating wave on a given edge is linked to k_ξ and k_f by a relation of the form

$$k_\xi = |k_f| \cos(\theta), \tag{3.42}$$

as illustrated in Fig. 3.7.

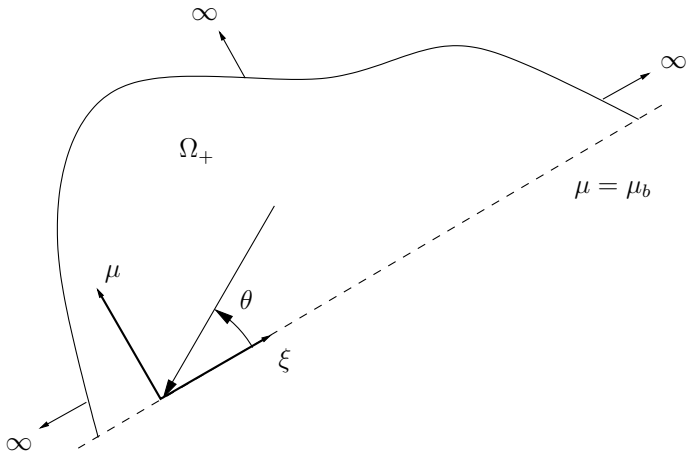

Figure 3.7: Representation of the angle of incidence of a wave on a plate edge.

Using such relation allows to represent the term R_{pp} as a function of the angle of incidence of the propagating wave on the edge, as shown in Fig. 3.8 for simply supported and clamped boundaries. Thus, simply supported and roller supported edges can be regarded as boundary conditions that are indifferent to the angle of incidence of waves. This is a major issue for the implementation of boundary conditions in the image source method. While including constant reflection matrices is straightforward, as detailed in chap. 2, taking into account angle dependence needs a partial reformulation of the image source method, which is the main goal of chap. 4.

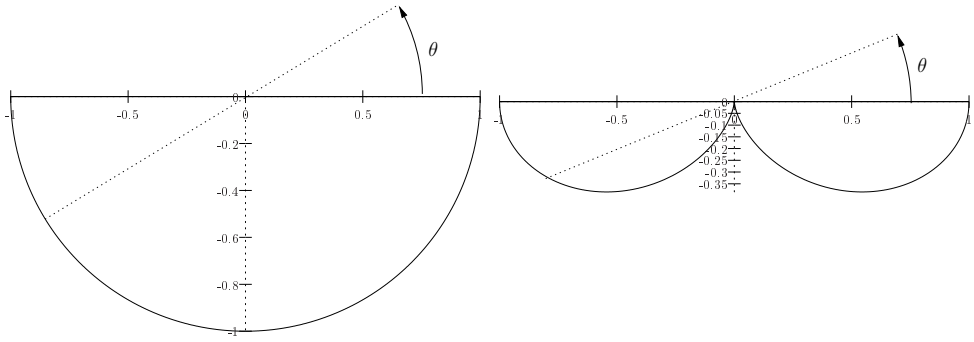

Figure 3.8: Real part of the first term R_{pp} of the reflection matrix for a simply supported edge (a) and a clamped edge (b), as a function of the angle of incidence of a propagating wave.

3.3.1.2 Translational and rotational edge stiffener

In order to simulate various kinds of boundary conditions within a single edge model, a generic set of boundary conditions with variable translational and rotational stiffnesses is proposed, as illustrated in Fig. 3.9.

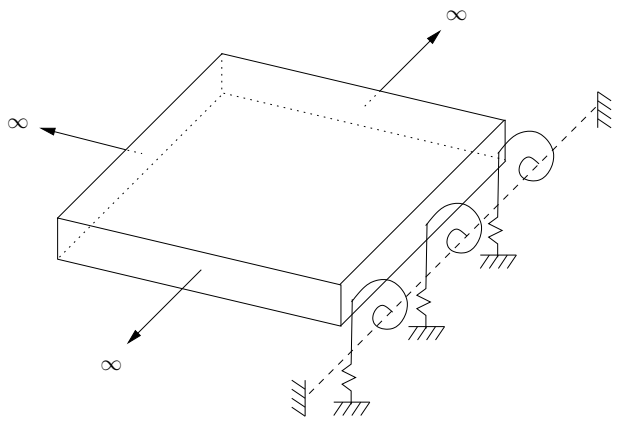

Figure 3.9: Schematic representation of an edge stiffener.

At a given edge located along line $\mu = \mu_b$, according to the orientations of Fig. 1.1, the two boundary conditions that are needed to ensure the equilibrium of shear force and bending moment are [93]

$$\begin{cases} k_t w(\xi, \mu = \mu_b) + V_\mu(\xi, \mu = \mu_b) = 0, & (3.43) \\ k_r \theta_\mu(\xi, \mu = \mu_b) - M_\mu(\xi, \mu = \mu_b) = 0, & (3.44) \end{cases}$$

where k_t and k_r are, respectively, the translational and rotational stiffnesses of the edge. The corresponding boundary matrix can be written as

$$\mathbf{B} = \begin{bmatrix} k_t & 0 & 0 & 1 \\ 0 & k_r & -1 & 0 \end{bmatrix}. \tag{3.45}$$

Substituting $\mathbf{B}$ in Eq. (3.31) yields the reflection matrix in the form

$$\mathbf{R} = \frac{1}{cf - ag} \begin{bmatrix} ae - bf & ah - df \\ ce - bg & ch - dg \end{bmatrix}, \tag{3.46}$$

where

$$\begin{cases} a = \sqrt{k_f^2 + k_\xi^2}k_r + D\left(k_f^2 + (1-\nu)k_\xi^2\right), \\ b = j\sqrt{k_f^2 - k_\xi^2}k_r - D\left(k_f^2 - (1-\nu)k_\xi^2\right), \\ c = j\sqrt{k_f^2 - k_\xi^2}k_r + D\left(k_f^2 - (1-\nu)k_\xi^2\right), \\ d = -\sqrt{k_f^2 + k_\xi^2}k_r + D\left(k_f^2 + (1-\nu)k_\xi^2\right), \\ e = k_t + Dj\sqrt{k_f^2 - k_\xi^2}\left(k_f^2 + (1-\nu)k_\xi^2\right), \\ f = k_t - D\sqrt{k_f^2 + k_\xi^2}\left(k_f^2 - (1-\nu)k_\xi^2\right), \\ g = -k_t + Dj\sqrt{k_f^2 - k_\xi^2}\left(k_f^2 + (1-\nu)k_\xi^2\right), \\ h = k_t + D\sqrt{k_f^2 + k_\xi^2}\left(k_f^2 - (1-\nu)k_\xi^2\right). \end{cases} \tag{3.47}$$

Tab. 3.2 represents the boundary conditions that can be achieved by choosing special values for k_t and k_r. In fact, $(k_t = 0, k_r = 0)$ corresponds to a free edge, $(k_t = \infty, k_r = 0)$ corresponds to a simply supported edge, $(k_t = 0, k_r = \infty)$ corresponds to a roller supported edge and $(k_t = \infty, k_r = \infty)$ corresponds to a clamped edge.

		k_t	
		0	∞
k_r	0	$\mathbf{B} = \begin{bmatrix} 0 & 0 & 0 & 1 \\ 0 & 0 & 1 & 0 \end{bmatrix}$ (free)	$\mathbf{B} = \begin{bmatrix} 1 & 0 & 0 & 0 \\ 0 & 0 & 1 & 0 \end{bmatrix}$ (simply supported)
	∞	$\mathbf{B} = \begin{bmatrix} 0 & 0 & 0 & 1 \\ 0 & 1 & 0 & 0 \end{bmatrix}$ (roller supported)	$\mathbf{B} = \begin{bmatrix} 1 & 0 & 0 & 0 \\ 0 & 1 & 0 & 0 \end{bmatrix}$ (clamped)

Table 3.2: Boundary matrices for the translational and rotational stiffener edge.

Fig. 3.10 shows the reflection matrix of the stiffener edge with the translational and rotational stiffnesses k_t and k_r arbitrarily varying from zero (free edge) to infinity (clamped edge). The curves corresponding to the free and clamped edges are respectively represented by solid and dashed lines, the intermediate states being represented by dotted

lines. The figure illustrates the wide variety of boundary conditions that can be achieved by such generic model.

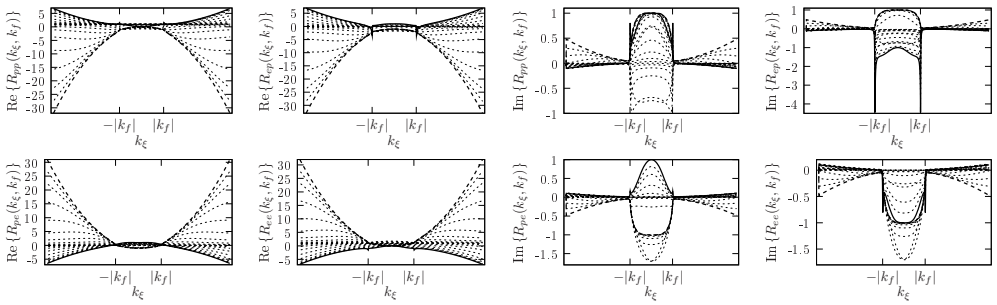

Figure 3.10: Reflection matrix of a stiffener edge with translational and rotational stiffnesses k_t and k_r arbitrarily varying from zero to infinity. (a) Real part, (b) Imaginary part. ——, $k_t = 0$ and $k_r = 0$ (free edge); - - - - -, $k_t = \infty$ and $k_r = \infty$ (clamped edge); · · · · · · , intermediary states.

3.3.2 Junctions

3.3.2.1 Virtual junction between two regions of an infinite plate

In order to validate the present approach, the scattering matrix of a virtual junction separating two regions of an infinite plate is computed. The boundary conditions are given by the continuity of all the state variables. Thus, the corresponding junction matrix assumes the form

$$\mathbf{J} = \begin{bmatrix} 1 & 0 & 0 & 0 & -1 & 0 & 0 & 0 \\ 0 & 1 & 0 & 0 & 0 & -1 & 0 & 0 \\ 0 & 0 & 1 & 0 & 0 & 0 & -1 & 0 \\ 0 & 0 & 0 & 1 & 0 & 0 & 0 & -1 \end{bmatrix}. \tag{3.48}$$

Substituting Eqs. (3.22) and (3.48) in Eq. (3.41) straightforwardly yields

$$\mathbf{S} = \begin{bmatrix} 1 & 0 & 0 & 0 \\ 0 & 1 & 0 & 0 \\ 0 & 0 & 1 & 0 \\ 0 & 0 & 0 & 1 \end{bmatrix}, \tag{3.49}$$

which shows that propagating and evanescent waves travel across the virtual junction without any reflection or wave conversion. The virtual junction is used in chap. 5 for validating a model of connected polygonal plates based on the image source method.

3.3.2.2 Simple support junction

A system consisting of two semi-infinite plates coupled by a simple support is described by zero displacement on the junction $\mu = \mu_b$ and equal slopes and bending moments at

both sides of the junction, μ_b^- and μ_b^+. Such boundary conditions are described by the junction matrix [64]

$$\mathbf{J} = \begin{bmatrix} 1 & 0 & 0 & 0 & 0 & 0 & 0 & 0 \\ 0 & 0 & 0 & 0 & 1 & 0 & 0 & 0 \\ 0 & 1 & 0 & 0 & 0 & -1 & 0 & 0 \\ 0 & 0 & 1 & 0 & 0 & 0 & -1 & 0 \end{bmatrix}. \tag{3.50}$$

Substituting Eqs. (3.22) and (3.50) in Eq. (3.41) yields

$$\mathbf{S} = \frac{1}{d} \begin{bmatrix} a & b & -b & -b \\ -a & -b & a & a \\ -b & -b & a & b \\ a & a & -a & -b \end{bmatrix}, \tag{3.51}$$

where

$$\begin{cases} a = j\sqrt{k_f^2 - k_\xi^2}, \\ b = -\sqrt{k_f^2 + k_\xi^2}, \\ d = \sqrt{k_\xi^2 + k_f^2} + j\sqrt{k_f^2 - k_\xi^2}. \end{cases} \tag{3.52}$$

Figs. 3.11 and 3.12 represent the real and imaginary parts of the scattering matrix of the simply supported junction. Each term is represented as a function of the axial wavenumber k_ξ. Eq. (3.51) and Figs. 3.11 and 3.12 show that even the simplest kind of non-trivial junction between two plates leads to a scattering matrix that depends on the axial wavenumber, i.e. the incidence angle of waves. This simple example reveals the importance of an appropriate formalism for describing wave reflection and transmission at plate boundaries.

Finally, as in the case of edges of semi-infinite plates, the junction equation can also be applied to the case of parametric boundary conditions such as internal stiffeners.

3.4 Conclusion

The central idea of this chapter is the derivation of the reflection matrix of a plate edge and the scattering matrix of a plate junction from the knowledge of the boundary conditions, by using a state vector approach. By describing the flexural motion of a thin plate using a state vector approach, the boundary conditions are expressed in a matrix form as requirements on the state variables, i.e. transverse displacement, slope, bending moment and shear force. Furthermore, the state vector is related to a wave vector, which contains the amplitudes of the different propagating and evanescent waves travelling in the plate. Thus, the different components of the wave vector are obtained from the boundary conditions, and thus reflection matrices of edges and scattering matrices for junctions are inferred. The reflection and scattering matrices obtained in this chapter can be used as an input parameter in the method developed in chaps. 4 and 5, for obtaining the harmonic Green's functions of polygonal plates and plate assemblies. Also, the particular case of simply supported edges, treated in chap. 2, appears as a special case in which the reflection matrix is constant.

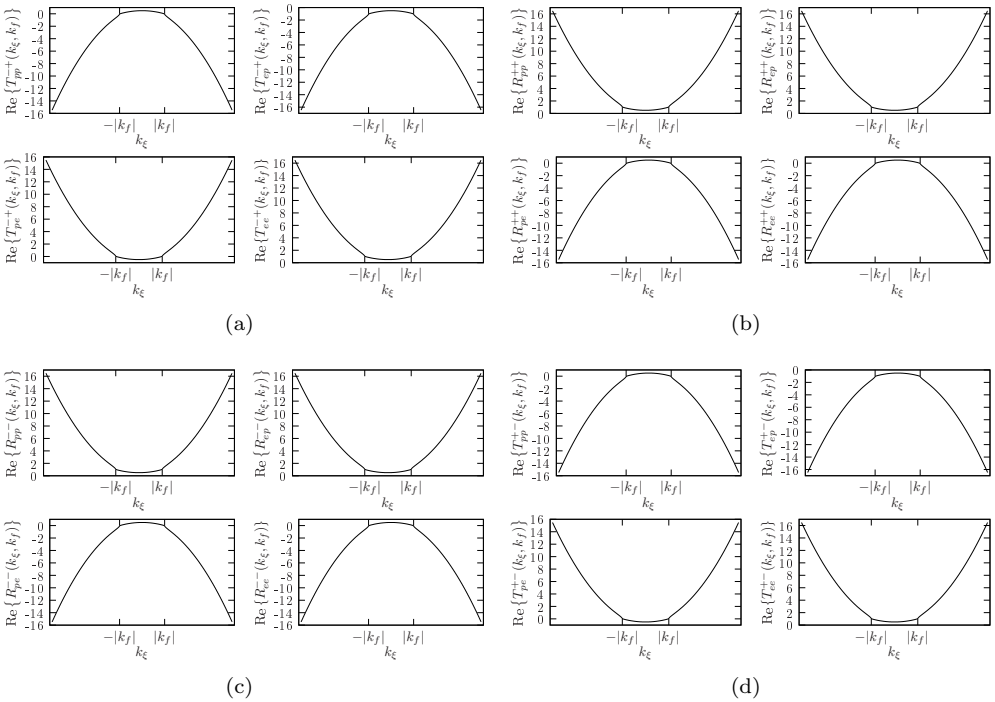

Figure 3.11: Real part of the scattering matrix of a simply supported junction between two regions of an infinite plate. (a) $\mathbf{T}_{-+}$, (b) $\mathbf{R}_{++}$, (c) $\mathbf{R}_{--}$, (d) $\mathbf{T}_{+-}$.

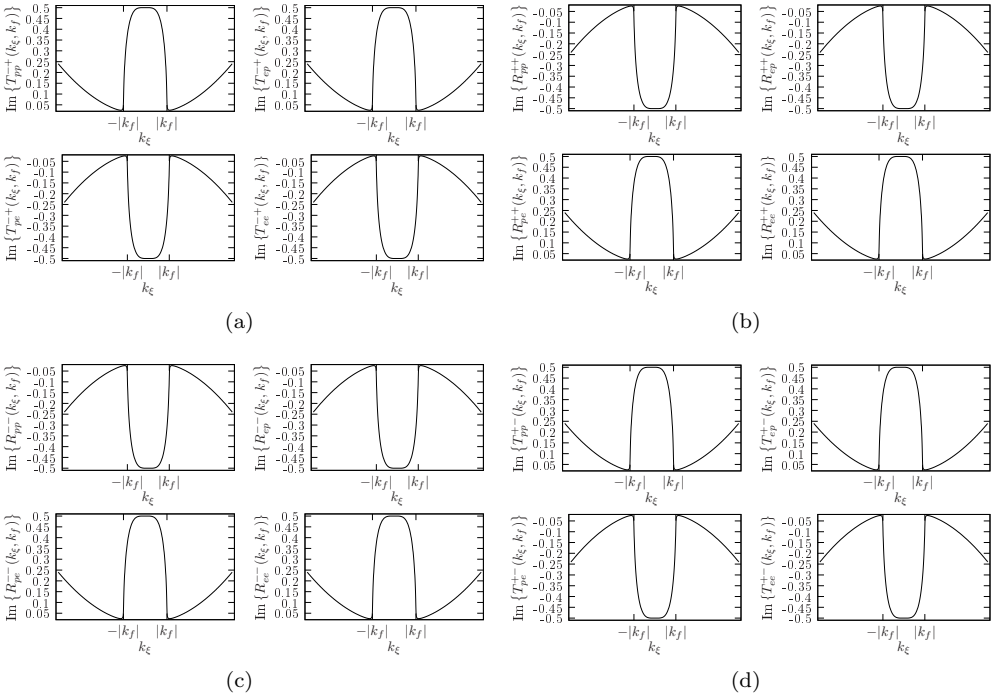

Figure 3.12: Imaginary part of the scattering matrix of a simply supported junction between two regions of an infinite plate. (a) $\mathbf{T}_{-+}$, (b) $\mathbf{R}_{++}$, (c) $\mathbf{R}_{--}$, (d) $\mathbf{T}_{+-}$.

Chapter 4

Harmonic Green's functions of semi-infinite and convex polygonal plates with arbitrary boundary conditions

This chapter is presented as an article submitted to the Journal of Sound and Vibration [19] in September 2009. A preliminary version of the model developed herein was presented at a conference [22]. Appendices 4.D and 4.E are not present in the original article and are here included for completeness.

Abstract

This paper aims at providing a method for obtaining the Green's function for flexural waves in semi-infinite and convex polygonal plates from the knowledge of the reflection matrix of each boundary, by using a generalized image source method. The latter consists in describing the response of the plate to a point source as a superposition of contributions from the original source and virtual sources located outside the plate, which represent successive reflections on the boundaries. By writing the original source as a continuous sum of propagating and evanescent plane waves incident on the boundaries, the image source contributions arise as continuous sums of reflected plane waves. For semi-infinite plates, the Green's function is obtained for any set of boundary conditions, as long as the corresponding reflection matrix is known. For polygonal plates, image sources corresponding to the first reflection on each edge are obtained from the associated semi-infinite plate Green's function. Image sources corresponding to the second and subsequent reflections are obtained in an approximate form by ignoring evanescent waves. Comparisons to exact and finite element solutions show some discrepancies in the nearfield of the edges that decrease with frequency and damping, which is the main advantage of the method.

4.1 Introduction

Automotive, aeronautic and aerospace applications require accurate models for predicting the flexural vibrations of flat panels, which are strongly related with radiated noise and damage of vibrating structures. The problem of obtaining the harmonic response of plates of both arbitrary shape and boundary conditions has been addressed in many papers and monographs [6, 33, 46, 47, 60, 91]. The most popular existing methods for obtaining the Green's function of polygonal plates are based on modal expansion. However, analytical modal expansion is limited to few geometries and sets of boundary conditions. Furthermore, they become impractical in the presence of high damping and at high frequencies, where modal density is significant, so that considering modes individually is not appropriate. Numerical tools, such as finite element or boundary element methods, are able to take into account complex geometries but present the same limitations with frequency and damping than analytical modal methods.

Gunda et al. [39] showed that the image source method is efficient for obtaining the response of beams and rectangular plates with simply supported and roller supported plates. In a previous paper [20], the authors examined the case of arbitrary convex polygonal plates with all edges simply supported, by using the image source method. The method provides exact Green's functions of plates of four polygonal geometries and gives efficient approximations in the case of convex polygonal plates of arbitrary geometry. Moreover, the accuracy increases with frequency and structural damping, contrarily to modal expansion or finite element methods. Therefore, the image source method can be used as an alternative tool for studying the vibrations of polygonal plates at high frequencies and for highly damped regimes. However, simply supported and roller supported edges are particular cases in which flexural wave reflection does not induce coupling between propagating and evanescent components of the field. Additionally, the corresponding reflection coefficients do not depend on frequency or the angle of incidence of waves on the boundaries. Reflection on other kinds of edges, such as clamped or free, involves wave conversion and depends on the angle of incidence of waves and on frequency and thus needs further analysis.

The purpose of this paper is to extend the image source method to polygonal plates with arbitrary boundary conditions in order to obtain approximated harmonic Green's functions for flexural waves. The key point of the method is the description of the original source as a continuous sum of plane waves. In such manner, the image sources are obtained by using classical reflection laws for the plane waves that describe the original source. The paper is organised as follows. First, the Green's function of an infinite plate is expressed as a continuous sum of propagating and evanescent plane waves, which describes the original source. A general expression of the harmonic Green's function of a semi-infinite plate with arbitrary boundary conditions is then obtained. For polygonal plates, the semi-infinite plate Green's function is used at each edge for calculating the contributions of image sources, which represent successive reflections of waves on the boundaries. The approximation of the contributions of image sources corresponding to the second and subsequent reflections by ignoring evanescent waves is discussed. The results are compared to the exact solution on a square plate and to a finite element solution on an arbitrary polygonal plate, both including simply supported and clamped edges.

4.2 Green's function of an infinite plate

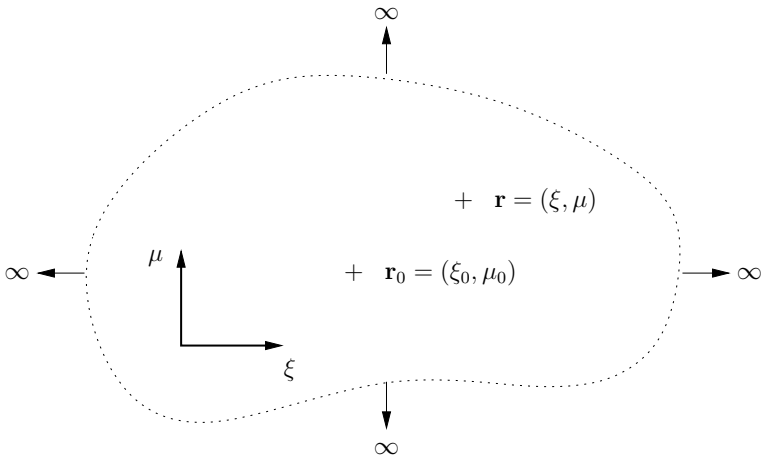

Figure 4.1: Green's problem for an infinite plate. $\mathbf{r}_0$, source point; $\mathbf{r}$, observation point.

Consider an infinite plate harmonically excited at point $\mathbf{r}_0 = (\xi_0, \mu_0)$, perpendicularly to the (ξ, μ) plane, as shown in Fig. 4.1. The time factor $e^{-j\omega t}$ is implicit in the following, ω being the excitation circular frequency. The Green's function of flexural vibrations G_∞ follows the equation

$$D\left(\nabla^4 - k_f^4\right) G_\infty(\mathbf{r}, \mathbf{r}_0; k_f) = \delta(\mathbf{r} - \mathbf{r}_0), \tag{4.1}$$

where the flexural rigidity D depends on the Young's modulus E, the Poisson's ratio ν and the plate thickness h in the form

$$D = \frac{Eh^3}{12(1-\nu^2)} \tag{4.2}$$

and the flexural wavenumber assumes the form

$$k_f = \left(\omega^2 \frac{\rho h}{D}\right)^{1/4}, \tag{4.3}$$

where ρ is the density of the plate material. According to the time dependence $e^{-j\omega t}$, structural damping is included in the Young's modulus by writing

$$E = E_0(1 - j\eta), \tag{4.4}$$

where η is the structural damping ratio.

For modelling semi-infinite and polygonal plates, discussed later-on in secs. 4.3 and 4.4, the Green's function of the infinite plate G_∞ describes the direct contribution of the source to the displacement field of the plate, which is also the incident field on the boundaries. Thus, it is convenient to write G_∞ in rectangular coordinates in order to describe wave reflection in a local coordinate system for each boundary. For such purpose, we use arbitrarily oriented coordinates (ξ, μ), where ξ is referred to as the axial coordinate, collinear to a given boundary, and μ is referred to as the transverse coordinate, normal to the boundary.

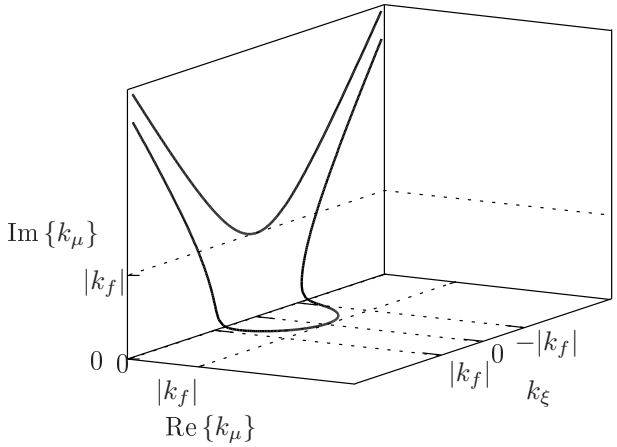

Figure 4.2: Transverse wavenumbers as functions of k_ξ. Upper curve, $k_\mu = j\sqrt{k_f^2 + k_\xi^2}$; lower curve, $k_\mu = \sqrt{k_f^2 - k_\xi^2}$.

The Green's function G_∞ is obtained using one-dimensional Fourier transform of Eq. (4.1) on coordinate ξ, as detailed in Appendix 4.A, and assumes the form

$$G_\infty(\mathbf{r}, \mathbf{r}_0; k_f) = \frac{j}{8\pi k_f^2 D} \int_{-\infty}^{+\infty} e^{jk_\xi(\xi-\xi_0)} \left(\frac{e^{j\sqrt{k_f^2-k_\xi^2}|\mu-\mu_0|}}{\sqrt{k_f^2 - k_\xi^2}} + j\frac{e^{-\sqrt{k_f^2+k_\xi^2}|\mu-\mu_0|}}{\sqrt{k_f^2 + k_\xi^2}} \right) dk_\xi, \tag{4.5}$$

which appears as a sum of plane waves. Fig. 4.2 shows the transverse wavenumbers $k_\mu = j\sqrt{k_f^2 + k_\xi^2}$ and $k_\mu = \sqrt{k_f^2 - k_\xi^2}$ as functions of the axial wavenumber k_ξ. From Fig. 4.2 and Eq. (4.5), it can be seen that the term $e^{j\sqrt{k_f^2-k_\xi^2}|\mu-\mu_0|}/\sqrt{k_f^2-k_\xi^2}$ represents a propagating wave for $|k_\xi| < |k_f|$ and an evanescent wave for $|k_\xi| > |k_f|$. Similarly, the term $je^{-\sqrt{k_f^2+k_\xi^2}|\mu-\mu_0|}/\sqrt{k_f^2+k_\xi^2}$ represents an evanescent wave for all values of k_ξ. Note that the flexural wavenumber k_f is complex because of structural damping, as defined in Eq. (4.4), and has a imaginary part that is small compared to its real part. This implies that the propagating term presents a slight decrease in amplitude with distance and the evanescent term presents a slow oscillatory behavior.

4.3 Green's function of a semi-infinite plate

4.3.1 Formulation of the problem

Considering a semi-infinite plate Ω, excited by a point source at $\mathbf{r}_0$ as represented in Fig. 4.3, the Green's function G_Ω is the solution of the set of equations

$$\begin{cases} D\left(\nabla^4 - k_f^4\right) G_\Omega(\mathbf{r}, \mathbf{r}_0; k_f) = \delta(\mathbf{r} - \mathbf{r}_0) & \mathbf{r} \in \Omega, \quad (4.6) \\ \text{Boundary conditions} & \mathbf{r} \in \partial\Omega. \quad (4.7) \end{cases}$$

The displacement field at $\mathbf{r}$ can be obtained as the superposition of the infinite plate Green's function G_∞ and the contribution of the image source [75] located at $\mathbf{r}_s$, G_s, which represents the reflected field on the boundary $\partial\Omega$. The general solution of Eqs. (4.6) and (4.7) is then

$$G_\Omega(\mathbf{r}, \mathbf{r}_0; k_f) = G_\infty(\mathbf{r}, \mathbf{r}_0; k_f) + G_s(\mathbf{r}, \mathbf{r}_s; k_f). \tag{4.8}$$

The aim of the following is to determine G_s.

The integrand of Eq. (4.5) contains two plane waves travelling from μ_0 in their respective half-planes $\mu > \mu_0$ and $\mu < \mu_0$. The latter represents a plane wave incident on the boundary $\partial\Omega$, located along axis $\mu = \mu_b$, and assumes the form

$$w_i(\xi, \mu, \xi_0, \mu_0; k_f) = e^{jk_\xi(\xi-\xi_0)} \left(Ae^{-j\sqrt{k_f^2-k_\xi^2}(\mu-\mu_b)} + Be^{\sqrt{k_f^2+k_\xi^2}(\mu-\mu_b)} \right), \tag{4.9}$$

where

$$A = \frac{j}{8\pi k_f^2 D} \frac{e^{-j\sqrt{k_f^2-k_\xi^2}(\mu_b-\mu_0)}}{\sqrt{k_f^2-k_\xi^2}} \tag{4.10}$$

and

$$B = \frac{j}{8\pi k_f^2 D} \frac{je^{\sqrt{k_f^2+k_\xi^2}(\mu_b-\mu_0)}}{\sqrt{k_f^2+k_\xi^2}}. \tag{4.11}$$

Similarly, the reflected wave is a superposition of a propagating term and an evanescent term, in the form

$$w_r(\xi, \mu, \xi_0, \mu_0; k_f) = e^{jk_\xi(\xi-\xi_0)} \left(Ce^{j\sqrt{k_f^2-k_\xi^2}(\mu-\mu_b)} + De^{-\sqrt{k_f^2+k_\xi^2}(\mu-\mu_b)} \right), \tag{4.12}$$

where C and D are obtained by applying the boundary conditions to the superposition of incident and reflected waves [34]. The relation between A, B, C and D is then given by

$$\begin{bmatrix} C \\ D \end{bmatrix} = \mathbf{R} \begin{bmatrix} A \\ B \end{bmatrix}, \tag{4.13}$$

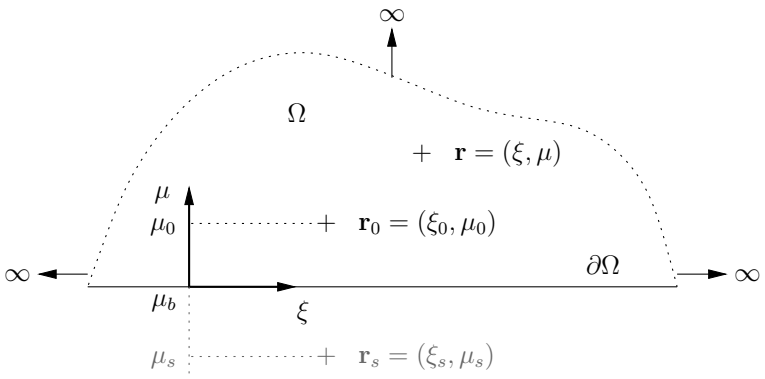

Figure 4.3: Green's problem for a semi-infinite plate. $\mathbf{r}_0$, original source; $\mathbf{r}_s$, image source; $\mathbf{r}$, observation point.

where

$$\mathbf{R}(k_\xi, k_f) = \begin{bmatrix} R_{pp}(k_\xi, k_f) & R_{ep}(k_\xi, k_f) \\ R_{pe}(k_\xi, k_f) & R_{ee}(k_\xi, k_f) \end{bmatrix} \tag{4.14}$$

is the reflection matrix of the boundary. Each term of the form R_{ir} represents wave conversion from incident wave i to reflected wave r, where i and r denote propagating (p) or evanescent (e) components. The left column of the reflection matrix contains the reflection coefficients for an incident propagating wave and can be obtained by applying the boundary conditions to the superposition of incident and reflected waves w_i and w_r letting $B = 0$. The same holds for the right column of the reflection matrix with $A = 0$.

The image source contribution G_s is given by the superposition of waves that are reflected at the boundary. It is therefore obtained by integrating Eq. (4.12) over $k_\xi \in \mathbb{R}$ using Eq. (4.13). Furthermore, the changes of variables $\xi_s = \xi_0$ and $\mu_b - \mu_0 = -(\mu_b - \mu_s)$ lead to the image source contribution in the form

$$G_s(\mathbf{r}, \mathbf{r}_s; k_f) = \frac{j}{8\pi k_f^2 D} \int_{-\infty}^{+\infty} e^{jk_\xi(\xi-\xi_s)} \begin{bmatrix} e^{j\sqrt{k_f^2-k_\xi^2}(\mu-\mu_b)} & e^{-\sqrt{k_f^2+k_\xi^2}(\mu-\mu_b)} \end{bmatrix} \begin{bmatrix} R_{pp}(k_\xi, k_f) & R_{ep}(k_\xi, k_f) \\ R_{pe}(k_\xi, k_f) & R_{ee}(k_\xi, k_f) \end{bmatrix} \begin{bmatrix} \dfrac{e^{j\sqrt{k_f^2-k_\xi^2}(\mu_b-\mu_s)}}{\sqrt{k_f^2-k_\xi^2}} \\ j\dfrac{e^{-\sqrt{k_f^2+k_\xi^2}(\mu_b-\mu_s)}}{\sqrt{k_f^2+k_\xi^2}} \end{bmatrix} dk_\xi. \tag{4.15}$$

Eq. (4.15) represents a sum of plane waves travelling along distance $(\xi - \xi_s, \mu - \mu_s)$ with wave conversion at $\mu = \mu_b$ involving propagating and evanescent components, and is valid in the $\mu > \mu_b$ half plane. The expression of the Green's function of the semi-infinite plate G_Ω is then given by Eq. (4.8), considering G_∞ from Eq. (4.5) and G_s from (4.15).

4.3.2 Validation of the formulation for simply supported, roller supported, clamped and free boundary conditions

Gunda et al. [38] obtained the Green's functions of clamped and free semi-infinite plates by applying corrections respectively to the simply supported and roller boundary conditions in order to satisfy the actual boundary conditions. The Green's function of the semi-infinite plate, Eq. (4.8), holds for any boundary condition described by a reflection matrix that satisfies Eq. (4.13) and thus can be compared to the aforementioned. Tab. 4.1 summarises the boundary conditions of simply supported, roller, clamped and free edges and their corresponding reflection matrices, obtained by the above procedure. It is worth noticing that the reflection matrix of the free boundary does not include flexural edge waves, which are also a solution of Eq. (4.6), as discussed by Norris et al. [82]. By replacing the reflection matrices of simply supported, roller, clamped or free edges in Eq. (4.15), it can be verified that Eq. (4.8) is identical to Eqs. (19), (22), (44) and (62) of Ref. [38], which validates the present approach.

Boundary conditions		Reflection matrix $\mathbf{R}(k_\xi, k_f)$
Simply supported	$\begin{cases} w(\xi,\mu_b)=0 \\ M_\mu(\xi,\mu_b)=0 \end{cases}$	$\begin{bmatrix} -1 & 0 \\ 0 & -1 \end{bmatrix}$
Roller	$\begin{cases} \dfrac{\partial w}{\partial \mu}(\xi,\mu_b)=0 \\ V_\mu(\xi,\mu_b)=0 \end{cases}$	$\begin{bmatrix} 1 & 0 \\ 0 & 1 \end{bmatrix}$
Clamped	$\begin{cases} w(\xi,\mu_b)=0 \\ \dfrac{\partial w}{\partial \mu}(\xi,\mu_b)=0 \end{cases}$	$\begin{bmatrix} -\dfrac{\sqrt{k_f^2+k_\xi^2}-j\sqrt{k_f^2-k_\xi^2}}{\sqrt{k_f^2+k_\xi^2}+j\sqrt{k_f^2-k_\xi^2}} & \dfrac{-2\sqrt{k_f^2+k_\xi^2}}{\sqrt{k_f^2+k_\xi^2}+j\sqrt{k_f^2-k_\xi^2}} \\ \dfrac{-2j\sqrt{k_f^2-k_\xi^2}}{\sqrt{k_f^2+k_\xi^2}+j\sqrt{k_f^2-k_\xi^2}} & \dfrac{\sqrt{k_f^2+k_\xi^2}-j\sqrt{k_f^2-k_\xi^2}}{\sqrt{k_f^2+k_\xi^2}+j\sqrt{k_f^2-k_\xi^2}} \end{bmatrix}$
Free	$\begin{cases} M_\mu(\xi,\mu_b)=0 \\ V_\mu(\xi,\mu_b)=0 \end{cases}$	$\begin{bmatrix} \dfrac{ad-bc}{ad+bc} & \dfrac{-2ac}{ad+bc} \\ \dfrac{-2bd}{ad+bc} & -\dfrac{ad-bc}{ad+bc} \end{bmatrix}$ $a=\left(k_f^2+(1-\nu)k_\xi^2\right)$ $b=\left(-k_f^2+(1-\nu)k_\xi^2\right)$ $c=-\sqrt{k_f^2+k_\xi^2}\left(k_f^2-(1-\nu)k_\xi^2\right)$ $d=j\sqrt{k_f^2-k_\xi^2}\left(k_f^2+(1-\nu)k_\xi^2\right)$

Table 4.1: Boundary conditions and corresponding reflection matrices for a simply supported, roller, clamped or free edge at $\mu=\mu_b$. The flexural moment and the total shear force are respectively defined as $M_\mu = -D\left(\frac{\partial^2 w}{\partial \mu^2}+\nu\frac{\partial^2 w}{\partial \xi^2}\right)$ and $V_\mu = -D\left(\frac{\partial^3 w}{\partial \mu^3}+(2-\nu)\frac{\partial^3 w}{\partial \xi^2 \partial \mu}\right)$.

4.4 Green's function of a convex polygonal plate

4.4.1 Formulation of the problem

Considering a polygonal plate Ω, as depicted in Fig. 4.4, the Green's function G_Ω is the solution of the set of equations

$$\begin{cases} D\left(\nabla^4-k_f^4\right)G_\Omega(\mathbf{r},\mathbf{r}_0;k_f)=\delta(\mathbf{r}-\mathbf{r}_0) & \mathbf{r}\in\Omega, \quad (4.16) \\ \text{Boundary conditions} & \mathbf{r}\in\partial\Omega. \quad (4.17) \end{cases}$$

In this case, the boundary $\partial\Omega$ forms a closed line and thus yields an infinite number of reflections in the plate Ω, which are in turn described by an infinite number of image sources. We propose an estimation of the Green's function of the polygonal plate in the form of a superposition of the contributions of the original source and the image sources, as

$$\tilde{G}_\Omega(\mathbf{r},\mathbf{r}_0;k_f)=G_\infty(\mathbf{r},\mathbf{r}_0;k_f)+\sum_{s=1}^{\infty}G_s(\mathbf{r},\mathbf{r}_s;k_f). \quad (4.18)$$

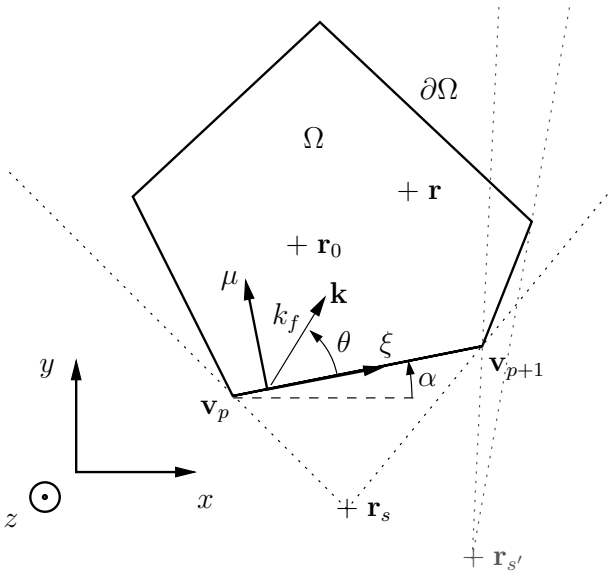

Figure 4.4: Green's problem for a convex polygonal plate. $\mathbf{r}_0$, original source; $\mathbf{r}_s$, image source of first order; $\mathbf{r}_{s'}$, image source of second order; $\mathbf{r}$, observation point; $\cdots\cdots$, validity zones of image sources.

The terms G_s represent the contributions of image sources to the displacement field, s being the image source index. The aim of the following is to determine G_s analytically.

4.4.2 Geometrical construction of image sources

Wave reflections at the boundaries of the domain are described by means of image sources, which are obtained by successive symmetries of the original source on the different plate edges. Thus, for a polygonal plate having N_v vertices, the original source generates N_v sources, one with respect to each edge. Subsequently, each image source generates $N_v - 1$ new image sources. The pattern resulting from such geometrical procedure corresponds to what one would observe by standing with a source of light in a polygonal room made of mirrors. The location of an image source s originating at edge p from a source located at $\mathbf{r}_m$, i.e. its "mother" source, can be noted $\mathbf{r}_s = \mathbf{r}_{m,p}$ and takes the form

$$\mathbf{r}_{m,p} = -\mathbf{r}_m + 2\mathbf{v}_p + 2\frac{(\mathbf{r}_m - \mathbf{v}_p)\cdot(\mathbf{v}_{p+1} - \mathbf{v}_p)}{|\mathbf{v}_{p+1} - \mathbf{v}_p|^2}(\mathbf{v}_{p+1} - \mathbf{v}_p)\,, \tag{4.19}$$

where $\mathbf{v}_p$ and $\mathbf{v}_{p+1}$ are the locations of the vertices of the generator edge, as illustrated in Fig. 4.4.

Furthermore, the edges of the plate are of finite length. Therefore, the reflected field giving rise to a given image source is valid in the zone delimited by the image source position $\mathbf{r}_s$ and the vertices $\mathbf{v}_p$ and $\mathbf{v}_{p+1}$ of the generator edge, as represented by the dotted lines in Fig. 4.4. The geometrical validity conditions of source s from observation

point $\mathbf{r}$ are given by

$$\begin{cases} \big((\mathbf{v}_{p+1} - \mathbf{r}_s) \times (\mathbf{r} - \mathbf{r}_s)\big) \cdot \mathbf{z} > 0, & (4.20) \\ \big((\mathbf{r} - \mathbf{r}_s) \times (\mathbf{v}_p - \mathbf{r}_s)\big) \cdot \mathbf{z} > 0, & (4.21) \end{cases}$$

where $\times$ denotes cross product and $\mathbf{z}$ is the unitary vector such that $(\mathbf{x}, \mathbf{y}, \mathbf{z})$ forms a right-handed basis. The validity conditions are included in the function $V(\mathbf{r}, \mathbf{r}_s)$ such that

$$V(\mathbf{r}, \mathbf{r}_s) = \begin{cases} 1 & \text{in the validity zone,} \\ 0 & \text{elsewhere.} \end{cases} \tag{4.22}$$

4.4.3 Image sources of first order

The contributions of the image sources of first order, i.e. directly generated from the original source at each one of the edges, can be computed using the approach developed above for semi-infinite plates, from Eq. (4.15), using a local coordinate system (ξ, μ) for each edge. Each image source contribution is then valid in the area defined by function $V(\mathbf{r}, \mathbf{r}_s)$. For a plate having N_v vertices, the contributions of image sources of first order, i.e. the first N_v image sources, can be expressed as

$$\begin{aligned} G_s^{(\mathrm{I})}(\mathbf{r}, \mathbf{r}_s; k_f) = \\ V(\mathbf{r}, \mathbf{r}_s) \frac{j}{8\pi k_f^2 D} \int_{-\infty}^{+\infty} e^{jk_\xi(\xi - \xi_s)} \left[e^{j\sqrt{k_f^2 - k_\xi^2}(\mu - \mu_b^{(s)})} \quad e^{-\sqrt{k_f^2 + k_\xi^2}(\mu - \mu_b^{(s)})} \right] \\ \begin{bmatrix} R_{pp}^{(s)}(k_\xi, k_f) & R_{ep}^{(s)}(k_\xi, k_f) \\ R_{pe}^{(s)}(k_\xi, k_f) & R_{ee}^{(s)}(k_\xi, k_f) \end{bmatrix} \begin{bmatrix} \dfrac{e^{j\sqrt{k_f^2 - k_\xi^2}(\mu_b^{(s)} - \mu_s)}}{\sqrt{k_f^2 - k_\xi^2}} \\ j\dfrac{e^{-\sqrt{k_f^2 + k_\xi^2}(\mu_b^{(s)} - \mu_s)}}{\sqrt{k_f^2 + k_\xi^2}} \end{bmatrix} dk_\xi, \end{aligned} \tag{4.23}$$

where $\mu = \mu_b^{(s)}$ defines the boundary giving rise to source s in the local coordinate system (ξ, μ), i.e. the symmetry axis between $\mathbf{r}_0$ and $\mathbf{r}_s$, and $R_{ir}^{(s)}$ are the different terms of the corresponding reflection matrix, which couples incident (i) waves from the original source to reflected (r) waves. Fig. 4.5 shows the displacement field due to one of the image sources of first order for an arbitrary polygonal plate clamped on the corresponding edge, computed numerically as described later-on in sec. 4.5.

4.4.4 Image sources of second and higher orders

For calculating the reflected field from a boundary, the incident and reflected fields must be expressed using local coordinates of the edge at which reflection occurs. Consequently, the incident and reflected fields exhibit a separated variable form, as shown by Eqs. (4.9) and (4.12), which both include a propagating component along the ξ axis and a superposition of propagating and evanescent components along the μ axis. However, a plane wave which is propagating in one direction and attenuating in the other cannot

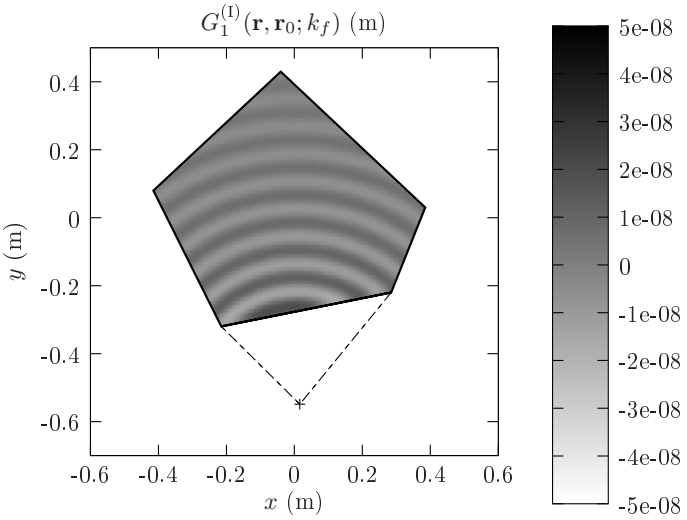

Figure 4.5: Displacement field due to one of the first order image sources for the arbitrary polygonal plate used in sec. 4.6.2.

be written in such separated variable form using two different coordinate systems in the general case. Therefore, the field resulting from the first reflection cannot be written in the form of Eq. (4.9) in the local coordinate system of another edge at which a second reflection may take place. Only the component representing propagating waves in the ξ and μ directions can be written in the same form in two different coordinate systems. Therefore, Eq. (4.23) cannot be used in its complete form for image sources of second and higher orders. This shows that the image source method is not able to provide an exact solution for an arbitrary polygonal plate. However, the contributions of such image sources can be approximated by neglecting the contribution of evanescent waves, as

$$G_s^{(\mathrm{II})}(\mathbf{r}, \mathbf{r}_s; k_f) = V(\mathbf{r}, \mathbf{r}_s) \frac{j}{8\pi k_f^2 D} \int_{-|k_f|}^{|k_f|} e^{jk_\xi(\xi-\xi_s)} A_{pp}^{(s)}(k_\xi, k_f) \frac{e^{j\sqrt{k_f^2-k_\xi^2}(\mu-\mu_s)}}{\sqrt{k_f^2-k_\xi^2}} dk_\xi, \quad (4.24)$$

where $A_{pp}^{(s)}$ is the amplitude weight of image source s, resulting from the successive reflections of propagating waves. In the considered integration domain, defined by $-|k_f| < k_\xi < |k_f|$, the transverse wavenumber coordinate $k_\mu = \sqrt{k_f^2 - k_\xi^2}$ is real, as shown in Fig. 4.2, such that the wavenumber coordinates k_ξ and k_μ are related to the flexural wavenumber by

$$k_f^2 = k_\xi^2 + k_\mu^2. \quad (4.25)$$

Alternatively, the use of wavenumber polar coordinates yields

$$k_\xi = |k_f| \cos(\theta), \quad (4.26)$$

where θ is the orientation of the plane propagating wave defined by k_ξ with respect to the reflecting edge, as shown in Fig. 4.4. Thus, the amplitude weight $A_{pp}^{(s)}$ is obtained as the

product of the scalar reflection coefficients R_{pp} of the edges that successively participate in the construction of image source s, in the form

$$A_{pp}^{(s)}(\theta) = \prod_{n=1}^{N(s)} R_n^{(s)}(\theta, \alpha_n), \tag{4.27}$$

where $n = 1, \ldots, N(s)$ denotes the order of reflection on edges for each image source s and α_n is the orientation of edge n with respect to the global coordinate system (x, y), as illustrated in Fig. 4.4.

4.4.5 Domain of applicability of the solution

The Green's function of the polygonal plate is obtained from Eq. (4.18), by considering Eqs. (4.5), (4.23) and (4.24) for the original source, first and second order image sources, respectively, in the form

$$\tilde{G}_\Omega(\mathbf{r}, \mathbf{r}_0; k_f) = G_\infty(\mathbf{r}, \mathbf{r}_0; k_f) + \sum_{s=1}^{N_v} G_s^{(\mathrm{I})}(\mathbf{r}, \mathbf{r}_s; k_f) + \sum_{s=N_v+1}^{\infty} G_s^{(\mathrm{II})}(\mathbf{r}, \mathbf{r}_s; k_f), \tag{4.28}$$

where N_v is the number of vertices or edges of the plate. The Green's function is then known for arbitrary boundary conditions as long as the reflection matrix of the edges are known in the form of Eq. (4.14). The obtained Green's function is an approximation based on neglecting evanescent waves in the calculation of the contributions of second order image sources, $G_s^{(\mathrm{II})}$. In fact, the displacement field related to the terms $R_{ep}(k_\xi, k_f)$, $R_{pe}(k_\xi, k_f)$ and $R_{ee}(k_\xi, k_f)$ of the reflection matrices is of low amplitude as long as both the source and the observation point are sufficiently distant from the edges. As a consequence, the proposed solution is inaccurate in the nearfield of the edges. In particular, the approach is not adapted to plates including sharp angles, since a given edge may be in the nearfield of another edge, leading to cumulative errors in the construction of image sources. Furthermore, Eq. (4.28) does not take into account the effects due to diffraction on the corners of the plate. However, the corresponding correction terms are significant only at low frequencies, as pointed out by Gunda et al. [37]

Some particular edges present a reflection matrix that is constant and does not include wave conversion, such as simply supported and roller supported edges. For plates having exclusively such kinds of edges, each image source contribution is obtained simply from the product of the contribution of its mother source by the reflection coefficient (see Appendix 4.B for more details).

4.5 Numerical implementation

In this section, the numerical implementation of Eq. (4.28) is discussed. Eq. (4.24) can be formulated as

$$G_s^{(\mathrm{II})}(\mathbf{r},\mathbf{r}_s;k_f) = V(\mathbf{r},\mathbf{r}_s)\frac{j}{8\pi k_f^2 D}\int_{-\infty}^{\infty} u\left(\frac{k_\xi}{2|k_f|}\right) e^{jk_\xi(\xi-\xi_s)} A_{pp}^{(s)}(k_\xi,k_f)\frac{e^{j\sqrt{k_f^2-k_\xi^2}(\mu-\mu_s)}}{\sqrt{k_f^2-k_\xi^2}}dk_\xi, \quad (4.29)$$

where

$$u\left(\frac{k_\xi}{2|k_f|}\right) = \begin{cases} 1 & k_\xi \in \left[-|k_f|,|k_f|\right] \\ 0 & \text{elsewhere} \end{cases} \quad (4.30)$$

is the rectangular window function of span $2|k_f|$ centred on $k_\xi = 0$. The integral in Eqs. (4.23) and (4.29) is interpreted as a one-dimensional inverse spatial Fourier transform (defined in Appendix 4.A) from wavenumber coordinate k_ξ to space coordinate ξ. The numerical implementation of such expressions is performed by using discrete inverse spatial Fourier transform from variable k_ξ to variable ξ, as defined in Appendix 4.C, in order to take advantage of a fast Fourier transform algorithm in terms of computational efficiency.

Furthermore, practical implementation requires the image source series to be truncated. Thus, image sources outside a truncation circle of radius r_t are ignored. The dimensionless parameter γ is used for controlling the truncation distance with respect to an arbitrary characteristic length r_c of the plate, in the form

$$\gamma = \frac{r_t}{r_c}, \quad (4.31)$$

where, by respectively denoting S and p the total area and the perimeter of the plate, r_c is taken as

$$r_c = \frac{\pi S}{p}, \quad (4.32)$$

which is the average distance between two successive image sources, also referred to as the mean free path of waves in the plate [62].

4.6 Results

In this section, the Green's function of different polygonal plates with various boundary conditions are computed and compared to exact or numerical solutions of reference. The main purpose is to validate the present method and to evaluate the errors due to neglecting edge effects.

Two plates are tested: a Levy-type plate, for which the analytical Green's function is known, and an arbitrary polygonal plate, for which the response is computed by using the finite element method (FEM). For both plates, one edge is clamped and the others are simply supported.

4.6.1 Levy-type plate: comparison to the exact solution

There exist only few sets of boundary conditions leading to an analytical expression of the response of a polygonal plate [60]. Rectangular plates with two opposite edges simply supported, i.e. Levy-type plates, are well-known configurations allowing an analytical solution [34, 91].

The square plate shown in Fig. 4.6 is here considered, with simply supported edges on $y = 0$, $y = L$ and $x = 0$, and a clamped edge on $x = L$. In the following, the side

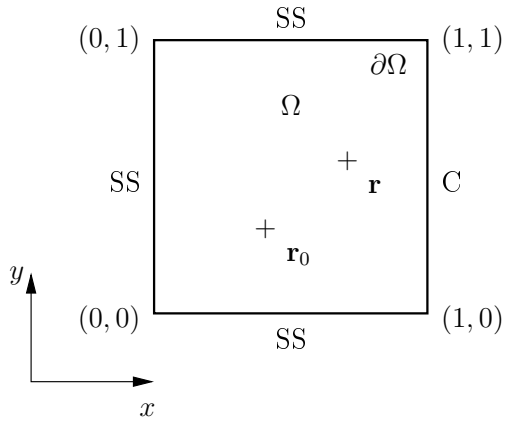

Figure 4.6: Square plate with three simply supported (SS) edges and one clamped (C) edge.

length of the plate is $L = 1$ m and the thickness is $h = 2$ mm. The plate material is steel, with density $\rho = 7850$ kg.m^{-3}, Young's modulus $E_0 = 210$ GPa and Poisson's ratio $\nu = 0.3$. The structural damping ratio is chosen as $\eta = 0.07$. The plate is excited by a harmonic point source at $\mathbf{r}_0 = (0.41\text{ m}, 0.3\text{ m})$ at the frequency $f = 3$ kHz. At this frequency, the modal overlap factor [20] is equal to 42, i.e. there is an average of 42 resonances in a -3 dB resonance band, which indicates that the computation is done in a significantly high-frequency regime. The solution of reference is obtained analytically by classical modal superposition [34], to which is compared the solution obtained by the proposed method, with $\gamma = 6$ (488 sources). The number of points for the fast Fourier transform is $N_F = 1024$.

In order to quantify the accuracy of the proposed method, an error indicator is computed for each vertical line of the plate, as

$$\varepsilon(x) = \frac{\sum_{i=1}^{N} |w(x, y_i) - w^{(\mathrm{ref})}(x, y_i)|^2}{\sum_{i=1}^{N} |w^{(\mathrm{ref})}(x, y_i)|^2}, \tag{4.33}$$

where N is the number of points on the vertical line at abscissa x and $w(x, y_i)$ and $w^{(\mathrm{ref})}(x, y_i)$ are respectively the displacement fields obtained by the present method and

from the reference solution. Eq. (4.33) thus represents a mean quadratic error on each vertical line of the plate, normalised by the mean quadratic value of the reference solution.

Figs. 4.7(a) and 4.7(b) show the real part of the Green's function, respectively obtained by the exact solution and the proposed method. Figs. 4.7(c) to Figs. 4.7(g) show the displacement field on vertical lines l_1 to l_5, respectively defined by $x_1 = 0.013L$, $x_2 = 0.484L$, $x_3 = 0.956L$, $x_4 = 0.972L$. Furthermore, $x_5 = 0.987L$ and Fig. 4.7(h) shows the error ε as a function of x. The agreement is satisfactory in the whole plate, except near the clamped edge, within a distance comparable to half the wavelength, which in the present case is equal to $\lambda/2 = 0.0405L = 4.05\,\text{cm}$.

Simply supported edges do not induce wave conversion between propagating and evanescent components, as observed in the corresponding reflection matrix in Tab. 4.1. In fact, edge effects near such boundaries are of low influence on the global displacement field since they correspond to pure evanescent waves generated at the source that reflect back. On the other hand, as recalled in Tab. 4.1, the reflection matrix of the clamped edge involves wave conversion between propagating and evanescent waves. Thus, propagating waves incident on the clamped boundary give rise to evanescent waves, which are ignored for sources of second and higher orders. As a consequence, higher discrepancies appear near the clamped edge.

4.6.2 Arbitrary polygonal plates: comparison to finite element method (FEM)

In order to validate the proposed method in a more general configuration[1], an arbitrary polygonal plate is considered, as shown in Fig. 4.8. The Green's function of the plate is computed as a function of frequency at three different observation points, $\mathbf{r}_1$, $\mathbf{r}_2$ and $\mathbf{r}_3$, for a point source at $\mathbf{r}_0$, for two different values of the structural damping ratio, $\eta = 0.07$ and $\eta = 0.14$, by the proposed method and by FEM.

For obtaining the Green's function as a function of frequency, the computation detailed above is performed at 99 different frequencies, from 80 Hz to 8 kHz, with the truncation parameter set to $\gamma = 4$. The number of points of the fast Fourier transform is $N_F = 1024$. A total of 46056 nodes is considered in the finite element model, giving rise to 91319 linear triangular elements. The average element length is 3 mm and the eigenmodes are computed up to the frequency 12 kHz, at which the wavelength is greater than 13 times the average element length.

The error of the response for a given observation point in the plate is computed by using an indicator as a function of frequency, given by

$$\varepsilon(f) = \frac{|w(f) - w^{(\text{ref})}(f)|^2}{\dfrac{1}{N}\displaystyle\sum_{i=1}^{N} |w^{(\text{ref})}(f_i)|^2}, \tag{4.34}$$

where N is the number of frequencies for the computation of the response and $w(f)$ and $w^{(\text{ref})}(f)$ are the responses computed, respectively, by the proposed method and by FEM at a given point. Eq. (4.34) thus represents the quadratic error at each frequency,

[1]The example here proposed includes clamped and simply supported boundaries. An additional example including free boundaries is given in Appendix 4.E.

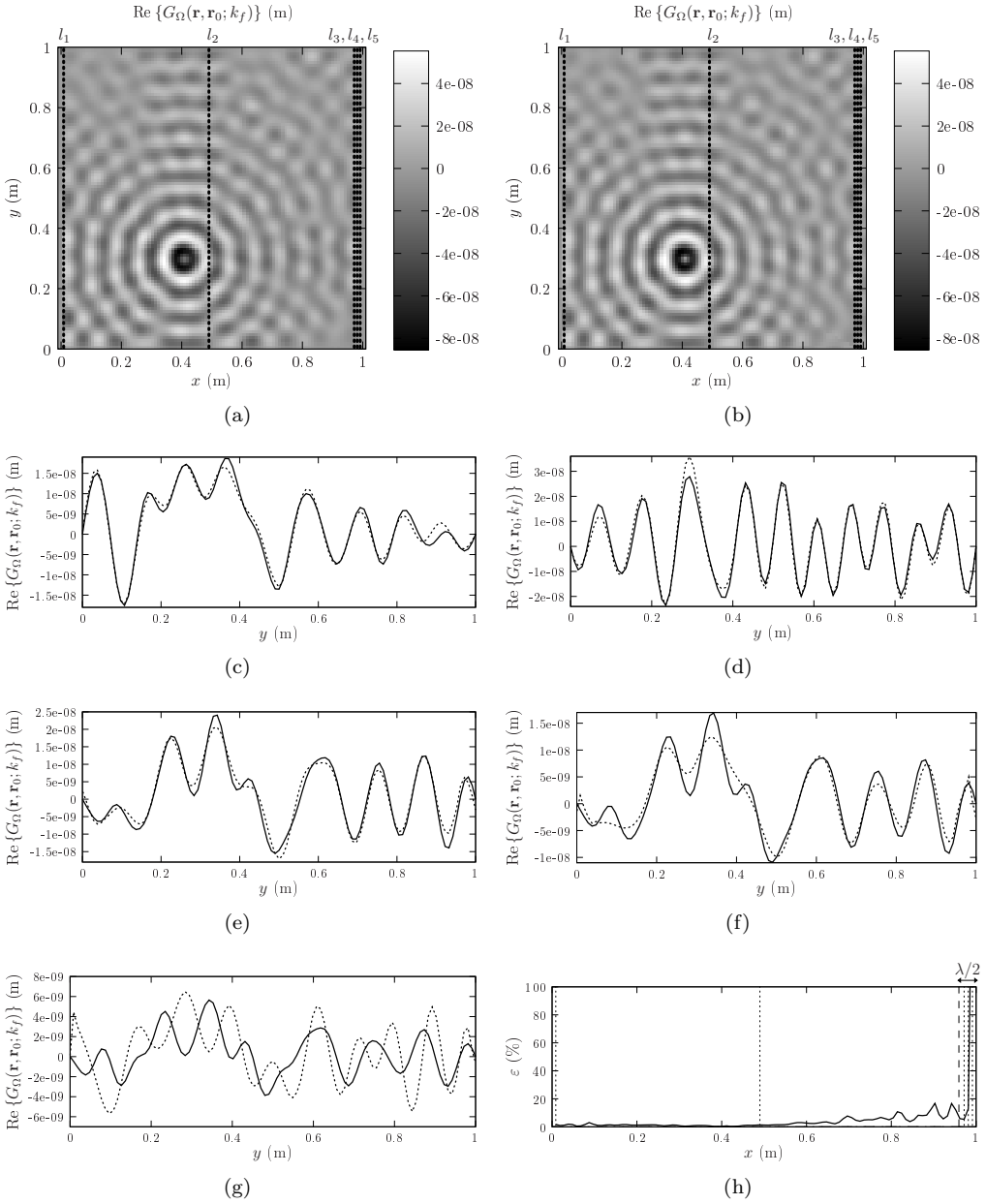

Figure 4.7: Amplitude of the Green's function for the square plate. (a) Exact; (b) proposed method; (c) to (g) displacement field on vertical lines l_1 to l_5; ——, exact; · · · · · ·, proposed method.

normalised by the mean quadratic value of the reference solution over the frequency range of the simulations.

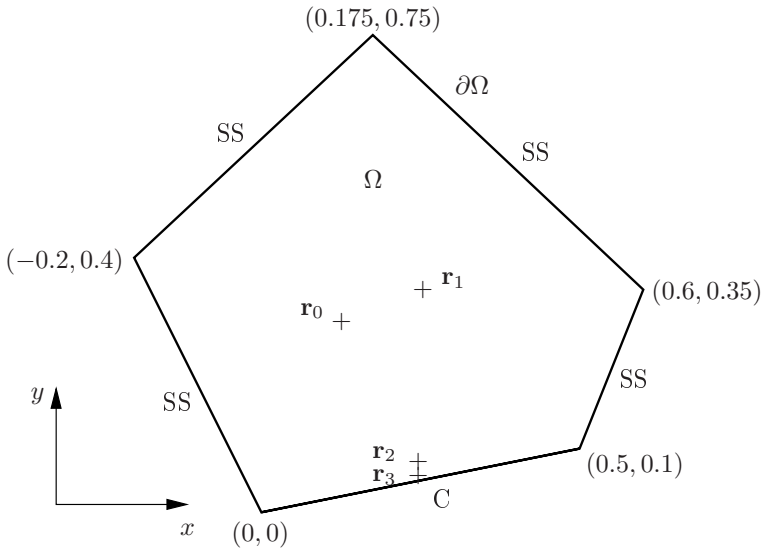

Figure 4.8: Polygonal plate for comparison of the proposed approach to FEM with clamped (C) and simply supported (SS) boundaries. $\mathbf{r}_0 = (0.125, 0.3)$, source; $\mathbf{r}_1 = (0.245778, 0.350778)$, $\mathbf{r}_2 = (0.245778, 0.073775)$ and $\mathbf{r}_3 = (0.245778, 0.058386)$, observation points. Coordinates are in meters.

Fig. 4.9 shows the modulus of the Green's function as a function of frequency, for the chosen parameters. The computed responses are in accordance with the finite element predictions in the central region of the plate, as observed on the displacement fields at the selected observation points $\mathbf{r}_1$ and $\mathbf{r}_2$. As the observation point reaches the clamped boundary at point $\mathbf{r}_3$, the image source method no longer predicts the field accurately. Moreover, Fig. 4.9 shows that the accuracy of the proposed method increases with frequency and structural damping ratio. That is to say that, for a given accuracy to be reached, the number of needed image sources decreases with frequency and damping. Such behaviour of the accuracy is opposite to that of the finite element method, which is limited in terms of computational time to low frequencies and high quality factors.

4.7 Conclusion

This paper provides a method for obtaining the Green's function of the flexural vibrations of thin semi-infinite and convex polygonal plates by using a generalised image source method. The latter consists in considering the Green's function of a semi-infinite or finite domain as the superposition of the contributions from the original source and its image sources with respect to the boundaries, which represent successive wave reflections. The original source contribution is described by the infinite plate Green's function, and is written as a continuous sum of propagating and evanescent plane waves incident on the boundaries. The contributions of image sources thus arise as continuous sums of reflected plane waves. For semi-infinite plates, a general expression of the Green's function is obtained for arbitrary boundary conditions, as long as the reflection matrix

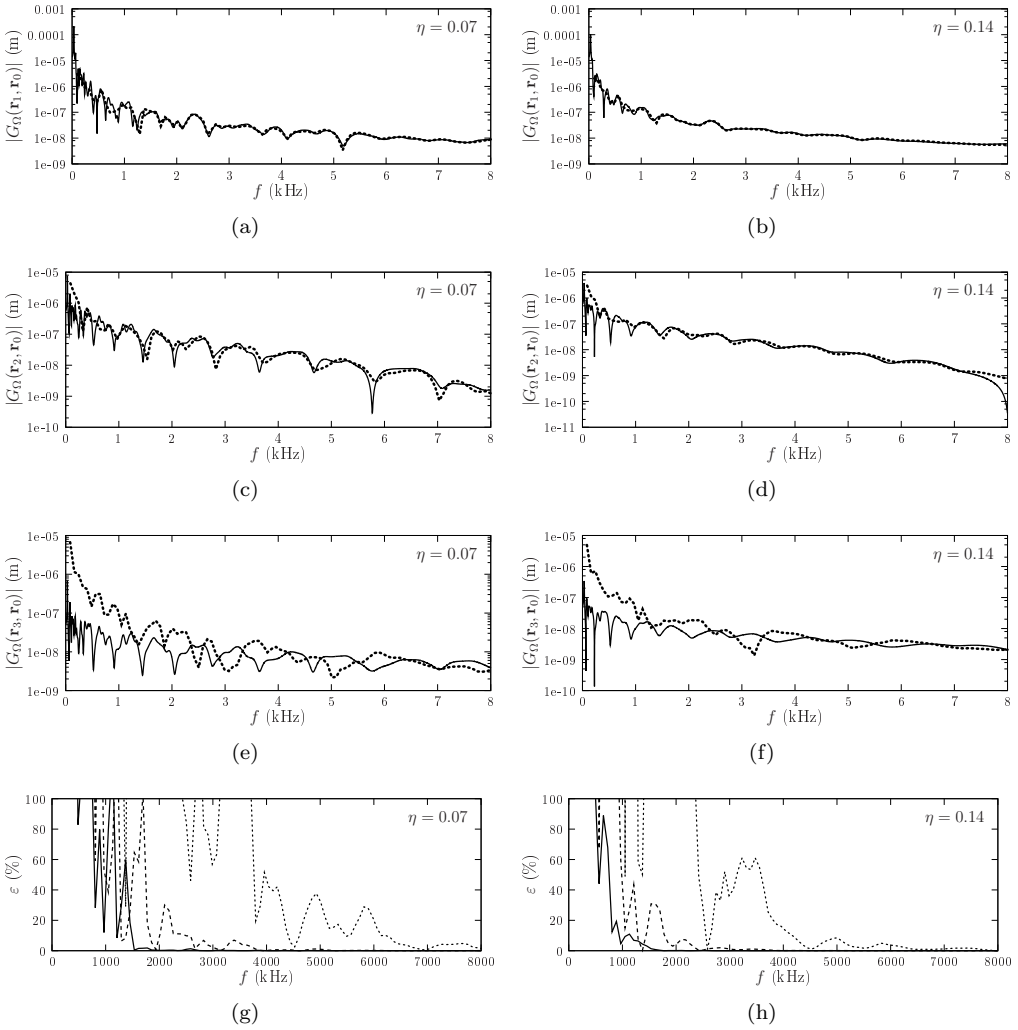

Figure 4.9: Modulus of the Green's function of the polygonal plate as a function of frequency computed by the proposed method (· · · · · ·) and by FEM (——), for $\eta = 0.07$ (left column) and $\eta = 0.14$ (right column), at points (a,b) $\mathbf{r}_1$, (c,d) $\mathbf{r}_2$ and (e,f) $\mathbf{r}_3$. (h,g) Error at points: ——, $\mathbf{r}_1$; - - - - -, $\mathbf{r}_2$; · · · · · ·, $\mathbf{r}_3$.

of the boundary is known. For polygonal plates, the image sources representing the first reflection at each one of the edges are obtained from the Green's function of the corresponding semi-infinite plate in the local coordinate system of the edge at which reflection occurs. The plane waves therein are in a separated variable form that cannot be transposed to local coordinate systems of other edges. Therefore, the contributions of image sources representing the second and subsequent reflections on boundaries cannot be obtained in their complete form. However, after the second reflection and at high frequencies, the distance travelled by waves is much larger than the wavelength. Evanescent waves are thus ignored in the calculation of the image sources of second and

subsequent orders. Comparisons to exact and finite element method results show that the displacement field is accurately predicted outside the nearfield area of the edges, which decreases with frequency and structural damping. The Green's functions obtained by the proposed method are applicable to any set of boundary conditions of which the reflection matrices are known.

A significant advantage of the method developed in this paper is that wave propagation, geometry and boundary conditions can be treated separately. Work is ongoing along this direction for using it as a tool for modelling and characterising mid- and high-frequency vibrations of plates of complex shapes and boundary conditions.

4.A Green's function of an infinite plate in rectangular coordinates

By defining spatial one-dimensional Fourier transform and inverse transform as

$$\bar{w}(k_\xi, \mu) = \mathcal{F}_\xi \left[w(\xi, \mu) \right] = \frac{1}{\sqrt{2\pi}} \int_{-\infty}^{+\infty} w(\xi, \mu) e^{-jk_\xi \xi} d\xi \tag{4.35}$$

and

$$w(\xi, \mu) = \mathcal{F}_\xi^{-1} \left[\bar{w}(k_\xi, \mu) \right] = \frac{1}{\sqrt{2\pi}} \int_{-\infty}^{+\infty} \bar{w}(k_\xi, \mu) e^{jk_\xi \xi} dk_\xi, \tag{4.36}$$

Fourier transform of Eq. (4.1) gives

$$D \left(\frac{\partial^4}{\partial \mu^4} - 2k_\xi^2 \frac{\partial^2}{\partial \mu^2} + k_\xi^4 - k_f^4 \right) \bar{G}_\infty(k_\xi, \mu, \xi_0, \mu_0; k_f) = \frac{e^{-jk_\xi \xi_0}}{\sqrt{2\pi}} \delta(\mu - \mu_0). \tag{4.37}$$

The associated homogeneous equation leads to the general form of the Fourier transform of the Green's function in the form

$$\bar{G}_\infty(k_\xi, \mu, \xi_0, \mu_0; k_f) = A_1 e^{jk_{\mu 2}(\mu - \mu_0)} + A_2 e^{-jk_{\mu 2}(\mu - \mu_0)} + B_1 e^{k_{\mu 1}(\mu - \mu_0)} + B_2 e^{-k_{\mu 1}(\mu - \mu_0)}, \tag{4.38}$$

where

$$k_{\mu 1} = \sqrt{k_f^2 + k_\xi^2}, \tag{4.39}$$

$$k_{\mu 2} = \sqrt{k_f^2 - k_\xi^2}. \tag{4.40}$$

Taking into account the fact that the plate is of infinite extent (Sommerfeld condition) and the continuity of the displacement field at $\mu = \mu_0$ yields

$$\bar{G}_\infty(k_\xi, \mu, \xi_0, \mu_0; k_f) = A e^{jk_{\mu 2}|\mu - \mu_0|} + B e^{-k_{\mu 1}|\mu - \mu_0|}. \tag{4.41}$$

In order to obtain the relation between A and B, Eq. (4.37) is integrated on the interval $\mu \in [\mu_0 - \varepsilon, \mu_0 + \varepsilon]$, yielding

$$\int_{\mu_0 - \varepsilon}^{\mu_0 + \varepsilon} \left(\frac{\partial^4}{\partial \mu^4} - 2k_\xi^2 \frac{\partial^2}{\partial \mu^2} + k_\xi^4 - k_f^4 \right) \bar{G}_\infty(k_\xi, \mu, \xi_0, \mu_0; k_f) d\mu = \frac{e^{-jk_\xi \xi_0}}{\sqrt{2\pi} D}. \tag{4.42}$$

The terms in $-2k_\xi^2 \frac{\partial^2}{\partial \mu^2}$ and $k_\xi^4 - k_f^4$ vanish and this yields, for $\varepsilon \to 0$,

$$-2\left(jk_{\mu 2}^3 A + k_{\mu 1}^3 B\right) = \frac{e^{-jk_\xi \xi_0}}{\sqrt{2\pi} D}. \tag{4.43}$$

Additionally, using the property of continuity of the slope at μ_0,

$$\lim_{\varepsilon \to 0} \left[\frac{\partial \bar{G}_\infty}{\partial \mu}\right]_{\mu_0 - \varepsilon}^{\mu_0 + \varepsilon} = 0, \tag{4.44}$$

yields

$$B = \frac{jk_{\mu 2}}{k_{\mu 1}} A. \tag{4.45}$$

Substituting A and B in Eq. (4.41) and using Eqs. (4.39) and (4.40) leads to the explicit expression of the Fourier transform of the Green's function

$$\bar{G}_\infty(k_\xi, \mu, \xi_0, \mu_0; k_f) = \frac{je^{-jk_\xi \xi_0}}{4\sqrt{2\pi} k_f^2 D} \left(\frac{e^{j\sqrt{k_f^2 - k_\xi^2}|\mu - \mu_0|}}{\sqrt{k_f^2 - k_\xi^2}} + j \frac{e^{-\sqrt{k_f^2 + k_\xi^2}|\mu - \mu_0|}}{\sqrt{k_f^2 + k_\xi^2}} \right). \tag{4.46}$$

The Green's function in the spatial domain is then given by the inverse Fourier transform of Eq. (4.46),

$$G_\infty(\xi, \mu, \xi_0, \mu_0; k_f) = \frac{j}{8\pi k_f^2 D} \int_{-\infty}^{+\infty} e^{jk_\xi(\xi - \xi_0)} \left(\frac{e^{j\sqrt{k_f^2 - k_\xi^2}|\mu - \mu_0|}}{\sqrt{k_f^2 - k_\xi^2}} + j \frac{e^{-\sqrt{k_f^2 + k_\xi^2}|\mu - \mu_0|}}{\sqrt{k_f^2 + k_\xi^2}} \right) dk_\xi. \tag{4.47}$$

4.B Green's function of a polygonal plate in the case of reflection without angular dependence

The purpose of this appendix is to give some details on the case of a plate with all boundaries characterised by a reflection matrix proportional to the identity matrix in the form

$$\mathbf{R}(k_\xi, k_f) = \begin{bmatrix} R & 0 \\ 0 & R \end{bmatrix}, \tag{4.48}$$

such as simply supported ($R = -1$) or roller ($R = 1$) boundary conditions (see Tab. 4.1). In such cases, it can be observed from Eq. (4.15) that the contributions of image sources of any reflection order may be written as

$$G_s(\mathbf{r}, \mathbf{r}_s; k_f) = V(\mathbf{r}, \mathbf{r}_s) A^{(s)} G_\infty(\mathbf{r}, \mathbf{r}_s; k_f), \tag{4.49}$$

where $A^{(s)}$ is the amplitude weight of source s and is independent of both the wavenumber coordinate k_ξ and the flexural wavenumber k_f. The amplitude weight of source s is given

by

$$A^{(s)} = \prod_{n=1}^{N(s)} R_n^{(s)}, \tag{4.50}$$

in which $R_n^{(s)}$ is the reflection coefficient of the edge number n that is needed for the construction of source s. Constant reflection matrices are a particular case allowing the calculation of exact Green's functions of several polygonal geometries, as shown in a previous paper [20].

4.C Discrete Fourier transform

By considering discrete variables $\xi = m\Delta\xi$, $\mu = n\Delta\mu$ and $k_\xi = p\Delta k_\xi$, Eqs. (4.35) and (4.36) assume the form [99]

$$\bar{w}(p\Delta k_\xi, n\Delta\mu) = \mathrm{F}_\xi\left[w(m\Delta\xi, n\Delta\mu)\right] = \frac{1}{\sqrt{2\pi}} \sum_{m=-\infty}^{\infty} w(m\Delta\xi, n\Delta\mu) e^{-jpm\Delta k_\xi \Delta\xi} \Delta\xi \tag{4.51}$$

and

$$w(m\Delta\xi, n\Delta\mu) = \mathrm{F}_\xi^{-1}\left[\bar{w}(p\Delta k_\xi, n\Delta\mu)\right] = \frac{1}{\sqrt{2\pi}} \sum_{p=-\infty}^{\infty} \bar{w}(p\Delta k_\xi, n\Delta\mu) e^{jpm\Delta k_\xi \Delta\xi} \Delta k_\xi, \tag{4.52}$$

where $\Delta\xi$ and Δk_ξ are the space and wavenumber sampling intervals. Practical implementation of Eqs. (4.55) and (4.56) requires a finite number N_F of sampling points. Therefore,

$$\Delta\xi = \frac{2\Xi}{N_F} \tag{4.53}$$

$$\Delta k_\xi = \frac{2K}{N_F} = \frac{2\pi}{2\Xi}, \tag{4.54}$$

where Ξ and K are respectively the maximum distance to the centre of the ξ axis and the maximum wavenumber, such that

$$\bar{w}(p\Delta k_\xi, n\Delta\mu) = \mathrm{F}_\xi\left[w(m\Delta\xi, n\Delta\mu)\right] = \frac{2\Xi}{\sqrt{2\pi}N_F} \sum_{m=-\infty}^{\infty} w(m\Delta\xi, n\Delta\mu) e^{-jpm\Delta k_\xi \Delta\xi} \tag{4.55}$$

and

$$w(m\Delta\xi, n\Delta\mu) = \mathrm{F}_\xi^{-1}\left[\bar{w}(p\Delta k_\xi, n\Delta\mu)\right] = \frac{\sqrt{\pi}}{\sqrt{2}\Xi} \sum_{p=-\infty}^{\infty} \bar{w}(p\Delta k_\xi, n\Delta\mu) e^{jpm\Delta k_\xi \Delta\xi}. \tag{4.56}$$

For the computation of the discrete inverse Fourier transforms of sec. 4.5, these parameters have to be chosen so as to avoid spatial aliasing by setting

$$\Xi \geq r_s^{max}, \tag{4.57}$$

where r_s^{max} is the distance from the centre of the (ξ, μ) coordinate system to the most distant image source.

4.D Impossibility of variable separation of multiple-type waves in two different coordinate systems

As mentioned in sec. 4.4.4, a wave field that is propagating in one direction of space and attenuating in another cannot be written in a separated-variable form in two different coordinate systems in the general case. This appendix aims at showing that explicitly. The coordinate systems of Fig. 4.10, which differ from an angle α by rotation about the z axis, are considered.

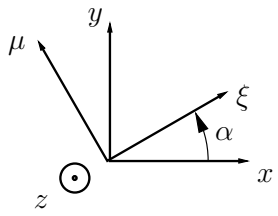

Figure 4.10: Two different coordinate systems.

A plane wave can be represented in coordinate system (ξ, μ) by the separated-variable wave field

$$w(\xi, \mu) = e^{\kappa_\xi \xi} e^{\kappa_\mu \mu}, \tag{4.58}$$

where each one of the propagation constants κ_ξ and κ_μ may be either real or imaginary. Given the coordinate change

$$\begin{cases} \xi = x\cos(\alpha) + y\sin(\alpha), \\ \mu = -x\sin(\alpha) + y\cos(\alpha), \end{cases} \tag{4.59}$$

w assumes the form, in coordinate system (x, y),

$$w(x, y) = e^{(\kappa_\xi \cos(\alpha) - \kappa_\mu \sin(\alpha))x} e^{(\kappa_\xi \sin(\alpha) + \kappa_\mu \cos(\alpha))y}. \tag{4.60}$$

It is easily observed that, in the case of a wave that is propagating in the ξ direction and attenuating in the μ direction, i.e. $\kappa_\xi \in \mathbb{I}$ and $\kappa_\mu \in \mathbb{R}$, the same cannot be said about w in the (x, y) coordinate system. That is, there does not exist a pair (κ_x, κ_y) that satisfies

$$e^{\kappa_x x} e^{\kappa_y y} = e^{\kappa_\xi \xi} e^{\kappa_\mu \mu}, \quad (\kappa_\xi \in \mathbb{I}, \kappa_\mu \in \mathbb{R}) \text{ or } (\kappa_\xi \in \mathbb{R}, \kappa_\mu \in \mathbb{I}). \tag{4.61}$$

In fact, only pure propagating waves ($\kappa_\xi \in \mathbb{I}, \kappa_\mu \in \mathbb{I}$) or pure attenuating waves ($\kappa_\xi \in \mathbb{R}, \kappa_\mu \in \mathbb{R}$) can be expressed in a separated-variable form in two different coordinate systems in the general case. In such cases, the corresponding variable change for the

propagation constants is

$$\begin{cases} \kappa_\xi = \kappa_x \cos(\alpha) + \kappa_y \sin(\alpha), \\ \kappa_\mu = -\kappa_x \sin(\alpha) + \kappa_y \cos(\alpha). \end{cases} \tag{4.62}$$

4.E Arbitrary polygonal plate with free boundaries

The purpose of this appendix is to validate the proposed method in the case a plate with all boundaries free. The arbitrary polygonal plate of Fig. 4.8 is considered, as illustrated in Fig. 4.11.

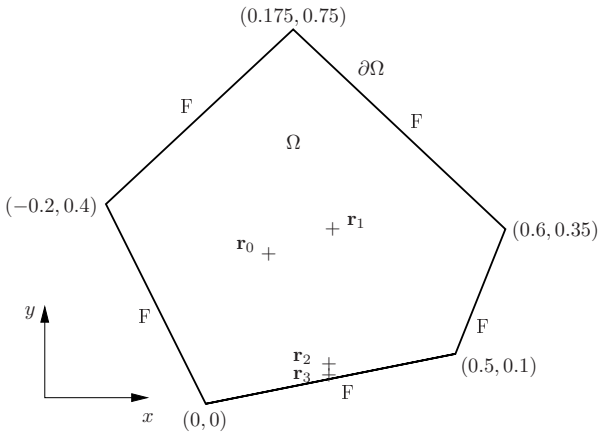

Figure 4.11: Polygonal plate for comparison of the proposed approach to FEM with free (F) boundaries. $\mathbf{r}_0 = (0.125, 0.3)$, source; $\mathbf{r}_1 = (0.245778, 0.350778)$, $\mathbf{r}_2 = (0.245778, 0.073775)$ and $\mathbf{r}_3 = (0.245778, 0.058386)$, observation points. Coordinates are given in meters.

The computation parameters are the same than for the configuration including clamped and simply supported edges. Fig. 4.12 shows the modulus of the Green's function as a function of frequency, for the chosen parameters.

The computed responses are in accordance with the finite element predictions in the central region of the plate, as observed on the displacement fields at the selected observation points $\mathbf{r}_1$ and $\mathbf{r}_2$. The figure shows that, as the observation point reaches the boundary at point $\mathbf{r}_3$, the image source method no longer predicts the field accurately, similarly than in the case of the plate with clamped and simply supported boundaries. Here again, the accuracy of the proposed method increases with frequency and structural damping ratio. However, the main difference with the plate previously studied is that the convergence is slower in the present case. This is due to the fact that all boundaries include a strong coupling between the propagating and evanescent components of the field such that ignoring evanescent waves in the computation of image sources of second and higher order reflections results in larger errors.

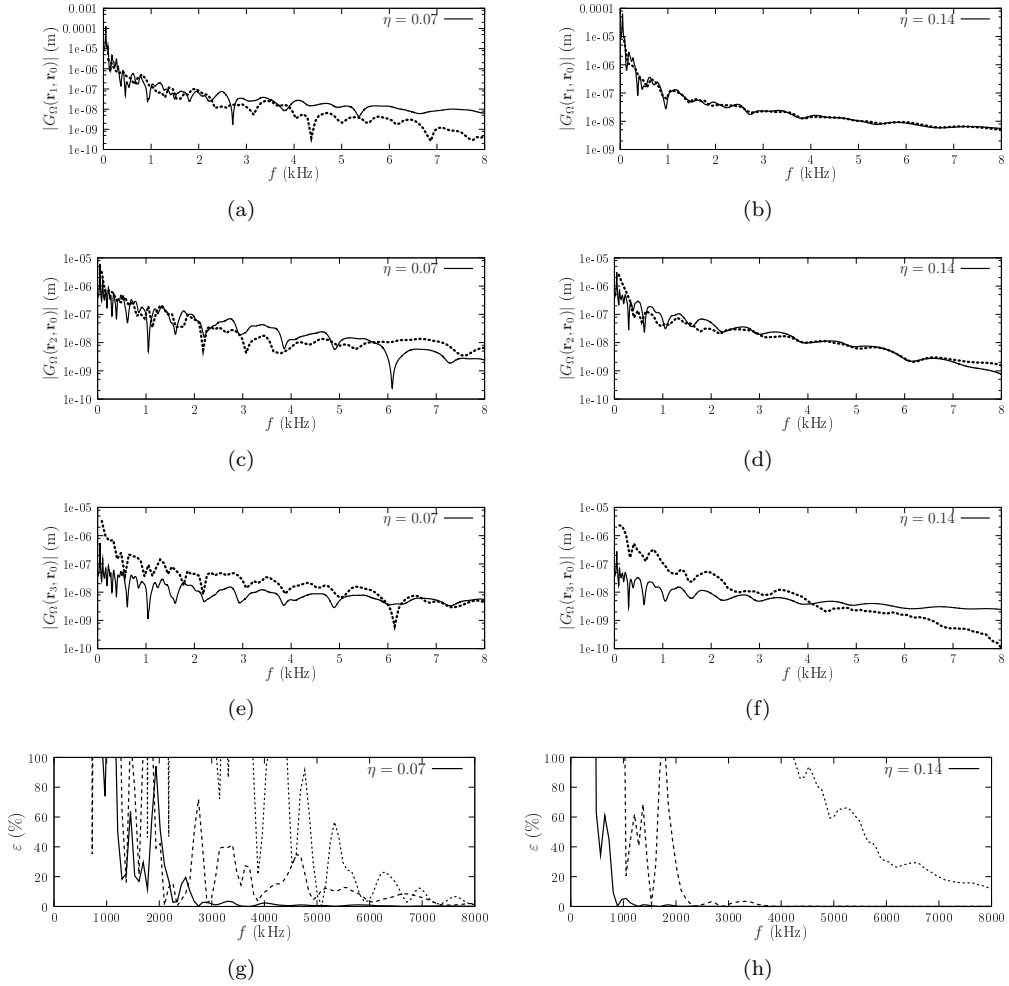

Figure 4.12: Modulus of the Green's function of the polygonal plate as a function of frequency computed by the proposed method (· · · · · ·) and by FEM (——), for $\eta = 0.07$ (left column) and $\eta = 0.14$ (right column), at points (a,b) $\mathbf{r}_1$, (c,d) $\mathbf{r}_2$ and (e,f) $\mathbf{r}_3$. (h,g) Error at points: ——, $\mathbf{r}_1$; - - - - -, $\mathbf{r}_2$; · · · · · ·, $\mathbf{r}_3$.

Chapter 5

On the extension of the image source method to plate assemblies

Abstract

This chapter explores the possibility to extend the image source method to the prediction of the flexural vibrations of a plane assembly of two plates. Using the ideas developed in chaps. 2 and 4, the additional difficulties in this case are including the junction between the plates and determining the positions of image sources. Wave transmission and reflection at the junction is described by a scattering matrix, which can be obtained using the formalism of chap. 3. The transmission matrix describing the junction is included in the terms describing the contributions of image sources to the total field of the plate. As discussed in chap. 4, evanescent waves are only taken into account for generating image sources directly from the original source. Similarly, wave transmission through the junction includes the evanescent components of the field related to the original source only. An example of validation including a virtual junction (i.e. continuity) between two polygonal plates is given. The methodology that is employed for determining the image sources can also be applied to the simulation of coupled acoustic cavities.

5.1 Statement of the problem

An assembly Ω of two connected plates Ω_1 and Ω_2, contained in a plane (x, y) is considered, as illustrated in Fig. 5.1. The assembled structure is excited by a harmonic point source at $\mathbf{r}_0$, located in plate Ω_1 and the displacement field is observed at a point $\mathbf{r}$ located anywhere in Ω. The Green's function of the assembly is the solution of the

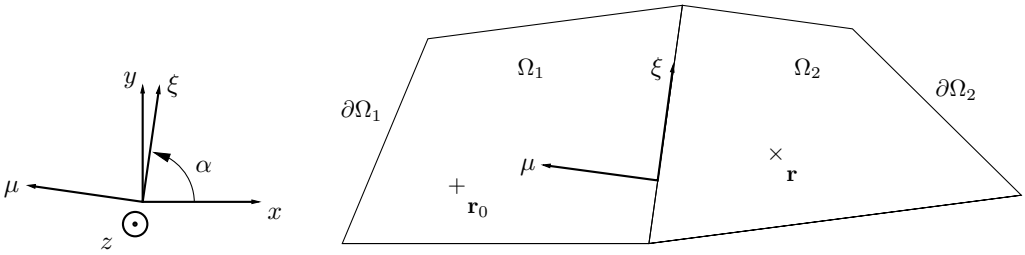

Figure 5.1: Assembly Ω of two plates Ω_1 and Ω_2. $\mathbf{r}_0$, source, $\mathbf{r}$, observation point, (x, y), global coordinate system, (ξ, μ), local coordinate system for computing reflection or transmission at a boundary.

generic system of equations

$$\begin{cases} D\left(\nabla^4 - k_f^4\right) G_\Omega(\mathbf{r}, \mathbf{r}_0; k_f) = \delta(\mathbf{r} - \mathbf{r}_0) & \mathbf{r} \in \Omega_1, \quad (5.1) \\ D\left(\nabla^4 - k_f^4\right) G_\Omega(\mathbf{r}, \mathbf{r}_0; k_f) = 0 & \mathbf{r} \in \Omega_2, \quad (5.2) \\ \text{Boundary conditions (edges of } \Omega_1) & \mathbf{r} \in \{\partial\Omega_1 \setminus (\partial\Omega_1 \cap \partial\Omega_2)\}, \quad (5.3) \\ \text{Boundary conditions (edges of } \Omega_2) & \mathbf{r} \in \{\partial\Omega_2 \setminus (\partial\Omega_1 \cap \partial\Omega_2)\}, \quad (5.4) \\ \text{Boundary conditions (junction)} & \mathbf{r} \in \{\partial\Omega_1 \cap \partial\Omega_2\}. \quad (5.5) \end{cases}$$

The Green's function is proposed in the form of a superposition of contributions from the original source and its image sources, which in this case represent successive reflections on the boundaries and transmissions through the junction. The aim of what follows is to determine the contributions of the different sources. It is worth noticing that the concept of image sources relies on specular reflection, which does not allow to include diffraction by the plate vertices [37]. Then, in the general case, the Green's function obtained by the image source method is an approximation.

5.2 Image source method for an assembly of two plates

5.2.1 Geometrical construction of image sources

The first step consists in determining the image sources with respect to the boundaries of plate Ω_1, which contains the original source, without taking into account wave transmission towards the second plate. Then, the transmission properties of the junction are applied to the image sources that are 'visible' from the second plate, Ω_2, as detailed in sec. 4.4. From such visible sources, a new set of image sources is computed with respect to the boundaries of plate Ω_2. The transmission properties of the junction are applied to the newly generated sources in Ω_2, that are visible from Ω_1. The process is repeated until the image sources fill a truncation radius, defined from Eq. (2.44) using the total perimeter and surface area of assembly Ω. Fig. 5.2 illustrates an example showing 'visible' and 'invisible' sources for two connected plates and Fig. 5.3 illustrates the different steps of the construction of the image source positions.

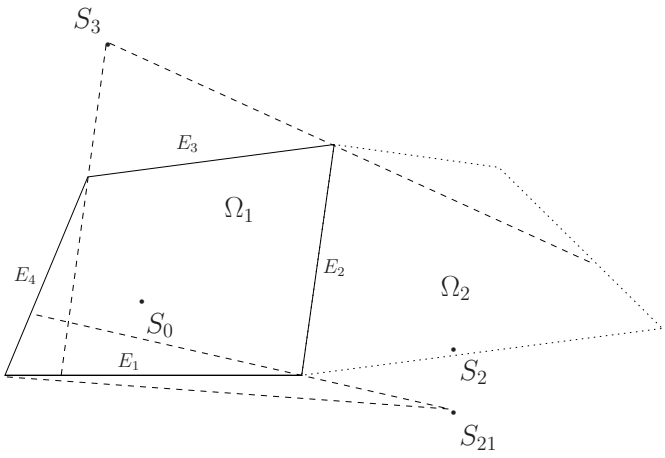

Figure 5.2: Example of visible and invisible image sources of plate Ω_1 (——) from a connected plate Ω_2 ($\cdots\cdots$). S_0, original source; S_2, image of S_0 on edge E_2; S_{21}, image of S_2 on edge E_1; S_3, image of S_0 on edge E_3; - - - - -, validity zones of image sources. Source S_3 is visible from a portion of both plates whereas source S_{12} is visible from a portion of plate Ω_1 but invisible from plate Ω_2.

5.2.2 Model of the junction

As defined in chap. 3 for two connected semi-infinite domains, the scattering matrix of the junction between plates Ω_1 and Ω_2 is given by

$$\mathbf{S} = \begin{bmatrix} \mathbf{T}_{12} & \mathbf{R}_{22} \\ \mathbf{R}_{11} & \mathbf{T}_{21} \end{bmatrix}. \tag{5.6}$$

Matrices $\mathbf{R}_{11}$ and $\mathbf{R}_{22}$ are the reflection matrices of the junction domains Ω_1 and Ω_2, respectively. Similarly, $\mathbf{T}_{12}$ and $\mathbf{T}_{21}$ are the transmission matrices from Ω_1 to Ω_2 and from Ω_2 to Ω_1, respectively. The different reflection and transmission matrices assume the form

$$\mathbf{R} = \begin{bmatrix} R_{pp} & R_{ep} \\ R_{pe} & R_{ee} \end{bmatrix}, \quad \mathbf{T} = \begin{bmatrix} T_{pp} & T_{ep} \\ T_{pe} & T_{ee} \end{bmatrix}, \tag{5.7}$$

in which p and e respectively denote propagating and evanescent waves, such that each term in the form R_{ir} (resp. T_{it}) represents the coupling between an incident (i) propagating or evanescent wave and a reflected (r) (resp. transmitted (t)) propagating or evanescent wave.

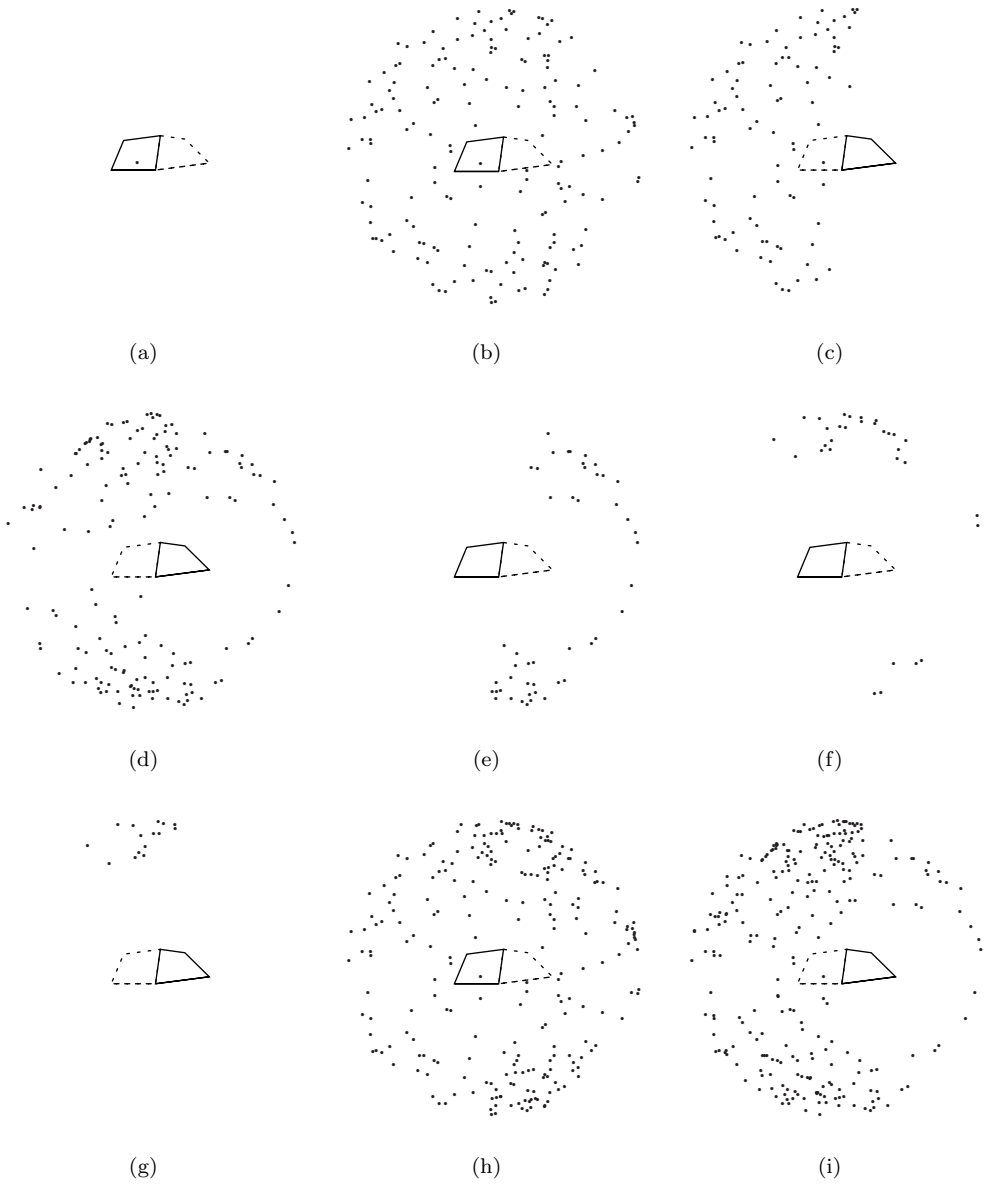

Figure 5.3: Steps for the construction of the image sources of the assembly. The original source (a) generates new image sources for plate Ω_1 (b). A subset of those new sources is visible from plate Ω_2 (c), which in turn generate new image sources for plate Ω_2 (d). A subset of those new sources is visible from plate Ω_1 (e), which in turn generate new image sources for plate Ω_1 (f). A subset of those new sources is visible from plate Ω_2 (g). In this example, the next iteration does not generate new image sources in the truncation radius. (h) and (i) show all the sources visible from plates Ω_1 and Ω_2, respectively.

5.2.3 Displacement field of the assembly

5.2.3.1 Contribution of the original source to Ω_1

The contribution of the original source to the field of the plate containing it (plate Ω_1) is given by Eq. (4.5),

$$G_\infty(\xi,\mu,\xi_0,\mu_0;k_f) = V(\mathbf{r},\mathbf{r}_0)\frac{j}{8\pi k_f^2 D}\int_{-\infty}^{+\infty} e^{jk_\xi(\xi-\xi_0)}\left(\frac{e^{j\sqrt{k_f^2-k_\xi^2}|\mu-\mu_0|}}{\sqrt{k_f^2-k_\xi^2}}+j\frac{e^{-\sqrt{k_f^2+k_\xi^2}|\mu-\mu_0|}}{\sqrt{k_f^2+k_\xi^2}}\right)dk_\xi, \quad (5.8)$$

which appears as a continuous sum of propagating and evanescent plane waves that are incident on the boundaries of plate Ω_1. In this expression, $V(\mathbf{r},\mathbf{r}_0)$ is the validity zone of the direct contribution from the original source. In fact, the direct field emitted by the original source is only valid in plate Ω_1. Its contribution to plate Ω_2 must include the transmission properties of the junction connecting both plates, as detailed hereafter.

5.2.3.2 Contribution of the original source to plate Ω_2 through the junction

If one of the boundaries of Ω_1 is connected to another plate Ω_2, the contribution of the original source to the vibrational field of the plate Ω_2 is a continuous sum of propagating and evanescent plane waves, generated at the original source point $\mathbf{r}_0$, transmitted through the junction. This can be expressed as

$$G_s^{(\mathrm{T})}(\mathbf{r},\mathbf{r}_0;k_f) = V(\mathbf{r},\mathbf{r}_0)\frac{j}{8\pi k_f^2 D}\int_{-\infty}^{+\infty} e^{jk_\xi(\xi-\xi_0)}\left[e^{j\sqrt{k_f^2-k_\xi^2}(\mu-\mu_b)} \quad e^{-\sqrt{k_f^2+k_\xi^2}(\mu-\mu_b)}\right]$$
$$\begin{bmatrix} T_{pp}(k_\xi,k_f) & T_{ep}(k_\xi,k_f) \\ T_{pe}(k_\xi,k_f) & T_{ee}(k_\xi,k_f)\end{bmatrix}\begin{bmatrix} \dfrac{e^{j\sqrt{k_f^2-k_\xi^2}(\mu_b-\mu_0)}}{\sqrt{k_f^2-k_\xi^2}} \\ j\dfrac{e^{-\sqrt{k_f^2+k_\xi^2}(\mu_b-\mu_0)}}{\sqrt{k_f^2+k_\xi^2}}\end{bmatrix} dk_\xi, \quad (5.9)$$

where

$$\mathbf{T}(k_\xi,k_f) = \begin{bmatrix} T_{pp}(k_\xi,k_f) & T_{ep}(k_\xi,k_f) \\ T_{pe}(k_\xi,k_f) & T_{ee}(k_\xi,k_f)\end{bmatrix} \quad (5.10)$$

is the transmission matrix of the junction and $V(\mathbf{r},\mathbf{r}_s)$ is the validity zone of $G_s^{(\mathrm{T})}$, i.e. the region of plate Ω_2 from which the original source is 'visible' through the junction. The transmitted field thus appears as a continuous superposition of propagating and evanescent transmitted plane waves.

5.2.3.3 Contributions of image sources corresponding to the first reflection in plate Ω_1

According to the model developed in chap. 4 for an individual plate, the contributions of the image sources corresponding to the first wave reflection on the boundaries of the plate containing the original source are given by

$$G_s^{(\mathrm{R})}(\mathbf{r},\mathbf{r}_s;k_f) = V(\mathbf{r},\mathbf{r}_s)\frac{j}{8\pi k_f^2 D}\int_{-\infty}^{+\infty} e^{jk_\xi(\xi-\xi_s)} \left[e^{j\sqrt{k_f^2-k_\xi^2}(\mu-\mu_b^{(s)})} \quad e^{-\sqrt{k_f^2+k_\xi^2}(\mu-\mu_b^{(s)})}\right] \begin{bmatrix} R_{pp}^{(s)}(k_\xi,k_f) & R_{ep}^{(s)}(k_\xi,k_f) \\ R_{pe}^{(s)}(k_\xi,k_f) & R_{ee}^{(s)}(k_\xi,k_f) \end{bmatrix} \begin{bmatrix} \dfrac{e^{j\sqrt{k_f^2-k_\xi^2}(\mu_b^{(s)}-\mu_s)}}{\sqrt{k_f^2-k_\xi^2}} \\ j\dfrac{e^{-\sqrt{k_f^2+k_\xi^2}(\mu_b^{(s)}-\mu_s)}}{\sqrt{k_f^2+k_\xi^2}} \end{bmatrix} dk_\xi, \quad (5.11)$$

where

$$\mathbf{R}^{(s)}(k_\xi,k_f) = \begin{bmatrix} R_{pp}^{(s)}(k_\xi,k_f) & R_{ep}^{(s)}(k_\xi,k_f) \\ R_{pe}^{(s)}(k_\xi,k_f) & R_{ee}^{(s)}(k_\xi,k_f) \end{bmatrix} \quad (5.12)$$

is the reflection matrix of the boundary at which reflection takes place and $V(\mathbf{r},\mathbf{r}_s)$ is the validity zone of $G_s^{(\mathrm{R})}$, as defined in chap. 4. Superscript (s) denotes variables that are expressed in the local coordinate system of the boundary giving rise to source s, such that $\mu = \mu_b^{(s)}$ is the location of the boundary. Eq. (5.11) also appears as a continuous sum of reflected propagating and evanescent plane waves.

5.2.3.4 Contributions of image sources generated after the first reflection or transmission

The integrand in Eqs. (5.8), (5.9), and (5.11) is in the form of a propagating wave along the ξ axis and a superposition of propagating and evanescent waves along the μ axis. As detailed in chap. 4 and appendix. 4.D, a plane wave which is propagating in one direction and attenuating in the other cannot be written in such separated variable form using two different coordinate systems, such that the contributions of new image sources generated from the first reflection or transmission must be approximated by neglecting evanescent waves as

$$G_s^{(\mathrm{II})}(\mathbf{r},\mathbf{r}_s;k_f) = V(\mathbf{r},\mathbf{r}_s)\frac{j}{8\pi k_f^2 D}\int_{-|k_f|}^{|k_f|} e^{jk_\xi(\xi-\xi_s)} A_{pp}^{(s)}(k_\xi,k_f)\frac{e^{j\sqrt{k_f^2-k_\xi^2}(\mu-\mu_s)}}{\sqrt{k_f^2-k_\xi^2}}dk_\xi, \quad (5.13)$$

where $A_{pp}^{(s)}$ is the amplitude weight of image source s, resulting from the successive reflections (on the boundaries of plates Ω_1 and Ω_2) and transmissions (through the junction) of propagating waves. In the considered integration domain, defined by $-|k_f| < k_\xi < |k_f|$, the transverse wavenumber coordinate $k_\mu = \sqrt{k_f^2-k_\xi^2}$ is real. Then, as shown by Eqs. (4.25) and (4.26), wavenumber coordinate k_ξ can be written using polar

coordinates $|k_f|$ and θ, as

$$k_\xi = |k_f| \cos(\theta), \tag{5.14}$$

where θ is the orientation of the propagating plane wave in coordinate system (ξ, μ) (see Fig. 3.7 on page 58). Thus, the amplitude weight $A_{pp}^{(s)}$ is obtained as the product of the scalar reflection and transmission coefficients R_{pp} and T_{pp} of the boundaries that successively participate in the construction of image source s, in the form

$$A_{pp}^{(s)}(\theta) = \prod_{n=1}^{N_R(s)} R_n^{(s)}(\theta, \alpha_n) \prod_{n=1}^{N_T(s)} T_n^{(s)}(\theta, \alpha_n), \tag{5.15}$$

where α_n are the orientations of the different boundaries (edges and junction) at which reflection and transmission occurs, with respect to the global coordinate system (x, y) as illustrated in Fig. 5.1. (Note that the local coordinate system relative to the junction has complementary orientations in plates Ω_1 and Ω_2.) Thus, source s represents the wave field having undergone a total number of $N_R(s)$ reflections on the edges of plates Ω_1 and Ω_2 and a total number of wave transmissions $N_T(s)$ through the junction. Eq. (5.15) thus contains the history of reflections and transmissions of each elementary propagating plane wave describing higher-order image sources. As for the model of individual plates developed in chap. 4, the numerical implementation of Eqs. (5.8), (5.9), (5.11) and (5.13) is done by using fast Fourier transform.

5.3 Validation

5.3.1 Virtual junction between two rectangular plates

In order to validate the present formulation, the simplest case of a virtual junction consisting of continuity between two rectangular plates Ω_1 and Ω_2 is considered, as illustrated in Fig. 5.4. The corresponding scattering matrix is given by Eq. (3.49), as the identity matrix

$$\mathbf{S} = \begin{bmatrix} 1 & 0 & 0 & 0 \\ 0 & 1 & 0 & 0 \\ 0 & 0 & 1 & 0 \\ 0 & 0 & 0 & 1 \end{bmatrix}. \tag{5.16}$$

The external boundaries of the assembly are simply supported. The plate material is aluminium, with density $\rho = 2700\,\mathrm{kg{\cdot}m^{-3}}$, Young's modulus $E_0 = 69 \cdot 10^9$ GPa, Poisson's ratio $\nu = 0.33$, The structural damping ratio is arbitrarily set to 0.07. For the image source method, the truncation parameter is chosen as $\gamma = 3$, which yields 243 sources for plate Ω (on the left of Fig. 5.4) and 232 sources for plate Ω_2 (on the right of the figure).

The solution obtained by the proposed method is compared to the reference solution obtained without the virtual junction. The quadratic error on a vertical line of abscissa

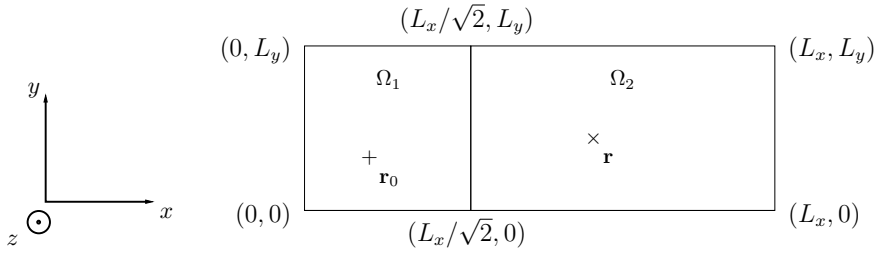

Figure 5.4: Assembly of two rectangular plates used for validation of the proposed approach, with $L_x = 1\,\mathrm{m}$ and $L_y = 0.7\,\mathrm{m}$. The source position is $\mathbf{r}_0 = (0.3\,\mathrm{m}, 0.27\,\mathrm{m})$. ——, plate edges; - - - - -, virtual junction.

x is used as a local criterion, as in Eq. (4.33), which is expressed as

$$\varepsilon(x) = \frac{\sum_{i=1}^{N} |w(x, y_i) - w^{(\mathrm{ref})}(x, y_i)|^2}{\sum_{i=1}^{N} |w^{(\mathrm{ref})}(x, y_i)|^2}, \tag{5.17}$$

where superscript ref relates to the reference solution. Fig. 5.5 shows the real part of the displacement field on the whole plate and on selected vertical lines for the reference solution and the solution with a virtual junction at a frequency of 3 kHz. The error obtained from Eq. (5.17) is also shown. It can be observed from Figs. 5.5(a,b) that the solution with the virtual junction is nearly indistinguishable from the reference solution. Figs. 5.5(c,g) show the displacement field on lines near the external boundaries in direction x and Figs. 5.5(d-f) show the displacement field along the junction and on vertical lines at the left and right of the latter. The major discrepancies in the solution are near the left and right edges of the assembly and not at the boundary.

Fig. 5.6 is analogous to Fig. 5.5 for a frequency of 7 kHz. It can be observed that the error is reduced by the increase of frequency. This indicates that the discrepancies are due to the missing evanescent terms in the description higher order image sources.

5.3.2 Virtual junction between two arbitrarily polygonal plates

Rectangular plates being a special case of boundary geometry, the solution obtained by the method proposed herein can be compared to a reference solution in the case of two polygonal plates of arbitrary shape, connected by a virtual junction consisting of continuity conditions. The plate dimensions are represented in Fig. 5.7. The material parameters are the same than for the responses simulated above, for a frequency $f = 3\,\mathrm{kHz}$.

The error estimation used above for lines parallel to the junction cannot be applied to this case since the number of spatial points varies with the distance from the junction. Instead, a qualitative comparison is possible by observing the estimated Green's function along horizontal lines crossing the junction. This is represented in Fig. 5.8. The figure shows fair agreement on both sides of the junction. However, similarly to the previous

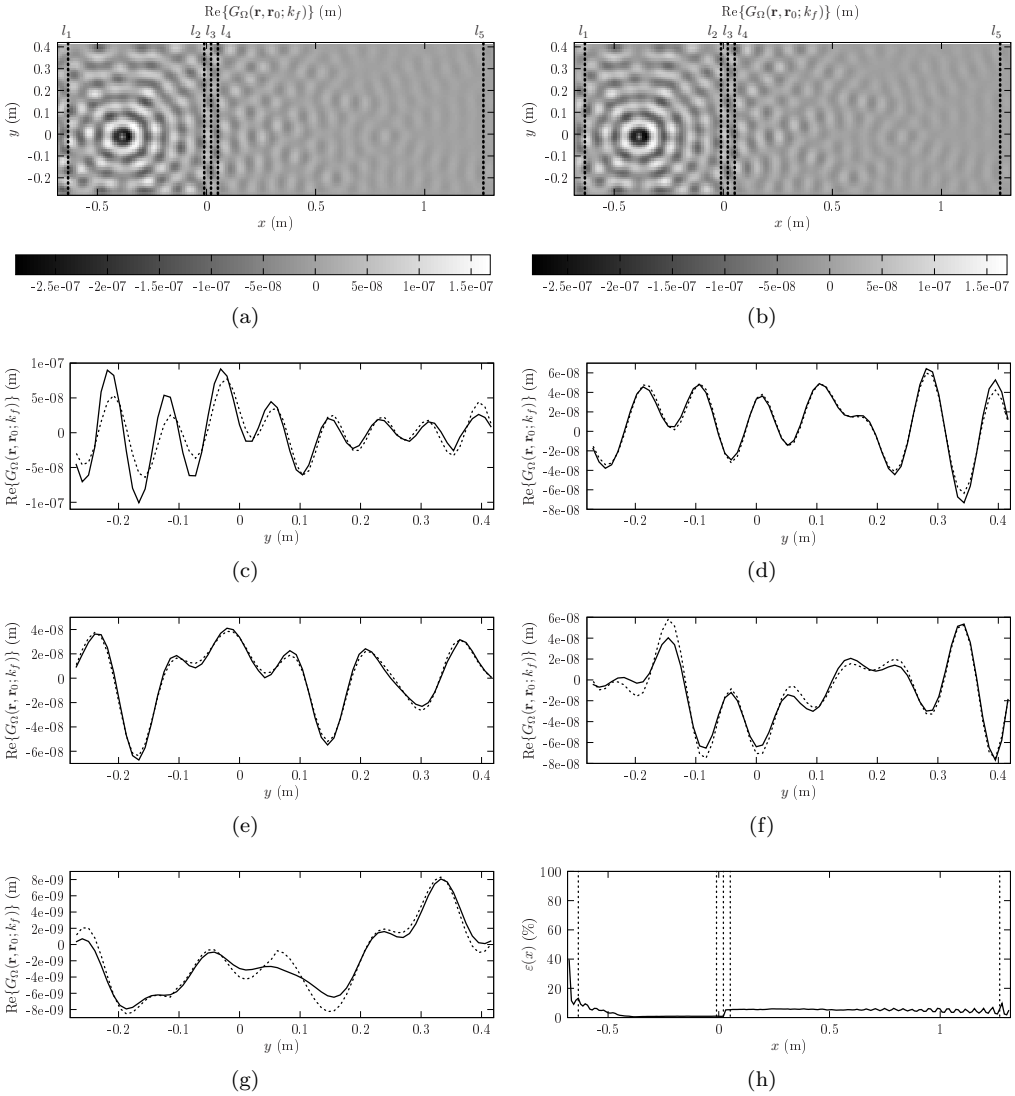

Figure 5.5: Real part of the Green's function of plate Ω at 3 kHz. (a) Reference solution, (b) solution with virtual junction; (c-g) displacement field on vertical lines l_1 to l_5; ——, reference; · · · · · ·, with virtual junction; (h) error from Eq. (5.17).

case, the proposed method presents higher discrepancies in the plate that does not contain the source.

5.4 Conclusion

This chapter discusses the extension of the image source method to assemblies of polygonal plates, based on the model developed in chap. 4. In the model, evanescent

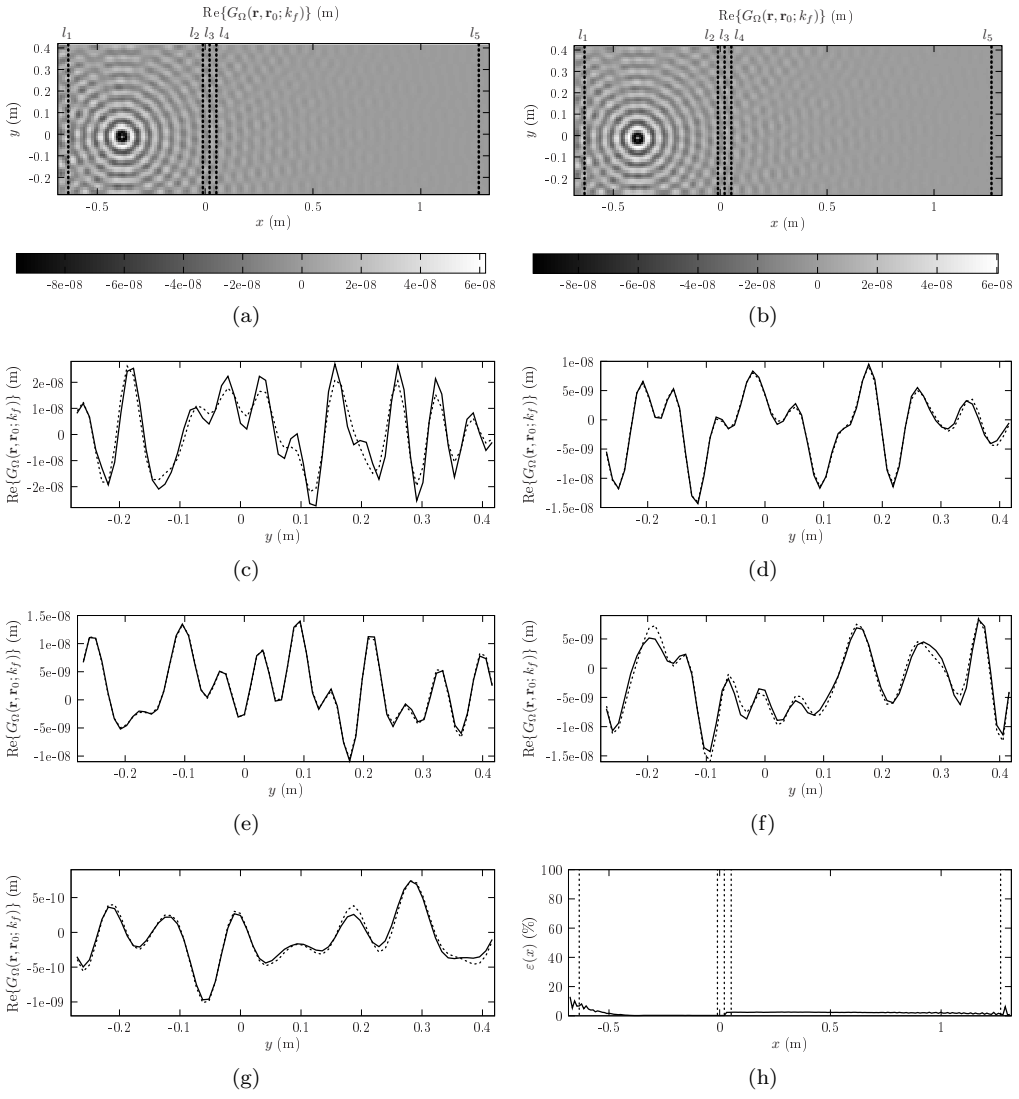

Figure 5.6: Real part of the Green's function of plate Ω at 7 kHz. (a) Reference solution, (b) solution with virtual junction; (c-g) displacement field on vertical lines l_1 to l_5; ——, reference; · · · · · ·, with virtual junction; (h) error from Eq. (5.17).

waves are ignored for the image sources generated after the first reflection (at the edges) and transmission (at the junction). The accuracy of the solution is correct in the academic case of validation consisting of a virtual junction describing continuity. The evolution of the error with frequency suggests that the discrepancies are due to the ignored evanescent field in the description of wave transmission at the junction. The model is then applicable in a high modal overlap context. However, the case of a virtual junction is very simplistic in that it does not include reflection or a dependency on frequency or on the angle of

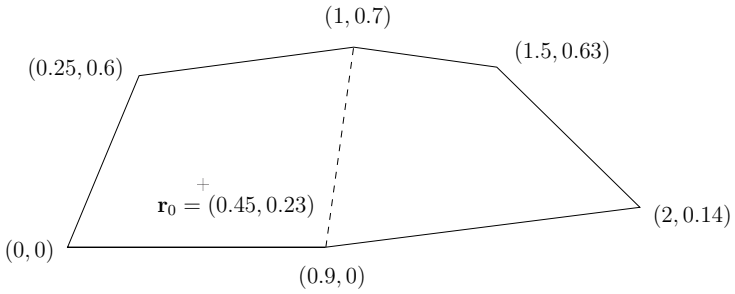

Figure 5.7: Assembly of two arbitrarily polygonal plates used for validation of the proposed approach (distances in meters). ——, plate edges; - - - - -, virtual junction.

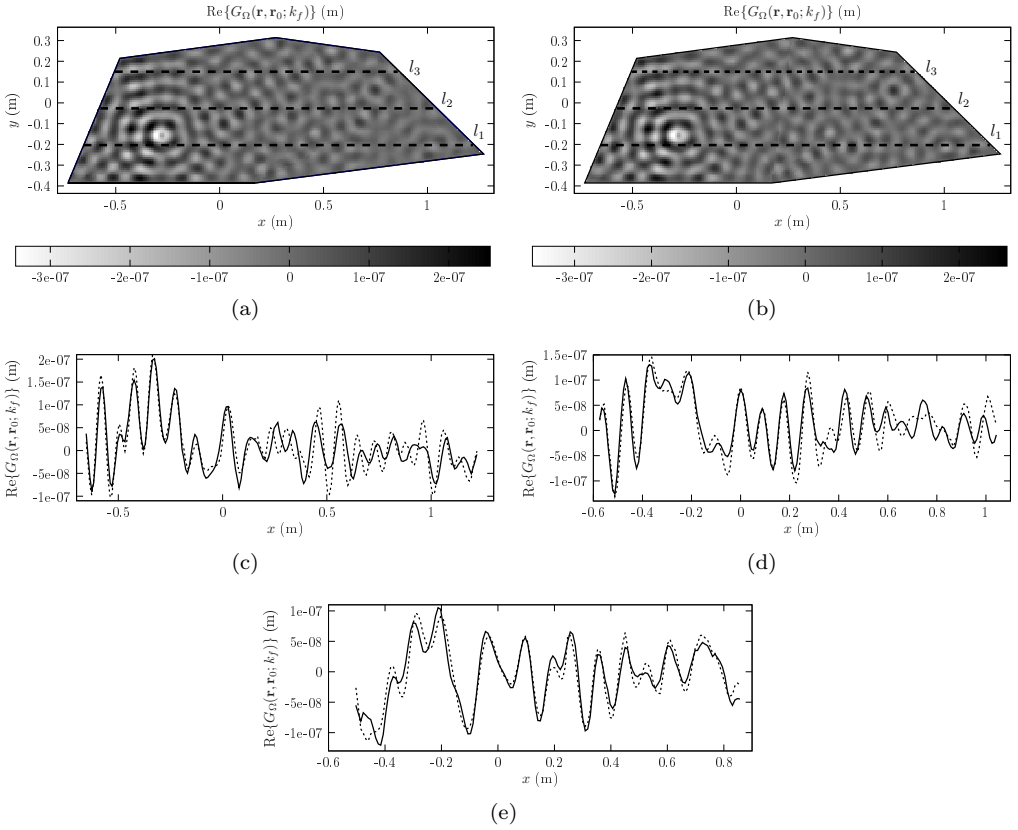

Figure 5.8: Real part of the Green's function for an assembly of two polygonal plates connected by a virtual junction. (a) Reference solution, (b) solution with virtual junction; (c-e) displacement field on horizontal lines l_1 to l_3; ——, reference; · · · · · ·, with virtual junction.

incidence of waves. Further validations on more complex junctions and geometries would be needed before applying the proposed model to non-academic configurations.

Chapter 6

Measurement of complex bending stiffness of a flat panel covered with a viscoelastic layer using the image source method

This chapter is presented as a conference paper [21]. The study results from a collaboration with Henkel Adhesive Technologies[1], who provided the car floor panel sample, and involved two Master's students, who helped in determining the feasibility of the methodology presented herein [1].

Abstract

Flat panels covered with viscoelastic layers are widely used in mechanical engineering. The equivalent complex bending stiffness of such panels is an important property, from which the equivalent Young's modulus and structural damping ratio can be derived. This paper aims at measuring such parameters for highly damped panels in the medium and high frequency ranges, by using the image source method (ISM). When considering a convex polygonal plate excited by a vibrating point source, ISM consists in describing the response as the superposition of the original source and virtual sources whose amplitudes and locations are determined in order to satisfy the boundary conditions. The accuracy of such method is known to increase with frequency and structural damping. First, the mobility of a covered panel to a driving point force is measured. The averaged mobility over frequency and the associated standard deviation are then computed and allow to adjust the ISM parameters in order to extract the Young's modulus and damping ratio. The method is applied to a flat portion of car floor panel and the capability of ISM to accurately describe experimental data is discussed.

[1] `http://www.henkel.com`

6.1 Introduction

A very important concern of aeronautic and automotive industries today is the reduction of the total mass of aircrafts and vehicles. A commonly encountered difficulty is that efficient vibration damping generally needs large amounts of added mass to the vibrating structure. Therefore, an optimal use of damping materials needs a sufficient knowledge of their vibrational behaviour. A common example of such materials is the viscoelastic material layer that generally covers vehicle floors, of which a sample is tested in the present paper.

It is known from experience that the vibrational behaviour of such damping materials depends on frequency, to which the measurement methods must be adapted. The methods for estimating the main mechanical parameters governing the vibrations, such as elasticity moduli and damping factors, are well established in the low frequency range (typically, tens of Hz to several hundreds of Hz). A common low-frequency measurement method is the Oberst beam technique [15], which consists in extracting the complex bending stiffness of a vibrating beam from the resonance frequencies and their corresponding half-value bandwidths. In the ultrasound frequency range, specific methods exist [27]. However, there is a need of measurement techniques for highly damped materials in the medium audio frequency range (typically several hundreds of Hz to several kHz), where modal density is significant.

The aim of the present paper is to use the image source method (ISM) as a model of the flexural vibrations of polygonal plates and as a tool for estimating the Young's modulus and the structural damping ratio of a highly damped plate in medium and high frequencies. ISM consists in describing the vibrational field of a polygonal domain as the superposition of the contributions of the original source and its image sources, which represent the successive reflections of waves on the boundaries. It has been previously shown that ISM is a reliable tool for predicting the flexural vibrations of polygonal plates in the mid- and high-frequency ranges [20, 22, 39]. The main particularity of ISM is that the accuracy of the computations is improved with frequency and structural damping. In fact, for a given degree of accuracy to be reached, the number of needed image sources decreases with frequency and structural damping. This is due to the fact that waves travelling from an image source to a given observation point in the plate are more rapidly damped as the frequency or the structural losses increase. Therefore, at a given frequency and for a given amount of structural damping, image sources located far from the observation point can be disregarded.

The main reason of using ISM as a model for estimating the complex bending stiffness of a plate is that the contributions of the original source and the image sources to the response of a plate are directly correlated with the modulus of elasticity and the structural damping ratio. In fact, Skudrzyk [90] showed that, for a finite structure, the mean line of the frequency response is given by the original source, whereas the peaks and valleys of the response are due to interferences between image sources. Moreover, the mean line of the frequency response is mainly governed by the modulus of elasticity and the deviation of peaks and valleys from the mean line is governed by damping. Thus, comparing an experimental input mobility to the ISM model allows to extract the Young's modulus and the structural damping ratio.

The ISM model and the experimental setup are first presented, and then the method for extracting the mechanical parameters of the plate is detailed.

6.2 Model

In a previous paper [20], the authors applied ISM to simply supported polygonal plates. However, the reflection coefficient associated to such boundary conditions is constant, which is a very particular case. The formulation has been generalised in order to include other boundary conditions, such as clamped of free edges [19, 22]. The generalised ISM model is here briefly presented in the case of free edges in order to set the basis for comparison to experimental results.

6.2.1 Green's problem of the flexural motion of the plate

The system under study is a square plate of side length L, excited perpendicularly by a harmonic point source at $\mathbf{r}_0$, as shown in Fig. 6.1. The space variable is denoted $\mathbf{r} = (x, y)$ in a global coordinate system, and $\mathbf{r} = (\xi, \mu)$ in the local coordinate system of a given edge. The four edges are free, which is modelled by zero normal bending moment M_μ and total shear force V_μ.

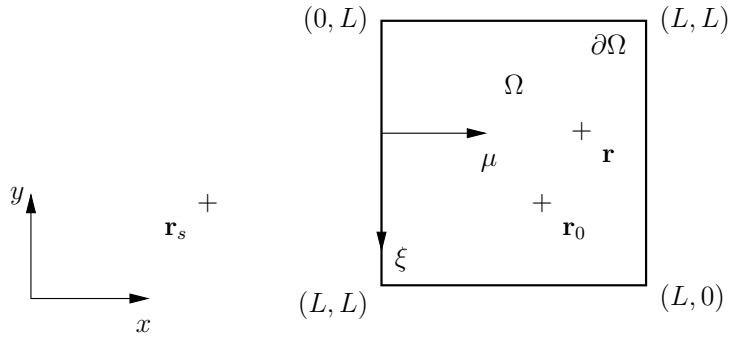

Figure 6.1: Square panel under consideration, with all edges free. Ω, interior domain; $\partial\Omega$, boundaries; $\mathbf{r}_0$, source; $\mathbf{r}$, observation point. (x, y), global coordinate system; (ξ, μ), local coordinate system to an edge.

In the framework of Kirchhoff's theory of thin plates [34] and assuming $e^{-j\omega t}$ time dependence, the Green's function corresponding to the displacement field due to flexural motion is a solution of the set of equations

$$\begin{cases} D\left(\nabla^4 - k_f^4\right) G_\Omega(\mathbf{r}, \mathbf{r}_0; k_f) = \delta(\mathbf{r} - \mathbf{r}_0) & \mathbf{r} \in \Omega, \quad (6.1) \\ M_\mu(\mathbf{r}, \mathbf{r}_0; k_f) = -D\left(\dfrac{\partial^2 G_\Omega}{\partial \mu^2} + \nu \dfrac{\partial^2 G_\Omega}{\partial \xi^2}\right) = 0 & \mathbf{r} \in \partial\Omega, \quad (6.2) \\ V_\mu(\mathbf{r}, \mathbf{r}_0; k_f) = -D\left(\dfrac{\partial^3 G_\Omega}{\partial \mu^3} + (2 - \nu) \dfrac{\partial^3 G_\Omega}{\partial \xi^2 \partial \mu}\right) = 0 & \mathbf{r} \in \partial\Omega, \quad (6.3) \end{cases}$$

where the bending stiffness or flexural rigidity of the plate assumes the form

$$D = \frac{Eh^3}{12(1-\nu^2)}, \tag{6.4}$$

in which E is the equivalent Young's modulus of the plate, ν is Poisson's ratio and h is the thickness of the plate. Structural losses are included in the Young's modulus by writing

$$E = E_0(1 - j\eta), \tag{6.5}$$

where η is the structural damping ratio.

6.2.2 Solution by the image source method (ISM)

The set of Eqs. (6.1) and (6.2,6.3) can be solved by using the image source method (ISM). The latter consists in satisfying the boundary conditions by appropriately placing virtual sources outside the boundaries $\partial\Omega$, obtained as the images of the original source by successive symmetries with respect to the boundaries. The image sources contributions represent the successive reflected waves by the boundaries, starting from the original source excitation.

Fig. 6.2 shows the original source and first 8 image sources for the plate of Fig. 6.1 and their corresponding validity zones, which are the zones of the plate from which the sources are "visible".

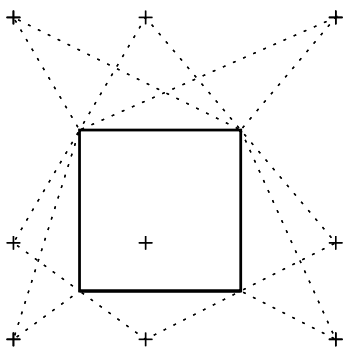

Figure 6.2: Original source and first 8 image sources of the plate. + Sources, ····· validity zones.

The Green's function of plate Ω is then modelled as the superposition of the excitations from the original source plus N image sources, which can be written as

$$\tilde{G}_\Omega(\mathbf{r}, \mathbf{r}_0; k_f) = G_\infty(\mathbf{r}, \mathbf{r}_0; k_f) + \sum_{s=1}^{N} G_s(\mathbf{r}, \mathbf{r}_s; k_f), \tag{6.6}$$

where

$$G_\infty(\mathbf{r}, \mathbf{r}_0; k_f) = \frac{j}{8k_f^2 D}\left(H_0^{(1)}(k_f|\mathbf{r} - \mathbf{r}_0|) - H_0^{(1)}(jk_f|\mathbf{r} - \mathbf{r}_0|)\right) \tag{6.7}$$

is the displacement field created by the original source, described by the Green's function of the associated infinite plate [99] and G_s is the excitation of image source s. For practical reasons, the number N of image sources for obtaining the response of the plate is finite.

6.2.2.1 Image sources of first order

The image sources excitations are then obtained from the classical reflection laws of plane waves, by first considering the original source contribution as a sum of plane waves. In this manner, the Green's function of the infinite plate can be written as

$$G_\infty(\xi,\mu,\xi_0,\mu_0;k_f) = \frac{j}{8\pi k_f^2 D}\int_{-\infty}^{+\infty} e^{jk_\xi(\xi-\xi_0)}\left(\frac{e^{j\sqrt{k_f^2-k_\xi^2}|\mu-\mu_0|}}{\sqrt{k_f^2-k_\xi^2}} + j\frac{e^{-\sqrt{k_f^2+k_\xi^2}|\mu-\mu_0|}}{\sqrt{k_f^2+k_\xi^2}}\right)dk_\xi. \quad (6.8)$$

The integrand of Eq. (6.8) consists of a propagating plane wave and an evanescent plane wave, which are the first incident waves on the plate boundaries. Thus, the original source, located at $\mathbf{r}_0$, generates an image source at point $\mathbf{r}_s = (\xi_s, \mu_s)$ from each boundary. Since the edges are of finite length, the displacement field created by each source is valid in a certain zone of the plate, described by the function

$$V(\mathbf{r},\mathbf{r}_s) = \begin{cases} 1 & \text{in the validity zone,} \\ 0 & \text{elsewhere.} \end{cases} \quad (6.9)$$

It can be shown [19] that the contribution of each image source of first order assumes the form

$$G_s^{(\mathrm{I})}(\mathbf{r},\mathbf{r}_s;k_f) = V(\mathbf{r},\mathbf{r}_s)\frac{j}{8\pi k_f^2 D}\int_{-\infty}^{+\infty} e^{jk_\xi(\xi-\xi_s)}\left[e^{j\sqrt{k_f^2-k_\xi^2}(\mu-\mu_b)} \quad e^{-\sqrt{k_f^2+k_\xi^2}(\mu-\mu_b)}\right] \begin{bmatrix} R_{pp}(k_\xi,k_f) & R_{ep}(k_\xi,k_f) \\ R_{pe}(k_\xi,k_f) & R_{ee}(k_\xi,k_f) \end{bmatrix} \begin{bmatrix} \dfrac{e^{j\sqrt{k_f^2-k_\xi^2}(\mu_b-\mu_s)}}{\sqrt{k_f^2-k_\xi^2}} \\ j\dfrac{e^{-\sqrt{k_f^2+k_\xi^2}(\mu_b-\mu_s)}}{\sqrt{k_f^2+k_\xi^2}} \end{bmatrix} dk_\xi, \quad (6.10)$$

where the terms $R_{pp}(k_\xi,k_f)$, $R_{ep}(k_\xi,k_f)$, $R_{pe}(k_\xi,k_f)$ and $R_{ee}(k_\xi,k_f)$ are the different components of the reflection matrix of the boundary, for incident and reflected propagating (p) and evanescent (e) plane waves, obtained from the boundary condition

set of free edges as in Eqs. (6.2) and (6.3) as [34]

$$\begin{bmatrix} \dfrac{ad-bc}{ad+bc} & \dfrac{-2ac}{ad+bc} \\ \dfrac{-2bd}{ad+bc} & -\dfrac{ad-bc}{ad+bc} \end{bmatrix}, \tag{6.11}$$

where

$$\begin{cases} a = \left(k_f^2 + (1-\nu)k_\xi^2\right), \\ b = \left(-k_f^2 + (1-\nu)k_\xi^2\right), \\ c = -\sqrt{k_f^2 + k_\xi^2}\left(k_f^2 - (1-\nu)k_\xi^2\right), \\ d = j\sqrt{k_f^2 - k_\xi^2}\left(k_f^2 + (1-\nu)k_\xi^2\right). \end{cases} \tag{6.12}$$

The integrand of Eq. (6.10) includes two terms, which represent propagating and evanescent plane waves, in the same manner than in Eq. (6.8). The term with the spatial dependence $e^{j\sqrt{k_f^2-k_\xi^2}(\mu-\mu_b)}$ represents propagating waves for $|k_\xi| < |k_f|$ and evanescent waves for $|k_\xi| > |k_f|$. The term with the spatial dependence $e^{-\sqrt{k_f^2+k_\xi^2}(\mu-\mu_b)}$ represents evanescent waves for all values of k_ξ.

6.2.2.2 Image sources of second and higher orders

After the first reflection, the influence of evanescent waves is low compared to propagating waves. The image sources associated to the second and the next reflections on each edge are thus obtained from the propagating component of first order image sources. Thus, the terms R_{ep}, R_{pe} and R_{ee} of the reflection matrices of the edges are disregarded and only the values $|k_\xi| < |k_f|$ are considered in the integral, such that the contributions from image sources of second and higher orders may be approximated as

$$\tilde{G}_s^{(\mathrm{II})}(\mathbf{r}, \mathbf{r}_s; k_f) = V(\mathbf{r}, \mathbf{r}_s)\frac{j}{8\pi k_f^2 D}\int_{-|k_f|}^{|k_f|} e^{jk_\xi(\xi-\xi_s)} A_{pp}^{(s)}(k_\xi, k_f)\frac{e^{j\sqrt{k_f^2-k_\xi^2}(\mu-\mu_s)}}{\sqrt{k_f^2-k_\xi^2}}dk_\xi, \tag{6.13}$$

where $A_{pp}^{(s)}$ is the amplitude function of the elementary plane propagating waves leading to image source s and is given by the cumulative product of the reflection coefficients of propagating waves, as

$$A_{pp}^{(s)}(\theta) = \prod_{n=1}^{N(s)} R_n^{(s)}(\theta, \alpha_n), \tag{6.14}$$

where $n = 1, \ldots, N(s)$ denotes the number of reflections in the construction of a given image source s and α_n is the orientation of edge n with respect to the global coordinate system (x, y), and θ is defined as the angle between the ξ axis and the direction of propagation of the plane wave, such that the relation between the axial wavenumber k_ξ and the flexural wavenumber k_f can be written as

$$k_\xi = |k_f|\cos(\theta). \tag{6.15}$$

The harmonic response of the plate is then given by Eq. (6.6). Furthermore, the integrals in Eqs. (6.10) and (6.13) are numerically implemented using fast Fourier transform.

6.3 Experimental setup

The aim of this section is to describe the experimental setup and the calibration of the measurement system.

6.3.1 Description of the experimental setup

The measurements are performed on a flat 50 cm × 50 cm sample of car floor, which is composed of 3 mm of steel and 2 mm of the damping material under test, provided by the company Henkel Adhesive Technologies. Fig. 6.3 shows the plate covered with the damping material as well as the excitation system used for the measurements.

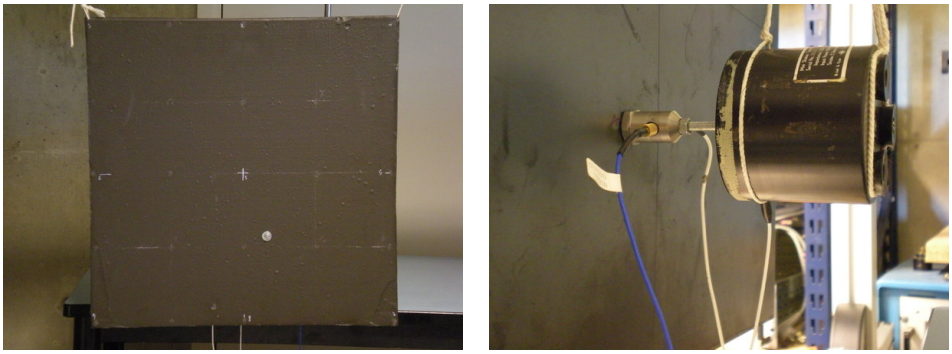

(a) (b)

Figure 6.3: Photography of the damped panel under test. (a) Front view, (b) rear view.

The plate is excited with a Brüel & Kjær type 4810 shaker and the driving point mobility is measured by means of a Brüel & Kjær type 8001 impedance head and NEXUS conditioning amplifier. The shaker excites the plate perpendicularly to its surface with a white noise. The data acquisition is performed within a rectangular window function of 12800 time samples at a sampling frequency of 32 kHz, which gives 6400 frequency points from 0 Hz to 16 kHz for the analysis. The measurements are averaged over 100 runs.

6.3.2 Calibration of the measurement system

In order to calibrate the measurement system, two known calibration masses, m_1 and m_2, are consecutively attached to the impedance head and the apparent mass is measured. At low frequencies, the measured apparent masses $\tilde{M}_1$ and $\tilde{M}_2$, given by the ratio of force to acceleration, are linked to masses m_1 and m_2 by

$$\begin{cases} \alpha\tilde{M}_1 = m_1 + m_z, \\ \alpha\tilde{M}_2 = m_2 + m_z, \end{cases} \tag{6.16}$$

where m_z is the mass of the mobile part of the measurement system, i.e. impedance head and coupling bar of the shaker, and α is the mass correction factor. Fig. 6.4 shows the measured driving point mobility after correction by factor α and the coherence function. The lower values of the coherence function are due to individual resonance peaks in the low frequency range.

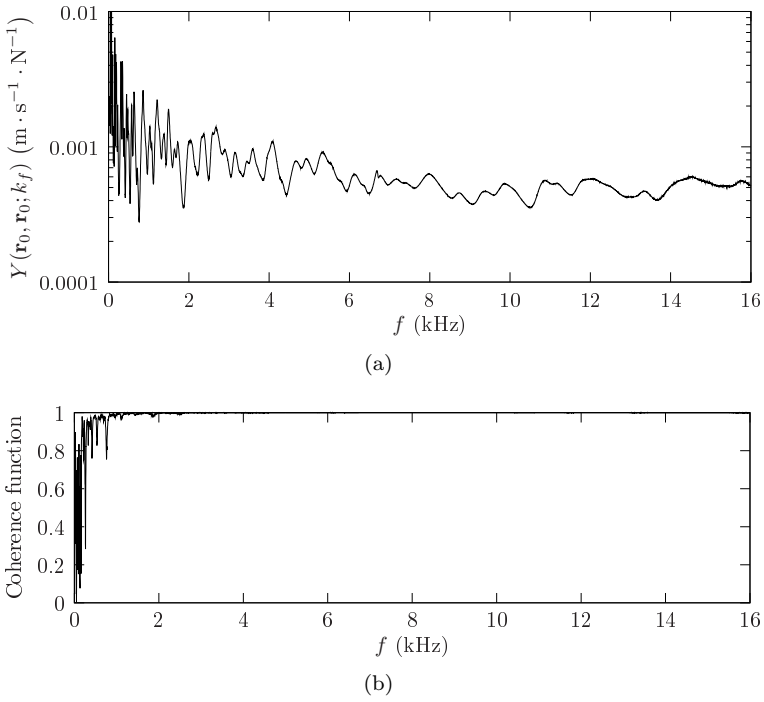

Figure 6.4: Measured driving point mobility of the plate. (a) Modulus, (b) coherence function.

6.4 Estimation of the bending stiffness of the panel

As detailed in sec. 6.2, the response of the plate is the superposition of the displacement fields due to the source and its image sources. According to Skudrzyk [90], the mean line of the frequency response corresponds to the contribution of the original source and is essentially governed by the Young's modulus. Furthermore, the variations of the response around the mean line are due to constructive and destructive interferences between waves reflecting on the edges, which can be represented as image sources. The level of such interferences depends on structural damping. If damping is high, waves in the plate are attenuated after a few reflections on the boundaries and the deviation of the response from the mean line is low. Inversely, if damping is low, the deviation from the mean line is significant.

The estimation of the Young's modulus and the structural damping ratio of the plate is performed in two steps. First, the mean value of the measured driving point mobility

is computed in each 1/3-octave band and compared to the driving point mobility of an infinite plate, which yields the modulus of the bending stiffness in each frequency band. Then, the driving point mobility is simulated by the image source method with various pairs of values for the Young's modulus and the structural damping ratio. The standard deviation for each 1/3-octave band is computed for both simulated and experimental frequency responses. The best fit of the standard deviation then yields the estimated Young's modulus and structural damping ratio per 1/3-octave band.

6.4.1 Modulus of the bending stiffness

The displacement field at the input point of an infinite plate is given by the asymptotic limit of the Green's function as the observation point approaches the input point, as [99]

$$\lim_{\mathbf{r}\to\mathbf{r}_0} G_\infty(\mathbf{r},\mathbf{r}_0;k_f) = \frac{j}{8k_f^2 D}. \tag{6.17}$$

Such displacement field is due to a unitary harmonic force at circular frequency ω. Thus, the modulus of the driving point mobility is given by

$$|Y(\mathbf{r}_0,\mathbf{r}_0;k_f)| = |j\omega \lim_{\mathbf{r}\to\mathbf{r}_0} G_\infty(\mathbf{r},\mathbf{r}_0;k_f)| = \frac{1}{8\sqrt{\rho h}|D^{1/2}|}, \tag{6.18}$$

in which the only unknown is the bending stiffness, D, defined in Eq. (6.4). For an isotropic metallic plate, the Young's modulus E_0 and the structural damping ratio η are independent of frequency, which yields a constant driving point mobility. In the case of a bi-layered plate, these parameters may depend on frequency. The bending stiffness is thus estimated from the mean value of the modulus of the driving point mobility for each 1/3-octave band. Fig. 6.5 shows the bending stiffness estimated using Eq. (6.18).

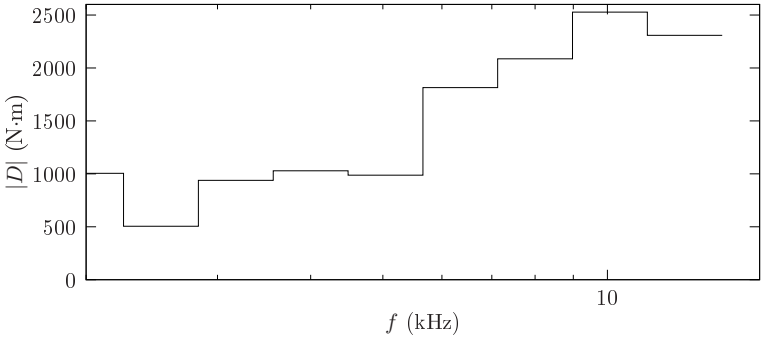

Figure 6.5: Modulus of the flexural rigidity per 1/3-octave band.

The Young's modulus can be computed from the modulus of the bending stiffness as a function of the structural damping ratio, which is unknown at this point, as

$$E_0 = \frac{|D|12\left(1-\nu^2\right)}{h^3\sqrt{1+\eta^2}}. \tag{6.19}$$

Fig. 6.6 shows the estimated Young's modulus per 1/3-octave band. The error bars represent the variability for a structural damping ratio from $\eta = 0.01$ to $\eta = 0.2$.

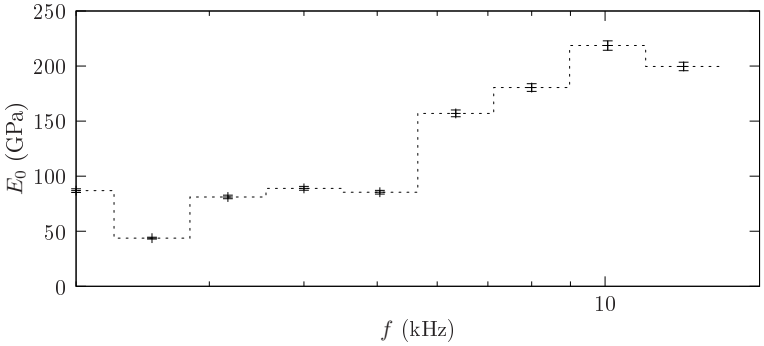

Figure 6.6: Estimated Young's modulus per octave band. The error bars represent the variability of the Young's modulus taking into account structural damping from $\eta = 0.01$ to $\eta = 0.2$.

6.4.2 Young's modulus and structural damping ratio

In order to estimate the Young's modulus E_0 and the structural damping ratio η of the plate, the modulus of the bending stiffness $|D|$ obtained above is used as an input parameter in the image source method. Various possible pairs of values (E_0, η) yielding the estimated values of $|D|$ for each 1/3-octave band are used. The different runs of the simulation are controlled by the structural damping ratio, from $\eta = 0.01$ to $\eta = 0.2$, which provide the driving point mobilities shown in Fig. 6.7.

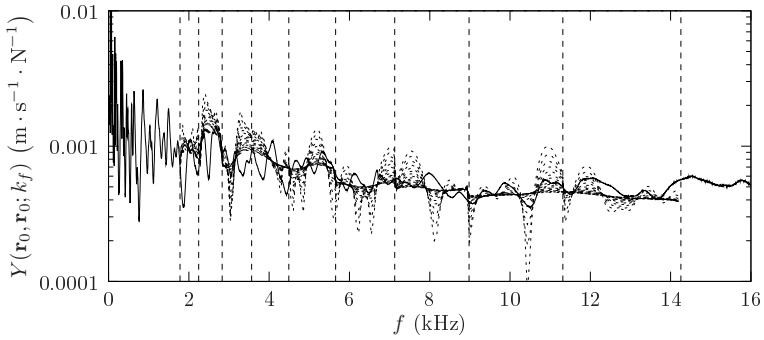

Figure 6.7: Experimental and simulated driving point mobilities with estimated Young's moduli for each 1/3-octave band. ———, experimental; · · · · · · , ISM for a damping ratio from $\eta = 0.01$ to $\eta = 0.2$; - - - - -, 1/3-octave-band limits.

The standard deviation of the driving point mobility for each 1/3-octave band is used as the criterion for comparison between simulated and experimental mobilities and is

given by

$$\sigma_i = \sqrt{\frac{1}{N_f - 1} \sum_{j=1}^{N_f} \left(Y_{ij} - Y_i^{(\text{mean})} \right)^2}, \tag{6.20}$$

where N_f is the number of frequency points in 1/3-octave band i.

Fig. 6.8 shows the difference between standard deviations of experimental and simulated driving point mobilities for each 1/3-octave band. The minimum for each curve corresponds to the (E_0, η) pair providing the best fit of ISM on experimental data, which is followed by a dotted line.

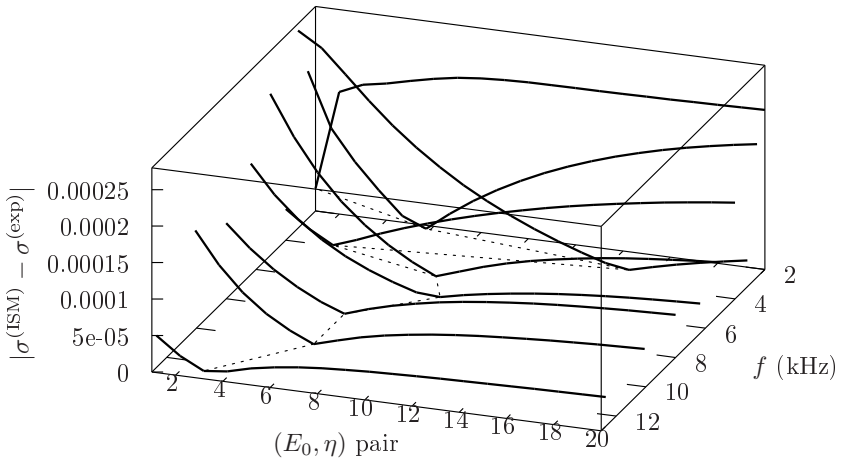

Figure 6.8: Search of optimum values of E_0 and η. ———, difference between standard deviations of experimental and simulated driving point mobilities for each 1/3-octave band; · · · · · ·, curve of minima across 1/3-octave bands.

Finally, the estimated Young's modulus and structural damping ratio are obtained in each 1/3-octave band, as shown in Fig. 6.9. The values of E_0 and η that are obtained represent equivalent parameters of the steel plate covered with the viscoelastic material.

6.5 Conclusion

This paper investigates the capability of the image source method (ISM) for estimating the Young's modulus and structural damping ratio of highly damped panels from measured data. ISM consists in modelling the response of a point driven polygonal domain as the superposition of the responses to the source and its image sources, which describe wave reflection at the boundaries. A remarkable particularity of ISM is that the contribution of the original source gives the mean line of the response and image sources describe the peaks and valleys corresponding to interferences due to successive reflections. Moreover, in the model, the geometry of the domain, the boundary conditions and the material properties are independent from each other. Through an example of application in the case of a car floor panel, it has been shown that the modulus of

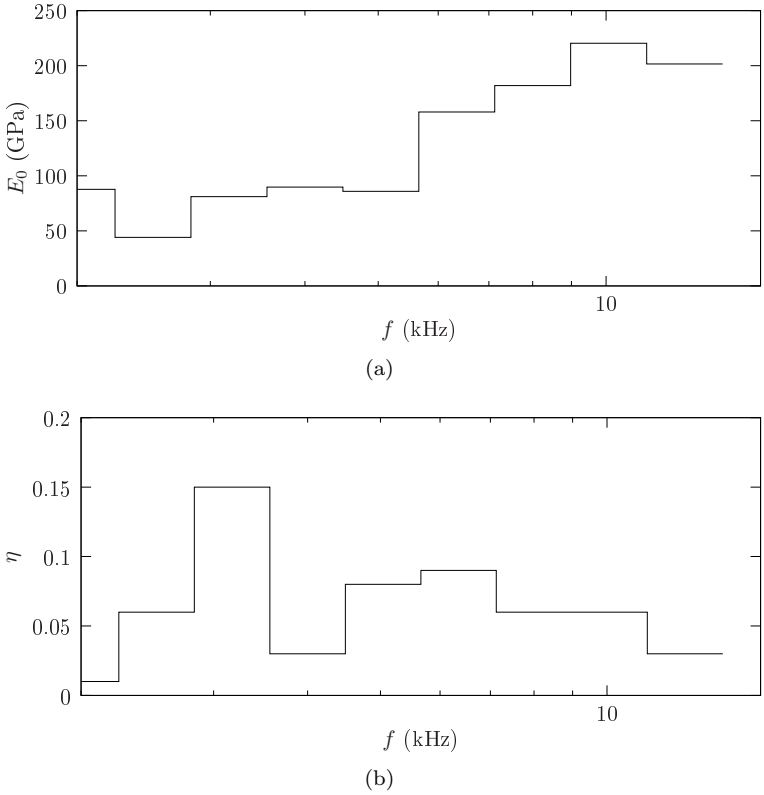

Figure 6.9: Estimated (a) Young's modulus and (b) damping ratio per 1/3-octave band.

the bending stiffness can be obtained from the contribution of the original source, i.e. the input mobility of an infinite plate. Furthermore, the Young's modulus and damping ratio arise as the optimal values giving the closest deviation of the response from its mean line. The values obtained by the proposed method are to be considered with precaution since they represent mechanical parameters of an equivalent isotropic plate. Also, a frequency-dependent calibration of the measurement system, as proposed by Arcas [3], can be considered as a means of refining the estimation. The main advantage of the present method is that a single measurement of the driving point mobility of a free plate is needed, whereas, in the well-known Oberst technique, specific boundary conditions are compulsory.

Part II

Vibration damping in beams and plates using the acoustic black hole effect

Chapter 7

Acoustic black hole effect in thin plates

The investigation presented in this chapter was done in the framework of a collaboration between LAUM and the Acoustics and Vibration Research Group of the Department of Aeronautical and Automotive Engineering of Loughborough University, UK. The numerical model presented in sec. 7.3 is part of an article submitted to the Journal of the Acoustical Society of America [31] in July 2009 and was developed in collaboration with the post-doctoral work of Vasil Georgiev at LAUM. The experimental results of sec. 7.4 were presented at a conference [28]. Experimental and numerical studies were also presented at a conference [30] and in the Master's internship report of Miguel Molerón [74], who contributed to the experimental work.

Abstract

It is well known that a flexural wave travelling in a thin plate or beam slows down in a zone of gradually decreasing thickness. If the thickness decreases sufficiently smoothly to zero, the wave slows down without being reflected back. Such principle has been used as a basis of the so-called "acoustic black hole effect", in the framework of geometrical acoustics. In practice, a thickness profile smoothly decreasing to zero is impossible to achieve and there always exists a truncation of the profile, which leads to non-zero reflection. The effect of the truncation can be compensated by the addition of a thin damping layer near the truncated edge. One of the most important aspects of such novel damping method is that it provides efficient reduction of vibration level at higher frequencies without added mass to the structure. This chapter presents numerical and experimental investigations on the black hole effect. A numerical model is developed, which allows to simulate the complete wave field with arbitrarily varying parameters. Thus, a parametric study is carried out for defining optimal values of the geometrical and mechanical parameters of the damping layer. A two-dimensional black hole thickness profile is designed, as a circular pit of power-law thickness, for including it at arbitrary locations in different plates whose boundaries induce a focusing of waves towards a zone treated with the decreasing-thickness profile. Experimental investigations are then done on plates whose boundaries induce a focusing of waves towards the black hole pit,

i.e. elliptical plates and polygonal plates with a parabolic boundary. The possibility of modelling a polygonal plate with a 'black hole boundary' by the image source method is also investigated.

7.1 Introduction

One major concern of the automotive, aeronautical and aerospace industries today is the reduction of mass in the structures to be designed. In the framework of vibration damping and sound absorption, the most commonly used techniques involve significant amounts of added mass, in the form of viscoelastic layers (see the example of chap. 6) or acoustic foams. Other approaches for vibration damping exist. In particular, the damping technique that is relevant for the present purposes consists on a gradual variation of mechanical properties with distance. In such manner, waves travelling in a continuously varying medium can progressively slow down and undergo weak reflection at the structure boundary (see for example the work of Vemula et al. [96]). Such structures can be directly included as part of the main structure to be damped in its design process, thus adding low amounts of mass, or no mass at all. Such is the principle of the acoustic black hole for the flexural vibrations of beams and plates, where the gradual variation of mechanical properties is obtained by a variation of thickness with distance or, as presented in chap. 8, by a variation of the Young's modulus with distance.

In the following, existing analytical models of the acoustic black hole effect are first summarised and adapted to the present study. Then a numerical tool capable of including arbitrarily varying mechanical parameters is developed and applied to the optimisation of the parameters of the structure. Experimental investigations follow on elliptical and polygonal plates. A model of the vibrations of a polygonal plate with an acoustic black hole structure is considered by using the image source method, presented in part I. The models and the experiments are confronted and the relevance of the application of the acoustic black hole to polygonal plates is discussed.

7.2 Existing models

7.2.1 Model of Mironov

Mironov [73] was the first to establish the theory of the acoustic black hole effect. He showed that a flexural wave can propagate towards a sharpened end of a plate without reflecting back. In fact, the phase and group velocities decrease if the thickness of the plate decreases. Thus, if the thickness varies smoothly to zero, the wave slows down and stops without being reflected.

The condition of sufficient smoothness consists in that the variation of the flexural wave with thickness must be small over a distance comparable to the wavelength. Such condition is fulfilled by a power-law thickness h in the form

$$h(x) = \varepsilon x^n, \tag{7.1}$$

where $n \geq 2$, as illustrated in Fig. 7.1.

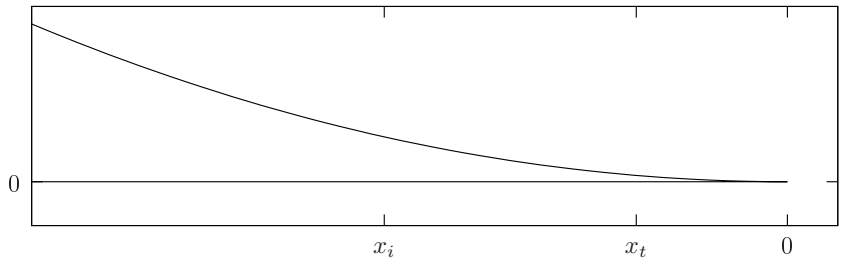

Figure 7.1: Power-law thickness profile.

Inserting such thickness profile in the expressions of the phase and group velocities c_ϕ and c_γ, defined in Eqs. (1.18) and (1.19), yields

$$c_\varphi(x) = \left(\frac{E\omega^2}{12\rho\,(1-\nu^2)}\right)^{1/4} \sqrt{h(x)} = \left(\frac{E\omega^2}{12\rho\,(1-\nu^2)}\right)^{1/4} \sqrt{\varepsilon} x^{n/2}, \tag{7.2}$$

$$c_\gamma(x) = 2\left(\frac{E\omega^2}{12\rho\,(1-\nu^2)}\right)^{1/4} \sqrt{h(x)} = 2\left(\frac{E\omega^2}{12\rho\,(1-\nu^2)}\right)^{1/4} \sqrt{\varepsilon} x^{n/2}. \tag{7.3}$$

It can easily be observed that the phase and group velocities tend to zero if x tends to zero. Furthermore, the travel time of a wave packet from a coordinate x_i to a coordinate x_t is

$$T = \int_{x_i}^{x_t} \frac{dx}{c_\gamma(x)}. \tag{7.4}$$

For example, for $n = 2$ and $n = 4$, the travel times are, respectively,

$$T_{n=2} = \frac{1}{2\sqrt{\varepsilon}} \left(\frac{12\rho\,(1-\nu^2)}{E\omega^2}\right)^{1/4} \ln\left|\frac{x_t}{x_i}\right| \tag{7.5}$$

and

$$T_{n=4} = \frac{1}{2\sqrt{\varepsilon}} \left(\frac{12\rho\,(1-\nu^2)}{E\omega^2}\right)^{1/4} \left(\frac{1}{x_i} - \frac{1}{x_t}\right), \tag{7.6}$$

which both tend to infinity if the final coordinate x_t tends to zero. In that case, flexural waves never reach the end of the profile.

Moreover, structural damping is taken into account in the Young's modulus, as defined in Eq. (1.20),

$$E = E_0(1 - j\eta).$$

In the framework of geometrical acoustics, the path length of a wave travelling from x_i to x_t and back to x_i is obtained from the flexural wavenumber $k_f(x)$ as

$$2\int_{x_i}^{x_t} k_f(x)dx = 2\left(\omega^2 \frac{\rho 12(1-\nu^2)}{E_0}\right)^{1/4} \frac{1+j\eta}{1+\eta^2} \int_{x_i}^{x_t} \frac{dx}{\sqrt{h(x)}}. \tag{7.7}$$

The reflection coefficient is thus given by

$$R = \exp\left(-\mathrm{Im}\left\{2\int_{x_i}^{x_t} k_f(x)dx\right\}\right). \tag{7.8}$$

For power-law profiles with $n = 2$ and $n = 4$, the corresponding expressions of the reflection coefficient are respectively

$$R = \exp\left(-2\left(\omega^2\frac{\rho 12(1-\nu^2)}{E_0}\right)^{1/4}\frac{\eta}{1+\eta^2}\frac{1}{\sqrt{\varepsilon}}\ln\left(\frac{x_t}{x_i}\right)\right) \tag{7.9}$$

and

$$R = \exp\left(-2\left(\omega^2\frac{\rho 12(1-\nu^2)}{E_0}\right)^{1/4}\frac{\eta}{1+\eta^2}\frac{1}{\sqrt{\varepsilon}}\left(\frac{1}{x_i}-\frac{1}{x_t}\right)\right), \tag{7.10}$$

which tend to zero if x_t tends to zero, showing that any non-zero amount of structural damping entirely absorbs the wave.

However, the practical realisation of such power-law profile is impossible in that a residual truncation thickness always exists at a non-zero abscissa x_t. Mironov showed that, even if the thickness of the plate varies by three orders of magnitude and the structural damping ratio is high, the reflection coefficient is high enough to render this application unattractive.

7.2.2 Model of Krylov

In order to compensate for the truncation of the black-hole thickness profile, Krylov et al. [51, 52, 54–56] proposed to combine a wedge of power-law thickness profile with a damping layer covering the wedge surface in the case of a beam, as illustrated in Fig. 7.2.

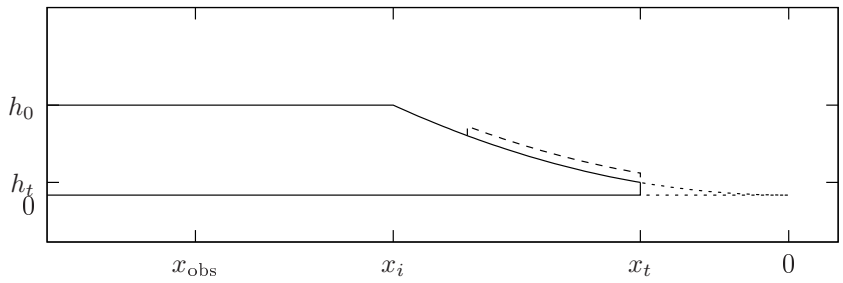

Figure 7.2: Side view of a beam with acoustic black hole profile and damping layer. ——, real profile; - - - - - -, damping layer of length l and thickness h_l; · · · · · · , ideal black hole profile. Abscissas x_i and x_t represent the beginning and the truncation of the profile.

In such model, only the attenuation mechanism associated with in-plane deformation of the damping layer is taken into account. Assuming that the thickness of the damping layer is much smaller than the thickness of the beam, the additional loss factor due to

the damping layer [87] can be written in the simplified form

$$\zeta(x) = 3\frac{h_l}{h(x)}\frac{E_l}{E_0}\eta_l, \tag{7.11}$$

where h_l, E_l and η_l are respectively the thickness, the Young's modulus and the loss factor of the damping layer. As in the original model of Mironov, the reflection coefficient is obtained from the imaginary part of the flexural wavenumber, which here assumes the form

$$\mathrm{Im}\left\{k_f(x)\right\} = \frac{1}{4}\left(\frac{12\rho}{E_0}\right)^{1/4}\sqrt{\frac{\omega}{h(x)}}\big(\eta + \zeta(x)\big), \tag{7.12}$$

where ρ and η are respectively the density and structural damping ratio of the beam material. Assuming the beam thickness in the form $h(x) = \varepsilon x^2$, the reflection coefficient of Eq. (7.8) assumes the form

$$R = e^{-2(\kappa_b + \kappa_l)}, \tag{7.13}$$

where

$$\kappa_b = \left(\frac{12\rho}{E_0}\right)^{1/4}\frac{\omega^{1/2}\eta}{4\varepsilon^{1/2}}\ln\left(\frac{x_t}{x_i}\right) \tag{7.14}$$

and

$$\kappa_l = \left(\frac{12\rho}{E_0}\right)^{1/4}\frac{3\omega^{1/2}\eta_l h_l}{8\varepsilon^{3/2}}\frac{E_l}{E_0}\left(\frac{1}{x_t^2} - \frac{1}{x_i^2}\right). \tag{7.15}$$

It can be verified that in the absence of damping layer ($\kappa_l = 0$), Eq. (7.13) is identical to Eq. (7.8) for a beam. The strong feature of this approach is that the reflection coefficient given by Eq. (7.13) can reach significantly low values, even in the case of a truncated profile.

The validity of Eqs. (7.11) to (7.15) is subjected to the condition that the damping layer is significantly thinner than the beam, even at the truncation, which is difficult to achieve in practice. Therefore, Krylov [54] proposed to take into account an arbitrary thickness h_l in the model. Assuming that $E_l/E_0 \ll 1$ (the Young's modulus of the beam is much greater than that of the damping layer) and that $\eta_l \ll 1$ and $\eta \ll 1$ (the loss factors of the beam and the layer are small), the imaginary part of the flexural wavenumber is

$$\mathrm{Im}\left\{k_f(x)\right\} = \frac{\left(\frac{12\rho}{E_0}\right)^{1/4}\omega^{1/2}\left(1 + \frac{\rho_l}{\rho}\frac{h_l}{h(x)}\right)^{1/4}\left(\eta + \eta_l\frac{E_l}{E_0}\left(3\frac{h_l}{h(x)} + 6\left(\frac{h_l}{h(x)}\right)^2 + 4\left(\frac{h_l}{h(x)}\right)^3\right)\right)}{4h^{1/2}(x)\left(1 + \frac{E_l}{E_0}\left(3\frac{h_l}{h(x)} + 6\left(\frac{h_l}{h(x)}\right)^2 + 4\left(\frac{h_l}{h(x)}\right)^3\right)\right)^{5/4}}. \tag{7.16}$$

The corresponding reflection coefficient, obtained by numerically integrating Eq. (7.8), can reach values close to zero with realistic parameters [54]. Another primary result

is that the reflection coefficient tends to zero with the increase of frequency. (see in particular Figs. 4 and 5 of Ref. [55]).

7.2.3 Discussion

The main limitation of the geometrical acoustics approach is that it only takes into account the propagating waves in the beam and the effect of evanescent waves is ignored. There is thus a need of a model taking into account the complete vibrational field of the structure. Furthermore, it is necessary to have a model capable to take into account arbitrary variations of the different parameters of the black hole beam in order to assess their role. Also, complexifying elements may be included, such as a temperature gradient, as described in chap. 8. The solution that has been adopted here is that of a numerical tool with adaptive discretisation steps, as described in what follows.

7.3 Model of the acoustic black hole effect using the state vector approach

In order to use the acoustic black hole effect in a practical configuration, a power-law thickness profile is considered near the edge of a beam, as depicted in Fig. 7.2. An ideal black hole profile, as studied by Mironov [73], would consist of a thickness profile smoothly decreasing to zero from $x = x_i$ to $x = 0$. As pointed out above, this is not possible and a truncation exists at a distance $x = x_t$. The resulting profile may be treated with a thin damping layer of length l and thickness h_l to overcome the effect of the truncation, as proposed by Krylov et al. [54–56]. The aim of the following is to model the flexural vibrations of such a beam, observed at point x_{obs}, including the complete wave field of the structure and arbitrary variations of the different parameters with distance.

7.3.1 Flexural vibrations of a variable-thickness beam covered with a damping layer

7.3.1.1 Riccati equation for the impedance matrix of the beam

The equations of flexural motion of a vibrating beam in a harmonic regime according to the time dependence[1] $e^{j\omega t}$, considering Euler-Bernoulli hypotheses [40], can be written in the form of a state equation as discussed in chap. 3 in the case of a plate, as

$$\frac{\partial \mathbf{W}}{\partial x} = \mathbf{H}\mathbf{W}, \tag{7.17}$$

[1] The conventions taken here for the time dependence, the order of the variables in the state vector and the order of the eigenvalues are arbitrary and are different from those taken in part I. This choice is made in order to retain coherence with the presented model [31].

where

$$\mathbf{W}(x) = \begin{bmatrix} w(x) \\ \theta(x) \\ V(x) \\ M(x) \end{bmatrix} \tag{7.18}$$

is the state vector, with w the flexural displacement, θ the slope, V the total shear force and M the bending moment. Matrix $\mathbf{H}$ is in this case given by

$$\mathbf{H} = \begin{bmatrix} 0 & 1 & 0 & 0 \\ 0 & 0 & 0 & 1/EI(x) \\ -\rho bh(x)\omega^2 & 0 & 0 & 0 \\ 0 & 0 & -1 & 0 \end{bmatrix} = \begin{bmatrix} \mathbf{H}_1 & \mathbf{H}_2 \\ \mathbf{H}_3 & \mathbf{H}_4 \end{bmatrix}, \tag{7.19}$$

where ω is the circular frequency, b and $h(x)$ are respectively the width and the thickness of the beam, ρ is the density, E is the Young's modulus of the beam and $I(x) = bh^3(x)/12$ is the second moment of area of the cross section of the beam. The relation between the kinematic and force variables at any point x of the beam is given by

$$\begin{bmatrix} V(x) \\ M(x) \end{bmatrix} = j\omega \mathbf{Z}(x) \begin{bmatrix} w(x) \\ \theta(x) \end{bmatrix}, \tag{7.20}$$

where

$$\mathbf{Z} = \begin{bmatrix} Z_1 & Z_2 \\ Z_3 & Z_4 \end{bmatrix} \tag{7.21}$$

is the impedance matrix of the beam, which depends on abscissa x. Substituting Eq. (7.20) in Eq. (7.17) yields the non-linear Riccati equation

$$\frac{\partial \mathbf{Z}}{\partial x} = -\mathbf{Z}\mathbf{H}_1 - j\omega \mathbf{Z}\mathbf{H}_2\mathbf{Z} + \frac{\mathbf{H}_3}{j\omega} + \mathbf{H}_4\mathbf{Z}. \tag{7.22}$$

The resolution of the Riccati equation is detailed hereafter.

7.3.1.2 Reflection matrix of the edge

In order to derive the reflection matrix of the edge of the beam, wave variables must be used instead of state variables. Using the formalism developed in sec. 3.1.3 and letting

$$\mathbf{H} = j\mathbf{N}, \tag{7.23}$$

the state vector can be written as

$$\mathbf{W} = \mathbf{E}\mathbf{V}, \tag{7.24}$$

where $\mathbf{V}$ is the wave vector and $\mathbf{E}$ is the matrix of eigenvectors of $\mathbf{N}$, linked to the corresponding matrix of eigenvalues $\mathbf{\Lambda}$ by the relation

$$\mathbf{N}\mathbf{E} = \mathbf{\Lambda}\mathbf{E}, \tag{7.25}$$

where

$$\mathbf{\Lambda} = \begin{bmatrix} -k_f & 0 & 0 & 0 \\ 0 & jk_f & 0 & 0 \\ 0 & 0 & k_f & 0 \\ 0 & 0 & 0 & -jk_f \end{bmatrix} \tag{7.26}$$

and

$$\mathbf{E} = \begin{bmatrix} j\alpha & \alpha & -j\alpha & -\alpha \\ \beta & -\beta & \beta & -\beta \\ \gamma & \gamma & \gamma & \gamma \\ -j\delta & \delta & j\delta & -\delta \end{bmatrix} = \begin{bmatrix} \mathbf{E}_1 & \mathbf{E}_2 \\ \mathbf{E}_3 & \mathbf{E}_4 \end{bmatrix}, \tag{7.27}$$

with

$$\alpha = \sqrt{\frac{k_f(x)}{\rho bh(x)\omega^3}}, \quad \beta = \sqrt{\frac{k_f(x)^3}{\rho bh(x)\omega^3}}, \quad \gamma = \sqrt{\frac{\rho bh(x)\omega}{k_f(x)}}, \quad \delta = \sqrt{\frac{\rho bh(x)\omega}{k_f^3(x)}}, \tag{7.28}$$

in which $k_f(x)$ is the flexural wavenumber. The wave vector can be written as

$$\mathbf{V} = \begin{bmatrix} \mathbf{V}_+ \\ \mathbf{V}_- \end{bmatrix}, \tag{7.29}$$

where $\mathbf{V}_+$ and $\mathbf{V}_-$ represent forward and backward travelling waves, which are linked together by the reflection matrix of the edge as

$$\mathbf{V}_- = \mathbf{R}\mathbf{V}_+. \tag{7.30}$$

Here, $\mathbf{R}$ is the reflection matrix of the whole region of the beam located between the observation point x and the end of the profile. Substituting Eqs. (7.20) and (7.30) in Eq. (7.24) yields the reflection matrix of the edge in the form

$$\mathbf{R}(x) = -\left(j\omega\mathbf{Z}(x)\mathbf{E}_2 - \mathbf{E}_4\right)^{-1}\left(j\omega\mathbf{Z}(x)\mathbf{E}_1 - \mathbf{E}_3\right), \tag{7.31}$$

which can be written as

$$\mathbf{R}(x) = \begin{bmatrix} R_{pp} & R_{ep} \\ R_{pe} & R_{ee} \end{bmatrix}, \tag{7.32}$$

where each term of the form R_{ir} is the reflection coefficient for incident wave i to reflected wave r, where i and r denote either propagating (p) or evanescent (e) waves. Similarly, the impedance $\mathbf{Z}$ can be specified in the form

$$\mathbf{Z}(x) = \frac{1}{j\omega}\left(\mathbf{E}_3 + \mathbf{E}_4\mathbf{R}(x)\right)\left(\mathbf{E}_1 + \mathbf{E}_2\mathbf{R}(x)\right)^{-1}. \tag{7.33}$$

7.3.1.3 Equivalent mechanical properties of the covered beam

The damping layer used for partially covering the thickness profile is characterised by its length l, thickness h_l, Young's modulus E_l and loss factor η_l. The equivalent bending stiffness of the covered beam can be defined by using the Ross-Ungar-Kerwin model [87]

for extensional damping, as is done by Krylov [54] and can be expressed as

$$E_{eq}I_{eq}(x)(1+j\eta_{eq}) = E_0 I(x)\times \left((1+j\eta) + \frac{E_l}{E_0}\frac{h_l}{h(x)}^3 (1+j\eta_l) + \frac{3\left(1+\frac{h_l}{h(x)}\right)^2 \frac{E_l}{E_0}\frac{h_l}{h(x)}\big(1-\eta\eta_l+j(\eta+\eta_l)\big)}{1+\frac{E_l}{E_0}\frac{h_l}{h(x)}(1+j\eta_l)} \right), \tag{7.34}$$

where E_{eq}, I_{eq} and η_{eq} are the equivalent Young's modulus, second moment of area and damping ratio of the composite beam. In the case when the thickness of the damping layer is comparable to the local thickness of the beam, the mass of the damping layer must also be taken into account. Thus, the equivalent density of the composite beam is

$$\rho_{eq} = \frac{\rho h(x) + \rho_l h_l}{h(x) + h_l}, \tag{7.35}$$

where ρ_l is the density of the damping layer. The flexural wavenumber and the phase velocity of the compound beam are then obtained as

$$k_f(x) = \left(\omega^2 \frac{\rho_{eq} b\big(h(x)+h_l\big)}{E_{eq}I_{eq}(x)(1+j\eta_{eq})} \right)^{1/4} \tag{7.36}$$

and

$$c_\varphi(x) = \frac{\omega}{k_f} = \left(\omega^2 \frac{E_{eq}I_{eq}(x)(1+j\eta_{eq})}{\rho_{eq} b\big(h(x)+h_l\big)} \right)^{1/4}. \tag{7.37}$$

7.3.2 Numerical implementation

The efficiency of the acoustic black hole is estimated by the reflection matrix of the edge, which can be obtained from the impedance matrix, as shown in Eq. (7.31). In order to take into account the widely varying scale of the thickness, which is expected to vary from 1.5 mm to approximately 1 μm, the impedance matrix is computed by solving Eq. (7.22) by using an adaptive Runge-Kutta-Fehlberg method [49] instead of using a classical method with a constant integration step.

The computation is performed assuming the boundary condition

$$\mathbf{Z}(x_t) = 0, \tag{7.38}$$

which describes the free edge at the truncation distance. The impedance matrix is obtained iteratively from x_t to a given observation distance x_{obs}. The error in the solution at integration step n is given by the difference between two estimates of the solution with numerical schemes of orders 4 and 5, in the form [32]

$$\varepsilon_n = z_n^{(4)} - z_n^{(5)}. \tag{7.39}$$

Such error estimation is used to adjust the integration step and to keep the magnitude of the local error below a prescribed tolerance.

7.3.3 Illustration of the black hole effect

The geometrical parameters of the beam under consideration are chosen as

$$\begin{cases} x_t = -0.01\,\mathrm{m}, \\ x_i = -0.06\,\mathrm{m}, \\ x_{\mathrm{obs}} = -0.08\,\mathrm{m}, \\ h_0 = 1.5 \cdot 10^{-3}\,\mathrm{m}, \\ b = 1.5 \cdot 10^{-3}\,\mathrm{m}, \\ h(x) = h_0 \left(\dfrac{x}{x_i} \right)^4. \end{cases} \tag{7.40}$$

The beam material is steel, with parameters defined as

$$\begin{cases} E_0 = 210\,\mathrm{GPa}, \\ \rho = 7800\,\mathrm{kg} \cdot \mathrm{m}^3, \\ \eta = 0.001, \end{cases} \tag{7.41}$$

and the material parameters of the damping layer are chosen as

$$\begin{cases} E_l = 0.5\,\mathrm{GPa}, \\ \rho_l = 950\,\mathrm{kg} \cdot \mathrm{m}^3, \\ \eta_l = 0.05. \end{cases} \tag{7.42}$$

The impedance of the real beam can be compared to an impedance of reference, obtained from Eq.(7.31) by assuming a zero reflection matrix, as

$$\mathbf{Z}^{(\mathrm{ref})} = \frac{1}{j\omega} \mathbf{E}_4 \mathbf{E}_2^{-1}. \tag{7.43}$$

Fig. 7.3 shows the first term of the real and reference impedance matrices as functions of x. The spatial oscillations of the impedance are due to non-zero reflection at the edge and thus show interferences between the incident and the reflected fields. In the part of the beam where the thickness is constant, the distance between two peaks of the impedance is equal to the wavelength. Furthermore, those oscillations become more rapid as the thickness decreases. Therefore, the acoustic black hole can be regarded as an accumulation point in which waves slow down. Moreover, the truncation of the profile, combined with the damping layer, defines the minimal value of the wavelength, which has a significant influence on the reflection coefficient of the edge at observation point x_{obs}.

Fig. 7.4 shows the first term of the reflection matrix, R_{pp} (propagating-to-propagating reflection) at point x_{obs} as a function of frequency, for different configurations. The figure shows that the combination of the power-law profile with the damping layer provides a

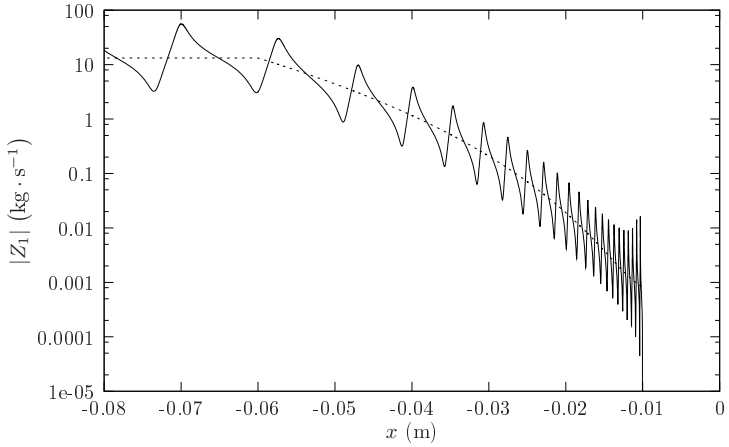

Figure 7.3: First term of the impedance matrix of a beam. ——, beam with black hole profile covered with a 10 μm damping layer; · · · · · ·, reference beam having a reflection matrix equal to zero.

lower reflection coefficient than the power-law profile alone or the constant thickness beam covered with a damping layer. Furthermore, it can be observed that the efficiency of the acoustic black hole is improved with frequency. Additionally, the oscillations of the reflection coefficient with frequency account for an additional feature of the acoustic black hole which cannot be observed by using the geometrical acoustics approach (see for example Fig. 5 of Ref. [55]).

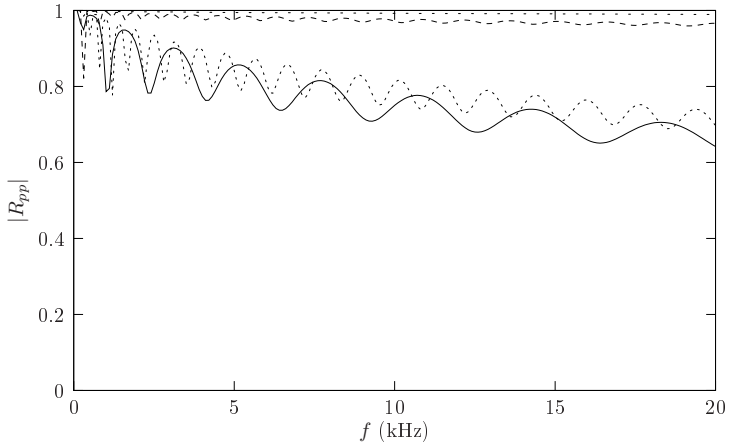

Figure 7.4: First term of the reflection matrix of a beam. · · ·, uniform beam covered with a 700 μm damping layer ($R_{20\text{kHz}}$=0.985); - - - - -, beam with black hole profile without damping layer ($R_{20\text{kHz}}$=0.97); · · · · · ·, beam with black hole profile covered with 10 μm of damping layer ($R_{20\text{kHz}}$=0.7); ——, beam with black hole profile covered with 700 μm of damping layer ($R_{20\text{kHz}}$=0.62).

7.3.4 Effect of the different parameters of the damping layer

The damping layer is intended to partially compensate for the non-zero reflection due to the truncation, where the accumulation of waves occurs. Thus, the most sensitive area to such treatment is near the truncation. However, the damping layer acts as an added mass, which can lead to an increase in the reflection coefficient. As a consequence, the role of the geometrical and material parameters of the damping layer must be individually studied. Using the values of the parameters defined in Eqs. (7.40), (7.41) and (7.42) as a starting point, the following study aims at defining the optimal parameters of the damping layer for which the reflection coefficient R_{pp} is minimal.

7.3.4.1 Thickness of the damping layer

Fig. 7.6 shows the wavelength of the covered beam for different thicknesses h_l of the damping layer. It is observed that the wavelength is increased near the edge by increasing the thickness of the damping layer. As a consequence, for a very large thickness, the accumulation phenomenon illustrated in Fig. 7.3 would disappear. Inversely, if the damping layer is too thin, significant reflection takes place at the edge, as previously shown in sec. 7.2.1. Then, for an efficient black hole effect to take place, an intermediate thickness must be chosen.

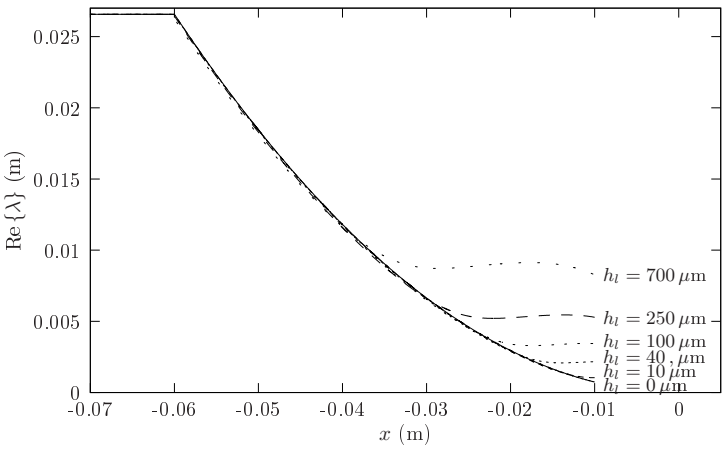

Figure 7.5: Real part of the wavelength for different thicknesses of damping layer.

In order to assess the impact of the thickness of the damping layer on the efficiency of the acoustic black hole effect, The loss factor of the covered beam can be estimated from the ratio of the imaginary part of the wavelength to its real part. This is shown in Fig. 7.6 for different thicknesses h_l of the damping layer. The figure shows that adding the damping layer results in a local maximum of the loss factor, whose position is controlled by the thickness of the added layer. By increasing the thickness, the maximum of the loss factor is shifted towards the thicker part of the beam, and vice-versa. It can be shown, with the chosen parameters, that the minimal reflection coefficient corresponds to a thickness of $40\,\mu$m, which is the value for which the maximum of the loss factor

is located at the truncation distance. This type of graph can then serve as a means of optimising the thickness of the damping layer.

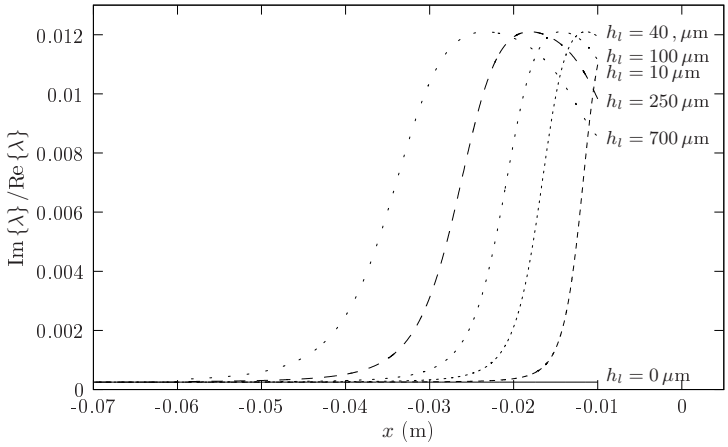

Figure 7.6: Ratio of the imaginary part to the real part of the wavelength for different thicknesses of damping layer.

7.3.4.2 Length of the damping layer

In order to evaluate the role of the length of the damping layer, the loss factor of the covered beam, estimated from the ratio of the imaginary part of the wavelength to its real part, is used. Fig. 7.7 shows such ratio for different lengths l of the damping layer. As it can be observed in the two bottom figures, covering the beam below the position $x = -0.03\,\text{m}$ does not result in a significant modification of the loss factor. This indicates that, in such area, the added layer will act as an added mass rather than as an added damping, for which it is not necessary. In fact, it can be verified that the reflection coefficients corresponding to the whole power-law entirely and partially ($x \in [-0.03, -0.01]\,\text{m}$) covered with damping layer do not differ significantly. However, if the damping layer is made shorter, the reflection coefficient increases. This indicates that the acoustic black hole effect allows to use a minimal amount of damping material, above which the damping is not significantly improved.

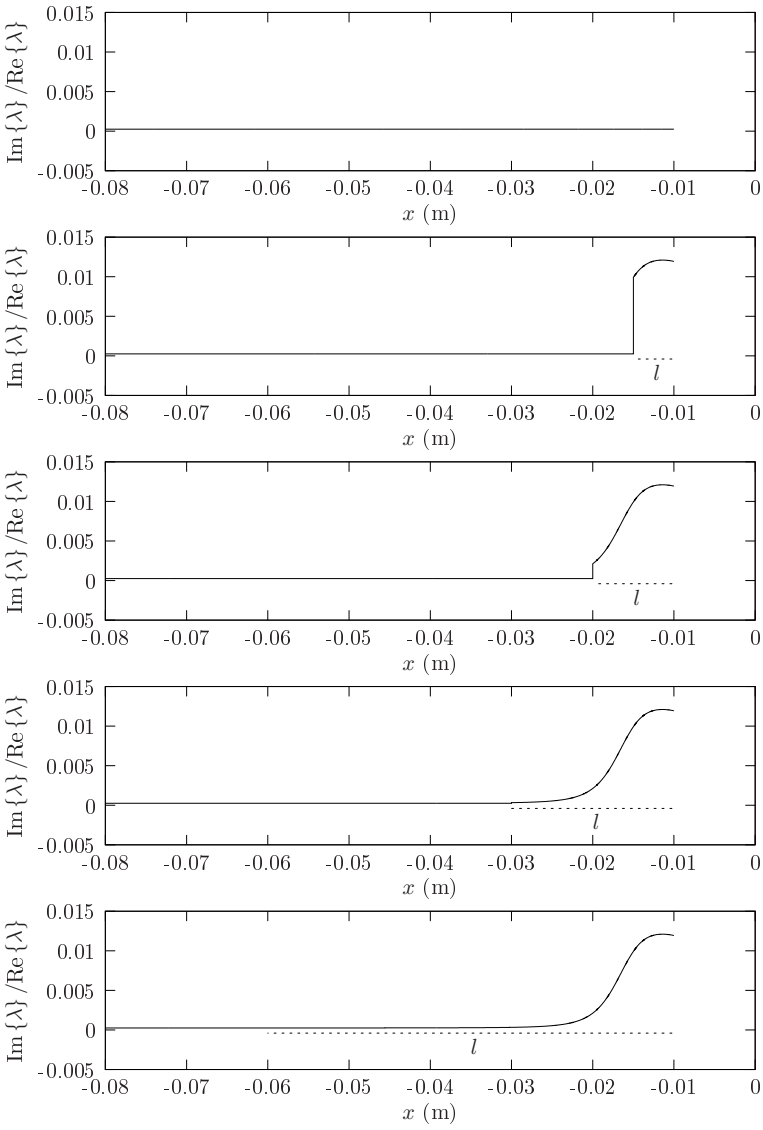

Figure 7.7: Ratio of the imaginary part to the real part of the wavelength for different lengths of the damping layer. The dotted line represents the portion of the beam that is covered with the damping layer.

7.3.4.3 Internal loss factor of the damping layer

In order to evaluate the role of the internal loss factor η_l of the damping layer, the same indicator as above is used, as shown in Fig. 7.8 for different values of η_l. Fig. 7.9 shows that increasing the internal loss factor of the damping layer leads to a global decrease of the reflection coefficient. Thus, for achieving efficient vibration damping, the loss factor must be increased as much as possible. However, the main difficulty consists in increasing the loss factor without increasing the added mass.

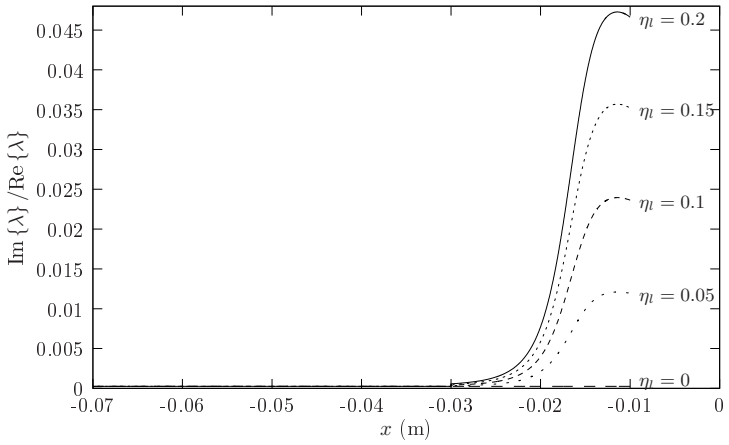

Figure 7.8: Ratio of the imaginary part to the real part of the wavelength for different values of the damping ratio of the damping layer.

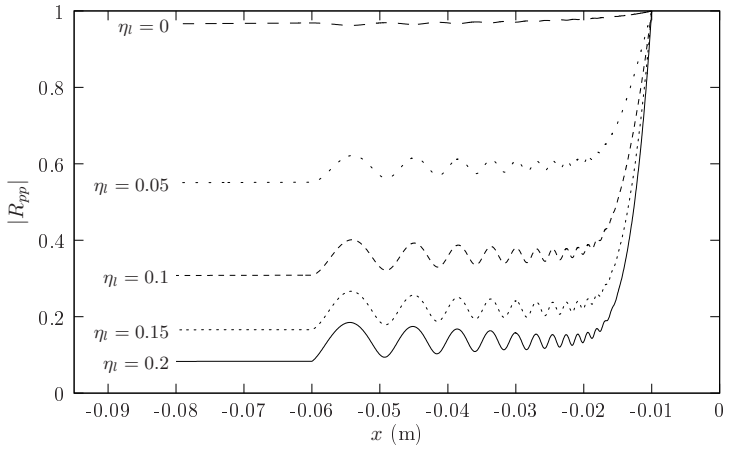

Figure 7.9: First term of the reflection matrix of the black hole beam for different values of the damping ratio of the damping layer, at frequency $f = 20\,\text{kHz}$.

7.3.4.4 Young's modulus of the damping layer

As shown in Fig. 7.10, decreasing the Young's modulus of the damping layer results in an increase of the global loss factor and shifts its maximum towards the edge, and vice-versa. Therefore, for achieving efficient vibration damping, the Young's modulus should be as low as possible.

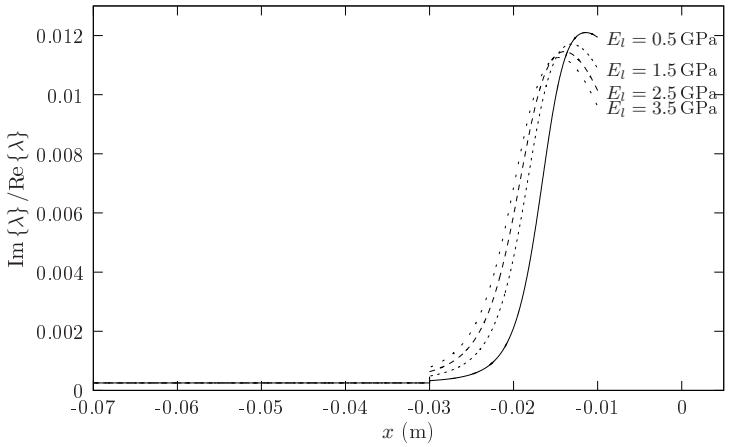

Figure 7.10: Ratio of the imaginary part to the real part of the wavelength for different values of the Young's modulus of the damping layer.

7.3.4.5 Summary of the rules for the design and optimisation of acoustic black hole profiles

As shown in the parametric study above, the directions to follow for achieving efficient vibration damping using the acoustic black hole effect in covered beams can be summarised as follows:

- The loss factor of the covered beam presents an optimal configuration in which reflection from the edge is minimal for an intermediate value of the thickness of the damping layer. This deserves careful attention and a parametric study in the form of Fig. 7.6 can serve as an aid for practical design.
- Increasing the length of the damping layer increases the loss factor of the covered beam. However, using a damping layer longer than a certain distance does not improve the global loss factor significantly. The length of the covered area must then be set to such distance in order to use a low amount of damping material.
- The internal loss factor of the layer must be chosen as high as possible in practice.
- The Young's modulus of the layer must be chosen as low as possible in practice.
- Recalling sec. 7.2.2, the truncation distance of the beam should be as short as possible. Also, the surface roughness of the profile must be as low as possible in order to avoid reflection at minor discontinuities.

7.3.5 Simulated driving-point mobilities

In practice, the effectiveness of the acoustic black hole can be easily observed by measuring the reduction of vibration level with the optimised parameters. The driving-point mobility of an acoustic black hole beam can be simulated from Eq. (7.20) by assuming a harmonic unit force and zero moment at the observation point x_{obs}. Fig. 7.11 shows the input mobility at point $x_{\text{obs}} = -0.25$m for an untreated uniform beam and a beam with power-law profile and a damping layer of thickness $h_l = 700\,\mu$m and of length 3 cm. The values of the other parameters are chosen as in Eqs. (7.40) to (7.42). It is observed that there is a significant reduction of the mobility, of more than 20 dB in the upper frequency range.

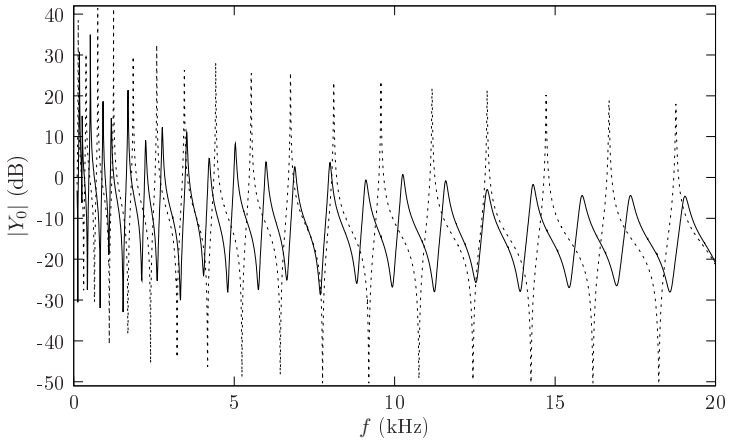

Figure 7.11: Simulated driving-point mobilities of a beam. ——, black hole beam; · · · · · ·, untreated uniform beam.

Moreover, as shown in Fig. 7.12, partially or entirely covering a uniform beam with a damping layer does not reduce significantly the driving-point mobility. These results show that the acoustic black hole effect provides efficient vibration damping and that it is much more efficient than conventional damping layers alone, even with a significantly lower amount of damping material.

7.4 Experimental results on elliptical plates

Most of the potential practical applications of the acoustic black hole effect concern two-dimensional structures. The question that naturally arises is how to adapt the one-dimensional approach to plate structures. On that account, an elliptical plate excited at one of its foci presents the particularity that all the generated waves converge towards the second focus after one reflection at the edges. In this regard, elliptical geometry is adequate for experimentally testing the one-dimensional acoustic black hole model, by creating a circular pit of power-law profile at the focus that is not being excited, as depicted in Fig. 7.13. The shape of the two-dimensional acoustic black hole is designed by rotational symmetry of the one-dimensional profile. The manufacturing process of this plate consists in electro-eroding a thick steel elliptical plate for achieving the pit of

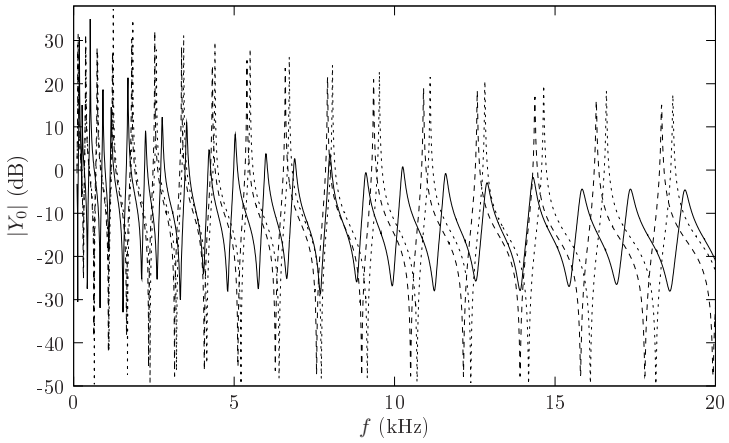

Figure 7.12: Simulated driving-point mobilities of a beam. ——, black hole beam; · · · · · · , uniform beam covered with damping layer in the black hole area; - - - - -, uniform beam entirely covered with damping layer.

power-law profile, then depositing a damping resin in the pit and finally reducing the thickness from the opposite side until a small hole is formed, whose diameter defines the truncation distance.

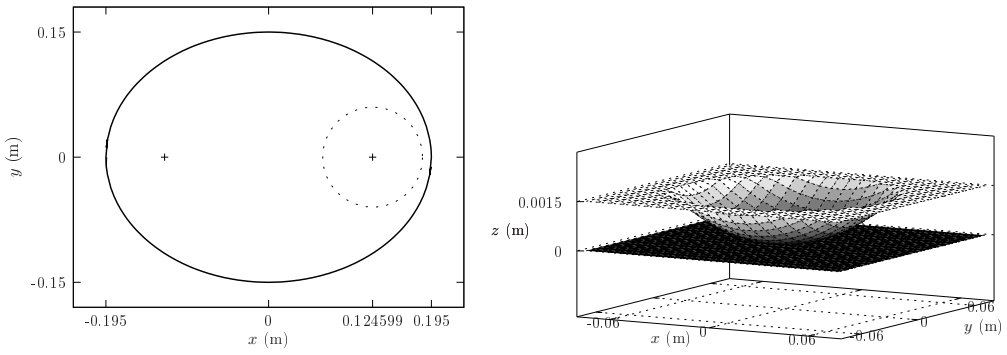

Figure 7.13: Elliptical plate with acoustic black hole profile at one of its foci. (a) Global view including dimensions in meters, (b) 3-D view of the top and bottom surfaces of the plate around the power-law pit. The radius of the pit is 6 cm, the maximum thickness of the plate is $h_0 = 1.5$ mm and the thickness profile follows a quadratic law with distance, i.e. $h(x) \sim x^4$.

The aim of following study is to bring relief to the efficiency of vibration damping in a plate treated with an acoustic black hole, compared to untreated or otherwise treated plates. Velocity field measurements on the entire plates are performed using a LDS V201 shaker and a Polytec OFV 056 vibrometer scanning head. Driving-point mobilities are measured by using a Brüel & Kjær impedance head of type 8001 and Brüel & Kjær

conditioning amplifier. All the measurements are done on vertically hung plates, for achieving free boundary conditions.

Fig. 7.14 shows examples of high frequency velocity fields of plates with and without acoustic black hole. The excitation force is applied at the left focus and the black hole profile is in the right one. It can be observed that the spatial patterns of the uniform plate are rather symmetric and equally distributed with some small increases in the area of the right focus, whereas those of the treated plate exhibit a accumulation of the velocity field in the area of the thickness profile. Such accumulation is similar to that shown in Fig. 7.3.

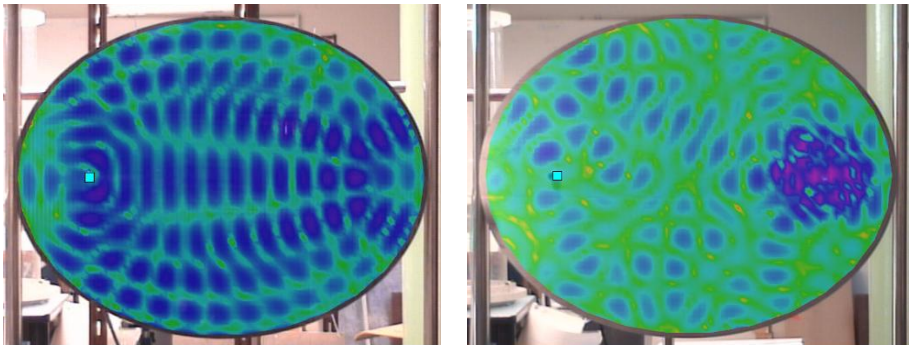

(a) (b)

Figure 7.14: Examples of velocity fields of plates with and without acoustic black hole for an excitation frequency of 9.514 kHz. (a) Uniform plate, (b) plate with acoustic black hole.

Fig. 7.15 represents the measured driving-point mobilities for the black hole plate and the untreated uniform plate. The mobilities show that treating the plate with a black-hole thickness profile results in a level reduction of 5 dB to 10 dB for frequencies above 7 kHz.

Similarly, the same mobility of acoustic black hole plate can be compared to driving-point mobilities of uniform plates partially and entirely covered with resin, as shown in Fig. 7.16. The partial covering of the plate with damping resin is done on a disk of 12 cm of diameter around the focus point that is not being excited. It can be observed that the level of the mobility is lower for the fully covered plate than for the partially covered plate, which eliminates the possibility that the efficacy of damping comes from the fact that the damping resin is placed at a particular point, i.e. a focus point. Furthermore, the level of the resonances and anti-resonances of the mobility of the black hole plate is still lower than for the two other damping treatments.

It can be observed that the experimental results are in accordance with the simulated driving-point mobilities. In particular, it is observed that the efficiency of such damping mechanism increases with frequency.

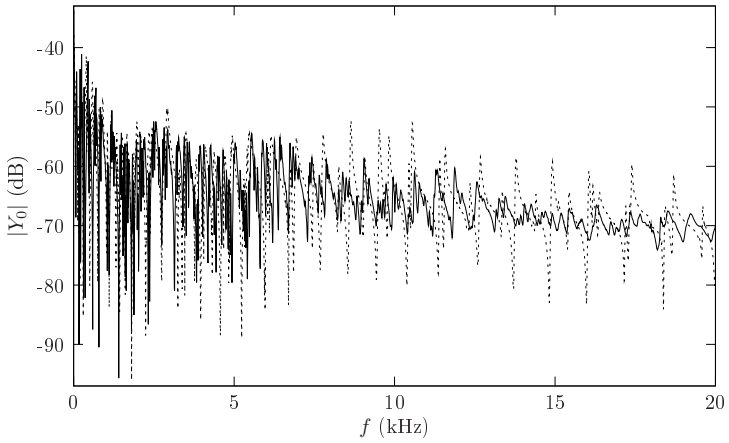

Figure 7.15: Measured driving-point mobilities of elliptical plates. ——, black hole plate; · · · · · ·, untreated uniform plate.

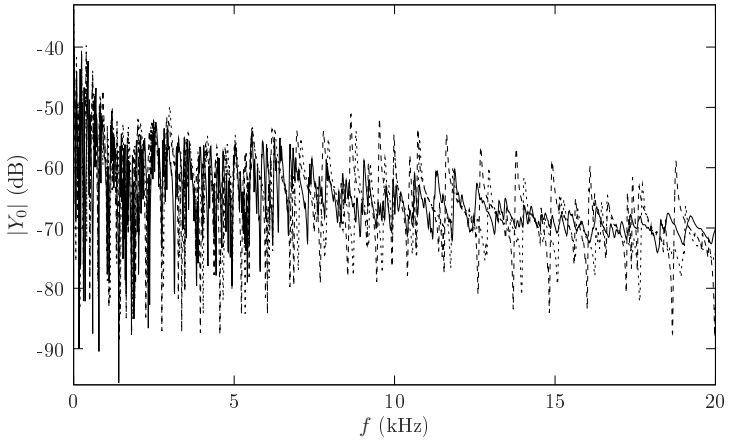

Figure 7.16: Measured driving-point mobilities of elliptical plates. ——, black hole plate; - - - - -, uniform plate covered with absorbing resin in the black hole area; · · · · · ·, uniform plate entirely covered with absorbing resin.

7.5 Vibration damping in polygonal plates using the acoustic black hole effect

7.5.1 Statement of the problem

The combination of the acoustic black hole effect with the focusing properties of elliptical plates can be regarded as a wave 'trap'. On that account, such combined effect can be adapted to structures of more complex shapes as a damping mechanism. The purpose of this section is to evaluate the efficiency of the acoustic black hole as a damping mechanism in polygonal plates of arbitrary shape. The main idea is to place a black-hole pit in a

polygonal plate and to induce wave focusing towards it by means of a parabolic edge, as illustrated in Fig. 7.17.

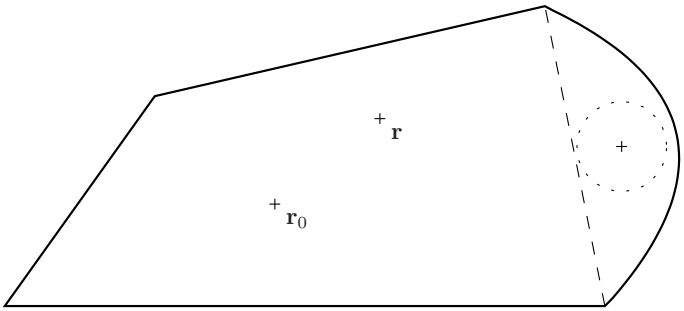

Figure 7.17: Polygonal plate with parabolic edge and acoustic black hole thickness profile. $\mathbf{r}_0$, source; $\mathbf{r}$, observation point; ·····, acoustic black hole pit; -----, virtual boundary separating the polygonal plate from the black hole zone.

Several plates were built for evaluating the effectiveness of the focusing parabolic edge and the presence of the black-hole pit. In the following, the manufacturing process of such plates is described and experimental results are presented. As it can be observed in Fig. 7.17, an artificial boundary is represented containing the black hole pit and the parabolic edge. Such artificial boundary is modelled by considering an equivalent black-hole reflection coefficient. Simulations using the image source method presented in chap. 4 are presented in order to evaluate the pertinence of the image source approach for describing this type of plates.

7.5.2 Manufacturing of the plates

The manufacturing technique of the acoustic black hole profiles of the plates presented in this section is different from the one presented in sec. 7.4 and results in more accurate thickness profiles. Instead of using an electro-erosion manufacturing, the power-law pits are achieved using high-speed machining. The photographs in Fig. 7.18 illustrate the different steps of the machining, done at the Institut Universitaire de Technologie (IUT) of Le Mans.

For this technique, aluminium is preferable to steel for the plate material because of its higher ductility. The surface of the manufactured profile is smoother than with the previous technique. In addition, the previous considerations on the plate dimensions are not affected by this choice of material. In fact, the phase and group velocities almost identical in steel and in aluminium for a given plate thickness [15]. However, the structural damping ratios may differ from aluminium to steel.

It can be observed in the last photograph of Fig. 7.18 that there is a perforation of the plate at the centre of the black hole pit, which determines the truncation distance of the profile. The pit radius is 6 cm and the thickness of the plate is 1.5 mm outside the black hole zone. The thickness profile follows a square law with distance, i.e. $h(x) \sim x^2$. The different manufactured plates present truncation radii between 2 and 4 mm and the residual thickness at the truncation radius is approximately of 10 μm.

(a) (b) (c)

Figure 7.18: Different steps of the black hole plates machining process. (a) Plate in the cutting machine with additional clamping plate, (b) prepared drill bit and high-speed machining with lubricating oil, (c) final black hole pit presenting a small truncation radius at its centre.

7.5.3 Experimental results

In the following, measurements of driving-point mobility and overall velocity field are carried on three different plates with and without a black hole pit. The first plate, shown in Fig. 7.19 is of elliptical shape and is tested in order to verify the reduction of vibration level using aluminium and larger dimensions than the previous tests presented in sec. 7.4. Figs. 7.20 and 7.21 show a rectangular plate and a convex polygonal plate of arbitrary proportions. Both plates include a black hole pit and a parabolic edge for focusing. Similar plates without black hole pit and also without the parabolic edge were built for comparison.

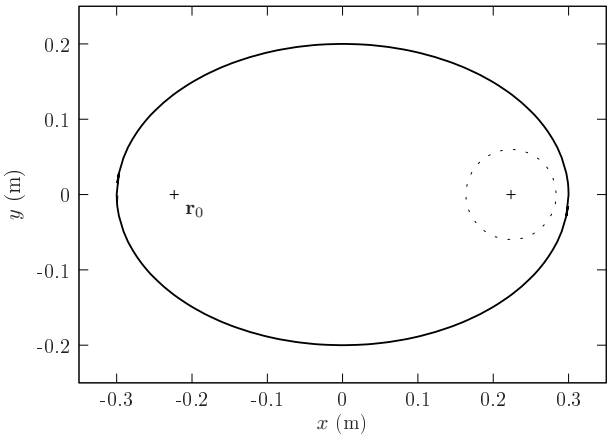

Figure 7.19: Elliptical plate with acoustic black hole thickness profile. $\mathbf{r}_0 = (-0.2236\,\mathrm{m}, 0\,\mathrm{m})$, source; $\cdots\cdots$, acoustic black hole pit. Semi-major and semi-minor axes are 30 cm and 20 cm, respectively. The radius of the black hole pit is 6 cm.

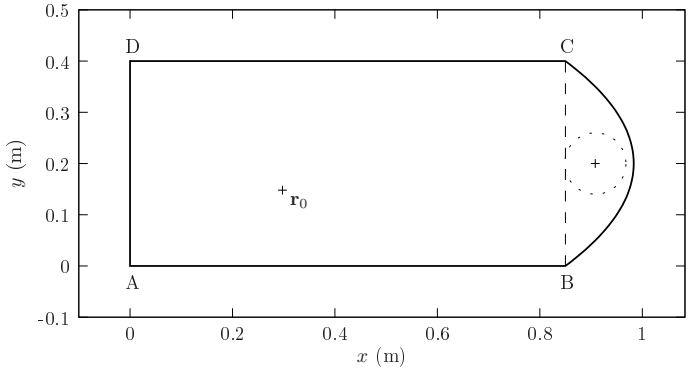

Figure 7.20: Rectangular plate with parabolic edge and acoustic black hole thickness profile. $\mathbf{r}_0 = (0.2975\,\text{m}, 0.148\,\text{m})$, source; $\cdots\cdots$, acoustic black hole pit. The coordinates of the edges of the rectangle are (in meters) $A = (0,0)$, $B = (0.85,0)$, $C = (0.85,0.4)$ and $D = (0,0.4)$. The centre of the parabolic edge is at 13.33 cm of the centre of BC and the centre of the black hole pit is at 5.83 cm of the centre of BC. The radius of the pit is 6 cm.

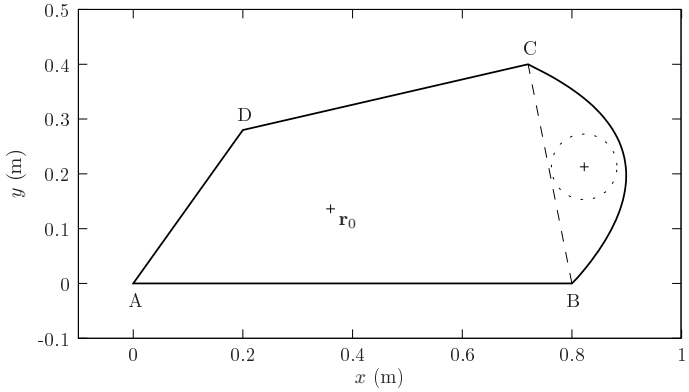

Figure 7.21: Polygonal plate with parabolic edge and acoustic black hole thickness profile. $\mathbf{r}_0 = (0.36\,\text{m}, 0.136\,\text{m})$, source; $\cdots\cdots$, acoustic black hole pit. The coordinates of the edges of the polygon are (in meters) $A = (0,0)$, $B = (0.8,0)$, $C = (0.72,0.4)$ and $D = (0.2,0.28)$. The centre of the parabolic edge is at 13.86 cm of the centre of BC and the centre of the black hole pit is at 6.36 cm of the centre of BC. The radius of the pit is 6 cm.

Measurements of the overall velocity field of the plates are presented in Fig. 7.22 at arbitrarily chosen frequencies. By comparing the different columns of the figure, it can be observed that the plates with black hole pit present a concentration of vibrational energy in the black hole zone. Furthermore, the level of vibration of such plates is low compared to the level at the black hole pit. In addition, the velocity fields loose their modal-like shapes when the black hole pits are present.

Fig. 7.23 represents examples of experimental driving-point mobilities of the different plates with and without black hole pit, obtained using an impact hammer and a laser

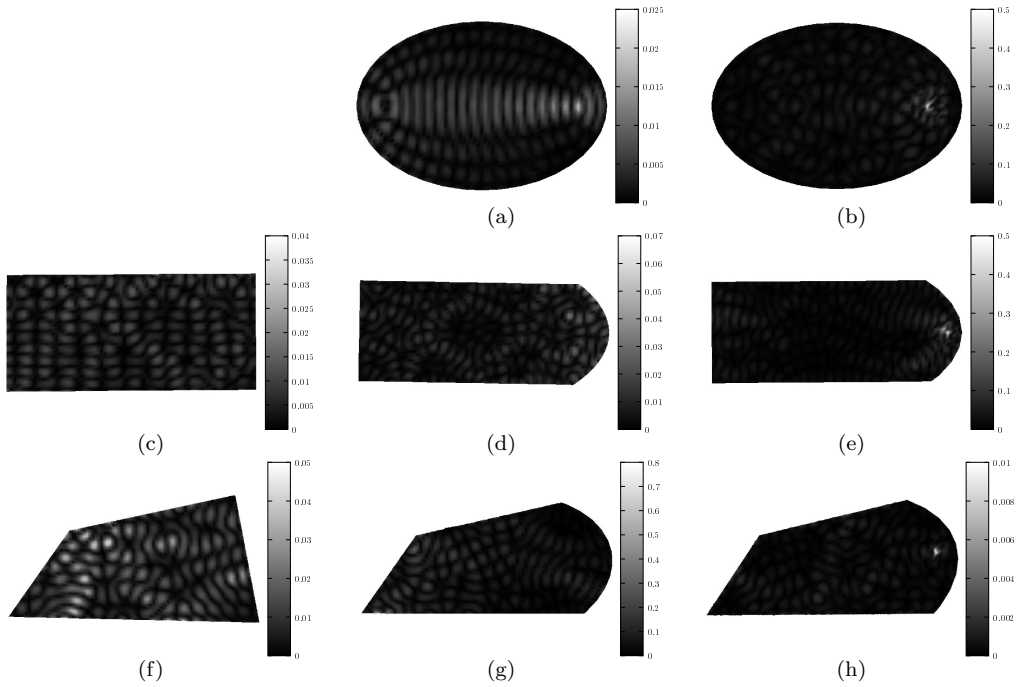

Figure 7.22: Magnitude of the experimental mobilities of different plates, in $\mathrm{m{\cdot}s^{-1}{\cdot}N^{-1}}$. (a) Elliptical at 5220 Hz, (b) elliptical with black hole pit at 5220 Hz, (c) rectangular at 3289 Hz, (d) rectangular with parabolic edge at 3289 Hz, (e) rectangular with black hole parabolic edge at 3289 Hz, (f) arbitrary polygonal plate at 3289 Hz, (g) arbitrary polygonal plate with parabolic edge at 3289 Hz and (h) arbitrary polygonal plate with black hole parabolic edge at 3289 Hz.

scanning vibrometer. For the three plates, the figures show reduction of vibration level, which is optimal in the case of the elliptical plate.

7.5.4 Model by the image source method

A global two-dimensional model of the vibrations of polygonal plates with black hole inclusions is a major difficulty due to the different geometric scales that are involved. A phenomenological model using the image source formalism developed in chap. 4 is here presented. The image source method is intended for polygonal boundaries and for isotropic and homogeneous material properties. Therefore, the black hole profile and the parabolic edge are taken into account by means of an equivalent black hole boundary condition defined at an artificial edge, as illustrated in Fig. 7.24. The equivalent black hole boundary condition is determined by its reflection matrix, defined as

$$\mathbf{R}(f) = \begin{bmatrix} R_{pp}(f) & R_{ep}(f) \\ R_{pe}(f) & R_{ee}(f) \end{bmatrix}. \tag{7.44}$$

Such reflection matrix is obtained from the one-dimensional model at a representative observation distance $x_{\mathrm{obs}} = -8\,\mathrm{cm}$ from the centre of the black hole pit (see Figs. 7.2

and 7.13(b)). The choice of such representative distance is arbitrary since the distance from the artificial black hole boundary to the centre of the pit varies. For the present simulation, according to the values of the different terms in simulated reflection matrices as in Fig. 7.9, the reflection matrix is arbitrarily set to

$$\mathbf{R} = \begin{bmatrix} 0.01 & 0 \\ 0 & 0.01 \end{bmatrix}. \tag{7.45}$$

Such reflection matrix thus represents a localised dissipative boundary condition. The parameters of aluminium that are necessary to the computations are

$$\begin{cases} \rho = 2700, \\ E_0 = 69 \cdot 10^9, \\ \nu = 0.33, \\ \eta = 0.001. \end{cases} \tag{7.46}$$

Using this parameters, which include a low structural damping ratio, the image source solution is observed to converge for a truncation parameter (see Eq. (2.45)) of $\gamma = 25$, which yields a total of 2934 sources. Fig. 7.25 shows the corresponding image source pattern. Fig. 7.26 shows the simulated driving-point mobilities of a plate with all edges free and a plate with three free edges and a black hole edge (see Fig. 7.24). As it can be observed by comparing Fig. 7.26 the graph on the right of Fig. 7.23, simulated and measured driving-point mobilities show similar a trend when providing the polygonal plate with a black hole parabolic edge. A difference of approximately 20 dB is observed between the maxima of the polygonal plate and of the plate with black hole boundary. Also, the resonant behaviour of the plate is highly reduced by adding the black hole boundary.

7.6 Conclusion

The central idea of the acoustic black hole effect for beams and plates is that vibration damping is achieved without added mass. The one-dimensional numerical model presented here is a flexible method that allows to simulate flexural wave propagation in beams of both variable thickness and mechanical properties. (In the next chapter, the same numerical model is applied to polymer beams subjected to spatial temperature variation in order to investigate further improvements of the acoustic black hole effect.) The numerical model allows to find optimal values of the geometrical and mechanical parameters of the additional damping layer of the acoustic black hole thickness profile, as a basis for the practical design of plates and beams. All the results presented in this chapter show that the acoustic black hole effect can reduce the level of vibration of beams and plates by several decibels to tens of decibels. Furthermore, the results show that the effect is improved with frequency. The results on polygonal plates are encouraging and show that this damping technique can be applied to structures of more complex shape. Moreover, the image source approach is pertinent for predicting the overall behaviour of an enclosed structure with a partial opening, which is in this case the acoustic black hole edge.

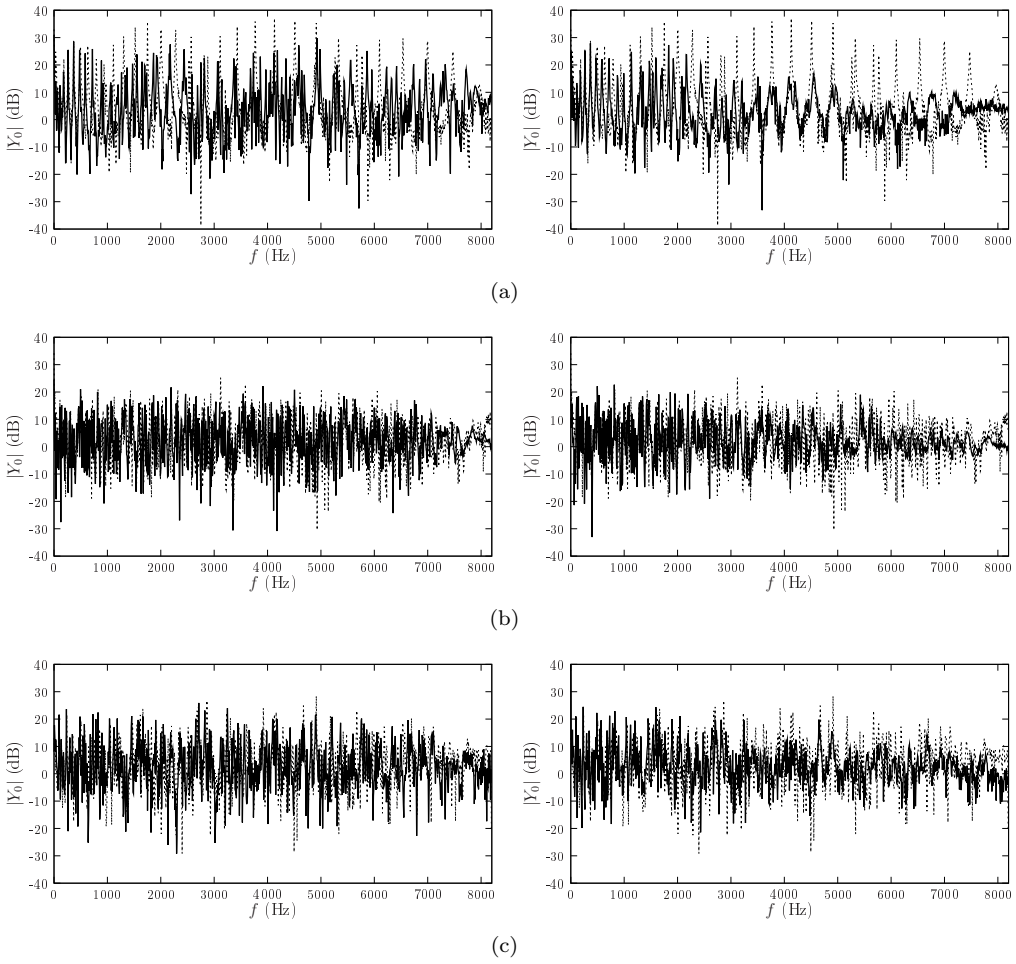

Figure 7.23: Driving-point mobilities of the different plates without black hole pit and with black hole pit with a thin absorbing film. (a) Elliptical plate, (b) rectangular plate, (c) arbitrary polygonal plate. Left: ·····, plate without acoustic black hole; ———, plate with acoustic black hole; right: ·····, plate without acoustic black hole; ———, plate with acoustic black hole and thin layer of absorbing film.

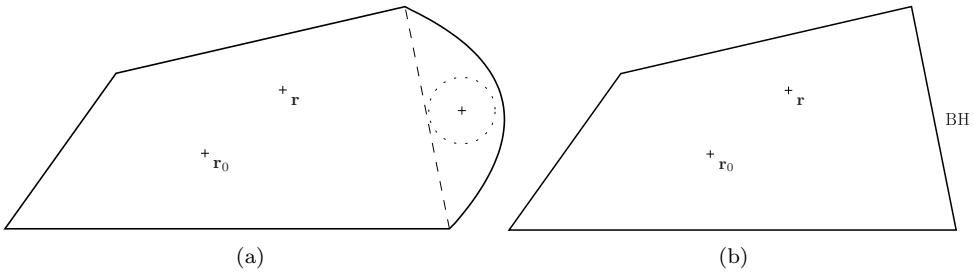

Figure 7.24: Equivalent polygonal plate to a polygonal plate with parabolic edge for wave focusing on a black hole profile. (a) Original plate, (b) equivalent plate.

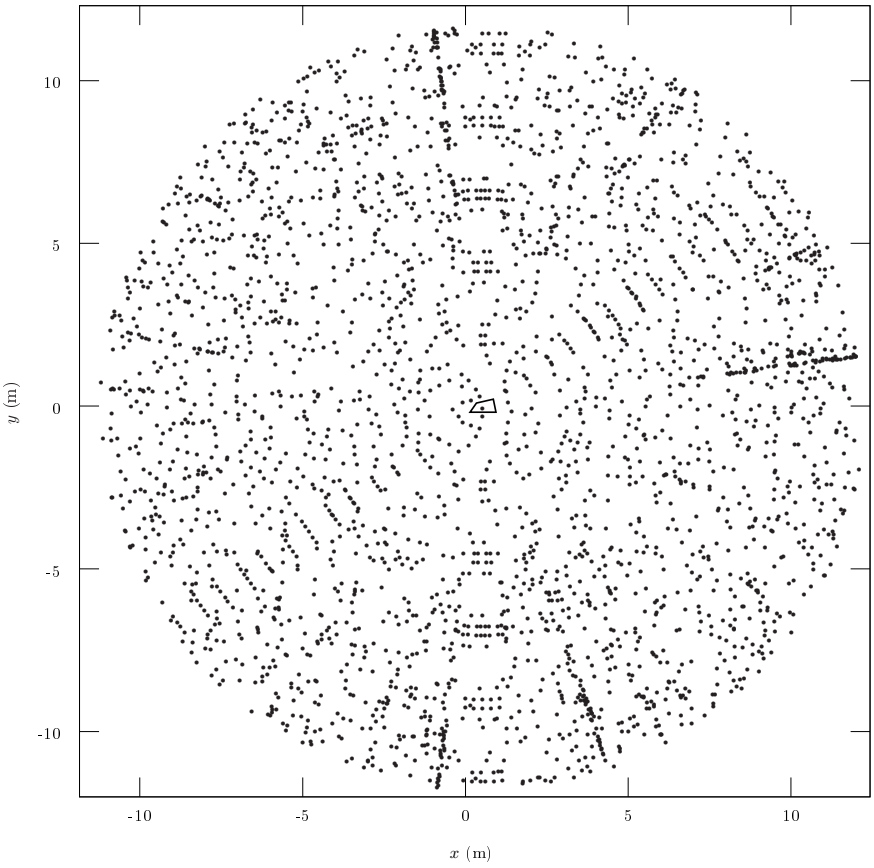

Figure 7.25: Image source pattern for the simulation of the polygonal plate with and without black hole boundary. ——, Plate boundaries; •, sources.

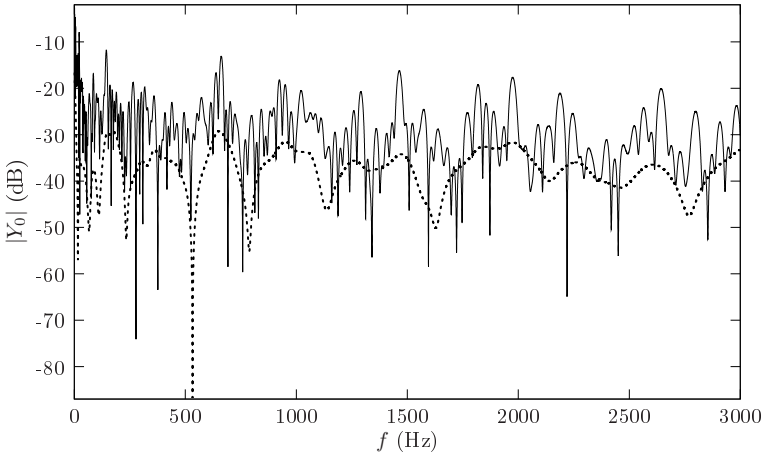

Figure 7.26: Simulated driving-point mobilities for a polygonal plate. ——, All edges free; · · · · · ·, with a black hole edge.

Chapter 8

Acoustic black hole effect in shape-memory materials

The investigation presented in this chapter has been made possible with the help of Emmanuel Foltête and Jan Klesa of Franche-Comté Électronique, Mécanique, Thermique et Optique – Sciences et Technologies (FEMTO-ST), Besançon, who made the polymer samples and provided their mechanical properties.

Abstract

The acoustic black hole effect in beams or plates consists in gradually decreasing the velocity of waves in a finite interval of space in order to produce non-reflecting boundaries. As it is studied in chap. 7, this can be achieved in a beam or plate with a smoothly decreasing thickness. However, the Young's modulus and the material density can also be controlled in order to obtain similar velocity profiles. This chapter investigates the possibility of producing the acoustic black hole effect in a beam with a spatially-dependent Young's modulus. This is achieved experimentally by using a shape-memory polymer, which allows to control the Young's modulus of a beam edge with temperature. The material properties that are relevant for the present study are first summarised. The general model developed in chap. 7 is then applied in order to derive the reflection coefficient of the edge treated with varying temperature. The combination of variable-thickness and thermoelastic effects is evaluated and discussed.

8.1 Introduction

As discussed in chap. 7, the principle of the acoustic black hole for flexural vibrations of thin plates consists in decreasing the phase velocity gradually to zero in a finite interval of space, in order to gradually slow-down waves and therefore to obtain a non-reflecting edge. In the theoretical, numerical and experimental studies reported therein, the decrease of velocity is achieved by decreasing the thickness of the beam or plate structures. However, it is possible to achieve a gradually decreasing velocity profile by controlling other parameters on which the phase velocity depends, such as the Young's modulus or the material density.

The aim of this chapter is to reproduce the acoustic black hole effect in a beam with spatially-dependent Young's modulus. This is achieved by using a temperature gradient in a shape-memory polymer in order to take advantage of its thermoelastic properties. First, the temperature-dependent Young's modulus is measured and simulations are performed using the model presented in sec. 7.3. Then, the driving-point response measurements are presented. In both the numerical and experimental studies, a uniform beam and a beam with varying thickness are considered in order to evaluate the efficiency of the combination of the geometrical and thermoelastic effects.

8.2 Model

8.2.1 Statement of the problem

The phase and group velocities c_φ and c_γ of a beam can be controlled by a variation of Young's modulus and/or thickness, as

$$c_\varphi(x) = \left(\frac{E(x)h^2(x)}{12\rho}\right)^{1/4}\sqrt{\omega} \tag{8.1}$$

and

$$c_\gamma(x) = 2\left(\frac{E(x)h^2(x)}{12\rho}\right)^{1/4}\sqrt{\omega}, \tag{8.2}$$

where E is the Young's modulus, h is the thickness of the beam, ρ is the material density and ω is the circular frequency. The Young's modulus can be controlled with a thermal load, as shown in Fig. 8.1 for a uniform beam and a beam with a power-law thickness edge.

The purpose of what follows is to model the acoustic black hole effect in beams with variable Young's modulus induced by a thermal load. The combination of this thermoelastic effect with the geometrical effect of variable thickness studied in chap. 7 is investigated as a means of optimising the effect.

8.2.2 Determination of the complex Young's modulus of the material

The material used for the present study is a styrene-based shape-memory polymer, Veriflex® from CRG Industries [17]. The property of such material that is relevant for the present investigation is that its Young's modulus significantly varies with temperature. The measurements allowing to determine the thermoelastic properties of the polymer were done by Jan Klesa et al. [50], who also made the samples tested herein. In the following, the Young's modulus of the material is written as

$$E = E' - jE'', \tag{8.3}$$

where E' is the storage modulus and E'' is the loss modulus. The measurements consist in determining E' and E'' within a given frequency interval at different temperatures, and then extrapolating the curves to lower and higher frequencies using the Willams-Landel-

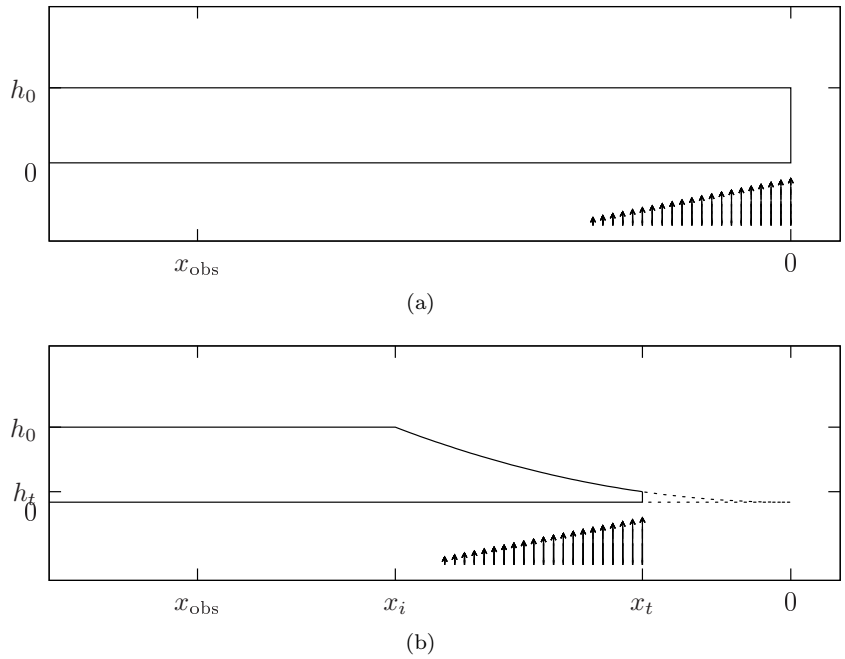

Figure 8.1: Side view of a beam exposed to a temperature gradient. (a) Uniform beam, (b) beam with power-law varying thickness (——, real profile with initial and truncation distances x_i and x_t; $\cdots\cdots$, ideal black hole profile). The arrows indicate the thermal load.

Ferry (WLF) approximation [100]. The latter is also used for predicting deformation of materials under high-speed collisions. According to the WLF model, there exists an equivalence between frequency (or time) and temperature, as described as follows. The measured curves of the storage and loss moduli as a function of frequency, $E'_\tau(f)$ and $E''_\tau(f)$, can be extrapolated to different frequencies at a reference temperature τ_r, such that

$$E'_\tau(f) = E'_{\tau_r}(a_\tau f) \tag{8.4}$$

and

$$E''_\tau(f) = E''_{\tau_r}(a_\tau f), \tag{8.5}$$

where a_τ is the scaling factor for each temperature τ and is given by [100]

$$\ln(a_\tau) = \frac{-C_1(\tau - \tau_r)}{-C_2 + \tau - \tau_r}, \tag{8.6}$$

where τ is the temperature for the frequency curve to be extrapolated and C_1 and C_2 are empirical constants following from the chosen reference temperature τ_r. Choosing the reference temperature at the glass transition temperature of the polymer, in this case 62°C [17], the values of the constants are $C_1 = 18.3$ and $C_2 = 70.54\,\text{K}$ [50]. The curves of E'_{τ_r} and E''_{τ_r} as a function of frequency are commonly referred to as master curves, since they gather several measurements at different temperatures. Using the master

curves and Eq. (8.6), the storage and loss moduli can be specified as functions of both temperature and frequency, as shown in Fig. 8.2. Such complex Young's modulus is used in the acoustic black hole model described below.

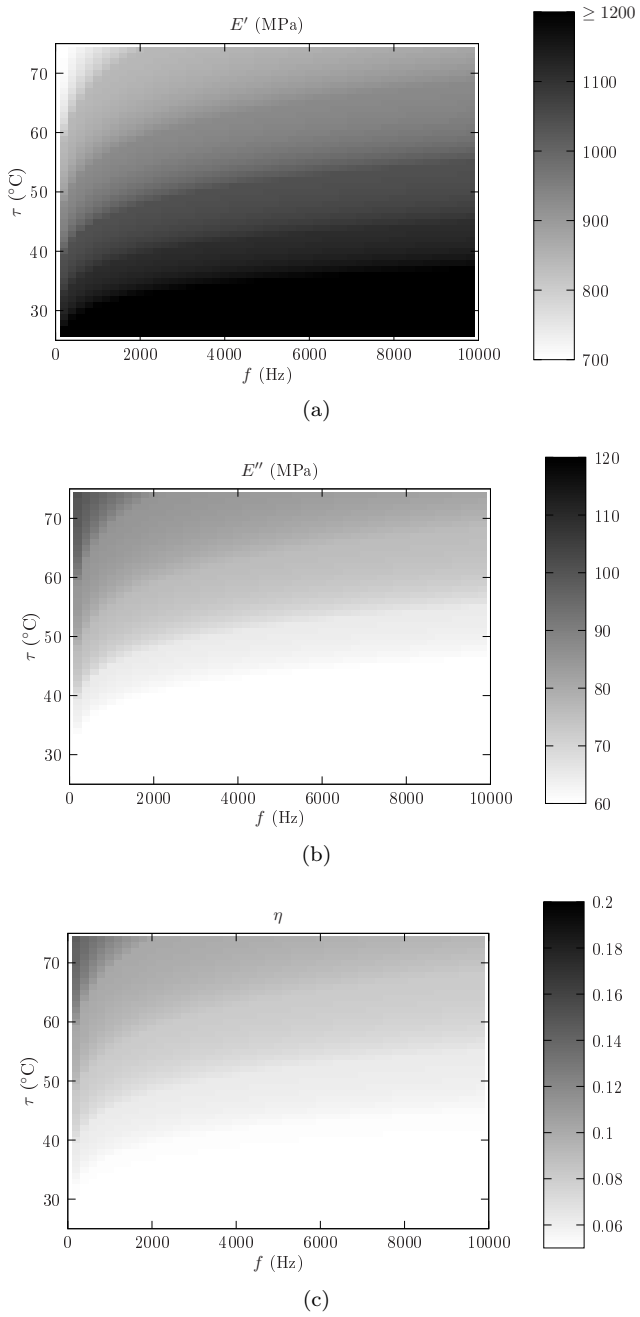

Figure 8.2: Young's modulus as a function of frequency and temperature. (a) Real part, (b) imaginary part, (c) associated structural damping ratio $\eta = E''/E'$.

8.2.3 Numerical simulations

The purpose of this paragraph is to model the flexural vibrations of a polymer beam subjected to a temperature change as an inhomogeneous waveguide. Using the data of Fig. 8.1, each position of the beam x corresponds to a given temperature $\tau(x)$, such that the Young's modulus depends on frequency, and abscissa x. Fig. 8.3 shows three temperature profiles obtained by infrared thermography in preliminary experimental investigations using the setup described later-on in Fig. 8.6.

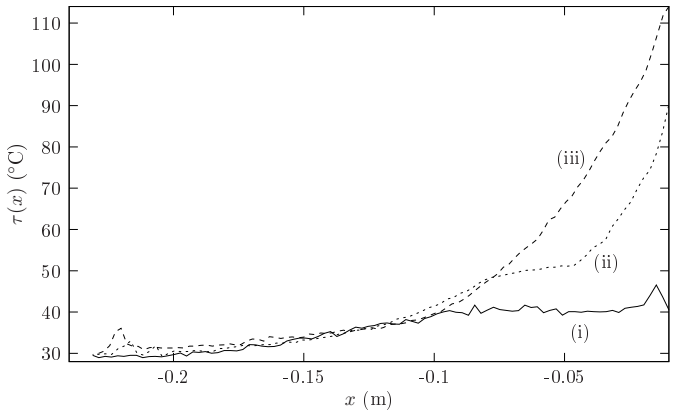

Figure 8.3: Measured temperature gradients on a uniform beam. Temperature at the bottom of the beam: ——, 40.5 °C; · · · · · ·, 90.3 °C; - - - - -, 114 °C.

Using the data of Figs. 8.2 and 8.3 in the model presented in sec. 7.3 allows to compute the impedance matrix of the beam and the reflection matrix as functions of the observation distance to the edge of the heated extremity. Fig. 8.4 shows the first term of the impedance matrix and the reflection coefficient for propagating waves as functions of distance x, for a uniform beam and a beam with power-law thickness according to the same profile of the aluminium plates described in sec. 7.5.

In the case of a uniform beam, the impedance curve shows that the temperature variation is followed by an accumulation of the wave field oscillations near the extremity, which clearly shows the decrease of velocity. Moreover, high variations in temperature result in pronounced accumulation of the oscillations. The associated reflection coefficients follow the same trend: the strongest temperature variation corresponds to the lowest reflection coefficient. For the beam with power-law varying thickness, the accumulation of oscillations is more pronounced than in the case of a uniform beam. Also, the reflection coefficient is lower than in the case of uniform thickness. Fig. 8.5 shows the driving-point mobilities of the uniform and power-law beams for the different temperature profiles. The results show that the mobility of the power-law beam is lower than for the uniform beam. Both configurations show significant reduction of the vibration level.

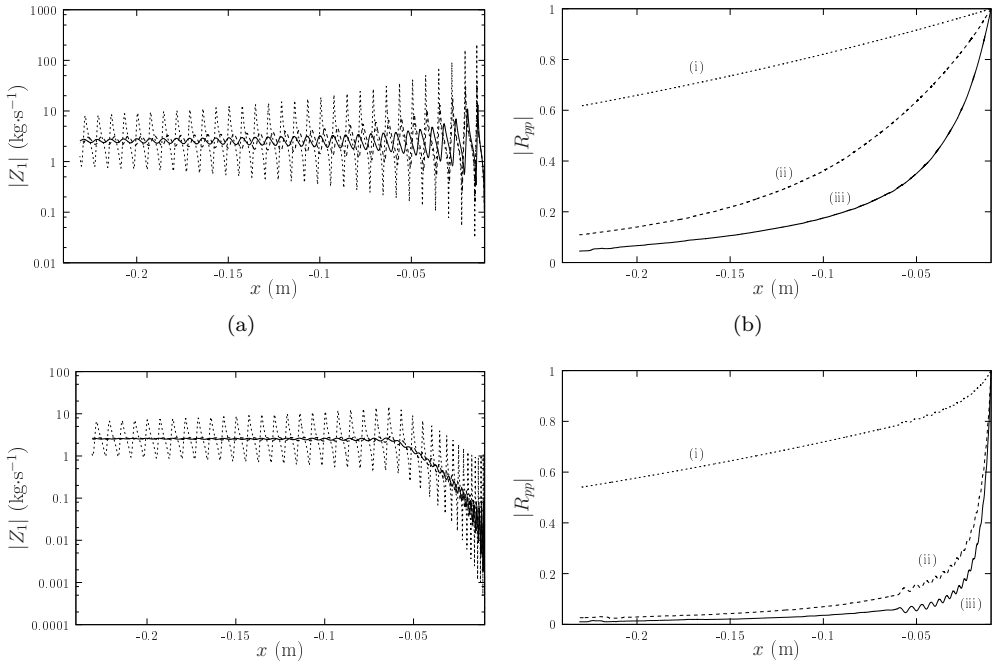

Figure 8.4: First term of the impedance and reflection matrices along a beam with power-law thickness, for different temperature gradients. (a,b) Uniform beam, (c,d) power-law thickness beam. (a,c) First term of the impedance matrix (· · · · · ·, no thermal load; - - - - -, temperature profile (i) of Fig. 8.3; ——, temperature profile (iii) of Fig. 8.3), (b,d) first term of the reflection matrix for temperature profiles (i), (ii) and (iii) of Fig. 8.3.

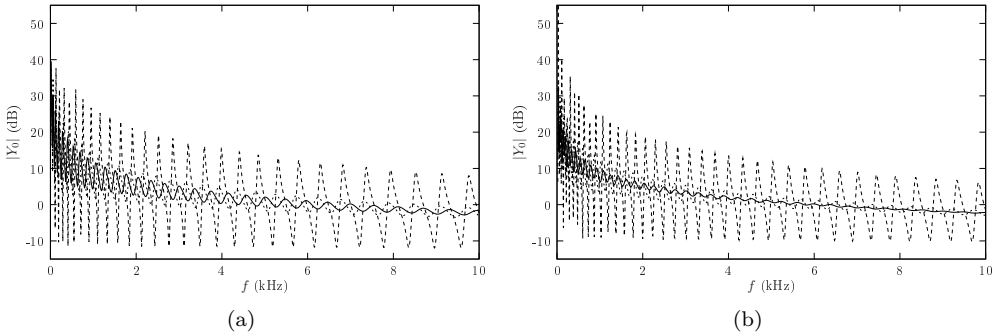

Figure 8.5: Driving-point mobilities for different temperature gradients. (a) Uniform beam, (b) beam with power-law thickness profile. · · · · · ·, no thermal load; - - - - -, temperature profile (i) of Fig. 8.3; ——, temperature profile (iii) of Fig. 8.3.

8.3 Experimental observations

8.3.1 Experimental setup

The experimental setup used for the measurements is shown in Fig. 8.6. Such setup allows to simultaneously measure the temperature of the beam and its driving-point response. Both uniform and power-law beams are considered.

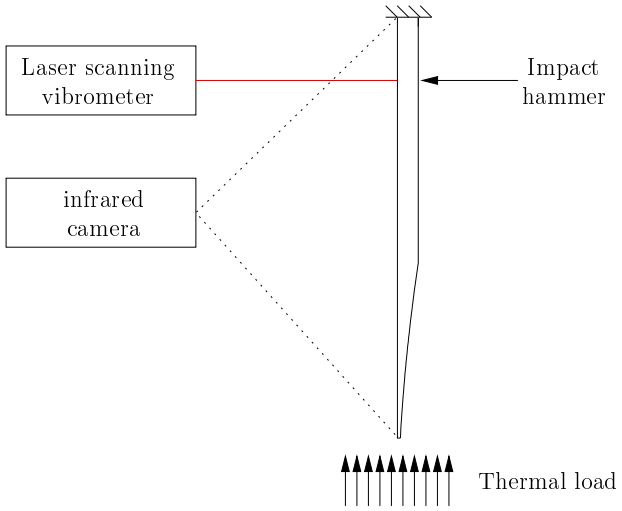

(a)

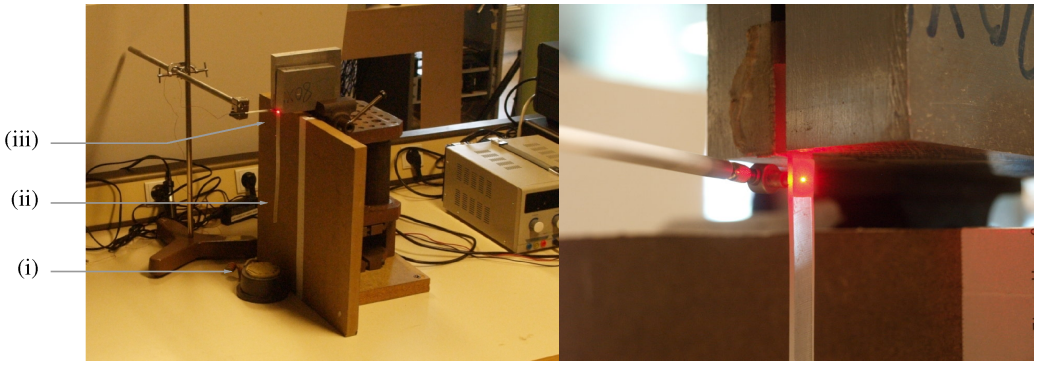

(b) (c)

Figure 8.6: Experimental setup simultaneously measuring the temperature and driving-point response of a beam. (a) Schematic view, (b) photograph showing the heating resistance (i), the polymer beam (ii), the impact hammer and laser spot (iii), (c) zoom on the impact hammer and the laser spot.

The beam is clamped in a vertical position letting a free length of 23.15 cm and it is heated at the bottom by a nickel-chromium resistance wire under high electrical current. The temperature is measured using an infrared camera. The input response is measured

by using impact hammer PCB 086D80 and laser vibrometer head OFV 056 together with LMS Scadas III acquisition system including Test Lab software.

8.3.2 Experimental results

Fig. 8.7 shows different measured temperature profiles with the corresponding input impedances for a uniform beam. In Figs. 8.7(b) and 8.7(c), the dotted line represents the input impedance of the beam without any thermal loading and the solid line represents the input impedance corresponding to the temperature profile under test. It can be observed that the more the temperature of the beam varies in the vicinity of the edge, the more the resonant behaviour of the structure is diminished. Thus, the temperature variation near the edge of the beam is of significant importance for the overall behaviour of the input response. This confirms that the acoustic black hole effect can be achieved by controlling the Young's modulus of the material, even without using a variation in thickness. Additionally, the relative vibration levels for the different thermal loads are in accordance with the simulated input mobilities.

Furthermore, the combination of the effect of a thermal load and the effect of non-uniform thickness can be studied as a means of optimising the effect. Thus, a beam of the same length as the previous one, with a power-law thickness profile near the edge was built. The thickness profile is defined as for the aluminium plates of sec. 7.5.2, that is, following a power-law of the form

$$h(x) = h_0 \left(\frac{x}{x_i} \right)^2 , \tag{8.7}$$

where $h_0 = 1.5\,\text{mm}$ is the thickness of the uniform region of the beam and $x_i = -6\,\text{cm}$ denotes the initial abscissa of the power-law profile, as depicted in Fig. 8.1(b).

Fig. 8.8 shows similar temperature profiles of both beams, uniform and with power-law thickness, and the corresponding measured input impedances. As observed in Fig. 8.8(b), the modal density of the beam with power-law thickness is higher due to the reduction of thickness. The measurements show that, for nearly indistinguishable temperature profiles, the resonant behaviour of the power-law beam is more highly reduced than for the uniform beam. This is the main result of this chapter, showing the importance of combining the variation of temperature and the variation of thickness.

8.4 Conclusion

This chapter investigates the possibility of reproducing the acoustic black hole effect in a beam whose Young's modulus varies with distance. Beams made of a shape-memory material are used in order to achieve the variation of the Young's modulus by exposing the beam to a temperature gradient along its length. Appropriately increasing the temperature near an edge of the beam yields a decreasing wave velocity profile which results in a weakly-reflecting edge. The numerical simulations show a shortening of the wavelength towards the edge exposed to the thermal load. Also, the predicted reflection coefficient is shown to be controllable with the temperature gradient and can be made close to zero by combining the thermoelastic effect with a power-law varying thickness.

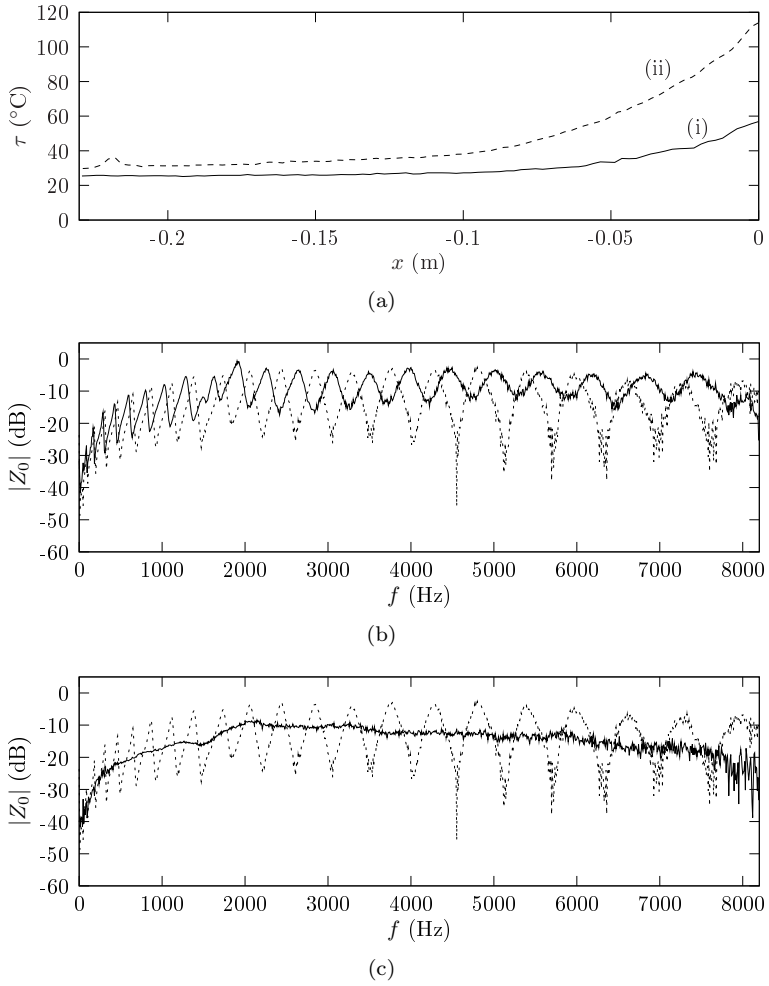

Figure 8.7: Measured temperature profiles and driving-point impedances for the uniform beam. (a) Temperature gradients; (b) ·····, reference input impedance with no thermal load; ——, input impedance for temperature profile (i); (c) ·····, reference input impedance with no thermal load; ——, input impedance for temperature profile (ii).

Both numerical and experimental results show a significant reduction of vibration level in the input responses by using a temperature gradient. The combination of thermoelastic and geometrical effects exhibits a higher reduction of the resonant behaviour than with the thermal loading alone. The global trends of the results are in accordance with those of chap. 7, where only a geometrical effect is present.

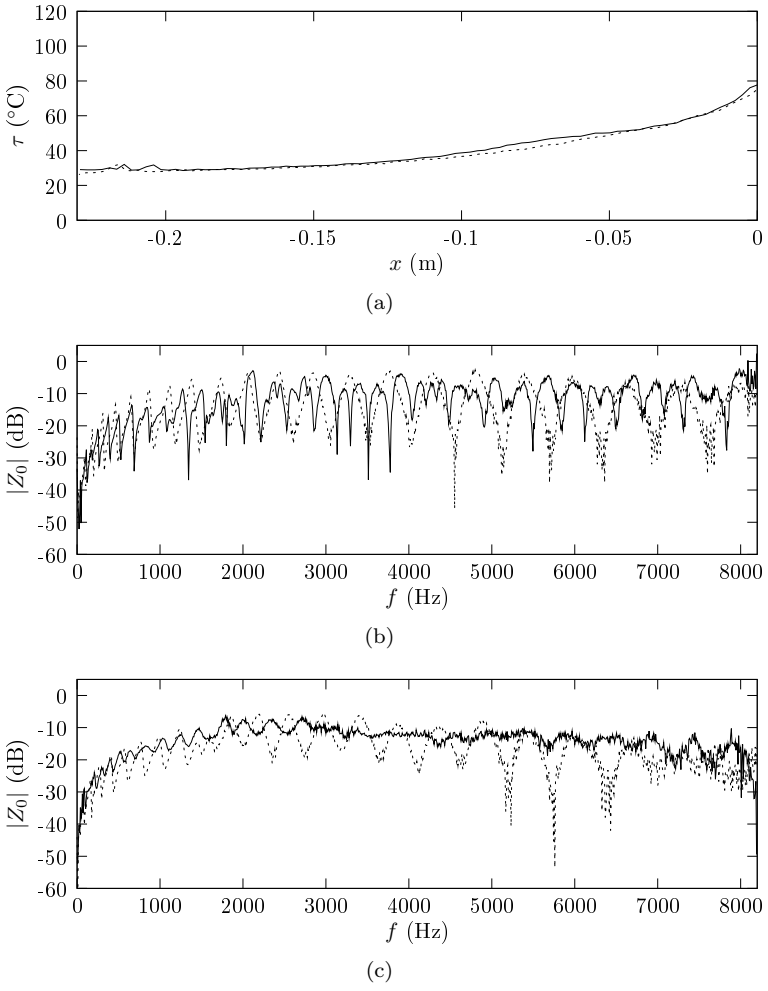

Figure 8.8: Comparison between uniform and varying-thickness beams. (a) Temperature profiles: - - - - -, uniform beam; ——, beam with power-law thickness. (b) Input impedances of the uniform beam, (c) input impedances of the power-law beam. · · · · · ·, with no thermal load; ——, with temperature profiles of (a).

Conclusion

The work presented in this dissertation has been done in the framework of the activities of the Laboratoire d'Acoustique de l'Université du Maine (LAUM) on the prediction and representation methods and damping techniques for mid- and high-frequency structural vibrations. In this thesis, a method for predicting the flexural vibrations of thin convex polygonal plates has been developed and a contribution has been made to the study of vibration damping using the acoustic black hole effect.

Summary of the results

Image sources are an intuitive and robust representation of successive wave reflections on the boundaries of enclosed polygonal or polyhedral domains. Such approach has been extensively used in room acoustics and its application to plate vibrations is relatively recent. The main reason for applying the image source method to polygonal plates is that the positions and amplitudes of image sources carry the information of the geometry and the boundary conditions of the plate. This renders the approach suitable for polygonal plates of arbitrary geometry and boundary conditions.

The image source method consists in considering the response of a polygonal plate to a harmonic point source as the superposition of different source contributions, including the original source and its image sources. The latter represent successive wave reflections on the plate boundaries and their positions are thus determined as successive symmetries of the original source with respect to the boundaries. In the particular case of boundary conditions described by reflection coefficients that are independent from the angle of incidence of waves, i.e. simply supported and roller supported edges, the amplitude of each image source arises as the product of the amplitude of its mother source (i.e. the source representing the previous reflection) and the reflection coefficient of the edge at which the reflection occurs. This allows to obtain a closed form of the Green's function of plates of rectangular, isosceles triangular, half-equilateral triangular and equilateral triangular plates. In fact, the successive symmetries of the original source point with respect to the boundaries of those polygons lead to a spatially-periodic pattern of image sources, such that the positions of the image sources are known by a simple law. Moreover, the Fourier series of a spatially-periodic function is a discrete function in the wavenumber domain, which allows to obtain the modal expansion of the Green's functions of those particular

plates.

For plates of arbitrary polygonal geometry, the image source positions must be calculated explicitly, which requires the source series to be truncated. On that account, it is shown that the estimated Green's functions converge towards reference solutions by increasing the number of sources. Furthermore, considering a given number of sources, the accuracy of the Green's function is improved by increasing the structural damping or the frequency. In fact, at high frequencies and for a high damping, the contributions from image sources that are far from the observation point can be disregarded. On that basis, the image source method is shown to be suitable for mid- and high-frequency vibrations.

Constant reflection coefficients are a special case that allows to model only a few types of boundary conditions. In a general situation, the reflection properties of plate boundaries depend on the angle of incidence of waves. The image source method is then generalised to polygonal plates including arbitrary boundary conditions. This is done by considering the contributions of the different sources as continuous sums of propagating and evanescent plane waves. The reflection of such plane waves at the plate discontinuities is determined by a reflection matrix, which can be obtained using a state vector approach. The Green's functions of the plates are obtained as the superposition of the contributions from the sources, within the assumption that evanescent waves are important for the first reflection on each boundary but can be ignored for the following reflections. It is shown that the image source method provides a good approximation of the Green's function of the plate, yet is not able to give an exact solution for arbitrary boundary conditions. The obtained Green's functions are accurately predicted in the central region of the plates and discrepancies remain in the nearfield of the edges due to the missing evanescent waves. However, the spatial extent of the nearfield decreases with frequency and structural damping, showing that the image source approach is relevant in mid- and high-frequency regimes.

Additionally, it has been shown that the image source method can be extended to the case of two connected polygonal plates. Describing the junction between the plates by a scattering matrix allows to treat wave transmission through the junction in the same manner as reflection at edges. Similarly to the case of individual plates, evanescent waves are ignored after the first reflection or transmission. An example of application of the method in the case of a virtual junction (i.e. continuity) between two polygonal plates shows that the vibrational field is accurately predicted in the plate containing the source and that some discrepancies remain in the connected plate, due to the missing evanescent waves.

Furthermore, the image source method allows to estimate the Young's modulus and structural damping ratio of highly damped panels. By computing the modulus of the bending stiffness of the panel from the mean value of the experimental driving-point mobility, a best fit of the Young's modulus and the damping ratio is obtained from the comparison of experimental and simulated mobilities. The method is applicable in a high modal overlap situation, for which few parameter estimation methods exist. The method is tested on a sample of car floor panel covered with a viscoelastic layer, provided

by Henkel Adhesive Technologies. The strong point of the proposed approach is that a single measurement of driving-point mobility is needed and that free boundary conditions can be used. This allows to rapidly characterise multiple panels, which is adequate to an industrial context.

The acoustic black hole effect in plates and beams is a novel passive vibration damping technique which consists in slowing down waves near an edge in order to produce a non-reflecting boundary. The existing approach consists in gradually decreasing the thickness of the structure, according to a power-law profile, from several millimetres to a minimum thickness of several micrometers inflicted by the cutting precision. Such thickness profile is a truncation of an ideal profile smoothly decreasing to zero and thus leads to significant wave reflection, which can be partially compensated by the addition of a thin damping layer. The relevance of such damping technique is that it involves no additional mass, contrarily to conventional damping methods. Realistic physical modelling and practical manufacturing of such thickness profiles are the main challenges of the topic.

In this framework, several aims have been achieved as a result of a collaboration between the Laboratoire d'Acoustique de l'Université du Maine (LAUM) and the Acoustics and Vibration Research Group of the Department of Aeronautical and Automotive Engineering of Loughborough University. The first aim consists in optimising the parameters of the additional damping layer for achieving low reflection with realistic parameters. This is done by means of a numerical tool allowing to predict the reflection matrix and the flexural field of a one-dimensional black hole structure including arbitrarily varying geometrical and mechanical parameters. The method relies on adaptive spatial sampling, which allows to deal with the significantly different orders of magnitude of the thickness of the structure. The model allows to find optimal values for the parameters of the damping layer, as a basis for the practical design of plates and beams.

Several plates were manufactured in the Institut Universitaire de Technologie (IUT) de l'Université du Maine in Le Mans, where the black hole thickness profiles are in the form of a circular pit of power-law thickness, with the minimum thickness at its centre. The black hole pits are placed at one focus of an elliptical plate, or in the focal zone of a parabolic edge within a polygonal plate. The experimental investigations on such plates show that there is a significant reduction of vibration level due to the acoustic black hole effect. In fact, the results show that the vibrational energy is successfully focused towards the black hole pits, where strong dissipation takes place. Furthermore, the measured input mobilities confirm that the addition of a thin damping layer is crucial and leads to a reduction up to 20 dB. As a secondary result, simulations of polygonal plates using the image source method are in accordance with the experimental results. The black hole effect is included in the method by defining an artificial boundary equivalent to the black hole pit plus the focusing parabolic edge. The result shows that the image source method is an appropriate formalism for simulating polygonal plates with acoustic black hole boundaries.

An alternative implementation of the acoustic black hole effect has been investigated by using beams made of a shape-memory polymer, in which the wave velocity can be

controlled by modifying the Young's modulus with a thermal load at one edge of the beam. Numerical and experimental investigations in the case of beams subjected to a temperature gradient according to distance show a significant reduction of vibration level, showing that the acoustic black hole effect can be achieved by using a variation of the Young's modulus. Furthermore, the efficacy of the effect is strongly dependent on the specific temperature profile along the beam and it is observed that the resonant behaviour of the structure completely vanishes with an appropriate thermal load. In addition, using a temperature gradient on a beam having a power-law thickness profile results in a similar reduction of the resonant behaviour of the structure for a less pronounced temperature gradient. This shows that the acoustic black hole effect can be optimised by appropriately taking advantage of the thermoelastic properties of materials.

Ideas for further directions

The image source approach has been used here within particular assumptions, some of which can be eliminated in order to generalise the method. In particular, the boundaries are assumed to be localised along straight lines and only point-source excitation is considered. Including spatially extended sources would allow to treat complex excitations and non-localised boundary conditions. As a first approximation, this can be done by discretising the spatially extended source, the discretisation points being sources on which the present image source approach can be used. Additionally, only flexural waves are considered in the proposed model, i.e. no coupling between out-of-plane and in-plane motions is taken into account. Therefore, the application of the image source to an assembly of plates is here restricted to planar assemblies. Including in-plane motion in the description of plate vibrations would allow to extend the method to plate assemblies occupying a three-dimensional space. Such investigation would consist in considering two propagation equations and twice the number of boundary conditions, leading to 8×8 scattering matrices for junctions and 4×4 reflection coefficients for edges. A significant advantage of the image source formalism is that the image source pattern or cloud is the same for both types of motion. Another limitation of the present method is that the plate assemblies must contain plates of the same material properties and the same thickness. Assemblies of plates of different material would need the consideration of Snell-Descartes laws for wave reflection and transmission at the junctions. The image source approach is adequate for such purpose in that the refracted field can be treated as an apparent translation of the source describing the incident field. Another point that should be given further consideration is diffraction by the plate corners, which is ignored in the model. In fact, the image source approach relies on specular reflection and therefore does not allow to account for such phenomena. Including wave diffraction at the plate corners would then need the use of another formalism than image sources. Also, as shown in chap. 4, including evanescent waves in the formulation of image sources of second and higher orders seems not to be possible using an image source approach.

Real structures are characterised by different degrees of complexity and uncertainty. The most common types of complexity are variability of shape, joint properties and material properties. A major difficulty for assessing structural complexity is the way of taking variability into account as part of the models. Although the image source approach pro-

posed in part I is deterministic, it easily allows to include these three types of variability in a simplified manner. In fact, the specific shape of the plate boundaries only affects the locations of image sources, the boundary conditions determine the contribution weights of image sources and the properties of the propagation medium, such as the material and the thickness, determine the behaviour of flexural waves travelling in the plate. On this basis, it could be possible to undertake investigations on a rather different approach to the image source method. For example, including irregularities on the plate material would be possible by including a flexural wavenumber that depends on the wavenumber coordinates, using for example the formalism developed by Maxit [71] in the case of periodically ribbed plates. The uncertainty on the geometry of the plate boundaries can be addressed in two ways. The first is by performing Monte Carlo simulations for random variations on the plate vertices and the second is to directly generate image sources at random locations, with the same mean free path (see chap. 2) characterising the geometry of reference.

Work is ongoing in LAUM on the acoustic black hole effect. Based on the promising results on academic geometries and polygonal plates presented in part II, the next step would consist in the study of the acoustic black hole effect on materials used in the aerospace or automotive industries for its practical implementation on real structures. An example of this is the use of metallic shape-memory materials such as the nickel-titanium family of alloys, which present remarkable hysteretic damping properties [79]. Also, the improvement of the effect by using wave focusing shows that this is an efficient solution, which requires further attention. In particular, it would be possible to induce wave focusing by using parabolic stiffeners as part of the structure to be damped.

References

[1] J. Aka and J.P. Binet. Vibrations de panneaux revêtus ou assemblés destinés à des structures automobiles. Master's project. École Nationale Supérieure d'Ingénieurs du Mans, February 2009. (In French).

[2] J.B. Allen and D.A. Berkley. Image method for efficiently simulating small-room acoustics. *Journal of the Acoustical Society of America*, 66(4):943–950, 1979.

[3] K. Arcas Castillo. *Simulation numérique d'un réverbérateur à plaque*. PhD thesis, École Nationale Supérieure de Techniques Avancées, 2009. (In French).

[4] J.R.F. Arruda, F. Gautier, and L.V. Donadon. Computing reflection and transmission coefficients for plate reinforcement beams. *Journal of Sound and Vibration*, 307:564–577, 2007.

[5] B.P. Belinskii and D.P. Kouzov. Green-type formulas for flexurally vibrating plates. *Soviet Physics – Acoustics*, 27(5):710–718, 1981.

[6] R.D. Blevins. *Formulas for Natural Frequencies and Mode Shape*. Krieger, 1993.

[7] M. Bonnet. *Advances in Boundary Element Methods*. Springer, 2000.

[8] J. Borish. Extension of the image model to arbitrary polyhedra. *Journal of the Acoustical Society of America*, 75(6):1827–1836, 1984.

[9] A. Le Bot. A vibroacoustic model for high frequency analysis. *Journal of Sound and Vibration*, 211(4):537–554, 1998.

[10] J. Brunskog. Image solution for clamped finite beams. *Journal of Sound and Vibration*, 287(4-5):1057–1064, 2005.

[11] G. Bézine. Boundary integral formulation for plate flexure with arbitrary boundary conditions. *Mechanics Research Communications*, 5(4):197–206, 1978.

[12] K.-S. Chae and J.-G. Ih. Prediction of vibrational energy distribution in the thin plate at high-frequency bands by using the ray tracing method. *Journal of Sound and Vibration*, 240(2):263–292, 2001.

[13] V. Cotoni, P. Shorter, and R. Langley. Numerical and experimental validation of a hybrid finite element-statistical energy analysis method. *Journal of the Acoustical Society of America*, 122(1):259–270, 2007.

[14] T. Courtois and V. Martin. Spectral quality of acoustic predictions obtained by the ray method in coupled two-dimensional damped cavities. *Journal of Sound and Vibration*, 270(1-2):259–278, 2004.

[15] L. Cremer, M. Heckl, and E.E. Ungar. *Structure-Borne Sound – Structural Vibrations and Sound Radiation at Audio Frequencies*. Springer-Verlag, Heibelberg, second edition, 1988.

[16] L. Cremer and H.A. Müller. *Principles and Applications of Room Acoustics*. Applied Science, London, 1982.

[17] CRG Industries. Veriflex shape memory polymer resin, product data sheet. `www.crg-industries.com`.

[18] J. Cuenca, F. Gautier, and L. Simon. Computing high frequency vibrations of polygonal plates by the image source method. In *Second EAA-ASA joint conference, Acoustics'08, Paris*. *Journal of the Acoustical Society of America*, 123:3373, 2008.

[19] J. Cuenca, F. Gautier, and L. Simon. Harmonic green's functions of semi-infinite and convex polygonal plates with arbitrary boundary conditions. *Submitted for publication in the Journal of Sound and Vibration*, 2009.

[20] J. Cuenca, F. Gautier, and L. Simon. The image source method for calculating the vibrations of simply supported convex polygonal plates. *Journal of Sound and Vibration*, 322(4-5):1048–1069, 2009.

[21] J. Cuenca, F. Gautier, and L. Simon. Measurement of complex bending stiffness of a flat panel covered with a viscoelastic layer using the image source method. In *Euronoise 2009*, Edinburgh, 26-28 October 2009.

[22] J. Cuenca, F. Gautier, and L. Simon. Modelling the vibrations of convex polygonal plates by the image source method. In *Noise and Vibration: Emerging Methods (NOVEM)*, Oxford, 5-8 April 2009.

[23] S.M. Dance and B.M. Shield. The complete image-source method for the prediction of sound distribution in non-diffuse enclosed spaces. *Journal of Sound and Vibration*, 201(4):473–489, 1997.

[24] W. Desmet, B. Pluymers, C. Vanmaele, and D. Vandepitte. A review of the wave based prediction technique for efficient interior acoustic analysis. In *Forum Acusticum 2005*, pages 151–160, Budapest, 2005. S Hirzel Verlag.

[25] S. Finnveden. Evaluation of modal density and group velocity by a finite element method. *Journal of Sound and Vibration*, 273(1-2):51–75, 2004.

[26] C.R. Fuller, S.J. Elliott, and P.A. Nelson. *Active Control of Vibration*. Academic Press, 1997.

[27] L. Garibaldi and M. Sidahmed. Matériaux viscoélastiques – atténuation du bruit et des vibrations. *Techniques de l'Ingénieur*, 720:943–950, 2007. (In French).

[28] F. Gautier, J. Cuenca, V.V. Krylov, and L. Simon. Experimental investigation of the acoustic black hole effect for vibration damping in elliptical plates. In *Second EAA-ASA joint conference, Acoustics'08, Paris*. *Journal of the Acoustical Society of America*, 123:3318, 2008.

[29] F. Gautier, M.H. Moulet, and J.C. Pascal. Reflection, transmission and coupling of longitudinal and flexural waves at beam junctions. Part I: measurement methods. *Acta Acustica united with Acustica*, 92:982–997, 2006.

[30] V.B. Georgiev, J. Cuenca, F. Gautier, M.A. Molerón Bermúdez, L. Simon, and V.V. Krylov. Numerical and experimental investigation of the acoustic black hole effect for vibration damping in beams and elliptical plates. In *Euronoise 2009*, Edinburgh, 26-28 October 2009.

[31] V.B. Georgiev, J. Cuenca, L. Simon, F. Gautier, and V.V. Krylov. Damping of structural vibrations in beams and elliptical plates using the acoustic black hole effect. *Submitted for publication in the Journal of the Acoustical Society of America*, July 2009.

[32] C.F. Gerald and P.O. Wheatley. *Applied Numerical Analysis*. Addison Wesley, New York, 1989.

[33] D.J. Gorman. *Vibration Analysis of Plates by the Superposition Method*. World Scientific, Singapore, 1999.

[34] K.J. Graff. *Wave Motion in Elastic Solids*. Dover, New York, 1991.

[35] T. Guignard. *Étude des fondements physiques possibles des concepts numériques utilisés dans les méthodes d'acoustique géométrique*. PhD thesis, École Polytechnique Fédérale de Lausanne, 2006. (In French).

[36] T. Guignard and V. Martin. Adjusted complex position of extra sources in the image source method. In *13th International Congress on Sound and Vibration*, Vienna, 2-6 July 2006.

[37] R. Gunda, S. M. Vijayakar, and R. Singh. Flexural vibration of an infinite wedge. *Journal of the Acoustical Society of America*, 102(1):326–334, 1997.

[38] R. Gunda, S. M. Vijayakar, R. Singh, and J.E. Farstad. Harmonic Green's functions of a semi-infinite plate with clamped or free edges. *Journal of the Acoustical Society of America*, 103(2):888–899, 1998.

[39] R. Gunda, S.M. Vijayakar, and R. Singh. Method of the images for the harmonic response of beams an rectangular plates. *Journal of Sound and Vibration*, 185(2):791–808, 1995.

[40] M. Géradin and D. Rixen. *Mechanical Vibrations – Theory and Application to Structural Dynamics*. John Wiley & Sons, second edition, 1997.

[41] B. Van Hal, W. Desmet, D. Vandepitte, and P. Sas. A coupled finite element - wave based approach for the steady state dynamic analysis of acoustic systems. *Journal of Computational Acoustics*, 11(2):255–283, 2003.

[42] F. Hartmann and R. Zotemantel. The direct boundary element method in plate bending. *International journal for numerical methods in engineering*, 23:2049–2069, 1986.

[43] A. Hayir and I. Bakirtas. A note on a plate having a circular cavity excited by plane harmonic SH waves. *Journal of Sound and Vibration*, 271:241–255, 2004.

[44] C. Hu, X.-Q. Fang, and W.-H. Huang. Multiple scattering of flexural waves in a semi-infinite thin plate with a cutout. *International Journal of Solids and Structures*, 44:436–446, 2007.

[45] Z.Y. Huang and W.K. Jiang. An effective method calculating acoustic Green's function for closed rectangular cavity using the Ewald's summation technique. *Acta Acustica united with Acustica*, 93:853–856, 2007.

[46] S.W. Kang. Free vibration analysis of arbitrarily shaped plates with a mixed boundary condition using non-dimensional dynamic influence functions. *Journal of Sound and Vibration*, 256(3):533–549, 2002.

[47] S.W. Kang and S.N. Atluri. Free vibration analysis of arbitrarily shaped polygonal plates with simply supported edges using a sub-domain method. *Journal of Sound and Vibration*, 327(3-5):271–284, 2009.

[48] E.M. Kerwin Jr. Damping of flexural waves by a constrained viscoelastic layer. *The Journal of the Acoustical Society of America*, 31:952, 1959.

[49] D.R. Kincaid and E.W. Cheney. *Numerical Analysis – Mathematics of Scientific Computing*. American Mathematical Society, 2009.

[50] Jan Klesa. Experimental evaluation of the rheological properties of veriflex shape memory polymer. Master's project. Département de Mécanique Appliquée, Université de Franche-Comté, 2009.

[51] V. Kralovic and V.V. Krylov. Damping of flexural waves in tapered rods of power law profile: Experimental studies. In *Proceedings of the Institute of Acoustics*, volume 5 of *29*, pages 66–73, 2007.

[52] V. Kralovic and V.V. Krylov. Some new methods of damping impact-induced vibrations in badminton racquets. In *Proceedings of the Institute of Acoustics*, volume 2 of *30*, pages 155–162, 2007.

[53] U.R. Kristiansen, A. Krokstad, and T. Follestad. Extending the image method to higher-order reflections. *Applied Acoustics*, 38(2-4):195–206, 1993.

[54] V.V. Krylov. New type of vibration dampers utilising the effect of acoustic 'black holes'. *Acta Acustica United With Acustica*, 90:830–837, 2004.

[55] V.V. Krylov and F.J.B.S. Tilman. Acoustic 'black holes' for flexural waves as effective vibration dampers. *Journal of Sound and Vibration*, 274:605–619, 2004.

[56] V.V. Krylov and R.E.T.B. Winward. Experimental investigation of the acoustic black hole effect for flexural waves in tapered plates. *Journal of Sound and Vibration*, 300:43–49, 2007.

[57] H. Kuttruff. *Room Acoustics*. Applied Science, London, 1973.

[58] P. Ladevèze. The variational theory of complex rays for the calculation of medium-frequency vibrations. *Engineering with Computers*, 18:193–214, 1999.

[59] E.A. Lehmann and A.M. Johansson. Prediction of energy decay in room impulse responses simulated with an image-source model. *Journal of the Acoustical Society of America*, 124(1):269–277, 2008.

[60] A.W. Leissa. *Vibration of Plates*. NASA, Washington D.C., 1969.

[61] L.M. Lyamshev. The theory of vibrations of nonhomogeneous elastic plates. *Soviet Physics – Acoustics*, 10(1):65–69, 1964.

[62] R.H. Lyon and R.G. Dejong. *Theory and Application of Statistical Energy Analysis*. Butterworth-Heinemann, Boston, 1995.

[63] R.H. Lyon and G. Maidanik. Power flow between linearly coupled oscillators. *Journal of the Acoustical Society of America*, 34:623, 1962.

[64] C.F. Lü, Y.Y. Lee, C.W. Lim, and W.Q. Chen. Free vibration of long span continuous rectangular Kirchhoff plates with internal rigid line supports. *Journal of Sound and Vibration*, 297:351–364, 2006.

[65] B.R. Mace. Wave reflection and transmission in beams. *Journal of Sound and Vibration*, 97(2):237–246, 1984.

[66] B.R. Mace, D. Duhamel, M.J. Brennan, and L. Hinke. Finite element prediction of wave motion in structural waveguides. *Journal of the Acoustical Society of America*, 117(5):2835–2843, 2005.

[67] V. Martin. *Éléments d'Acoustique Générale – De Quelques Lieux Communs de l'Acoustique à une Première Maîtrise des Champs Sonores*. Presses Polytechniques et Universitaires Romandes, 2007. (In French).

[68] V. Martin and T. Guignard. Justification of the image sources in ray-tracing method. In *12th International Congress on Sound and Vibration*, Lisbon, 11-14 July 2005.

[69] V. Martin and T. Guignard. Image-source method and truncation of a series expansion of the integral solution – case of an angular sector in two dimensions. *Journal of the Acoustical Society of America*, 120(2):597–610, 2006.

[70] V. Martin and T. Guignard. Graft of the boundary integral method onto the image-source method for vehicle acoustics. In *14th International Congress on Sound and Vibration*, Cairns, 9-12 July 2007.

[71] L. Maxit. Wavenumber space and physical space responses of a periodically ribbed plate to a point drive: A discrete approach. *Applied Acoustics*, 70(4):563 – 578, 2009.

[72] F.P. Mechel. Improved mirror source method in room acoustics. *Journal of Sound and Vibration*, 256(6):873–940, 2002.

[73] M.A. Mironov. Propagation of a flexural wave in a plate whose thickness decreases smoothly to zero in a finite interval. *Soviet Physics – Acoustics*, 34:318–319, 1988.

[74] M.A. Molerón Bermúdez. Amortissement de vibrations par effet trou noir acoustique. Master's project, September 2009. (In French).

[75] P.M. Morse and H. Feshbach. *Methods of Theoretical Physics*. McGraw-Hill, New York, 1953.

[76] M.H. Moulet. *Les jonctions en mécanique vibratoire: représentation par matrice de diffusion et caractérisation expérimentale pour des poutres assemblées*. PhD thesis, Université du Maine, 2003. (In French).

[77] M.H. Moulet and F. Gautier. Reflection, transmission and coupling of longitudinal and flexural waves at beam junctions. Part II: experimental and theoretical results. *Acta Acustica united with Acustica*, 93:37–47, 2007.

[78] J.M. Muggleton, T.P. Waters, B.R. Mace, and B. Zhang. Approaches to estimating the reflection and transmission coefficients of discontinuities in waveguides from measured data. *Journal of Sound and Vibration*, 307(1-2):280–294, 2007.

[79] NASA. *Damping Structural Vibrations with Shape-Memory Metals*. University Press of the Pacific, 2005.

[80] A.D. Nashif, D.I.G. Jones, and J.P. Henderson. *Vibration Damping*. Wiley-Interscience, 1985.

[81] A.N. Norris. Flexural waves on narrow plates. *Journal of the Acoustical Society of America*, 113:2647, 2003.

[82] A.N. Norris, V.V. Krylov, and I.D. Abrahams. Flexural edge waves and comments on "A new bending wave solution for the classical plate equation" [J. Acoust. Soc. Am. 104, 2220-2222 (1998)]. *Journal of the Acoustical Society of America*, 107(3):1781–1784, 2000.

[83] B. Pluymers, W. Desmet, D. Vandepitte, and P. Sas. On the use of a wave based prediction technique for steady-state structural-acoustic radiation analysis. *Journal of Computer Modeling in Engineering & Sciences*, 7(2):173–184, 2005.

[84] G. Rabbiolo, R.J. Bernhard, and F.A. Milner. Definition of a high-frequency threshold for plates and acoustical spaces. *Journal of Sound and Vibration*, 277:647–667, 2004.

[85] J.W.S. Rayleigh. *The Theory of Sound*. The Macmillan Company, 1896. Dover, New York, 1945.

[86] Y. Ren and C.F. Beards. Identification of joint properties of a structure using FRF data. *Journal of Sound and Vibration*, 186(4):567 – 587, 1995.

[87] D. Ross, E.E. Ungar, and E.M. Kerwin. Damping of plate flexural vibrations by means of viscoelastic laminae. In J.E. Ruzicka, editor, *Structural Damping*, pages 49–87, Oxford, 1960. Pergamon Press.

[88] P. Rouch and P. Ladevèze. The variational theory of complex rays: a predictive tool for medium frequency vibrations. *Computer Methods in Applied Mechanics and Engineering*, 192:3301–3315, 2003.

[89] M.R. Schroeder. Statistical parameters of the frequency response curves of large rooms. *Journal of the Audio Engineering Society*, 35:299–306, 1987.

[90] E. Skudrzyk. The mean-value method of predicting the dynamic response of complex vibrators. *Journal of the Acoustical Society of America*, 67(4):1105–1135, 1980.

[91] W. Soedel. *Vibrations of Shells and Plates*. Marcel Dekker, New York, 2004.

[92] M. Stern. A general boundary integral formulation for the numerical solution of plate bending problems. *International journal of solids and structures*, 15:769–782, 1979.

[93] R. Szilard. *Theories and Applications of Plate Analysis: Classical, Numerical and Engineering Methods*. John Wiley and sons, New York, 2004.

[94] C. Vanmaele, W. Desmet, and D. Vandepitte. On the use of the wave based method for the steady-state dynamic analysis of three-dimensional plate assemblies. In *Proceedings of the International Conference on Noise and Vibration Engineering*, pages 1002–1013, Leuven, 2004.

[95] C. Vanmaele, D. Vandepitte, and W. Desmet. An efficient wave based prediction technique for plate bending vibrations. *Computer Methods in Applied Mechanics and Engineering*, 196(33-34):3178–3189, 2007.

[96] C. Vemula, A.N. Norris, and G.D. Cody. Attenuation of waves in plates and bars using a graded impedance interface at edges. *Journal of Sound and Vibration*, 196(1):107–127, 1996.

[97] Y. Waki, B.R. Mace, and M.J. Brennan. Free and forced vibrations of a tyre using a wave/finite element approach. *Journal of Sound and Vibration*, 323(3-5):737 – 756, 2009.

[98] Z. Wang and A.N. Norris. Waves in cylindrical shells with circumferential submembers: a matrix approach. *Journal of the Acoustical Society of America*, 181(3):457–484, 1995.

[99] E.G. Williams. *Fourier Acoustics: Sound Radiation and Nearfield Acoustic Holography*. Academic Press, 1999.

[100] M.L. Williams, R.F. Landel, and J.D. Ferry. The temperature dependence of relaxation mechanisms in amorphous polymers and other glass-forming liquids. *Journal of the American Chemical Society*, 77:3701–3707, 1955.

[101] Ling Ye, George Cody, Minyao Zhou, Ping Sheng, and Andrew N. Norris. Observation of bending wave localization and quasi mobility edge in two dimensions. *Physical Review Letters*, 69(21):3080–3083, Nov 1992.

[102] O.C. Zienkiewicz and R.L. Taylor. *The Finite Element Method for Solid and Structural Mechanics*. Butterworth-Heinemann, 2005.

Wave models for the flexural vibrations of thin plates

Model of the vibrations of polygonal plates by the image source method
Vibration damping using the acoustic black hole effect

Jacques Cuenca

Doctoral thesis in Acoustics, Université du Maine, Le Mans, France

Flexural vibrations of thin structures are strongly related to sound radiation and structural damage, for which they deserve careful attention in many domains of science and engineering. Two aspects that are of crucial importance are accurate tools for the prediction and analysis of vibrations, which require appropriate modelling methods and numerical tools, and efficient vibration damping. The first aim of this thesis is to develop a model for predicting the flexural vibrations of thin polygonal plates of arbitrary convex shape in the medium and high frequency ranges. The second aim is to contribute to the development and understanding of the acoustic black hole effect as an alternative technique for passive vibration damping. Those two topics are developed in two separate parts.

In the first part of the dissertation, a model of the flexural vibrations of thin convex polygonal plates based on the image source method is presented. Considering a polygonal plate excited by a harmonic point source, the image source method consists in describing the successive wave reflections on the boundaries of the plate as contributions from virtual sources, obtained by successive symmetries of the original source with respect to the boundaries. First, the approach is applied to simply supported polygonal plates, which present the particularity that the reflection coefficient of the boundaries does not depend on the angle of incidence of waves. Then, the approach is generalised to the case of arbitrary boundary conditions in the case of individual plates and plate assemblies. This is achieved by representing the contributions of the different image sources as continuous sums of elementary waves. The relative weights of such elementary waves are determined by the reflection and transmission matrices of the boundaries, obtained from a state vector approach. It is shown that the method is particularly suitable for mid- and high-frequency dynamics, in that its accuracy is improved with an increase in frequency or structural damping. A tool for estimating the Young's modulus and structural damping ratio of highly damped flat panels is also proposed, using the image source method as a means of separately identifying the influence of stiffness and damping in the response.

The second part of the dissertation is an investigation on vibration damping using the acoustic black hole effect. It is well known that a flexural wave travelling in a thin plate or beam slows down in a zone of decreasing thickness. Thus, if the thickness decreases sufficiently smoothly to zero, the wave velocity reaches zero and the wave stops travelling, without being reflected back. Such is the principle of the so-called acoustic black hole effect. Because of technological difficulties in achieving such a thickness profile, a thin damping layer partially covering the structure allows to compensate for non-zero reflection, leading to efficient vibration damping with a low amount of additional mass. In the present study, a model of the flexural vibrations of such profile is proposed, allowing to determine optimal geometrical and material properties for the damping layer allowing to maximise vibration damping. Experimental studies are then carried on plates whose boundaries induce a focusing of waves towards a zone treated with the thickness profile. The measured responses show a reduction of vibration level up to 20 decibels. An alternative implementation of the acoustic black hole effect is investigated, consisting in decreasing wave velocity near the edge of a beam by decreasing its Young's modulus. This is achieved by using a temperature gradient in a shape-memory polymer, leading to similar results to those obtained by a geometrical control of thickness. Finally, combining the thermoelastic and geometrical approaches leads to significant vibration damping.